Physically-based meso-scale modelling of unidirectional CFRPs for impact loading applications

Daniel Martin Thomson

Solid Mechanics and Materials Engineering Group
Department of Engineering Science
University of Oxford

Thesis Submitted for the Degree of
Doctor of Philosophy

Trinity Term 2019

Abstract

While the physical understanding of UD CFRPs and the processes that govern their mechanical response is continuously improving, macro-scale modelling still often relies on empirical, over-simplified constitutive laws and failure criteria. In addition, many aspects of the rate-dependency and pressure or multiaxial loading effects on the behaviour of UD CFRPs, which are crucial for applications where composite structures may be subjected to dynamic loading, are still not fully understood.

The present work aimed to investigate some of these aspects and propose a more physically-based constitutive model for macro-scale applications. Since, in UD CFRPs, the complex rate and pressure effects observed in most of the failure modes come from the properties of the polymer matrix, where possible, the proposed criteria have been derived from the matrix-dominated nonlinear behaviour.

The main new development in this work is the proposal of a physically-based localisation plane plasticity theory that is able to describe all of the complex pressure and strain rate dependencies observed in the matrix-dominated nonlinear behaviour as the effect of the frictional rate-dependent shear response acting on different localisation planes. However, further research is needed to establish the physical meaning behind some of the model parameters and their relation to the constituent properties, especially with regard to the effects of strain rate.

Next, an in-depth study into the effects of strain rate on IFF has been performed, and the relation between this failure mode and nonlinear constitutive behaviour has been explored by comparing the yield and failure envelopes and criteria.

Last, an experimental investigation into the effects of strain rate and off-axis loading on fibre compression failure has been carried out, showing a significant increase in strength under dynamic loading, which is accurately predicted by Budiansky and Fleck’s fibre kinking theory when coupled with a rate-dependent

constitutive model. However, the fibre kinking theory was unable to capture the effects of shear, severely under-predicting the off-axis compression strengths.

Instead, a more pragmatic approach has been proposed to predict the longitudinal compression strength under multiaxial stress states, using the damage to the shear modulus from the off-axis loads to degrade the uniaxial compression strength.

The above models were coupled with a smeared damage formulation of the kind proposed by Pinho for the LaRC criteria, and implemented in an explicit FE solver to produce a ‘unified’ model for UD CFRPs, where all rate and pressure effects derive from the frictional rate-dependent shear behaviour along certain localisation planes. This model has been validated against a series of coupon-scale tests, showing its ability to accurately describe the nonlinear response and strengths across different strain rates and off-axis loading cases.

Finally, to conclude the present study, a series of component-scale plate impact tests were carried out to benchmark the model’s performance at higher loading rates and length scales, from which a number of areas for future work have been identified.

Acknowledgements

I would like to begin by thanking my supervisor, Nik Petrinic, who made this all possible, for somehow, against great odds, always finding the time to support and guide me through the challenges I inevitably came across during my research – it is truly appreciated.

Next I would like to thank my co-supervisor, Borja Erice, who made it all easier, whose expertise in areas of constitutive modelling proved invaluable, and whose continued assistance and attention to detail elevated the quality of my work to a higher standard.

Just as important, I would like to acknowledge the financial support from Rolls-Royce plc, through the Solid Mechanics University Technology Centre at the University of Oxford, which allowed me to pursue this research in the first place.

I would also like to thank Prof JN Reddy, Prof Antoine Jerusalem, Dr Hao Cui, and Dr Antonio Pellegrino, whose additional direction and supervision in times of need was crucial and cannot be understated; as well as Karen, Hisham, Jeff, Stuart, Graham, Pete, and all other administrative and technical support staff at Oxford without whom I never would have made it this far; and, finally, all the people at the Impact Engineering Laboratory who embraced me and who it was a pleasure to work with throughout my time here.

Last but not least, I would like to thank my family and loved ones, especially my parents, Graham and Clare, my brother, Rory, and my sister, Zoë, who put up with me for all these years; my friends, old and new, who had to put up with me less and less as I became more consumed with my research; and all of the other in my life who distracted me from my work over these past four years, making it so much slower but also so much more enjoyable than it would have been otherwise.

Table of Contents

List of Figures

List of Tables

Chapter 1

Introduction

Thanks to their high specific strength and stiffness, fibre-reinforced polymers (FRPs) in general, and carbon fibre composites (CFRPs) in particular, have become an integral part of many modern industries in the transportation sector. In the automotive, naval and aerospace industries, FRPs are steadily replacing traditional metallic materials in a growing number of applications, in part to try and comply with upcoming emissions and efficiency regulations [1,2]. While their use was at first largely limited to simple structural components, such as skin and body panels on aeroplane wings or fuselage, more and more they are being considered for increasingly complex, high-end, applications, such as the Rolls Royce Advance3 and UltraFan aircraft engines, which will both use CFRP/Titanium hybrid (CTi) fan blades, depicted in Figure 1.1 [3].

Figure 1.1. CFRP-Titanium hybrid (CTi) fan blades used in the Rolls Royce Advance3 and UltraFan demonstrator engines [4,5].

At the same time, even though research on these materials has matured significantly since the 1950s and 60s, their use in ever more demanding applications, especially in those subject to potential impact or crash loading, requires even deeper understanding of material behaviour and failure mechanisms and more reliable predictive capabilities. For dynamic loading conditions in particular, properly accounting for effects of pressure, multi-axial loading, strain rate, and even temperature becomes crucial to the design process. However, the complex heterogenous nature of fibre composite materials, means that many of these aspects are not yet fully understood to a sufficient degree of certainty. In addition, with numerical modelling tools such as Finite Element Analysis (FEA) replacing physical experimentation in many stages of the industrial design process, there is a need not only for better theoretical understanding but also for more robust and accurate modelling capabilities.

1.1. Aim and objectives

Therefore, building on the work that has been done to understand the behaviour of CFRPs under quasi-static loading conditions, the present investigation aims to improve the current understanding of and predictive modelling capabilities for CFRP composites under dynamic loading, with a special focus on strain rate and multi-axial loading effects.

However, there are multiple different types of CFRP composites depending on the length, orientation, and configuration of the carbon fibres. The present work focused on the study and modelling of unidirectional (UD) CFRPs primarily at the meso- or ply-scale.

Although there are many other ways of stacking and weaving carbon fibres, each with its own advantages and drawbacks, unidirectional CFRPs, composed of long fibres in a single direction, are still widely used in many applications and may be considered one of the basic building blocks for many of the more complex composites. Therefore, while other types of laminates were not directly addressed in this investigation, parts of this work may also be applicable to unidirectional yarns or plies within different types of weaves and multi-level stacking in more complex laminates.

In addition, since one of the main motivations for the present work was the improvement of constitutive modelling capabilities for industrial applications, the developed solutions had to be practical for structural or component scale models. By focusing on modelling at the meso-scale, defined here as the length scale where unidirectional fibres and matrix within a ply can be considered as a homogeneous continuum, Figure 1.2, this can be achieved without excessively compromising the reliability and physical basis of the solution, whereas larger macro-scale modelling may tend towards oversimplification of the material behaviour.

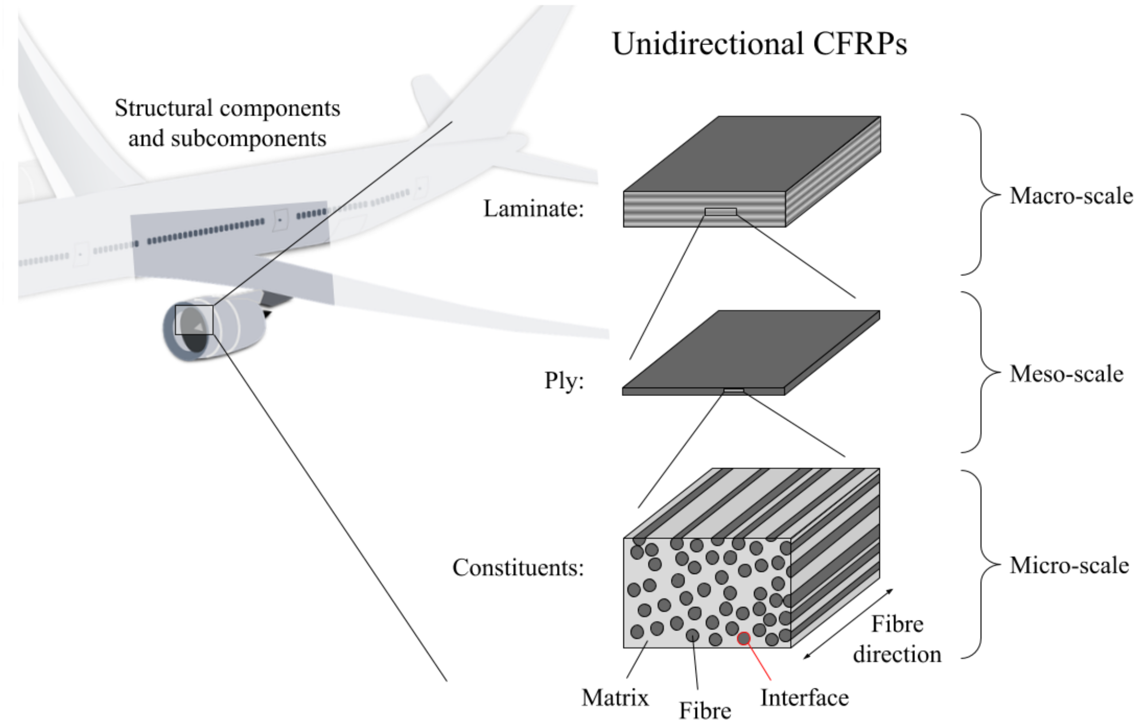

Figure 1.2. Typical structure of UD CFRP laminates across different length scales.

Within the scope defined above, the objectives were, more specifically, to evaluate the current understanding and modelling capabilities of each of the major deformation and failure modes observed in UD CFRPs, with a focus on some of the key aspects for impact or dynamic loading applications, such as rate-dependency and the effects of pressure or multi-axial stresses. To do so, each of the main deformation modes have been studied independently, starting with the underlying constitutive behaviour before failure and then each of the three failure modes observed in UD CFRPs, matrix or inter-fibre fracture (IFF), fibre tension, and fibre compression or kinking (FK). As the scope of the project is limited to the bulk UD material, inter-ply failure or delamination is not explicitly covered except to note that in certain scenarios it may be treated as a specific case of IFF.

Where possible, available experimental data from the literature was used for characterisation of the material behaviour and validation of any investigated models. However, in certain cases it was necessary to produce new experimental data, especially for dynamic and off-axis loading in certain failure modes.

Therefore, throughout the project, the Hexcel IM7/8552 UD composite, which is a commercially available CFRP made from a high performance carbon fibre prepreg and a high strength structural epoxy matrix [6,7], is used for all experimental and modelling work because of the wealth of data already available on this material in the literature.

Finally, where current theories were found lacking, either modifications to some of the existing models or entirely new models have been proposed within the numerical modelling framework presented in the following section.

1.2. Numerical modelling framework

Since one of the principal objectives revolves around modelling of CFRP composites, which are nonlinear and time-dependent in nature, at the component or subcomponent scales, which tends to involve complex geometries and loading conditions, the numerical modelling work will be carried out using the Finite Element Method (FEM) with explicit time integration. In explicit FEM, dynamic problems can be solved incrementally in time by iteratively solving the governing Partial Differential Equations (PDEs), in this case the equation of motion, discretised into sufficiently small spatial elements and time steps, following a procedure of the type described in Figure 1.3 [8,9].

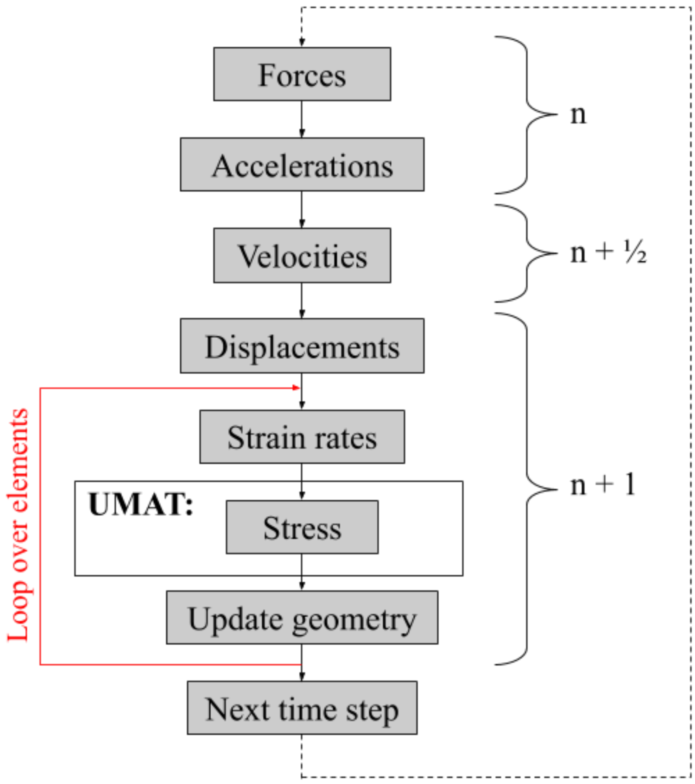

Figure 1.3. Simplified flowchart of the central difference scheme used for the numerical integration of the equation of motion in explicit time integration FEM solvers, such as LS-DYNA [8].

Using this method, the equation of motion is evaluated every time step, at a time $t_{(n)}$ and used to update the displacements at the following time step, $t_{(n+1)}$. To complete the loop, the internal stresses in the material must be determined from the applied strain increments so that the forces for the next iteration can be obtained. This is where the material behaviour must be accurately represented by defining a series of governing laws to describe its response to successive strain increments.

In the present study, the commercial explicit FEM solver, LS-DYNA R9.0 [10], is used for the numerical modelling, as it allows for user-defined material behaviour in the form of a user material subroutine or ‘UMAT’ [11], with which new constitutive laws and failure criteria can be implemented.

The user-defined material model has been developed for use with single integration point 8-node solid, or hexahedral, elements in LS-DYNA version R9.0, to describe the UD CFRP material at the meso-scale. Therefore, a single element will be able to represent a region of material with a single material orientation. For multi-directional laminates, different elements must be used to represent the material within different plies.

The subroutine, written in the FORTRAN language and compiled with the rest of the LS-DYNA solver, accepts a series of arguments describing the applied strain increments and the state of the material at the end of the previous time step and must return the updated state of the material at the end of the current step. To do so, the material behaviour is broken down into the following sections within the user-defined subroutine, as illustrated in Figure 1.4. The model begins with the underlying constitutive laws for the initial elastic and nonlinear behaviour, implemented as a plasticity model based on Puck’s localisation plane (LP) theory [12], and is followed by the failure criteria and damage laws for each of the three failure modes.

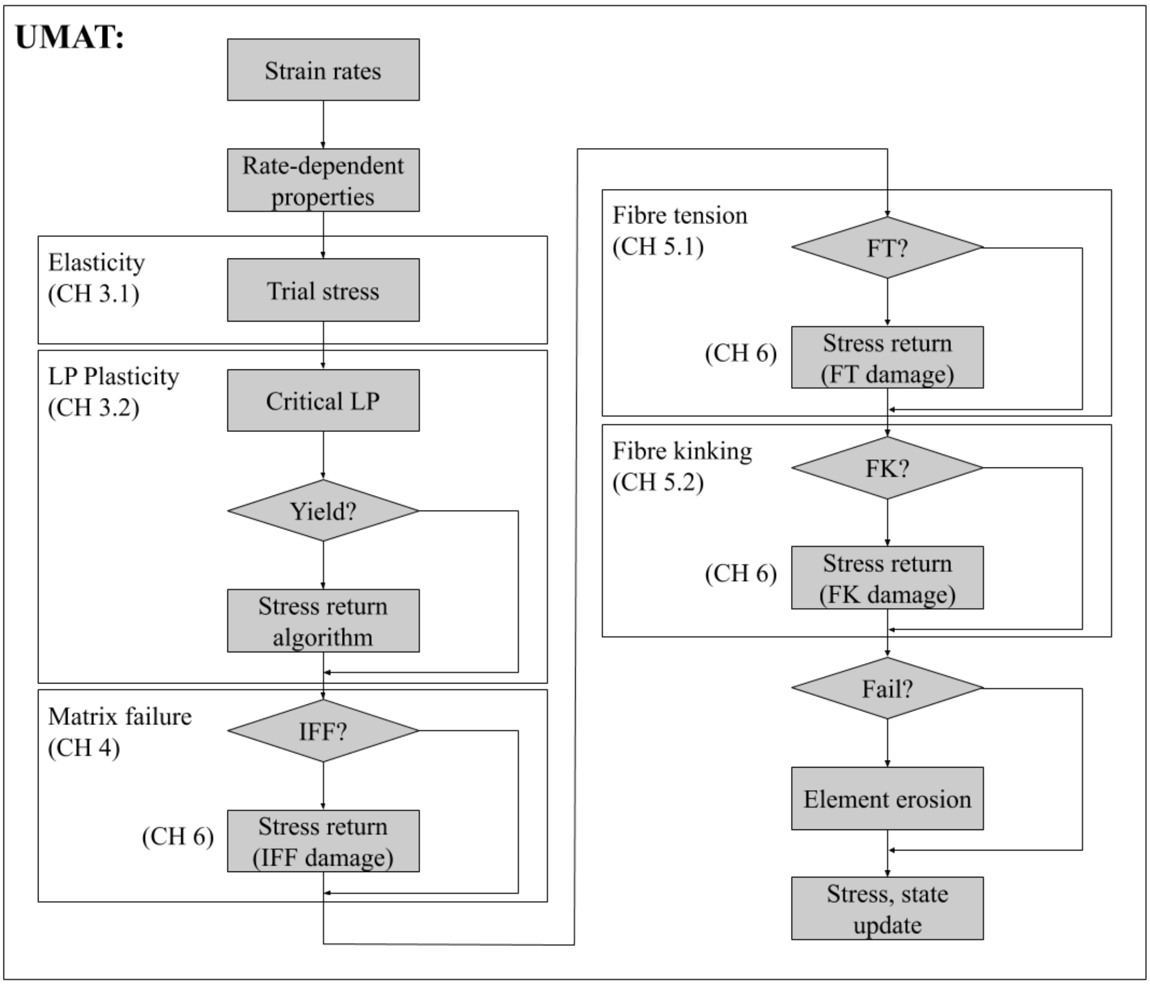

Figure 1.4. Simplified flowchart describing the main components of the user-defined material subroutine.

1.3. Thesis layout

The present study, which consists of not only numerical modelling work but also new experimental characterisation and validation work, will be presented following a similar structure to that of the material model outlined in Figure 1.4.

Chapter 2 presents an initial overview of the literature on UD CFRP materials, where the specific areas needing the most work within each of the main deformation and failure modes have been identified.

Chapter 3 then describes the work done on the underlying constitutive behaviour before failure, starting with the approach used to model the rate-dependent anisotropic elastic behaviour in section 3.1. Following that, a simple, physical model based on Puck's localisation plane theory [12] is proposed to explain the complex macro-scale effects of pressure and strain rate on the matrix-dominated nonlinear behaviour in section 3.2, parts of which have been published in [13,14]. In addition, since the initial literature review found the inter-fibre fracture and fibre kinking failure modes to be strongly related to the matrix-dominated nonlinear behaviour, the matrix and fibre failure criteria presented in the following chapters, have been derived from this proposed LP plasticity model.

Chapter 4 presents the work done on matrix or inter-fibre fracture, for which a series of quasi-static and dynamic off-axis loading tests have been carried out to complement the data available in the literature and used to investigate the effects of strain rate on this failure mode, parts of which have been published in [15]. In addition, the relation between the nonlinear constitutive model in 3.2 and well-established IFF theories and failure criteria from the literature has been explored.

Chapter 5 then presents the work done on fibre failure modes. Section 5.1 simply describes the criterion used for fibre tension failure and includes no new developments, as the literature review showed it to be already well understood and it exhibits no significant rate-dependency or interactions with other modes. This section is included for the sake of completeness, so as to fully define the constitutive model used in the final validation and benchmarks chapter. Section 5.2, in contrast, includes novel experimental work to characterise the longitudinal compression or fibre kinking strength of UD CFRPs under quasi-static and dynamic off-axis loading. These experiments are then used to study the validity of leading theories used to explain this particular type of failure and to propose an improved model for its prediction under multi-axial loading conditions. As with the work in Chapter 4, the relation between this failure mode and the matrix-dominated nonlinear behaviour has also been explored and the proposed criterion derives all pressure- and rate-dependent behaviour from the model in section 3.2. The quasi-static experimental study has been published in [16] and the remaining dynamic and modelling work has been submitted for publication in [17].

Chapter 6, like section 5.1 before it, is included for completeness' sake, as it contains no new developments, and describes the smeared damage formulation used with the failure criteria in Chapter 4 and Chapter 5 to describe damage evolution in the developed material model. The implemented smeared damage approach is based on the work by Pinho in [18] and Wiegand in [19].

With the work presented up to this point, a complete constitutive model for UD CFRPs can be defined, where all complex interactions, rate-, and pressure-effects are directly derived from the localisation plane plasticity model presented in section 3.2. In this way, reducing the number of independent assumptions and providing a less empirical and more unified theory for the different aspects of the material response.

Chapter 7 then provides a comprehensive series of FE validation and benchmark tests for the developed model. In 7.1, different quasi-static and dynamic off-axis loading cases are simulated, showing the model's ability to capture all major deformation and failure modes. Next, in 7.2 a series of ballistic impact tests have been used to benchmark the model's performance at the application or component scale and to investigate its limitations and areas for future work. The ballistic impact test data and some preliminary numerical results using an earlier version of the model were presented in [20].

Chapter 8 finally presents a general summary and overall conclusions for the presented work and outlines the main areas identified for potential improvement in the future.

Chapter 2

Literature Review

Since they were first developed in the 1930s, FRP and later CFRP composites have been researched extensively for their potential use in the aviation industry in particular [21]. The following literature review aims to give a comprehensive outline of the current state of research on UD CFRPs in order to justify the specific objectives outlined in the introduction chapter. However, it will not cover every topic in depth. For each of the main developments presented in this thesis, a more detailed account of the relevant literature will be included as new concepts and ideas are introduced.

This initial review is divided into two main sections: the first covering the experimental work that has been done to characterise and understand the behaviour and failure mechanisms observed in UD CFRPs; and the second describing the models and failure theories that best explain these experimental observations.

2.1. Material properties and mechanical behaviour

As was mentioned in the introduction, UD CFRPs consist of long unidirectional fibres embedded within a polymeric matrix. For modern composites, the ratio between fibre and matrix volume, or fibre volume fraction, is typically around 60%, as is the case for the specific IM7/8552 composite used in this study [6]. This combination of different constituents is what gives the resulting composite its complex macroscopic properties, such as material anisotropy or the different modes of failure that can occur under different loading conditions. Therefore, to understand the overall behaviour of the composite, it is also crucial to understand the properties of each of its constituents as well as the macroscopic deformation and failure mechanisms that result from the combination of the two.

For UD CFRPs, in the transverse direction to the fibre reinforcement the material response is dominated by the relatively weak properties of the matrix, resulting in nonlinear shear behaviour, caused by yielding and damage in the matrix and fibre-matrix interfaces, and eventual inter-fibre fracture (IFF). In addition, when multiple plies are stacked to form a laminated composite, similar behaviour can be observed in the resin-rich areas between them, which are susceptible to inter-ply failure, or delamination.

On the other hand, in the direction of the fibre reinforcement, or longitudinal direction, the material response is dominated by the fibre properties, which tend to have high strength and stiffness and show little or no sign of damage before catastrophic failure. However, in this direction, the material can exhibit very different behaviour in tension and in compression due to initial fibre waviness, with even slight differences observed in the elastic modulus [6,22]. This imperfect alignment of the fibres tends to correct itself in tension, increasing the stiffness of the composite with respect to the material response under compression, where the fibres eventually buckle at loads far below their tensile strength [6,22,23].

Previous research in all of these areas will be described in the following sections with a focus on strain rate effects. In studying these effects, a number of different experimental methodologies have been developed to test materials at quasi static and dynamic loading rates. On the one hand, quasi-static testing is usually performed using screw-driven or hydraulic universal testing machines (UTM). For dynamic testing, on the other hand, a number of different methods can be used. With the correct damping solutions, hydraulic machines have been used to test materials at strain rates between around 1 and 200 s^{-1} [24,25]. Similarly, a drop weight set-up can be used with different drop heights to generate strain rates above 10 s^{-1} [26]. However, in the last few decades the combination of the Split Hopkinson Bar (SHB) with high-speed cameras has become increasingly popular method for high-rate dynamic testing at rates in the order of 100 s^{-1} and above. Typically, these systems are configured either for tension, in the Split Hopkinson Tension Bar (SHTB), or for compression loading, in the Split Hopkinson Pressure Bar (SHPB). However, more complex set ups designed for other types of loading cases can be found in the literature [27–31].

2.1.1. Constituent properties

The carbon fibres used in CFRPs are typically obtained by carbonisation or graphitisation of polymeric fibres, producing filaments 5 to 10 micrometres in diameter with an atomic structure similar to that of graphite. These are then bundled together into tows containing thousands of individual filaments [32]. The filaments have very high strength and stiffness in tension, typically of the order of 400 GPa and 4000 MPa, respectively [32]. However, they lack lateral rigidity without additional support. In tension, the fibres tend to fail in a sudden catastrophic manner, which has been shown to be rate-independent [33], as can be seen in Figure 2.1 below. The specific IM7 fibres used in this study are surface treated, PAN-based fibres available in 12K tows and have a diameter of 5.2 microns, elastic modulus 276 GPa and tensile strength of approximately 5500 MPa [7].

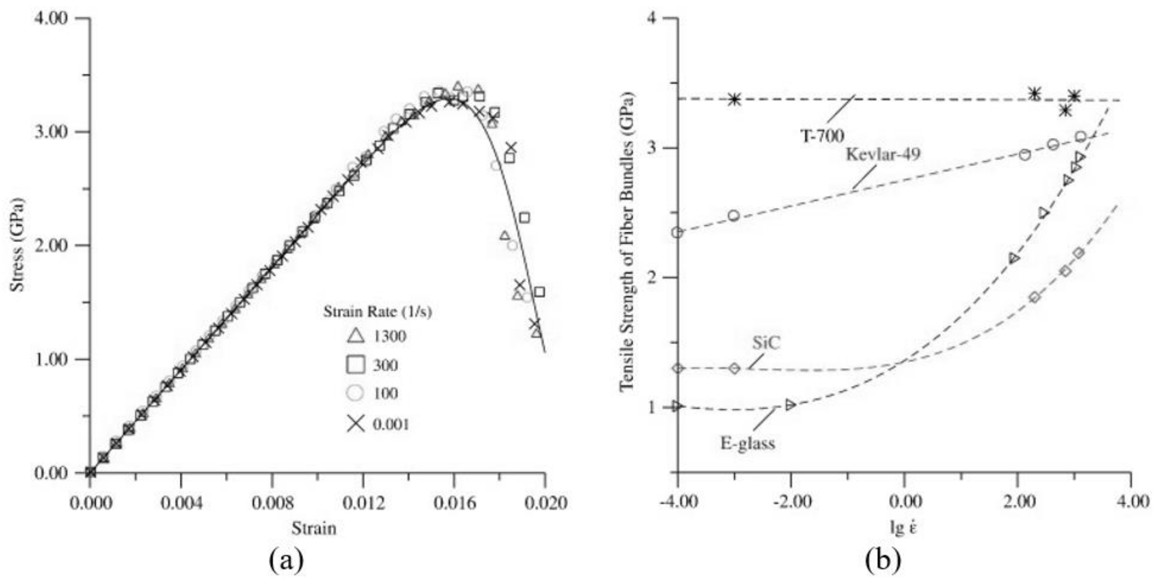

Figure 2.1. Experimental results from [33] showing (a) rate-independent behaviour of T700 carbon fibres and (b) a comparison between the rate effects observed in T700 carbon fibres and other common types of fibre.

In order to give the fibres lateral support, different kinds of polymeric matrices can be used, with epoxy resins being one of the most common for CFRPs in the aerospace industry. Epoxy resins have very low strength and stiffness properties with respect to the fibres, typically in the order of 100 MPa and 10 GPa, and tend to exhibit viscoplastic behaviour under dynamic loading [6,34,35]. The effects of strain rate on epoxy resins have been studied in [34,35], showing an increase in strength and stiffness but reduced ductility with increasing strain rates, as can be seen in Figure 2.2 for an RTM-6 epoxy resin [35]. Studies have also showed important effects of temperature and hygrothermal ageing in epoxy resins [34,36,37]. However, these do not fall within the scope of the present study and will not be considered further. The specific 8552 resin used in the studied IM7/8552 composite is a toughened, high-performance epoxy matrix with a base strength of 121 MPa and stiffness of 4.67 GPa under dry, room-temperature conditions and quasi-static loading [6].

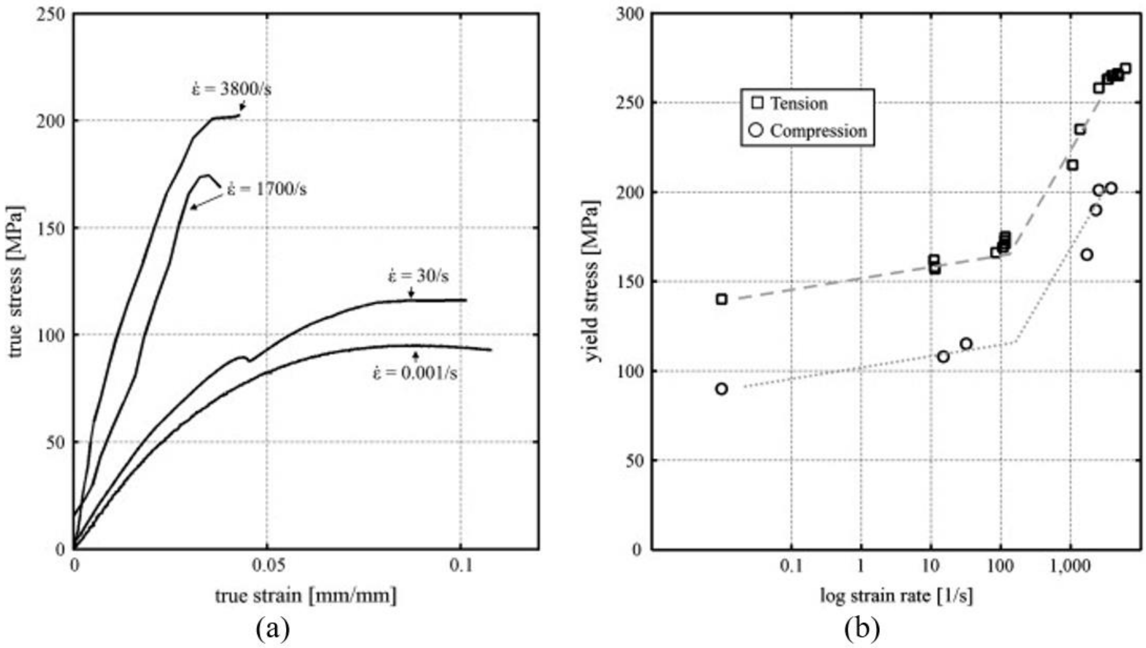

Figure 2.2. Results from [35] showing (a) the rate-dependent stress-strain response of RTM-6 resin, where a clear increase in strength and stiffness can be observed, (b) and evolution of the yield stress in tension and compression at different strain rates.

2.1.2. Composite elastic properties

Due to this combination of constituents, CFRP composites exhibit properties of both the polymeric matrix material and of the reinforcing carbon fibres. However, just as important as the individual mechanical properties of the constituents is the way in which they are combined and how they interact with each other.

For UD CFRPs, in which all the fibres are aligned in a single direction, the material has significantly different properties in the longitudinal and transverse directions. The elastic properties in each direction can be approximated by the rule of mixtures [38,39] using the elastic properties of the constituents, given in section 2.1.1, and the fibre volume fraction, 57.7% for the studied IM7/8552, as follows:

$$E_l = V_f E_f + (1 - V_f) E_m \tag{2.1}$$

$$E_t = \left(\frac{V_f}{E_f} + \frac{1 - V_f}{E_m} E_m\right)^{-1} \tag{2.2}$$

where E_l and E_t are the elastic moduli of the composite in the longitudinal and transverse directions, respectively, f is the fibre volume fraction, E_f is the elastic modulus of the fibres, and E_m is the modulus of the matrix.

This directional dependence, or anisotropy, of the elastic properties can be treated as orthotropic elasticity if the material is considered symmetric along the three orthogonal planes defined by the longitudinal, the in-plane transverse, and the out-of-plane material directions [40]. Alternatively, both the transverse directions (in-plane and out-of-plane) are assumed to be symmetric around the longitudinal axis, the behaviour of the composite can be assumed to be transversely isotropic [40].

While the longitudinal properties of UD CFRPs have generally been found to be rate-independent, Zhang et al. in [41] claimed to find noticeable increase in longitudinal strength and stiffness at strain rates above 20 s^{-1}. However, such results have not been observed by other researchers and the validity of the non-standard test and data reduction methods would need to be independently validated, especially since the fibres themselves have also been shown to be rate independent [33].

In contrast, in epoxy-based CFRPs such as the IM7/8552 composite subject of the present study, the moduli in both transverse directions and in shear show significant rate-dependency due to the viscous nature of the matrix [42–44]. Typical effects of strain rate on the longitudinal, transverse, and shear moduli for carbon/epoxy CFRPs are shown in Figure 2.3 for a UD T700S/2500 composite laminate [42].

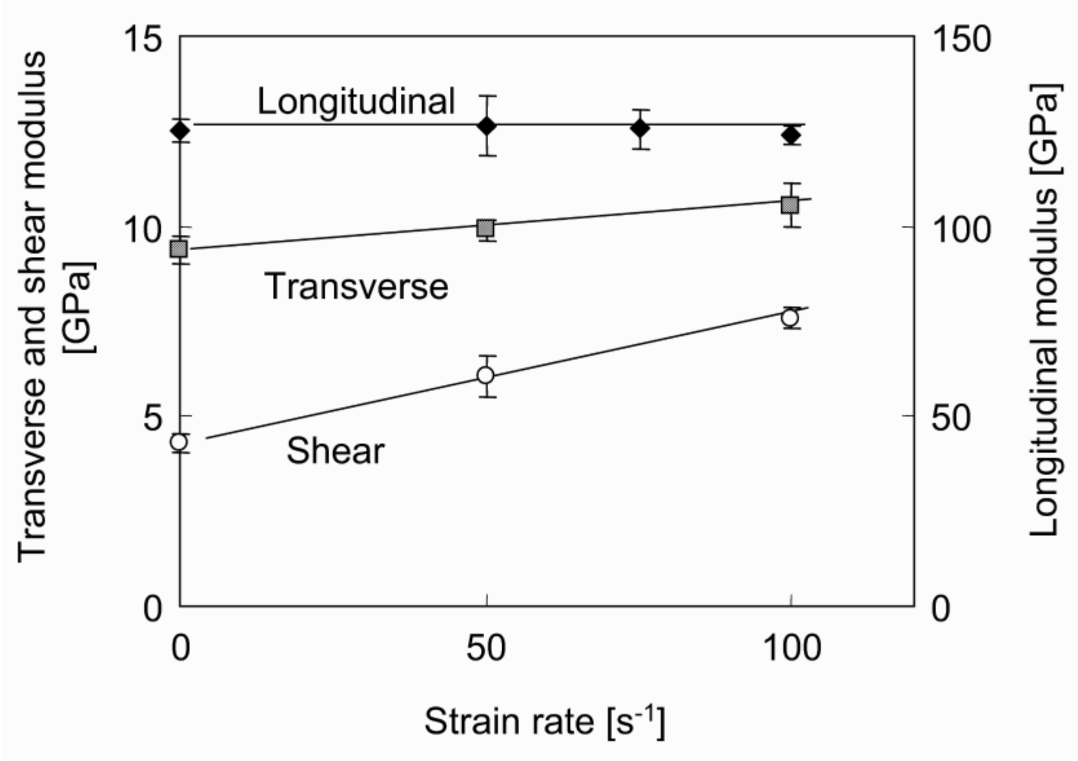

Figure 2.3. Results from [42] showing difference between longitudinal, transverse and shear elastic moduli in a unidirectional T700S/2500 carbon/epoxy CFRP and the different effects of strain rate on each.

The viscoelastic behaviour of the material in the transverse and shear directions has often been described by spring and damper rheological models, such as the generalized Kelvin or Maxwell models [45–48] where groups of springs and dampers are combined in series or in parallel. The disadvantage of these is that they require extensive characterisation to obtain stiffness and damping properties for each range of frequencies and, even then, are only valid within those ranges. As an example, Treutenaere [48] used Dynamic Mechanical Analysis (DMA) to measure some of these properties for a CFRP composite. However, the generalized Maxwell model he used required N viscoelastic parameters for each component of the elastic stiffness matrix, making it difficult to fully characterise in practice. Wiegand [19] and later Koerber [49] used a more empirical approach, showing that a simple scaling function of the type,

$$r(\dot{\varepsilon}) = 1 + \sqrt{K\dot{\varepsilon}} \tag{2.3}$$

where $r(\dot{\varepsilon})$ is the scaling function, K is the rate-dependent parameter, and $\dot{\varepsilon}$ is the strain rate, could be used to describe the rate-dependency of elastic properties in UD CFRPs, as shown in Figure 2.4. This kind of approach has been used successfully in [19,35,49,50] but, although much simpler, it lacks the physical basis of the proper viscoelastic models.

For the studied IM7/8552 material, the longitudinal and transverse elastic moduli are given for different material conditions in the manufacturer's data sheet, along with longitudinal and transverse strength properties [6].

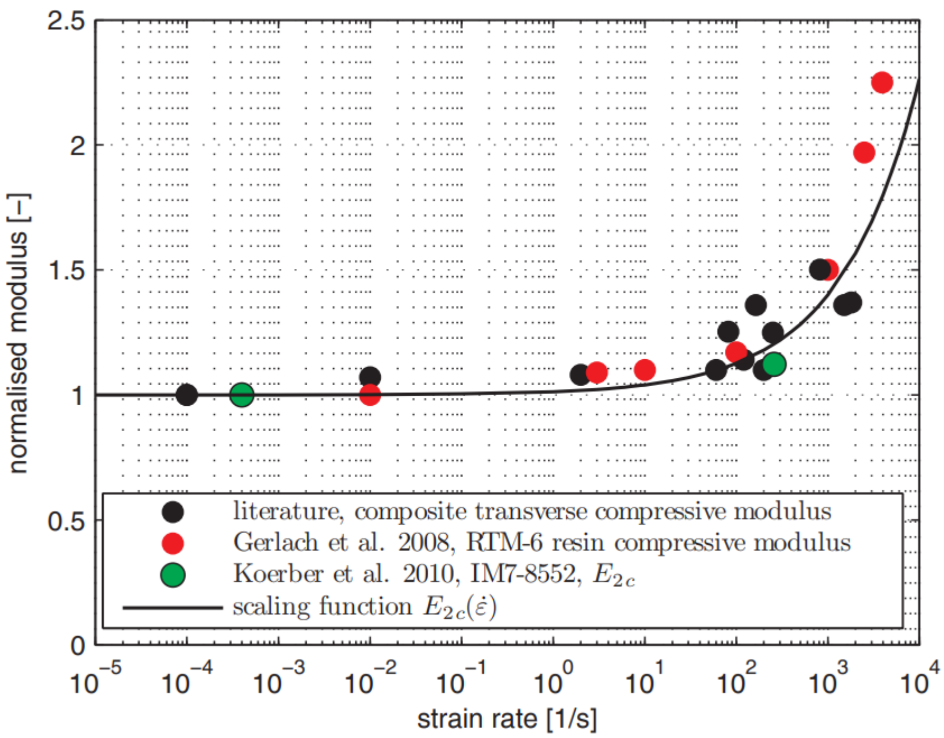

Figure 2.4. Data from [49] showing a compilation of normalised transverse compression modulus results on different UD CFRPs at different strain rates against a fitted scaling function of the type described in eqn. (2.3).

2.1.3. Matrix-dominated nonlinear behaviour

Because of the nonlinear viscoplastic properties of the epoxy resins used in CFRPs, as seen in section 2.1.1, the resulting composites tend to show similar nonlinear, rate-dependent behaviour in the matrix-dominated transverse loading directions [44,51,52]. This nonlinear behaviour, which is most pronounced in shear, cannot be entirely attributed to the viscoplastic properties of the matrix, however, as research in [53–55] showed that the fibre-matrix interface properties also played an important part. Sket et al. in [52] showed apparent fibre-matrix interface damage increasing with shear nonlinearity in a ±45° CFRP laminate, as can be seen in Figure 2.5. Naya et al. [54] and Gonzalez et al. [56] showed using micromechanical modelling that the fibre-matrix interface properties were crucial in order to capture the macroscopic shear response of the composite. In addition, cyclic loading tests on CFRP laminates in [48,57] showed increasing damage to the shear modulus as well as increasing residual, or inelastic, strain at increasing levels of nonlinearity. In conjunction, the above observations appear to indicate that the nonlinear behaviour in shear cannot be attributed exclusively to inelastic behaviour or to damage but is more likely a combination of the two.

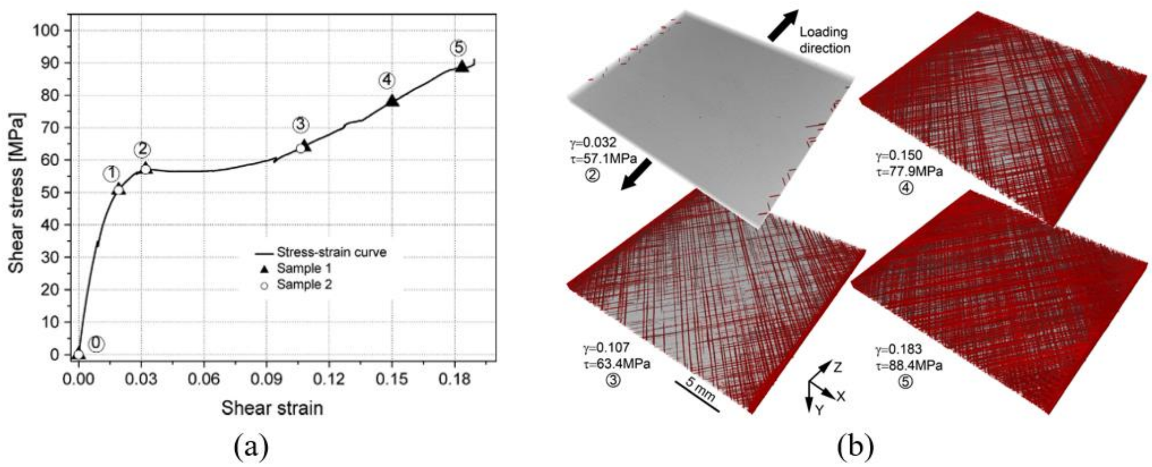

Figure 2.5. Increasing damage in a ±45° CFRP laminate observed using X-ray tomography at different points in the nonlinear shear stress-strain curve [52]. Matrix cracks, shown in red, were observed predominantly along the fibre directions (±45°), with some delamination appearing at the intersections between cracks in different plies.

As expected, this nonlinear shear behaviour is also strongly rate-dependent. Treutenaere [48] and Cui et al. [51] showed an important increase in the yield stress and a reduction in ductility in ±45° CFRP laminates at increasing strain rates, similar to what was observed for the epoxy resin in section 2.1.1. In addition, Koerber et al. in [44] performed a series of SHPB dynamic transverse compression tests on UD IM7/8552 CFRP specimens at different orientations, from 15° to 90°, showing important effects of strain rate on the yield stress and nonlinear behaviour, even in the 90° transverse compression tests, as can be seen in Figure 2.6.

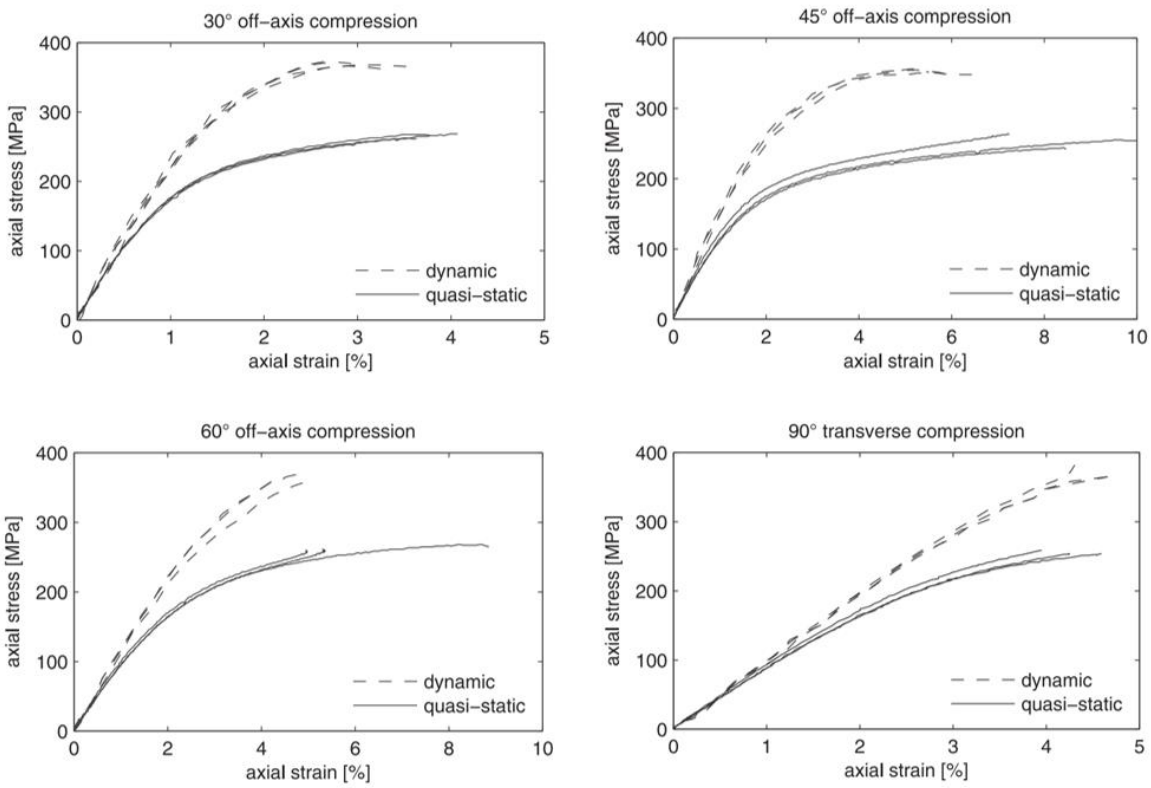

Figure 2.6. Nonlinear response of a UD IM7/8552 CFRP composite under compression at different off-axis angles and strain rates [44].

This work by Koerber [44] also showed an increase in the yield stress under greater transverse compression as the off-axis angle increased, resulting in a pressure-dependent yield locus. Pae et al. in [58], tested 45° and 90° transverse compression specimens under different amounts of superimposed hydrostatic pressure, showing a noticeable effect on the nonlinear behaviour of UD CFRPs, Figure 2.7.

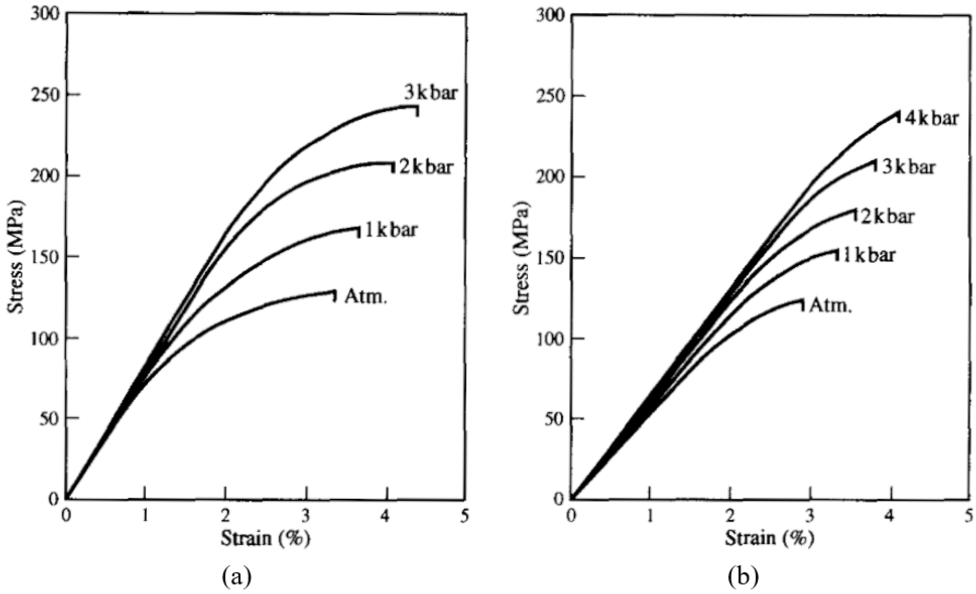

Figure 2.7. Transverse compression tests with different amounts of superimposed hydrostatic pressure carried out on (a) 45°, and (b) 90° UD graphite/epoxy composite specimens [58].

Finally, several authors have noted the importance of fibre rotation to the macroscopic response of the composite at large shear strains, especially for multi-directional laminates [51,52]. As can be observed by comparing the response of the UD laminate in Figure 2.6 to that of a ±45° laminate in Figure 2.5 (b), the ±45° material appears to stiffen significantly after strains of around 6%. This can be explained by the rotation of the fibres to align themselves with the loading direction in tension as damage in the matrix and fibre-matrix interfaces increases.

2.1.4. Inter-fibre fracture

Matrix or inter-fibre fracture (IFF), where failure occurs due to cracking in the matrix parallel to the fibre direction, Figure 2.8, presents many similar traits to what has been described in the previous section for the nonlinear shear behaviour. Under transverse loads, the relatively low strength of the matrix and of the fibre-matrix interface dictate the ultimate strength of the composite. Again, due to the viscous nature of the epoxy resins typically used in industrial CFRPs, this mode of failure also shows strong strain rate dependency and, similarly to what was observed for the yielding behaviour in the previous section, has also been shown to be strongly pressure-dependent [19,49,58–60].

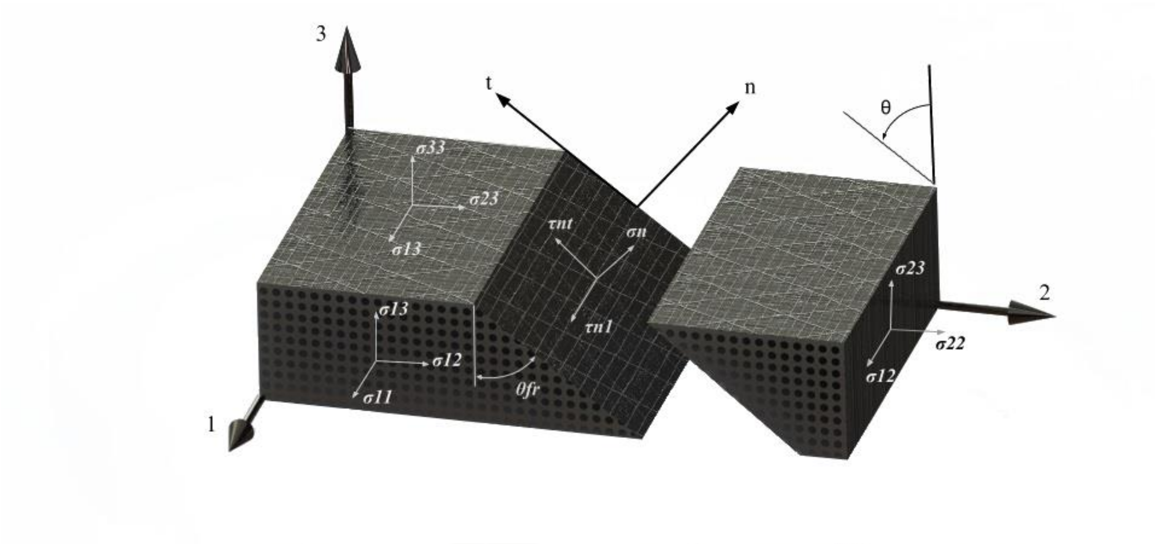

Figure 2.8. Schematic showing a typical IFF failure plane parallel to the fibre orientation and at an angle, θ_{fr}, with respect to the out-of-plane direction.

The material coordinate system is typically defined as shown in Figure 2.8 for UD CFRPs, where the 1 axis is defined by the longitudinal orientation of the fibres, the axis 3 is the through-thickness direction and 2 is the in-plane transverse fibre orientation. Recall that the effect on the IFF in 1 direction is negligible since the fibres carry the greater part of the load in that direction. When plotted in these material coordinates and ignoring the longitudinal stress component, the ultimate stress data from UD off-axis transverse compression tests [44,49,61] reveals a complex failure envelope where the strength appears to increase with transverse compression, Figure 2.9 (a). In addition, the work by Pae [58], Figure 2.7, showed the strength in 45° and 90° off-axis compression specimens increasing under hydrostatic pressure, consistent with the apparent effects of hydrostatic pressure on the IFF failure envelope observed in [12,44,62].

Furthermore, as the off-axis angle increases towards 90° transverse compression, the orientation of the fracture plane, θ in Figure 2.8, has been observed to increase from 0°, parallel to the out-of-plane or through-thickness direction, to around 50°, as shown in Figure 2.9 (b).

All together, these observations point towards IFF being a frictional, shear-dominated failure mode, as suggested by some of the leading failure theories described in section 2.2 [62,63].

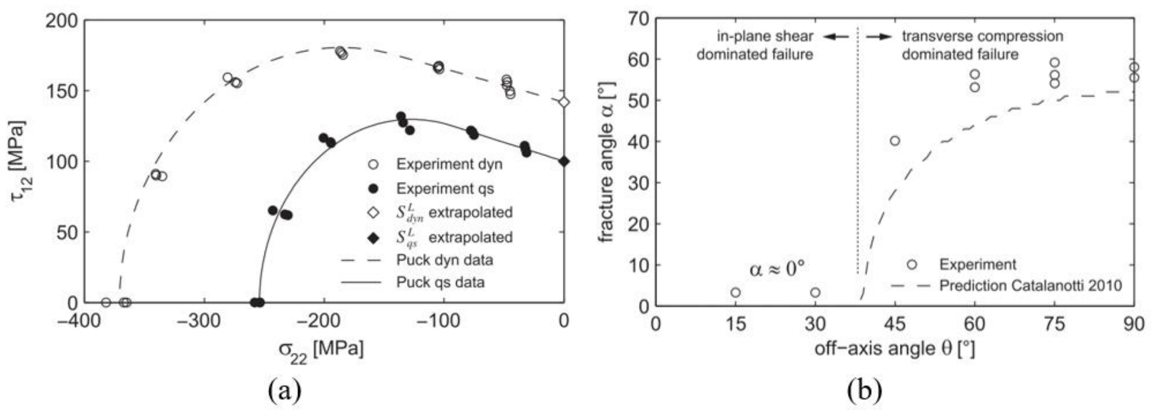

Figure 2.9. Off-axis transverse compression test data from IM7/8552 UD CFRP specimens showing: (a) quasi-static and dynamic failure envelopes plotted in material coordinates (transverse compression, σ_{22}, and in-plane shear, τ_{12}); and (b) the change in fracture plane orientation with increasing transverse compression measured from failed QS specimens [44].

At the same time, IFF being a matrix-dominated failure mode, it is also strongly rate-dependent, as was the nonlinear shear behaviour described in the previous section. Koerber [49] showed that the IFF strength in UD off-axis transverse compression tests increased with the strain rate across all specimens, as depicted in Figure 2.9 (a). In addition, Wiegand in [19] and later Koerber [49] showed the ability of a simple scaling function of the type given in equation (2.3) to describe the effects of loading rate on the

IFF strength properties of UD CFRPs. However, the failure envelope for the dynamic compression tests in [49] and Figure 2.9 (a) was calibrated from tests carried out at different strain rates, from around 120 to 330 s^{-1}, and the potential effects of strain rate on the shape of the envelope, have not been thoroughly investigated.

Finally, as the material begins to fail, there are two main mechanisms of dissipation which affect the damage evolution behaviour during IFF. The first is the propagation and coalescence of cracks along the matrix and fibre-matrix interface, which accounts for most of the energy released through the failure process and causes a steep drop in the supported load. Then, as the crack propagates between the fibres, some of these remain attached to different sides of the crack surface. This fibre bridging effect can give the material some residual strength as the fibres must be broken or pulled out from the matrix for the crack to continue propagating, which results in a second stage of energy dissipation, acting predominantly at greater crack lengths and increasing the fracture toughness [64,65]. In addition, since there are different possible modes of fracture, mode I or opening, mode II or sliding, and mode III or tearing, there are different energies associated with each [66–72]. However, these properties are difficult to measure experimentally and, as a result, there is no clear consensus on whether effects of strain rate, temperature, or other factors may influence the fracture propagation mechanisms and energy release rates [72–76].

2.1.5. Delamination

One particular kind of matrix failure is when the crack/fracture occurs between two different plies within a laminate, known as inter-laminar failure or delamination. This failure mode has many similarities with the general IFF mode, or intra-laminar failure, as they both treat different cases of essentially the same type of failure propagating through the matrix and fibre-matrix interfaces. Very similar characteristics can therefore be expected, with delamination showing comparable strain rate and pressure effects to those observed in IFF [65,69,77–81]. In addition, the same type of frictional, pressure-dependent failure criteria used for IFF have been used to accurately predict delamination failure in the past [82–85].

However, there are also some important differences between the two. By definition, delamination occurs in the resin-rich interface area between two different plies, which can have different fibre orientations, and may show significant differences in the local microstructure, such as fibre volume fraction, fibre orientation or waviness, etc. As a result, there is no clear consensus on whether delamination can or should be treated as a subcase of IFF or not. Many characterisation and modelling efforts have produced strength properties equivalent to IFF while others have obtained different values for the two different modes [65,82].

Finally, fracture propagation is treated in much the same way as it is for IFF, considering the three possible fracture modes and their associated fracture energies. In addition, as described above for IFF, there is a lack of consensus on whether or not the fracture toughness properties for delamination failure should be considered rate-dependent or not [73,74,86,87].

2.1.6. Fibre tension

Having covered the main matrix-dominated modes, only the two fibre failure modes remain. When loaded in the fibre direction, UD CFRPs can fail by completely different mechanisms whether in tension or in compression.

Fibre tension failure is the simpler of the two as it depends only on the properties of the carbon fibres up to the point of failure, showing no noticeable strain rate or pressure effects [42,43,88]. As previously mentioned in section 2.1.2, for the longitudinal stiffness properties, contradictory results were given in [41] that appeared to show rate-dependent fibre tension strength properties. However, these were most likely an effect of the non-standard testing and data reduction methods, since similar results have not been observed elsewhere.

While there are still some interesting areas of research related to the stochastic nature of this failure mode at the microstructural scale, at the macroscopic scale, fibre failure appears to be well understood, with failure occurring once the load in the fibre direction reaches a critical value. This can be predicted from the constituent properties using the rule of mixtures [38,39]. In addition, fibre tension failure shows no complex interactions with or other off-axis loads or effects of strain rate [62,63].

With regards to the stochastic nature of fibre tension failure, this mostly affects the fracture mechanics. At the critical load and depending on their micro-scale properties, fibres start to fail as they reach their individual strengths. As different fibres fail at different points along their length and are pulled out of the matrix, the fracture toughness increases to include not only the energy released through fibre failure but also through fibre pull-out, which is driven mainly by the fibre-matrix interface. As such, it may well be affected by the viscous nature of the matrix, which may explain why different measures of fracture toughness in fibre tension failure have been obtained for the quasi-static and dynamic response [75].

However, at the macro-scale, the resulting strength and fracture toughness properties for a given CFRP tend to be measured experimentally instead of attempting to derive them the micromechanical fibre and matrix properties that drive them.

2.1.7. Fibre compression

In contrast, compressive fibre failure in composites is possibly the more complex of the observed modes of failure. Depending on various factors, failure can occur by micro-buckling instability in the fibres, pictured in Figure 2.10 below, or by fibre crushing, if the fibres are relatively weak, although there are many other possible subclassifications [23,89]. In CFRP composites, since the fibres tend to be much stronger than the matrix, failure tends to occur in the form of buckling instability, or kinking, before the fibres reach their compressive strength. Because of this, the overall strength of the composite in compression is usually around 60% of the strength in tension, as is the case for the investigated IM7/8552 [6]. While it is still possible for the crushing strength of the carbon fibres to be reached if the material is sufficiently constrained, fibre kinking is the mode of greatest interest for UD CFRPs under longitudinal compression.

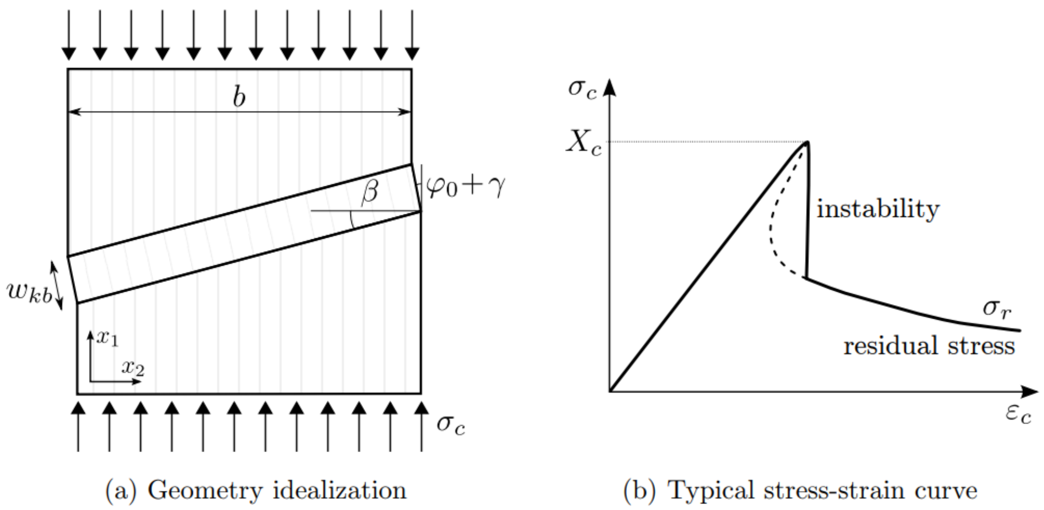

Figure 2.10. Illustration of (a) the typical kink band geometry and (b) stress-strain curves observed in UD CFRP composites from [90].

However, the experimental characterisation of longitudinal compression strength in CFRPs is challenging even under 'standard' conditions (uniaxial, quasi-static, room temperature) due to the extreme difference in matrix and fibre properties. Lee and Soutis

[91] detailed the difficulties in obtaining reliable measurements of FK strength in CFRPs using the ASTM standard methodology [92], which requires a complex alignment and clamping fixture to prevent premature failure at the specimen boundaries. However, this set-up is not well suited for dynamic testing and, even in quasi-static conditions does not fully avoid boundary issues, and can be highly susceptible to specimen or fixture set-up by the operator. Because of this, most experimental studies on fibre kinking strength have been carried out under uniaxial, quasi-static loading conditions [91–94].

While there have been some studies on the longitudinal compression strength under multi-axial loading before, the scarcity of experimental data, the scatter in the results, and the uncertainty as to the experimental methods mean there is insufficient conclusive evidence to judge the nature of the interaction between the uniaxial compression strength and off-axis loads. To date, the main source of biaxial test data for fibre compression strength are still the tests performed for the World-Wide Failure Exercise (WWFE), Figure 2.11, obtained from torsion and compression of UD CFRP tubes, which has given rise to a number of differing failure theories and predictions without providing sufficiently strong validation for any of them [63]. Other than that, Parry et al. [88] performed a study on the fibre kinking strength of a UD CFRP under superimposed hydrostatic pressure, showing increasing compressive strength under higher pressure, which would seem to give credence to theories that fibre kinking failure is governed by the nonlinear shear response of the composite [23,62,95]. Also in agreement with these theories is the more recent work by Matsuo et al. [94], in which a series of uniaxial compression tests on a thermoplastic UD CFRP showed the fibre kinking strength changing in proportion to the change in the nonlinear shear response at different temperatures.

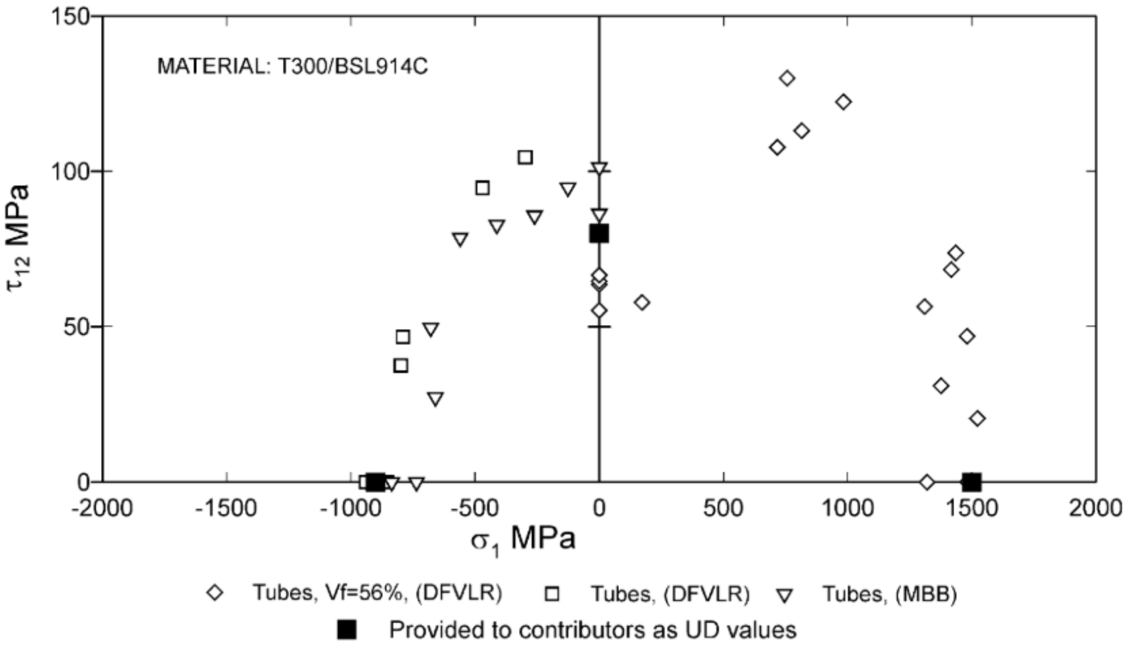

Figure 2.11. Biaxial test data from UD CFRP tubes under longitudinal and shear loading, the region of interest for biaxial longitudinal compression falls under the negative values of σ_1 [61].

Following on from these previous observations, if theories such as [23,62,95] are correct, then rate-dependent shear behaviour should translate into rate-dependency in the longitudinal compression strength. However, the very few studies on this topic have met with only limited success. Hsiao et al. [26] were the first to perform a thorough investigation into the rate-dependency of the longitudinal compression strength, using a drop-weight impact tests, and showed the strength increasing with strain rate. However, they noted a change in failure mode at high strain rates and the strength increase from quasi-static to high rate of almost 80% was far greater than what would be expected on the basis of the effects they observed in the nonlinear shear response. Together, these observations indicate that all specimens tested may not have failed under the desired mode or that there may be some uncertainty in the Force extraction method used for the dynamic tests. Wiegand in 2009 [19] attempted to perform dynamic uniaxial compression tests on UD CFRP specimens using a SHPB system but encountered many issues related to stress concentrations and boundary effects that may have led to premature failure and the apparent lack of significant strain rate effects on the kinking strength. Later, Koerber [49] performed similar quasi-static and dynamic SHPB compression tests on UD IM7/8552 specimens but while he did show noticeable strain rate effects the tests suffered from similar stress concentration issues, failing at the fixture boundaries far below the expected strength for this same material reported in [91].

Therefore, much work remains to be done to experimentally characterise and understand fibre kinking failure under multi-axial loading and, especially, under dynamic loading, for which there appears to be a lack of valid experimental data. It is only more recently that Ploeckl et al. [96], in parallel to similar work performed in this study and presented in section 5.2, manage to extract longitudinal compression strength values from quasi-isotropic (QI) laminate specimens that matched the expected strength in quasi-static loading, showing a reasonable increase in strength at high strain rates.

Finally, after the initial fibre kinking instability, under certain conditions if the material is sufficiently constrained, a post-peak residual stress, as shown in Figure 2.10 (b), can sometimes be observed as fracture propagates and the kink band reaches a second stable state of fibre rotation [90,97,98].

2.2. Numerical modelling

Having given a brief overview of the principal observed deformation and failure modes for UD CFRPs in the previous sections, the following sections will describe the main advances in the modelling and numerical prediction of the experimental results.

As mentioned in the introduction and objectives, this project is focused on the material response at the meso-scale, which considers the homogenised behaviour of UD material within a ply or UD laminate. Therefore, the numerical modelling techniques described in this section treat the material at the same or similar length scale. While micro-mechanical modelling at the fibre scale can provide a much greater level of detail with a potentially stronger physical basis, it is still far from feasible for the modelling or prediction of material behaviour at an industrial application scale and, in practical terms, such applications do not tend to consider details below the scale of individual plies.

Therefore, in general, the models and criteria reviewed in this section treat the material as a continuum at the ply-scale, ignoring lower-scale discontinuities, such as fibres, matrix and fibre-matrix interfaces, and base their predictions on the homogenised state of the material at the meso-scale, such as ply strains or stresses.

While more detailed accounts of the literature relevant to each chapter will be given as they required, this initial literature review will summarise of the main developments in damage and fracture prediction of UD CFRPs to date.

2.2.1. WWFE

Over the years, a great number of competing damage and failure theories have been developed for CFRP composites. However, due to the number of materials used by different research teams for calibration, testing, and validation of these models, it has often been difficult to find a common ground on which to compare the different theories. The World-Wide Failure Exercise (WWFE), carried out from 1991 to 2004, was the first attempt at a comprehensive evaluation of the leading failure theories of the time based on a common set of material properties and calibration data points and allowing each research group to give their predictions for the expected failure envelopes under different biaxial stress states [63].

In the first stage of this WWFE, 19 theories were compared against each other in terms of their blind predictions of the expected failure envelopes and a number of specific test cases without prior knowledge of the experimental results. This initial comparison noted the different methodologies used, the differences in their predictions, and the possible reasons behind them, before a second, more complete, evaluation was carried out.

While this was the most extensive study of its time, it considered only quasi-static, in-plane loading conditions, without any consideration of three-dimensional stress states or dynamic loading. In addition, most theories did not consider nonlinear shear behaviour or at best used experimental curves to interpolate the nonlinear behaviour of the in-plane shear, lacking any kind of progressive damage or plasticity models.

2.2.1.1. Inter-Fibre Failure

As can be seen in Figure 2.12 (a), several theories were able to give good predictions for IFF under in-plane biaxial stress states, showing it to be a fairly well understood failure mode, although the lack of data under three-dimensional stress states limited the extent to which these theories could be validated.

2.2.1.2. Fibre Tension Failure

For fibre tension failure, there was a general consensus that the maximum stress in the fibre direction dictated the ultimate admissible load and showed little or no interaction with shear or off-axis loads, as shown by the positive values of σ_x in Figure 2.12 (b).

2.2.1.3. Fibre Compression Failure

For fibre compression failure, on the other hand, the conclusions were less clear. The quality of the experimental data made it difficult to judge between different theories and even vastly different predictions appeared to fall within the experimental scatter, as seen for the negative values of σ_x in Figure 2.12 (b).

In general, there was some uncertainty in the test methods, especially in combined longitudinal and shear loading, resulting in the lack of a clear conclusion regarding fibre compression failure and leading some researchers to question the validity of some of the experimental data, such as the apparent shear strength increase under longitudinal tension in Figure 2.12 (b).

2.2.1.4. Conclusions

Overall, however, the WWFE was a very useful exercise and by far the most detailed experimental and modelling campaign up until that time, helping to identify some of the leading failure theories used to date, such as Puck's IFF theory [12], by comparing not only the accuracy of their predictions but also their underlying physical basis.

In conclusion, the study recommended Puck's [12] and Tsai's [99] models, among a couple others, as the best performing but, for greater confidence, advised using multiple criteria in design applications [100]. Puck's IFF theory, in particular, which has since gained considerable traction, was praised for its strong physical basis, 3D nature, and ability to account for pressure effects, although these could not be evaluated with the available in-plane test data.

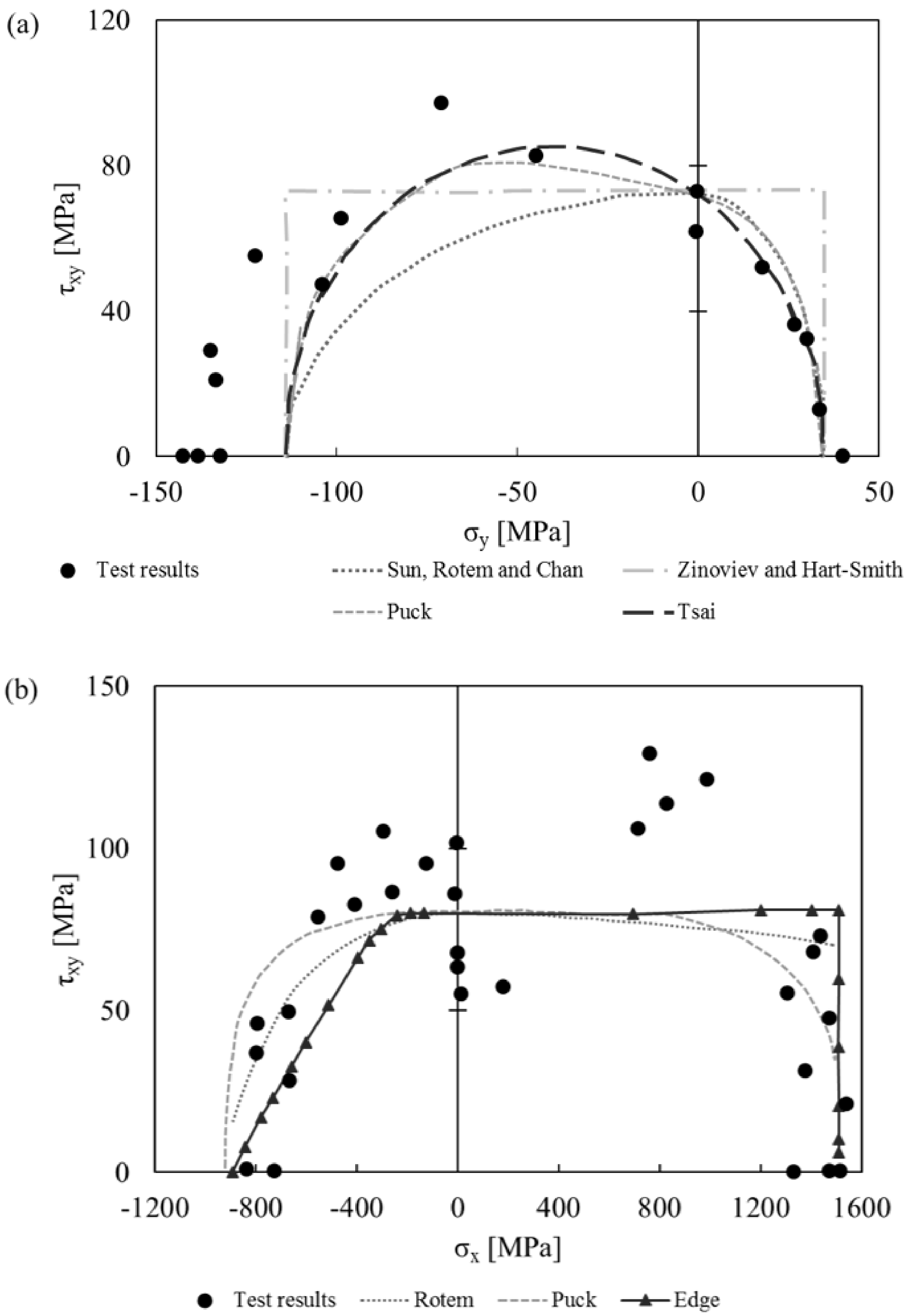

Figure 2.12. Biaxial test data from the WWFE compared to several leading failure theories. (a) shows the IFF failure envelopes against in-plane transverse compression and shear data and (b) shows predictions and experimental data for combined longitudinal compression and in-plane shear, in the negative region of σ_X, and combined longitudinal tension and shear, in the positive region [63].

A follow-up exercise was carried out for the WWFE-II in 2012, but while the first focused on in-plane failure criteria, the second aimed to evaluate the validity of the top theories in more complex loading conditions leading to 3D states of stress [101].

Puck's theory for the prediction of IFF, which is based on the Mohr-Coulomb criterion and will be explained in more detail in Chapter 4, was again identified as one of the best performing models [102,103]. It was already among the top theories in WWFE-I and for WWFE-II it was implemented in a finite element package, producing good predictions for the evaluated test cases, although it lacked suitable progressive damage and failure models for nonlinear shear behaviour and damage evolution, respectively [63,100,102,103].

2.2.2. LaRC failure criteria

Following the first WWFE, Dávila et al. at NASA Langley Research Center [104] concluded that, while it was a good assessment of the available methods for failure prediction in FRPs, the comparison showed that most theories differed significantly from the experimental results. This uncertainty in the theoretical methods for failure prediction in FRPs led them to carry out their own assessment and bring together the best performing failure theories and criteria, developing new theories where necessary.

Over the years, several subsequent iterations of these LaRC failure criteria, named after the Langley Research Center, were developed by Dávila, Camanho, and then Pinho et al. [62,104]. The first of these, LaRC02 and LaRC03, only looked at in-plane stress conditions and focused on prediction of failure envelopes using strength-based criteria for use with FEA, ignoring the effects of shear nonlinearity [104]. Later, Pinho et al. [62] expanded on these previous criteria, building on the same theories but making the models three-dimensional and including effects of nonlinear shear by interpolation and extrapolation of the material state from experimental curves.

2.2.2.1. Inter-Fibre Failure

Early in the development of these criteria, Hashin's theory [105] and the proposed modifications to it by Sun [106] and Puck [12] from the WWFE, shown in Figure 2.12, were identified as the most promising for the prediction of IFF. Hashin's original criterion introduced the concept of evaluating failure due to tractions acting on the plane of failure. While the failure plane under tension and shear was known to be the plane parallel to the fibres in the direction normal to the ply surface (0° in Figure 2.13), Hashin was unable to predict the fracture plane under transverse compression, using a quadratic interaction between stress invariants. Therefore, his predictions did not always fit the experimental results [63]. Sun [106] proposed an empirical modification to Hashin's criterion where a frictional parameter was introduced so that the shear strength would increase under pressure, producing a better fit with the experimental results. Nevertheless, it was still not able to predict the failure plane under compression. However, in order to avoid the type of inconsistencies observed in many models from the WWFE, it was considered important to use more physically-based, non-empirical, criteria. Hence, a criterion of the type proposed by Puck [12] was eventually selected.

Puck's theory, like Hashin's, was based on the Mohr-Coulomb criterion and considered IFF failure to occur along a certain plane due to the tractions acting upon it. Failure on a particular plane was assumed to be driven by the effective shear tractions acting on that plane, with a pressure dependent strength, defined by the normal traction and a frictional parameter. In order to determine the failure plane, this Mohr-Coulomb-based criterion was evaluated on all potential failure planes with the one closest to failure being considered the most critical. Thus, Puck's criterion was able to account for effects of pressure, giving good predictions for the in-plane failure envelope as found by Hinton and Soden in the WWFE [63], while also being able to determine the orientation of the failure plane with reasonable accuracy, which was shown to go from 0° in tension and shear up to around 50° in transverse compression.

A graphical representation of this approach from [104] is shown in Figure 2.13. Figure 2.13 (a) shows the evaluation of the Mohr-Coulomb criterion for the case of pure transverse compression. Figure 2.13 (b) shows how the failure envelope for transverse compression and in-plane shear is obtained by considering different potential failure planes. A more detailed look at Puck's criterion and its mathematical formulation is given in Chapter 4, where potential modifications and other applications are investigated.

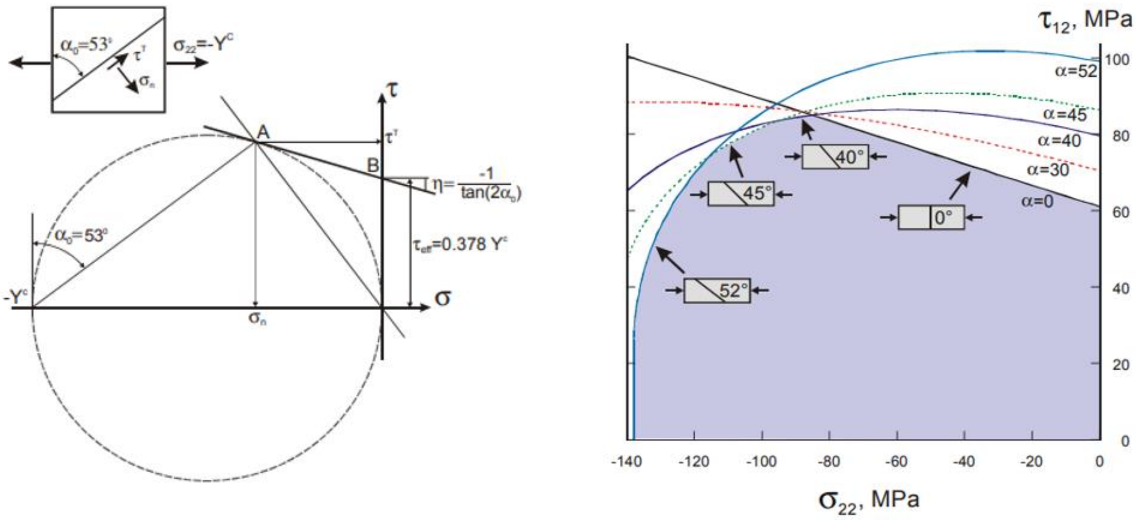

(a) (b)

Figure 2.13. Graphical representation of the Puck IFF theory. (a) shows the evaluation of the Mohr-Coulomb criterion for the case of pure transverse compression and (b) shows how the failure envelope for transverse compression and in-plane shear is obtained by considering different potential failure planes [104].

2.2.2.2. Fibre Tension

For fibre tension, the LaRC models used a simple maximum stress criterion in the longitudinal direction with no shear interactions, based on observations from the WWFE [62,104].

2.2.2.3. Fibre Compression

Finally, for fibre compression failure, the LaRC criteria deviated from the models proposed by Hashin and Puck [12,105], which were more empirical, and instead opted for the more physical, micromechanics-based kink band approach proposed by Fleck [23]. Fleck's theory was based on the micromechanics of the problem and predicted the longitudinal compression strength by considering the elasto-plastic buckling of a series of fibres in a plastic medium, building on previous work by Rosen [107] and Argon [108]. Fibre kinking is assumed to be caused by the initial waviness, or misalignment, of the fibres from the manufacturing process. Under longitudinal compression, this initial waviness causes a local state of shear in the misaligned frame that will eventually become the failed kink band, shown in Figure 2.10 (a). This local state of shear in turn causes additional fibre rotation, following the nonlinear shear behaviour of the composite as described in section 2.1.7, until a state of equilibrium is reached. However, at sufficiently great compressive loads, this additional rotation can become unstable and cause the fibres to buckle. Budiansky extended this theory to consider the evolution of the kink band after the initial instability and showed that it would continue to rotate until it reached a second stable state [23]. Thus, giving the material a residual stress in compression, as observed in [90,97,98] and illustrated in Figure 2.10 (b).

For uniaxial compression, the critical load leading to unstable fibre rotation and compressive failure can be determined analytically from the initial fibre waviness and the nonlinear shear behaviour of the composite. However, for more general plane stress problems, Fleck proposed an iterative solution method to obtain the compression strength under different loading scenarios [23].

Dávila and Camanho [104] developed a version of this criterion for the LaRC02 and LaRC03 models whereby failure under any stress state was assumed once the critical fibre rotation for uniaxial compression was reached. The initial misalignment angle was determined from the measured uniaxial compression strength and the additional rotation could be approximated for any in-plane stress state without the need for iteration. Later, Pinho [62] expanded on this approach for the LaRC04 model, generalising it into the three-dimensional stress space and considering shear nonlinearity within the kink band, which was not included in the previous implementation. These new implementations had the advantage over Fleck's original criterion of being better suited for use with FEM while still giving similar predictions. The LaRC04 version gave more realistic predictions for cases with combined longitudinal and transverse compression and cases with hydrostatic pressure thanks to the inclusion of shear nonlinearity. However, as discussed in section 2.1.7, the scarcity and reliability of the available experimental data for fibre kinking failure under multi-axial loading makes it difficult to properly evaluate any of these criteria and further work in this area is required before any of them can be used with confidence. A more detailed review of the theory and mathematical formulations behind these criteria can be found in section 5.2, where fibre kinking failure under different, complex loading scenarios is investigated in more depth.

2.2.2.4. Damage model

To complete the LaRC04 FEM implementation, Pinho developed a three-dimensional damage model to go with the set of failure criteria described above [18]. As opposed to the Continuum Damage Mechanics (CDM) approaches used in [109–111], Pinho proposed the use of smeared damage formulation to avoid issues with mesh-dependency surrounding the strain localisation that occurs during fracture in most CFRP failure modes, given that local damage formulations were unable to capture such phenomena.

In the proposed smeared formulation, the fracture energy is distributed over the entire volume of the element and is released after failure initiation following a linear stress degradation law. Depending on the type of failure predicted and the ratio between opening and shearing tractions on the fracture plane, a mixed mode fracture toughness is computed with the material intralaminar mode I and mode II fracture toughness parameters. This mixed mode fracture toughness is used together with the fracture plane area to establish the linear stress degradation path from the initial stress and strain states at the onset down to the final strain at complete failure, as illustrated in Figure 2.14 for the case of transverse tension. For different stress states at the onset, the fracture area is determined from the element geometry and the predicted fracture plane orientation.

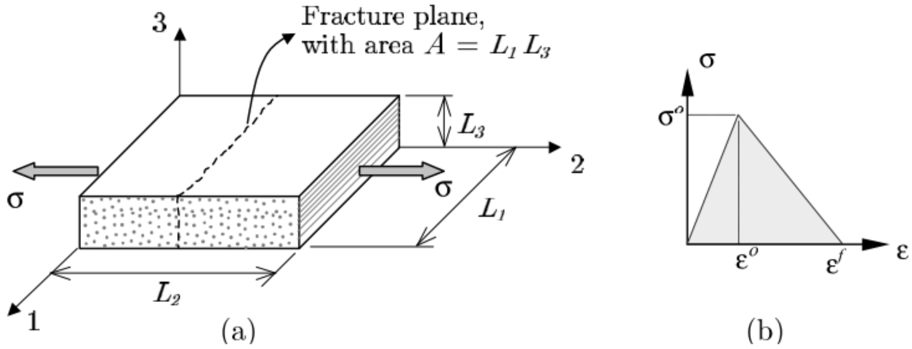

Figure 2.14. Illustration of the smeared damage formulation proposed by Pinho, showing (a) the determination of the fracture area and (b) the linear stress degradation law for a case of transverse tension [18].

2.2.2.5. Conclusions

Altogether, the LaRC models provided a simpler and clearer set of guidelines for modelling UD CFRPs, with some improvements over the criteria studied in the WWFE, making this knowledge more easily accessible. They consequently gained a lot of popularity and have been widely used for modelling of CFRP components both in industrial and academic, or research, environments, even being implemented in commercially available FEM software, see *MAT_261 and *MAT_262 models in LS-DYNA [11,112]. However, they still have several important shortcomings, such as the lack of strain rate effects or a proper nonlinear shear model, and the need for further validation of the fibre kinking criteria used, all of which are crucial for impact applications [11,112].

More recently, Vyas, working with Pinho to address one of these issues, proposed a pressure-dependent plasticity model based on Drucker-Prager plasticity to describe the nonlinear shear behaviour of UD CFRPs in [113] but the proposed model still lacks rate-dependency, necessary to describe the material behaviour under dynamic loading conditions.

As a final side note, interestingly, Pinho showed that the model described above could even capture the onset and evolution of delamination failure to some extent, thanks to the ability of the IFF criterion to locate the fracture plane. In this particular case, 90° coincides with the interlaminar fracture angle, and the smeared damage formulation can be used to describe the damage localisation and propagation [18].

2.2.3. Rate-dependent models

Following the development of the LaRC criteria, one of the most important shortcomings of the available UD CFRP modelling capabilities, especially for dynamic loading applications, was the lack of rate-dependency in the models and, since then, several authors have focused their work on this topic.

Shortly after Pinho's work, Wiegand studied the effects of strain rate in UD CFRPs in [19], where he built on the three-dimensional criteria included in LaRC04 with an FEM implementation of his own that used scaling functions of the kind described in eqn. (2.3) [35] to make the material properties rate-dependent. Taking experimental data from the literature, Wiegand showed that, using an empirical damping function and scaled strength and stiffness properties, criteria of the kind described in LaRC04 were able to match the dynamic failure data. In the case of fibre compression failure, which in Fleck's theory [23] is governed by the transverse and shear properties, the criterion automatically became rate-dependent by including strain rate effects in the matrix-dominated behaviour. In addition, following Pinho's work in [18], Wiegand showed that Puck's IFF criterion coupled with a suitable damage model was able to capture some of the effects of delamination damage at quasi-static and dynamic strain rates. However, other than including strain rate effects, Wiegand's model still suffered from the same limitations as the LaRC models before it. Wiegand did not include a nonlinear shear model in his work and did not provide any further validation for the LaRC failure criteria under multi-axial loading beyond what was previously available, in that he only performed uniaxial compression tests.

Later, Koerber performed a more extensive experimental campaign on UD IM7/8552 material, including many off-axis transverse tension and compression tests at both quasi-static and high strain rates, using Split Hopkinson Bar systems [49]. Like Wiegand, he used empirical scaling functions like eqn. (2.3) with Puck's IFF criterion to predict IFF under dynamic loading, showing good agreement with the experimental data across the entire in-plane IFF failure envelope. For fibre compression, Koerber's experiments did show significant strain rate effects under uniaxial loading and he was able to capture this behaviour using a similar strength scaling approach with the LaRC fibre kinking failure criterion. However, his experimental results were far below the expected values for the tested material, obtaining a strength around 1000 MPa as opposed to the expected value of around 1500 MPa [91], indicating they may have suffered premature failure. In addition, like the previous studies, he also failed to provide any further validation test cases for the fibre kinking criterion, which was calibrated with and validated against the same uniaxial compression test data. Finally, Koerber showed the ability of the plasticity model developed by Sun and Chen [114] to describe the nonlinear behaviour in matrix dominated loading directions across a number of different test cases, from 15° to 90° off-axis transverse compression, both at quasi-static and high strain rates. However, he did not include a rate-dependent formulation and instead simply showed the ability of such a model to capture the nonlinear behaviour at different rates using different sets of calibrated parameters.

Most recently, Hoffman [72] developed a rate-dependent multi-directional laminate scale model based on similar principles as Wiegand [19] or Koerber's [49] models but with a greater focus on rate-dependent damage evolution, including novel high-rate experimental characterisation of the fracture toughness parameters. While Hoffmann's model presented similar limitations the as previous described models in terms of constitutive behaviour before failure and the prediction of fibre kinking, it provided an important investigation into the rate-dependency of CFRP damage modelling and energy release rate parameters using a smeared damage formulation like the one proposed by Pinho in [18].

In parallel, other authors have proposed physically-based progressive damage models for the viscoplastic nonlinear response of CFRPs, such as the recent work by Treutenaere [48] based on the micromechanical continuum damage mechanics models of Lemaitre, Chaboche, Ladevèze, among others [109–111]. However, models of this kind, while boasting a sounder physical basis and mathematical formulation, also present several drawbacks. Treutenaere’s model was developed for woven composites and thus did not consider nonlinearity in transverse compression, which has been observed in UD composites [48], and treats only the nonlinear in-plane shear behaviour. In addition, as discussed in section 2.1.2, the viscoelastic portion of the model alone required seven parameters obtained from DMA for each elastic stiffness component, in addition to a series of damage, plasticity, and friction parameters to describe the nonlinear response. As a result, the number of parameters and cost of calibrating this kind of model are likely to make it less convenient for practical applications. Furthermore, without proper experimental calibration of all of the required material properties, the strong physical basis of the model itself may be seen as less important than the uncertainty in its calibration.

2.3. Conclusions

In summary, the literature review presented in the previous sections, while not exhaustive, gives a good enough initial overview to judge the current state of research into UD CFRPs and the areas that require further investigation.

From this initial evaluation, three areas have been identified as most important for the focus of the present work:

- **Nonlinear damage or plasticity modelling**: In the past most of the work on modelling UD CFRPs has focused on failure criteria and only to a lesser extent on the nonlinear behaviour, with the few available nonlinear models lacking rate-dependency and/or multiaxial (3D) or pressure-dependent formulations
- **Validation of fibre kinking theories**: There is a severe lack of reliable experimental data for fibre kinking failure in general and especially under multi-axial loading, which is necessary for a more thorough validation of widely used theories, such as Fleck's [23,62,104], which are often calibrated with and validated against the same uniaxial compression test data
- **Rate-dependent modelling**: Current rate-dependent modelling capabilities for UD CFRPs in general have been found lacking:
  - No suitable nonlinear shear model has been found that includes rate-dependency as well as pressure or multi-axial loading effects
  - A common approach for both the nonlinear behaviour and failure criteria has been the use of dynamic material properties within a rate-independent formulation instead of fully rate-dependent formulations
  - Dynamic failure properties tend to be calibrated from a series of dynamic tests carried out at a range of different strain rates instead of taking into consideration the strain rate of each individual test or group of tests
  - For fibre kinking failure in particular, there is little reliable dynamic test data, leaving much uncertainty as to how strain rate affects this failure mode and what theories and modelling approaches may be most suitable

By focusing on these key aspects, the aim of the current project is to develop an improved numerical model for UD CFRPs under dynamic loading by building on the previous work by Dávila, Camanho, and Pinho, who established a solid foundation for the modelling of CFRPs under quasi-static loading in the LaRC models, and later Wiegand and Koerber, who began to extend those models into dynamic loading regimes.

Therefore, the following chapters will try to answer some of these questions regarding the matrix-dominated nonlinear behaviour in Chapter 3, the rate-dependency of IFF in Chapter 4, and rate and off-axis effects on fibre kinking failure in Chapter 5.

In addition, previous studies have shown that most of the observed failure modes and the pressure and strain rate effects are all strongly related to the macroscopic nonlinear shear behaviour of the composite, which is driven by the viscoplastic behaviour of the matrix and micro-scale damage in the fibre-matrix interfaces. While micromechanical modelling at that scale is not feasible at the scale of most practical applications, all matrix-dominated failure criteria and pressure and strain rate effects will, if possible, be derived from an accurate representation of the (viscous) nonlinear shear behaviour at the macro-scale.

Chapter 3

Nonlinear constitutive response

The first of the main objectives for the present work, justified by the literature review in the previous chapter, was the development of a rate- and pressure-dependent constitutive model able to describe the complex nonlinear behaviour observed in UD CFRPs. To this end, a viscoplastic model based on Puck's localisation plane theory [12] is proposed in section 3.2, which, coupled with the underlying anisotropic viscoelasticity described in section 3.1, is able to accurately explain all of the observed behaviour in a simple, physically-based manner.

Within the numerical modelling framework described in section 1.2, the constitutive equations have been formulated in a corotational configuration, where the 6x6 rotation matrices, $\boldsymbol{T}_\sigma$ and $\boldsymbol{T}_\varepsilon$, are used to transform the rate of Cauchy stress and rate-of-deformation vectors, $\dot{\boldsymbol{\sigma}} = \{\dot{\sigma}_{11}\ \dot{\sigma}_{22}\ \dot{\sigma}_{33}\ \dot{\tau}_{12}\ \dot{\tau}_{13}\ \dot{\tau}_{23}\}^T$ and $\boldsymbol{d} = \{d_{11}\ d_{22}\ d_{33}\ d_{12}\ d_{13} d_{23}\}^T$, respectively, from the fixed global coordinate system to the local or material coordinates by:

$$\dot{\hat{\boldsymbol{\sigma}}} = \boldsymbol{T}_\sigma\, \dot{\boldsymbol{\sigma}} \tag{3.1}$$

and

$$\hat{\boldsymbol{d}} = \boldsymbol{T}_\varepsilon\, \boldsymbol{d} \tag{3.2}$$

with $\dot{\hat{\boldsymbol{\sigma}}}$ and $\hat{\boldsymbol{d}}$ being the rate of Cauchy stress and rate-of-deformation vectors in the material coordinate system.

The two rotation matrices, $\boldsymbol{T}_\sigma$ and $\boldsymbol{T}_\varepsilon$, which are not orthogonal nor symmetric and do not represent any tensorial magnitude, are defined as follows:

$$\boldsymbol{T}_\sigma = \begin{bmatrix} Q_{11}^2 & Q_{21}^2 & Q_{31}^2 & 2Q_{21}Q_{11} & 2Q_{31}Q_{21} & 2Q_{11}Q_{31} \\ Q_{12}^2 & Q_{22}^2 & Q_{32}^2 & 2Q_{22}Q_{12} & 2Q_{32}Q_{22} & 2Q_{12}Q_{32} \\ Q_{13}^2 & Q_{23}^2 & Q_{33}^2 & 2Q_{23}Q_{13} & 2Q_{33}Q_{23} & 2Q_{13}Q_{33} \\ Q_{12}Q_{11} & Q_{22}Q_{21} & Q_{32}Q_{31} & Q_{22}Q_{11} + Q_{12}Q_{21} & Q_{32}Q_{21} + Q_{22}Q_{31} & Q_{12}Q_{31} + Q_{32}Q_{11} \\ Q_{13}Q_{12} & Q_{23}Q_{22} & Q_{33}Q_{32} & Q_{23}Q_{12} + Q_{13}Q_{22} & Q_{33}Q_{22} + Q_{23}Q_{32} & Q_{13}Q_{32} + Q_{33}Q_{12} \\ Q_{11}Q_{13} & Q_{21}Q_{23} & Q_{31}Q_{33} & Q_{21}Q_{13} + Q_{11}Q_{23} & Q_{31}Q_{23} + Q_{21}Q_{33} & Q_{11}Q_{33} + Q_{31}Q_{13} \end{bmatrix} \tag{3.3}$$

$$\boldsymbol{T}_\varepsilon = \begin{bmatrix} Q_{11}^2 & Q_{21}^2 & Q_{31}^2 & 2Q_{21}Q_{11} & 2Q_{31}Q_{21} & 2Q_{11}Q_{31} \\ Q_{12}^2 & Q_{22}^2 & Q_{32}^2 & 2Q_{22}Q_{12} & 2Q_{32}Q_{22} & 2Q_{12}Q_{32} \\ Q_{13}^2 & Q_{23}^2 & Q_{33}^2 & 2Q_{23}Q_{13} & 2Q_{33}Q_{23} & 2Q_{13}Q_{33} \\ 2Q_{12}Q_{11} & 2Q_{22}Q_{21} & 2Q_{32}Q_{31} & Q_{22}Q_{11} + Q_{12}Q_{21} & Q_{32}Q_{21} + Q_{22}Q_{31} & Q_{12}Q_{31} + Q_{32}Q_{11} \\ 2Q_{13}Q_{12} & 2Q_{23}Q_{22} & 2Q_{33}Q_{32} & Q_{23}Q_{12} + Q_{13}Q_{22} & Q_{33}Q_{22} + Q_{23}Q_{32} & Q_{13}Q_{32} + Q_{33}Q_{12} \\ 2Q_{11}Q_{13} & 2Q_{21}Q_{23} & 2Q_{31}Q_{33} & Q_{21}Q_{13} + Q_{11}Q_{23} & Q_{31}Q_{23} + Q_{21}Q_{33} & Q_{11}Q_{33} + Q_{31}Q_{13} \end{bmatrix} \tag{3.4}$$

where Q_{ij} are the components of the second-order rotation tensor expressed as a 3x3 matrix with:

$$\boldsymbol{Q} = \begin{bmatrix} Q_{11} & Q_{21} & Q_{31} \\ Q_{12} & Q_{22} & Q_{32} \\ Q_{13} & Q_{23} & Q_{33} \end{bmatrix} = \begin{bmatrix} \boldsymbol{e}_1 \cdot \boldsymbol{e}'_1 & \boldsymbol{e}_1 \cdot \boldsymbol{e}'_2 & \boldsymbol{e}_1 \cdot \boldsymbol{e}'_3 \\ \boldsymbol{e}_2 \cdot \boldsymbol{e}'_1 & \boldsymbol{e}_2 \cdot \boldsymbol{e}'_2 & \boldsymbol{e}_2 \cdot \boldsymbol{e}'_3 \\ \boldsymbol{e}_3 \cdot \boldsymbol{e}'_1 & \boldsymbol{e}_3 \cdot \boldsymbol{e}'_2 & \boldsymbol{e}_3 \cdot \boldsymbol{e}'_3 \end{bmatrix} \tag{3.5}$$

Here $\boldsymbol{Q}$ is an orthogonal matrix ($\boldsymbol{Q}^{-1} = \boldsymbol{Q}^T$) that defines a transformation from the material $(\boldsymbol{e}'_1, \boldsymbol{e}'_2, \boldsymbol{e}'_3)$ to global $(\boldsymbol{e}_1, \boldsymbol{e}_2, \boldsymbol{e}_3)$ coordinate system such as $\boldsymbol{e}'_i = \boldsymbol{Q}^T\, \boldsymbol{e}_i$. The local material coordinate system evolves with the spin tensor $\dot{\boldsymbol{Q}} = \boldsymbol{W}\,\boldsymbol{Q}$ and the rotation tensor has an initial value of $\boldsymbol{Q}_{t=0} = \boldsymbol{I}$, being $\boldsymbol{I}$ the second order unit tensor.

In this way, the constitutive laws described in the following sections can be defined in a local reference frame that rotates and translates with the finite elements in the spatial discretisation to stay aligned with the material directions. Therefore, in the following sections material coordinates will be assumed unless stated otherwise, where 1 is the longitudinal, or fibre, direction, and 2 and 3 are the in-plane and out-of-plane transverse directions, respectively.

3.1. Linear viscoelastic behaviour

To begin defining their constitutive behaviour, the underlying elastic response of the UD composite materials before they undergo any kind of nonlinear deformation or damage must be defined. In UD CFRPs, due to the different properties of their constituents, this initial response can be described as linear anisotropic and viscoelastic.

In the corotational local coordinate system, the directional dependence, or anisotropy, of the material stiffness properties can be described in Voigt notation by the generalised Hooke's Law in rate form,

$$\dot{\hat{\boldsymbol{\sigma}}} = \widehat{\boldsymbol{C}}\,\widehat{\boldsymbol{d}}^{e} = \widehat{\boldsymbol{C}}\left(\widehat{\boldsymbol{d}} - \widehat{\boldsymbol{d}}^{p}\right) \tag{3.6}$$

where $\widehat{\boldsymbol{C}}$ is a 6 x 6 symmetric stiffness matrix with 21 independent elastic constants [40], $\widehat{\boldsymbol{d}}^{\boldsymbol{e}}$ and $\widehat{\boldsymbol{d}}^{p}$ are the elastic and plastic parts of the rate-of-deformation vector, assuming additive decomposition, and the rate form is used to account for the effects of strain rate in the following sections.

In UD CFRPs, three orthogonal symmetry planes in the longitudinal, transverse, and out-of-plane directions, reduced the number of independent constants to nine: the three stiffness moduli in each of the material directions, E_1, E_2, and, E_3, the three shear moduli, G_{12}, G_{13}, and, G_{23}, and the three Poisson's ratios, ν_{12}, ν_{13}, and, ν_{23}.

The stiffness matrix, $\widehat{\boldsymbol{C}}$, for the case of material orthotropy is then given by:

$$\widehat{\boldsymbol{C}} = \begin{bmatrix} C_{11} & C_{12} & C_{13} & 0 & 0 & 0 \\ C_{12} & C_{22} & C_{23} & 0 & 0 & 0 \\ C_{13} & C_{23} & C_{33} & 0 & 0 & 0 \\ 0 & 0 & 0 & C_{44} & 0 & 0 \\ 0 & 0 & 0 & 0 & C_{55} & 0 \\ 0 & 0 & 0 & 0 & 0 & C_{66} \end{bmatrix} \tag{3.7}$$

where its individual components, C_{ij}, are obtained by inverting the orthotropic compliance matrix, $\hat{\boldsymbol{S}}$:

$$\hat{\boldsymbol{S}} = \begin{bmatrix} \frac{1}{E_1} & -\frac{\nu_{21}}{E_2} & -\frac{\nu_{31}}{E_3} & 0 & 0 & 0 \\ -\frac{\nu_{21}}{E_2} & \frac{1}{E_2} & -\frac{\nu_{32}}{E_3} & 0 & 0 & 0 \\ -\frac{\nu_{31}}{E_3} & -\frac{\nu_{32}}{E_3} & \frac{1}{E_3} & 0 & 0 & 0 \\ 0 & 0 & 0 & \frac{1}{2G_{12}} & 0 & 0 \\ 0 & 0 & 0 & 0 & \frac{1}{2G_{23}} & 0 \\ 0 & 0 & 0 & 0 & 0 & \frac{1}{2G_{13}} \end{bmatrix} \tag{3.8}$$

In addition, if both the in-plane and out-of-plane transverse directions are assumed to be symmetric around the longitudinal axis, the material behaviour is considered transversely isotropic and the number of independent elastic constants is reduced to five, as $E_2 = E_3$, $G_{12} = G_{13}$, $\nu_{12} = \nu_{13}$, and $C_{55} = \frac{1}{2}(C_{22} - C_{23})$.

The assumption of transverse isotropy may not always hold true, especially for laminated composites, where the inter-ply properties may be slightly different to the transverse intra-ply properties. Nevertheless, in the absence of any strong evidence to the contrary for the studied UD IM7/8552 material, the elastic response will be treated as transversely isotropic in the present work.

3.1.1. Strain rate effects

So far, the above formulation makes no mention of viscous or time-dependent nature of the initial elastic response. However, from the literature review in Chapter 2, the matrix-dominated transverse and shear moduli are known to be rate-dependent.

Various approaches used to account for these effects in the past have been reviewed in section 2.1.2. Having considered the possible alternatives, the rate-sensitivity of the transverse and shear moduli has been implemented using linear damping and a single-parameter rate-scaling function, as in [19,35,49], which was found to strike a good balance between simplicity or usability and reliability.

By this approach, first, the following single-constant artificial viscous damping function is used to take into account the time-dependent material response [19]:

$$\dot{\hat{\boldsymbol{\varepsilon}}}_{(n+1)} = \xi \dot{\hat{\boldsymbol{\varepsilon}}}_{(n)} + (1-\xi)\frac{\Delta\hat{\boldsymbol{\varepsilon}}}{\Delta t} \tag{3.9}$$

where $\dot{\hat{\boldsymbol{\varepsilon}}} = \{\dot{\hat{\varepsilon}}_{11} \quad \dot{\hat{\varepsilon}}_{22} \quad \dot{\hat{\varepsilon}}_{33} \quad \dot{\hat{\gamma}}_{12} \quad \dot{\hat{\gamma}}_{13} \quad \dot{\hat{\gamma}}_{23}\}^T$ is the viscously damped corotational strain rate vector at the time $n+1$; $\Delta\hat{\boldsymbol{\varepsilon}} = \Delta t\, \widehat{\boldsymbol{d}}_{(n+1/2)}$ is the corotational time increment vector computed at the midpoint time step $n+1/2$; and ξ is the damping constant, which must be calibrated to ensure that only higher frequency spurious oscillations are dampened and the rate of deformation in the range of interest is not affected.

Then, a rate scaling function of the kind introduced in section 2.1.2, eqn. (2.3), is used to individually stiffen each of the elastic moduli, $\boldsymbol{s}[\dot{\hat{\boldsymbol{\varepsilon}}}] = \{E_1 \quad E_2 \quad E_3 \quad G_{12} \quad G_{13} \quad G_{23}\}^T$, as was done in [19,35,49]:

$$\boldsymbol{s}[\dot{\hat{\boldsymbol{\varepsilon}}}] = \boldsymbol{R}_C[\dot{\hat{\boldsymbol{\varepsilon}}}]\, \boldsymbol{s}^0 \tag{3.10}$$

with

$$\boldsymbol{R}_C[\dot{\hat{\boldsymbol{\varepsilon}}}] = \begin{bmatrix} 1 & 0 & 0 & 0 & 0 & 0 \\ 0 & r_C[\dot{\hat{\varepsilon}}_{22}] & 0 & 0 & 0 & 0 \\ 0 & 0 & r_C[\dot{\hat{\varepsilon}}_{33}] & 0 & 0 & 0 \\ 0 & 0 & 0 & r_C[\dot{\hat{\gamma}}_{12}] & 0 & 0 \\ 0 & 0 & 0 & 0 & r_C[\dot{\hat{\gamma}}_{23}] & 0 \\ 0 & 0 & 0 & 0 & 0 & r_C[\dot{\hat{\gamma}}_{13}] \end{bmatrix} \tag{3.11}$$

where $\boldsymbol{s}^0$ refers to the quasi-static stiffness properties and the scaling function, $r_C[\dot{\hat{\varepsilon}}_{ij}] = 1 + \sqrt{K_C \dot{\hat{\varepsilon}}_{ij}}$, is used to scale each of the transverse and shear moduli with the rate-dependent stiffness parameter, K_C.

For reference, alternative damping approaches are available in the literature, which can be used if the above is found too simplistic for certain applications. The most common alternative is the moving average approach, used in several of LS-DYNA's built-in material models [11], where the strain rate is averaged over a number of previous time steps or time units. More recently, Hoffman [72] also proposed a low-pass filter type approach that only dampens strain rate increments above a certain threshold:

$$\dot{\hat{\boldsymbol{\varepsilon}}}^v_{(n+1)} = \dot{\hat{\boldsymbol{\varepsilon}}}^v_{(n)} + \Delta\dot{\hat{\boldsymbol{\varepsilon}}}_{proc} \tag{3.12}$$

with the damped strain rate increment, $\Delta\dot{\hat{\boldsymbol{\varepsilon}}}_{proc}$, defined by:

$$\Delta\dot{\hat{\boldsymbol{\varepsilon}}}_{proc} = \begin{cases} \Delta\dot{\hat{\boldsymbol{\varepsilon}}}_{raw} & \text{for } \Delta\dot{\hat{\boldsymbol{\varepsilon}}}_{raw} \leq \Delta\dot{\hat{\boldsymbol{\varepsilon}}}_{tsh} \\ \Delta\dot{\hat{\boldsymbol{\varepsilon}}}_{tsh} + \left(\Delta\dot{\hat{\boldsymbol{\varepsilon}}}_{lim} - \Delta\dot{\hat{\boldsymbol{\varepsilon}}}_{tsh}\right)\left(1 - e^{-\frac{\Delta\dot{\hat{\boldsymbol{\varepsilon}}}_{raw} - \Delta\dot{\hat{\boldsymbol{\varepsilon}}}_{tsh}}{\Delta\dot{\hat{\boldsymbol{\varepsilon}}}_{lim} - \Delta\dot{\hat{\boldsymbol{\varepsilon}}}_{tsh}}}\right) & \text{for } \Delta\dot{\hat{\boldsymbol{\varepsilon}}}_{raw} > \Delta\dot{\hat{\boldsymbol{\varepsilon}}}_{tsh} \end{cases} \tag{3.13}$$

where $\Delta\dot{\hat{\boldsymbol{\varepsilon}}}_{raw}$ is the raw increment computed by the FE solver at the current time step, and $\Delta\dot{\hat{\boldsymbol{\varepsilon}}}_{tsh}$ and $\Delta\dot{\hat{\boldsymbol{\varepsilon}}}_{lim}$ are the threshold and limit parameters that define the filtering.

3.2. Matrix-dominated nonlinear behaviour

With the underlying viscoelastic formulation in place, an additional set of constitutive laws needs to be defined to describe the material response as it starts to deviate from the linear elastic behaviour.

Many ways to treat this material nonlinearity, summarized in section 2.2, have been proposed in the past, from more pragmatic, purely empirical approaches – such as interpolation and extrapolation of the experimental data [62] or the use of a predefined mathematical relation between stress-strain, such as the Ramberg-Osgood relation which was originally developed for metals [115] – to more proper mathematical or physically-based formulations, such as the reviewed plasticity and damage models [48,109–111,113]. However, none of these macro-scale modelling approaches was found suitably able to describe the anisotropic, multi-axial, or pressure-dependent, and the viscous, or rate-dependent, behaviour observed in UD CFRPs.

In addition, there are indications that the observed nonlinear behaviour is closely related to the eventual matrix-dominated IFF failure mode that it precedes.

Therefore, a viscoplastic model capable of describing the material's complex nonlinear behaviour is proposed in the following sections, which is based on Puck's localisation plane theory for IFF [12] with the assumption that the two are driven by similar mechanisms

3.2.1. Introduction

The presented plasticity model aims to accurately describe the effects of multiaxial loading, pressure, and strain rate on unidirectional FRPs, while doing so in an intuitive and physically-based manner. In this model, following the localisation plane theory used by Puck [12] to predict IFF, it is assumed that yielding occurs primarily due to shear stresses acting on a critical localisation plane while normal compressive stresses have a strengthening effect similar to pressure effects in a Drucker-Prager model [116]. In this way, the orientation of the localisation plane, which depends on the stress state of the material, deals with the issues of anisotropy and multiaxiality and the effects of pressure are accounted for by the Drucker-Prager based yield criterion.

The main appeal of this approach is that a complex three-dimensional problem is essentially reduced to a case of 2D plasticity, which is conceptually very simple and easier to interpret. In addition, this model is supported by a strong physical basis, as it is constructed from the well-established Mohr-Coulomb and Drucker-Prager theories.

First, however, a series of experimental results are provided in support of the hypotheses on which the proposed theory is based, which are later used to validate the model and demonstrate its ability to reproduce the complex observed behaviour.

3.2.2. Background

Due to their anisotropic nature, CFRPs present a serious challenge when it comes to the prediction of damage and failure. Well-known effects in the polymeric matrix materials, such as pressure and rate dependencies, become more complex with the addition of the anisotropic fibre reinforcement. This translates into an extremely complex mechanical response on the part of the composite material as a result of the interaction between all of these individual properties [44,58,60,117]. These effects have been well accounted for in various IFF failure criteria [63,118], which not only provide a good correlation between experimental observations and their predictions but also give plausible physical explanations for the material behaviour. However, the same level of maturity has not been reached in the modelling of the nonlinear shear behaviour before failure. Therefore, in order to raise the degree of confidence in the nonlinear constitutive modelling of UD CFRPs, it is important not only to be able to predict known experimental results but also to provide a strong physical justification of the theory behind it.

3.2.2.1. Experimental observations

As introduced in the literature review, UD CFRPs can exhibit significant nonlinear behaviour in matrix-dominated loading directions as a result of the micromechanical response of the polymeric matrix and fibre-matrix interfaces [119]. However, due to the heterogeneous, anisotropic structure of the composite, the degree of non-linearity in the stress-strain response can vary considerably depending on the loading direction [44,117] and the underlying matrix properties also make this response pressure and strain rate dependent [58,60]. Relevant experimental data showing the effects of pressure on a UD graphite/epoxy in [58,60] and the rate-dependent multiaxial response of the IM7/8552 composite in [44] has been reproduced in Figure 3.1 below.

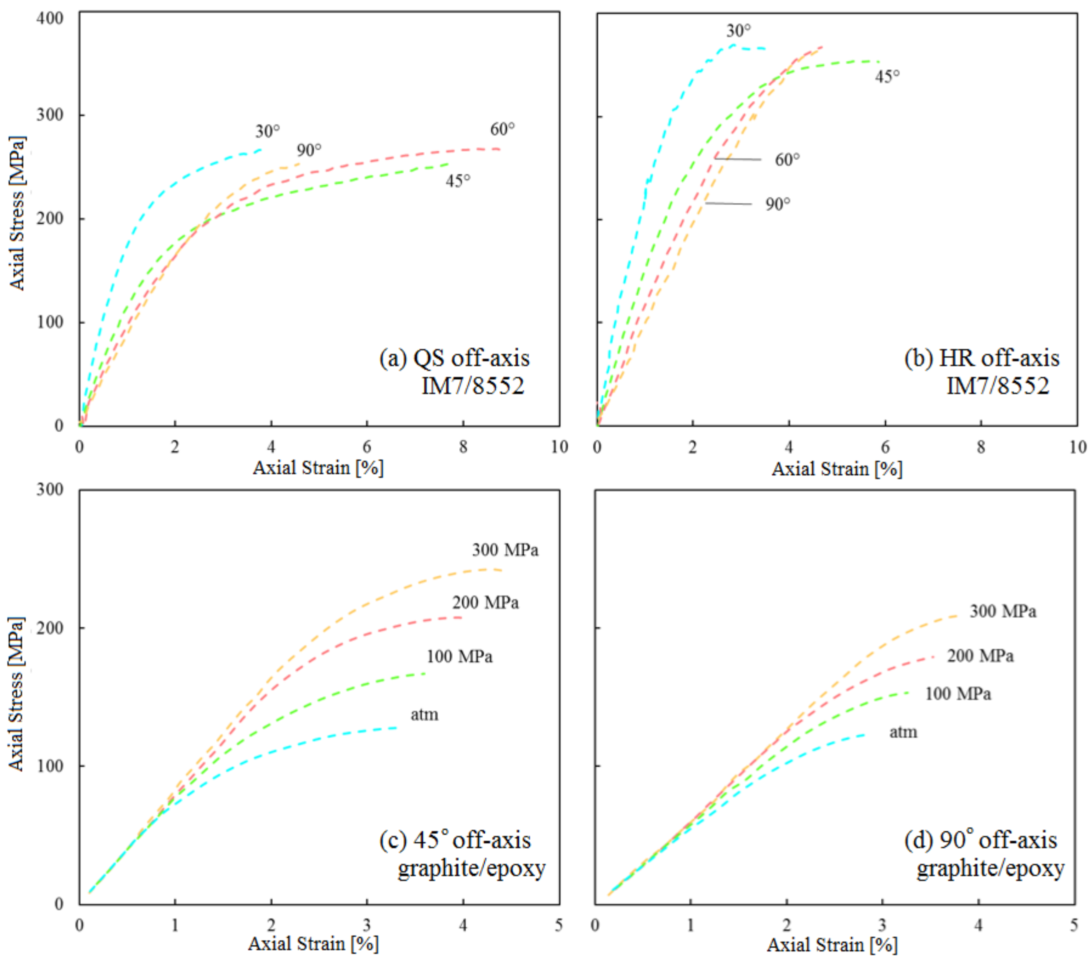

Figure 3.1. (a) Quasi-static and (b) dynamic off-axis compression data from [44] and (c) 45° and (d) 90° off-axis compression under hydrostatic pressure from [58].

This macroscopic nonlinear response is associated with the accumulation of micro-scale yielding and damage in the matrix and fibre-matrix interfaces, as observed in [52,120], where X-ray Computed Tomography (XCT) scans of CFRP laminates deformed in shear showed increasing signs of damage at different points along the nonlinear shear curve. In addition, the Digital Image Correlation (DIC) analysis [121] of quasi-static off-axis compression tests in [44] as well as results from a similar quasi-static test carried out in-house by Hoffmann [72], Figure 3.2, show signs of strains localising along the eventual fracture plane long before failure. More details on the waisted specimen design and experimental methodology for this specific test are given in section 4.2.

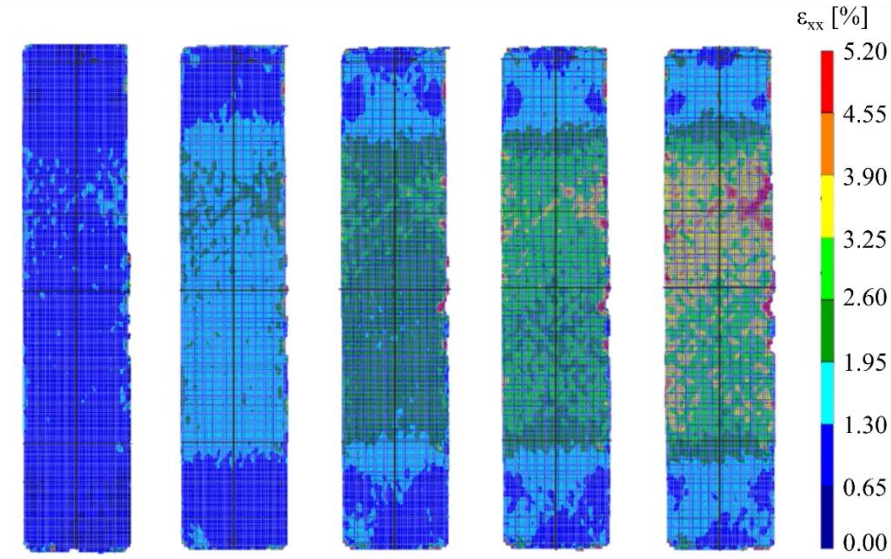

Figure 3.2. DIC measured longitudinal strain at different stages during a 90° off-axis quasi-static compression test from Hoffmann in [72] following the experimental methodology described in section 4.2. Here the strains can be seen to begin localising along the eventual fracture plane in the early stages of the test.

All together, these observations may point to a closer relation between the macroscopic nonlinear response and IFF failure in UD CFRPs than is generally assumed, which led to the proposal of the localisation plane plasticity model in section 3.2.3. Before that, however, the need for an alternative nonlinear constitutive modelling approach is justified in the following section.

3.2.2.2. Constitutive models for UD FRPs

While there exist a number of constitutive models capable of predicting several of the afore-mentioned effects, none has been found that encompasses them all, particularly the viscous, or rate-dependent, behaviour, which is crucial for dynamic and impact or crashworthiness problems, as has been discussed in section 2.2 of the literature review.

Several of these were considered as a possible starting point for the development of a fully rate-dependent multiaxial and pressure-sensitive model. However, none of the reviewed models was found suitable for various different reasons. CDM-based models such as the one developed by Treutenaere in [48], while providing a strong physical basis for the viscous nonlinear behaviour of the composite under in-plane shear, only considered nonlinearity in the 12 direction, lacking anisotropic and multiaxial behaviour. In addition, such models were found excessively complex for the desired application, requiring many material characterisation properties not easily available for the IM7/8552 composite at the time, and extending them into three-dimensions would only add to the problem. Different plasticity models, such as Sun and Chen [114], Vyas et al. [113] or others [50,122], have been shown to describe the multiaxial and pressure-dependent nonlinear behaviour but they lack rate-dependency and the yield criteria they use are just as empirical as many of the IFF failure criteria from the WWFE that were considered unsuitable for the LaRC models in [62,104].

Instead, following the experimental observations from the previous section, a localisation plane-based approach similar to that used for the physically-based IFF failure criteria has been developed, inspired by Puck's proposal in [123].

3.2.3. Localisation plane plasticity model

From the results in [44,52,120] it appears that, after yielding, plastic strains in UD FRPs tend to localise along certain planes around the fibre direction. Furthermore, it also seems that these same localisation planes end up developing into the ultimate inter-fibre fracture (IFF) failure planes that can be accurately explained by Puck's failure criterion [12]. In addition, the yield envelopes (defined as the stresses corresponding to a 0.02% plastic shear strain) obtained in [44] for both quasi-static and high strain rates closely match the shape of the failure envelopes that are obtained with Puck's IFF criterion.

With this in mind, it seems reasonable to assume that the same physical phenomena behind Puck's failure criterion might also be behind the complex nonlinear response observed in UD FRPs. Therefore, on the basis of Puck's IFF theory, the following localisation plane plasticity model is built on the assumption that the inelastic behaviour in these materials is caused by the shear stresses acting on a critical plane around the fibre direction, on which a linear Drucker-Prager type equivalent stress is maximised.

3.2.3.1. Yield criterion

In the same way as the potential fracture plane in Puck's IFF criterion introduced in section 2.2, in this model, yielding is assumed to occur along a plane parallel to the fibre direction. Therefore, in order to evaluate the yield condition, the potential yield plane must first be determined. In the same way as for Puck's IFF criterion, the localisation plane is obtained by evaluating the yield criterion at different plane orientations and determining the most critical. The orientation of the yield plane, θ_y, illustrated in Figure 3.3, is the angle where the equivalent stress, $\bar{\sigma}$, defined by the criterion is maximum, indicating the plane most likely to yield.

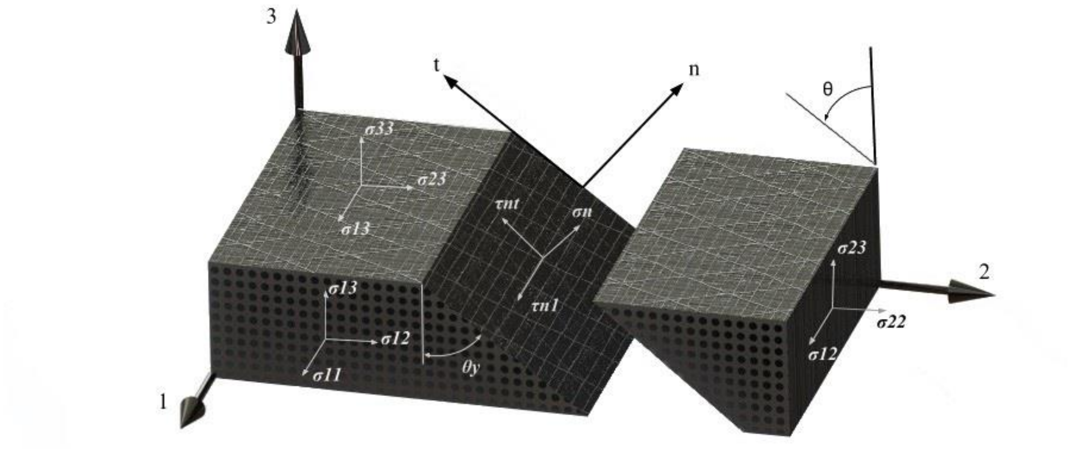

Figure 3.3. Traction plane stresses, σ_n, τ_{n1} and τ_{nt}, acting on the potential yield plane at an angle, θ_y,around the fibre direction, 1.

Starting in the local material coordinates, the Cauchy stress vector, $\hat{\boldsymbol{\sigma}} = \{\hat{\sigma}_{11}\ \hat{\sigma}_{22}\ \hat{\sigma}_{33}\ \hat{\tau}_{12}\ \hat{\tau}_{23}\ \hat{\tau}_{13}\}^T$, is rotated around the fibre direction, 1, by an angle, θ, to obtain the stresses acting on that particular plane, $\hat{\boldsymbol{\sigma}}_\theta = \{\sigma_1\ \sigma_n\ \sigma_t\ \tau_{n1}\ \tau_{nt}\ \tau_{1t}\}^T = \boldsymbol{R}_\sigma[\theta]\ \hat{\boldsymbol{\sigma}}$, with the rotation matrix, $\boldsymbol{R}_\sigma[\theta]$, given by:

$$\boldsymbol{R}_\sigma[\theta] = \begin{bmatrix} 1 & 0 & 0 & 0 & 0 & 0 \\ 0 & c^2 & s^2 & 0 & 2\,c\,s & 0 \\ 0 & s^2 & c^2 & 0 & -2\,c\,s & 0 \\ 0 & 0 & 0 & c & 0 & s \\ 0 & -c\,s & c\,s & 0 & c^2 - s^2 & 0 \\ 0 & 0 & 0 & -s & 0 & c \end{bmatrix} \tag{3.14}$$

Similarly, the strains can be rotated onto the localisation plane by:

$$\boldsymbol{R}_\varepsilon[\theta] = \begin{bmatrix} 1 & 0 & 0 & 0 & 0 & 0 \\ 0 & c^2 & s^2 & 0 & 2\,c\,s & 0 \\ 0 & s^2 & c^2 & 0 & -2\,c\,s & 0 \\ 0 & 0 & 0 & c & 0 & s \\ 0 & -2\,c\,s & 2\,c\,s & 0 & c^2 - s^2 & 0 \\ 0 & 0 & 0 & -s & 0 & c \end{bmatrix} \tag{3.15}$$

where $c = \cos[\theta]$, $s = \sin[\theta]$ and the inverse rotation matrices used to return the localisation plane components to the material coordinate system are $\boldsymbol{R}^{-1}[\theta] = \boldsymbol{R}[-\theta]$.

Since Puck's localisation plane theory is built using only the normal, σ_n, and shear, τ_{n1} and τ_{nt}, components of stress, a reduced stress vector can be defined as $\tilde{\boldsymbol{\sigma}} = \{\sigma_n \ \tau_{n1} \ \tau_{nt}\}^T$. The likelihood of yielding is then evaluated on a number of planes, θ, and the localisation plane, θ_y, can be determined through an efficient numerical search method described in Appendix A as the plane that maximises the equivalent stress, $\bar{\sigma}$, within following yield criterion:

$$f_y\left[\hat{\boldsymbol{\sigma}}, \theta, \bar{\varepsilon}_p, \dot{\bar{\varepsilon}}\right] = f_y\left[\tilde{\boldsymbol{\sigma}}, \bar{\varepsilon}_p, \dot{\bar{\varepsilon}}\right] = \bar{\sigma}[\tilde{\boldsymbol{\sigma}}] - \tau_y\left[\bar{\varepsilon}_p\right] r_y[\dot{\bar{\varepsilon}}] = 0 \tag{3.16}$$

where $\bar{\varepsilon}_p$ and $\dot{\bar{\varepsilon}}_p$ are the equivalent plastic strain and the equivalent strain rate respectively, $\tau_y\left[\bar{\varepsilon}_p\right]$ is the yield stress corresponding to in-plane shear with plastic strain hardening and a strain rate hardening parameter $r_y[\dot{\bar{\varepsilon}}]$ described in section 3.2.3.4.

Here the equivalent stress, $\bar{\sigma}$, is what defines the shape of the yield surface as well as the critical localisation plane, θ_y. As mentioned in section 3.2.2, yielding in FRPs has been observed to be pressure dependent. In addition, according to the data in [58,60], as observed by Vyas et al. in [113], this relation between pressure and yield stress can be considered linear. Therefore, the following linear Drucker-Prager-type criterion has been used, illustrated in Figure 3.4, where yielding is assumed to be primarily caused by a combination of the shear stresses, τ_{n1} and τ_{nt}, on the plane, θ_y, while the normal stress, σ_n, adds the frictional pressure effect.

$$\bar{\sigma}[\tilde{\boldsymbol{\sigma}}] = \alpha\sigma_n + \sqrt{{\tau_{n1}}^2 + e{\tau_{nt}}^2} = \alpha\sigma_n + \tau_{eff} \tag{3.17}$$

where α is the equivalent to the friction coefficient in a Drucker-Prager model and e is an elliptical shear interaction parameter that defines the difference between the longitudinal and transverse shear, τ_{n1} and τ_{nt}, respectively.

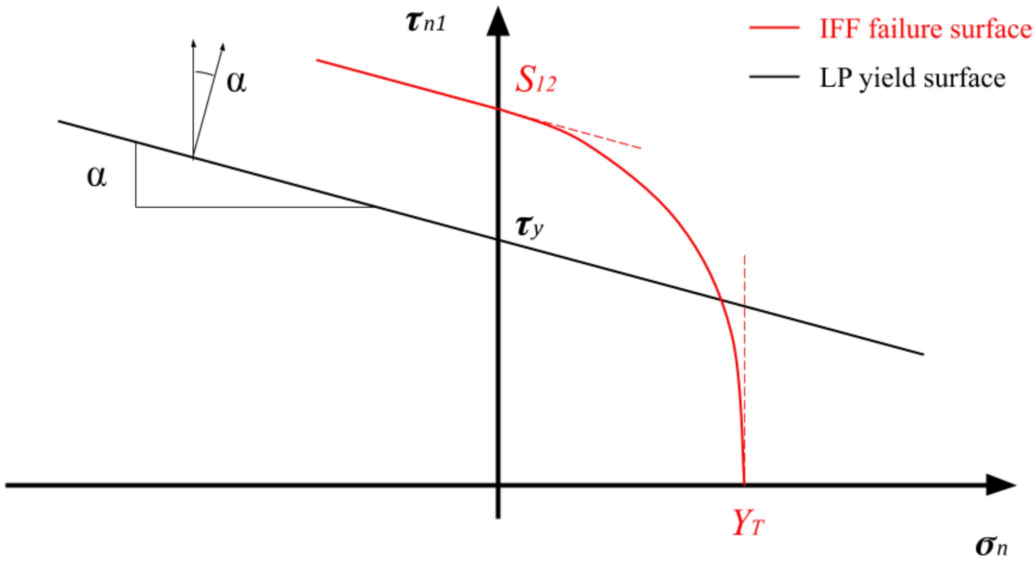

Figure 3.4. Illustration of the Drucker-Prager based yield criterion on the reduced $\sigma_n - \tau_{n1}$ plane. The solid red line illustrates how the IFF envelope intersects the yield surface under transverse tensile loads.

While Puck originally used a quadratic function to describe the pressure effects on the IFF strength, here the suggested linear relation is shown to be enough to describe the yielding behaviour in section 3.2.4. In addition, since the tip of the conical yield surface is intersected by the IFF envelope under transverse tension, $\sigma_n > 0$, due to the low tensile strength of the matrix, Y_T, any potential singularity issues at the vertex are avoided and the material response is described as linear elastic until failure.

3.2.3.2. Flow rule

Continuing the analogy with a Drucker-Prager-type plasticity model, a non-associative plastic flow rule has been implemented as:

$$\tilde{\boldsymbol{d}}^p = \dot{\lambda}\,\boldsymbol{m} = \dot{\lambda}\frac{\partial g[\tilde{\boldsymbol{\sigma}}]}{\partial \tilde{\boldsymbol{\sigma}}} = \dot{\lambda}\begin{Bmatrix} \partial g/\partial \sigma_n \\ \partial g/\partial \tau_{n1} \\ \partial g/\partial \tau_{nt} \end{Bmatrix} \tag{3.18}$$

where the flow vector $\boldsymbol{m}$ is defined with the following flow potential, g,

$$g[\tilde{\boldsymbol{\sigma}}] = \alpha_g \sigma_n + \sqrt{{\tau_{n1}}^2 + e_g {\tau_{nt}}^2} \tag{3.19}$$

which follows the same form as the effective stress function, $\bar{\sigma}$, with material parameters α and e replaced by $\alpha_g$and e_g.

Here $\alpha_g$would correspond to the dilatancy coefficient in a Drucker-Prager model, which accounts for dilatant sliding in frictional materials. The elliptical shear flow interaction parameter, e_g, is added to allow different flow rates along and transverse to the fibre direction, which should be expected given the anisotropic nature of FRPs.

Finally, the evolution equation for the equivalent plastic strain can be obtained from the work conjugacy, $\tilde{\boldsymbol{\sigma}}^T \, \tilde{\boldsymbol{d}}^p = \bar{\sigma} \, \dot{\bar{\varepsilon}}_p$:

$$\dot{\bar{\varepsilon}}_p = \dot{\lambda} \frac{\tilde{\boldsymbol{\sigma}}^T \boldsymbol{m}}{\bar{\sigma}} = \dot{\lambda} \, h \tag{3.20}$$

As a side note, within the above non-associated flow rule, associated flow behaviour can be recovered, if desired, when $\boldsymbol{n} = \partial f / \partial \tilde{\boldsymbol{\sigma}} = \boldsymbol{m}$, by imposing $\alpha_g = \alpha$ and $e_g = e$.

3.2.3.3. Strain hardening

Due to the lack of experimental data on cyclic loading on UD FRPs, a priori there is no strong evidence favouring either kinematic or isotropic hardening. Therefore, for simplicity, strain hardening has been modelled as isotropic with two different possible hardening laws given below. While several other types of hardening behaviour could be used, a simple power law and a more complex Voce-type hardening function have been implemented [124] to allow for the modelling of different types of behaviour in different materials:

$$\tau_y[\bar{\varepsilon}_p] = A + B\left(\bar{\varepsilon}_p\right)^C \tag{3.21}$$

$$\tau_y\left[\bar{\varepsilon}_p\right] = A + B_1(1 - e^{-C_1\bar{\varepsilon}_p}) + B_2(1 - e^{-C_2\bar{\varepsilon}_p}) \quad (3.22)$$

Where A, B, C, B_1, B_2, C_1, and C_2 are the material parameters that define the shape of the two possible hardening functions, with $A = \tau_{y0}$ being the quasi-static yield strength.

3.2.3.4. Rate effects

Finally, the strain rate hardening function, $r[\dot{\bar{\varepsilon}}]$, is defined below, using the same kind of radical scaling function used for the rate-dependent stiffness in eqn. (2.3), section 1.2:

$$r_y[\dot{\bar{\varepsilon}}] = 1 + \sqrt{K_y\dot{\bar{\varepsilon}}} \quad (3.23)$$

Where K_y is the strain rate dependent factor, calibrated from yield stress data at different strain rates, and $\dot{\bar{\varepsilon}}$ is the equivalent strain rate defined as:

$$\dot{\bar{\varepsilon}}[\widehat{\boldsymbol{d}}] = \sqrt{\frac{2}{3}\widehat{\boldsymbol{d}}^T\widehat{\boldsymbol{d}}} \quad (3.24)$$

as a pragmatic solution to allow for the same strain rate measure to be used here and for the failure criteria, including longitudinal compression where otherwise no strain rate effects would be observed due to the lack of plastic strain in the fibre direction.

The scaling function described in eqn. (2.3) has been used successfully in the past to fit the rate-dependent behaviour of matrix stiffness and strength properties in UD CFRPs at different loading rates [19,35,125]. It therefore seems reasonable to assume that the yield stress may follow a similar trend, especially considering that the developed model is based on the same principles as Puck's IFF criterion, which has been shown to work with the same type of scaling function.

3.2.3.5. Stress return algorithm

Having defined all of the model's individual components, the numerical stress integration algorithm used to implement it within the modelling framework presented in section 1.2 is described below.

Following the initial linear elastic trial step, which is defined incrementally as:

$$\hat{\boldsymbol{\sigma}}^{tr}_{(n+1)} = \hat{\boldsymbol{\sigma}}_{(n)} + \hat{\boldsymbol{C}}\,\Delta t\,\hat{\boldsymbol{d}}_{(n+1/2)} \tag{3.25}$$

the stresses are rotated onto the critical localisation plane using $\hat{\boldsymbol{\sigma}}_{\theta} = \boldsymbol{R}_{\sigma}\left[\theta_y\right]\hat{\boldsymbol{\sigma}}$ and reduced to obtain $\tilde{\boldsymbol{\sigma}}$, with which the yield criterion is evaluated. To do so, the critical localisation plane can be determined using the algorithm presented in Appendix A.

In addition, the effective strain rate, eqn. (3.24), which is used to scale the yield stress, is obtained from the rate of deformation at the midpoint time step $n + 1/2$ as:

$$\dot{\bar{\varepsilon}}_{(n+1)} = \dot{\bar{\varepsilon}}\left[\hat{\boldsymbol{d}}_{(n+1/2)}\right] \tag{3.26}$$

If the rate-dependent yield stress is surpassed, the material starts to deform plastically and the plastic strain increment that returns the stress onto the yield surface must be determined. However, since both the effective stress and the strain hardening, which dictates the size of the yield surface, depend on the plastic strain following eqn. (3.27) to (3.29) below, an iterative solution method is needed to determine the amount of plastic deformation that return the tri yield condition, $f_y = 0$.

Since the plastic strain is proportional to the plastic multiplier, following the plastic flow rule in section 3.2.3.2, both the effective stress and the yield function can be defined incrementally as a function of the plastic multiplier increment, $\Delta\lambda$. Therefore, the following system of equations must be solved to return the effective stress onto the yield surface, with the plastic multiplier as the only unknown:

$$f_{y(n+1)}[\Delta\lambda] = \bar{\sigma}_{(n+1)}\left[\widetilde{\boldsymbol{\sigma}}_{(n+1)}\right] - \tau_{y(n+1)}\left[\bar{\varepsilon}_{p(n+1)}\right] r_{y\,(n+1)}\left[\dot{\bar{\varepsilon}}_{(n+1)}\right] = 0 \tag{3.27}$$

$$\widetilde{\boldsymbol{\sigma}}_{(n+1)} = \widetilde{\boldsymbol{\sigma}}^{tr}_{(n+1)} - \Delta\lambda\, \widetilde{\boldsymbol{C}}\, \boldsymbol{m}_{(n+1)} \tag{3.28}$$

$$\bar{\varepsilon}_{p(n+1)} = \bar{\varepsilon}_{p(n)} + \Delta\lambda_{(n+1)} \frac{\left(\widetilde{\boldsymbol{\sigma}}_{(n+1)}\right)^T \boldsymbol{m}_{(n+1)}}{\bar{\boldsymbol{\sigma}}_{(n+1)}} \tag{3.29}$$

Where $\widetilde{\boldsymbol{C}}$ is the reduced 3x3 matrix obtained by retaining only the necessary components of the rotated 6x6 stiffness matrix $\widehat{\boldsymbol{C}}_{\theta} = \boldsymbol{R}_{\varepsilon}\left[-\theta_y\right] \widehat{\boldsymbol{C}}\, \boldsymbol{R}_{\sigma}\left[\theta_y\right]$. However, in the case of transverse isotropy, by definition no rotation is necessary.

The Newton-Raphson scheme described in Simo and Hughes [126] is used to solve the system by iterating over the linearised yield function below:

$$f^{(i+1)}_{y(n+1)} \approx f^{(i)}_{y(n+1)} + \left(\boldsymbol{n}^{(i)}_{(n+1)}\right)^T \delta\widetilde{\boldsymbol{\sigma}} + \left.\frac{\partial f_y}{\partial \bar{\varepsilon}_p}\right|^{(i)}_{(n+1)} \delta\bar{\varepsilon}_p = 0 \tag{3.30}$$

where the superscript (i) indicates the iteration step and $\delta(\star) = (\star)^{(i+1)}_{(n+1)} - (\star)^{(i)}_{(n+1)}$, so:

$$\delta\widetilde{\boldsymbol{\sigma}} = -\delta\lambda\, \widetilde{\boldsymbol{C}}\, \boldsymbol{m}^{(i)}_{(n+1)} \tag{3.31}$$

$$\delta\bar{\varepsilon}_p = \delta\lambda\, h^{(i)}_{(n+1)} \tag{3.32}$$

The linearised yield function can then be transformed to estimate of the plastic multiplier increment, which is updated every iteration by:

$$\Delta\lambda^{(i+1)} = \Delta\lambda^{(i)} + \delta\lambda \tag{3.33}$$

where $\delta\lambda$ is the increment estimated from eqn. (3.30).

This iterative procedure is repeated until the updated yield function converges to a satisfactory tolerance:

$$\left| \frac{f_{(n+1)}^{(i+1)}}{\tau_{y(n+1)}^{(0)} \, r_{y\,(n+1)}} \right| \leq TOL \tag{3.34}$$

Once the condition above is fulfilled, the stress and plastic strain are updated for the current time step and the subroutine can continue onto the evaluation of the different failure criteria, which will be defined in the next chapters.

3.2.4. Single element evaluation

In order to test the ability of the proposed model to reproduce the various complicated effects observed in the nonlinear shear response of UD CFRPs, it was implemented in LS-DYNA within the framework described in section 1.2 and used to simulate a number of different experimental test cases.

The objective for this preliminary evaluation was simply to test the model's capabilities, with a more thorough model validation campaign carried out in Chapter 7 once all other aspects of the material behaviour, such as matrix and fibre failure, have been introduced. The following test cases have therefore been modelled with single 8-node solid elements without aiming to reproduce all of the physical test conditions, such as specimen geometry or boundary conditions.

3.2.4.1. Multi-axial behaviour

The first set of experiments to be modelled were the quasi-static off-axis transverse compression tests by Koerber et al. on IM7/8552 [44]. A Voce hardening law, eqn. (3.22), with the material parameters shown in Table 3.1, was found to produce a good fit against the experimental stress-strain curves, as can be seen in Figure 3.5 (a).

While these results may be improved with more realistic modelling of the testing conditions and better calibrated elastic and plastic properties, they show the ability of the developed model to capture the anisotropy and multiaxiality of the nonlinear response. For comparison, the same tests modelled using the classic one-dimensional plasticity approach are shown in Figure 3.5 (b), where the nonlinear shear properties were calibrated to minimise the accumulated error across all four curves.

Table 3.1. Model parameters used for the quasi-static and dynamic off-axis compression tests from [44].

Elastic Properties

E_{11T} [MPa]	E_{11C} [MPa]	$E_{22}(=E_{33})$ [MPa]	(high rate) $E_{22}(=E_{33})$ [MPa]	G_{12} $(=G_{13})$ [MPa]	(high rate) G_{12} $(=G_{13})$ [MPa]	G_{23} [MPa]
160000	140000	9000	10000	4500	6000	2150

Plastic Properties

B_1	C_1	B_2	C_2	$A = \tau_{y0}$	α	α_g	e	e_g	K_y
33	130	25	10	60	0.1	0.23	0.9	1	1E-03

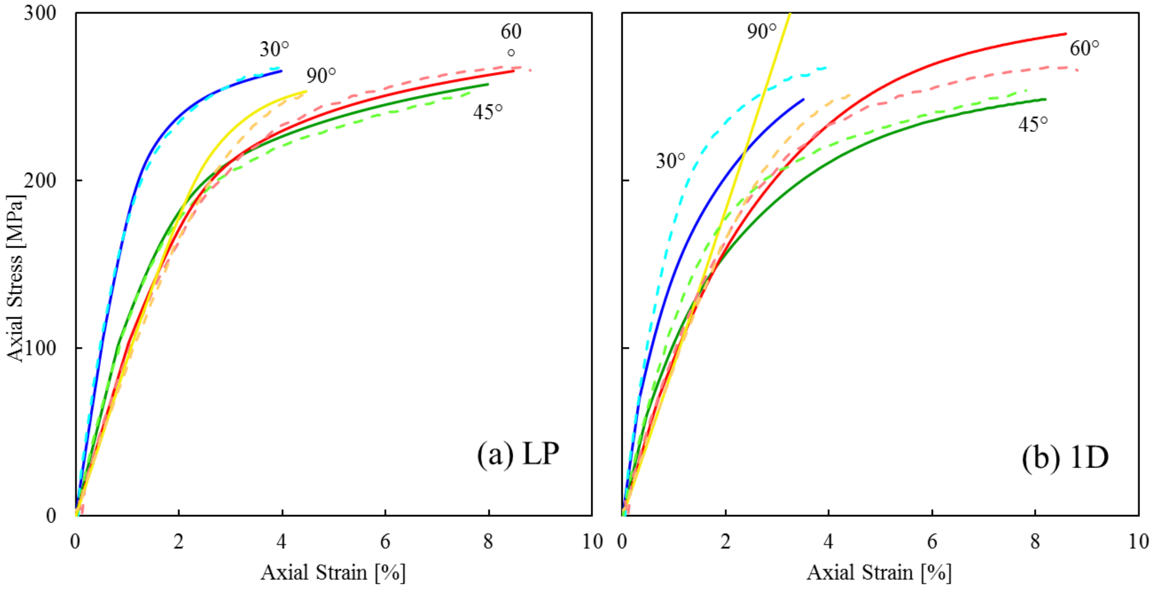

Figure 3.5. Numerical (solid) and experimental (dashed) axial stress – axial strain curves for the quasi-static off-axis loading cases from [44] modelled using (a) the proposed LP plasticity model, and (b) the classic 1D plasticity approach.

3.2.4.2. Strain rate effects

Next, continuing with the IM7/8552 off-axis compression tests from Koerber et al. [44], the dynamic SHPB test data was used to evaluate the rate-dependency of the proposed constitutive model. For each off-axis test case, a different constant velocity was applied to one face of the solid brick element in order to match the different strain rates measured in each test in [44]. Using the same plastic material parameters as the previous section, given in Table 3.1, with the rate dependent factor, K_y, calibrated from 45° compression test, the results shown below in Figure 3.6 were obtained.

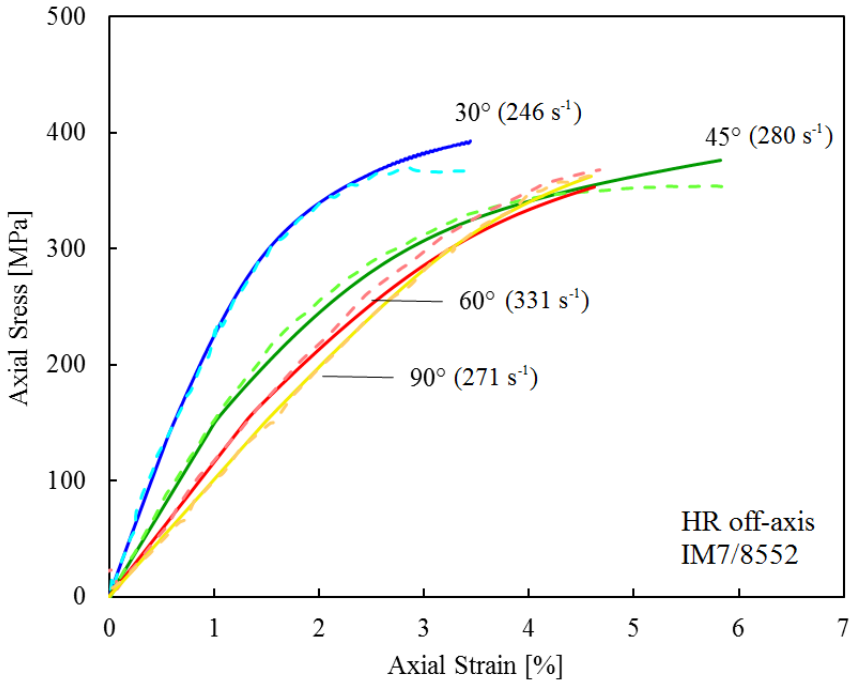

Figure 3.6. Numerical (solid) and experimental (dashed) axial stress – axial strain curves for the high strain rate (200-300 s^{-1}) off-axis loading cases from [44].

Again, a good prediction of the overall experimental response was obtained. However, some more noticeable deviations from the target curves can be observed near the end of the 30° and 45° test cases in particular. This may be due to the simplified test conditions in the simulations, where a constant strain rate was applied in contrast to the gradually decreasing strain rate observed in the experiments [44]. A more realistic simulation of the test conditions may, once more, improve the model's results, as a fall in the strain rate towards the end of the tests would reduce the strain rate hardening and may bring the predicted curves closer to the experimental results. In addition, previous attempts to model these same test cases by Koerber in [49] showed similar issues. Therefore, the preliminary results in Figure 3.6 were considered good enough to validate the ability of the proposed model to describe the rate-dependent and multi-axial behaviour of UD CFRPs at this early stage in its development.

3.2.4.3. Hydrostatic pressure effects

Finally, the off-axis compression tests with superimposed hydrostatic pressure carried out by Pae et al. [58] were simulated to test the pressure-dependency of the proposed model. In [58], a UD graphite/epoxy composite was tested in off-axis compression at 45° and 90° under superimposed hydrostatic pressures of 0, 100, 200 and 300 MPa. Since the exact material properties for the Thornel 300/3M PR319 composite were not known, the parameters given in Table 3.2, calibrated from the two 0 MPa curves, were used instead.

The results of these simulations are given in Figure 3.7, showing very good agreement between predictions and experiments across all tests. These test cases are especially interesting because in the proposed model, it is the same frictional parameter, α, that defines the shape of the yield surface and the effects of hydrostatic pressure. Therefore, the fact that the same material parameters calibrated from the 45° and 90° tests at 0 MPa also accurately describe the effects of superimposed hydrostatic pressure, provides additional validation for the localisation plane theory to describe the nonlinear behaviour of UD CFRP composites.

Table 3.2. Model parameters used for the 45° and 90° off-axis compression tests under hydrostatic pressure from [58].

Elastic Properties

E_{11T} [MPa]	$E_{22}(=E_{33})$ [MPa]	G_{12} ($=G_{13}$) [MPa]	G_{23} [MPa]
24000	6000	3000	2150

Plastic Properties

B_1	C_1	B_2	C_2	$A = \tau_{y0}$	α	α_g	e	e_g
21.45	236.3	21.83	23.53	23.11	0.143	0.122	1.119	0.660

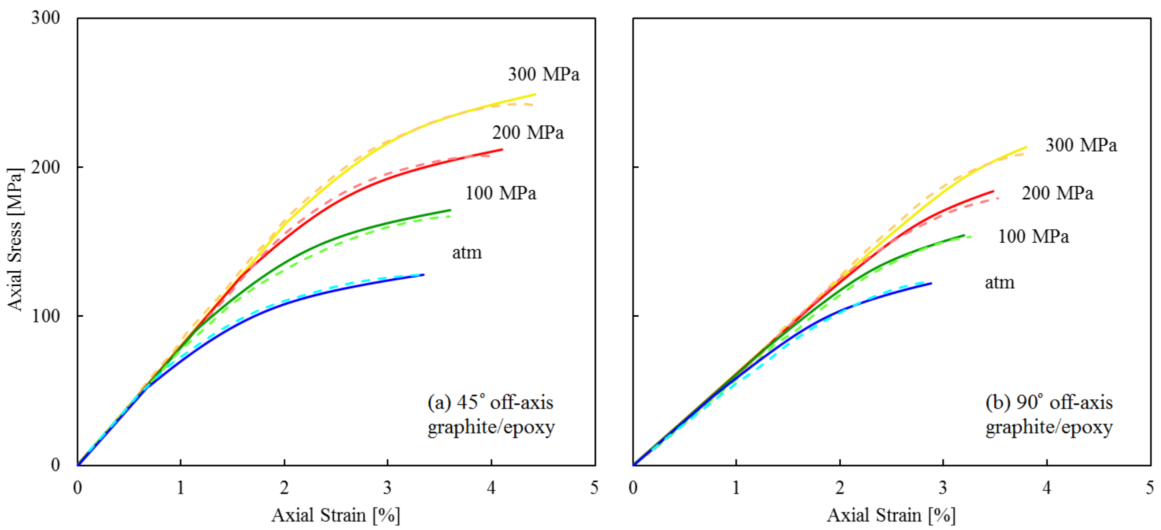

Figure 3.7. Numerical (solid) and experimental (dashed) axial stress – axial strain curves for the 45° (top) and 90° (bottom) compression tests under various levels of hydrostatic pressure from [58].

3.2.5. Conclusions

Given the lack of suitable alternatives in the literature, a novel nonlinear constitutive model for UD CFRP laminates has been developed in section 3.2.3 with the aim of presenting a conceptually simple yet accurate explanation for the various types of complex nonlinear behaviour exhibited by this type of material, such as the effects of multiaxial loading, hydrostatic pressure, and strain rate.

The proposed model is inspired by Puck's localisation plane theory used to predict IFF [12] and several experimental observations such as the shape of the yield surface under combined loading or the appearance of localisation bands early on in the nonlinear stages of stress-strain curves [44]. With this in mind, a localisation plane-based plasticity model has been developed, where the macroscopic nonlinear behaviour of the composite is assumed to be caused by shear-dominated strain localisation along certain planes, defined by a Mohr-Coulomb type yield criterion. The deformation along these localisation planes is assumed to follow pressure-dependent linear Drucker-Prager behaviour dictated by a frictional parameter, α. Finally, a strain rate hardening parameter is used to proportionally scale the yield surface.

The preliminary set of single element validation test cases in section 3.2.4 show the model's ability to capture all of the experimentally observed effects of multiaxial loading, hydrostatic pressure, and strain rate, providing some validation for the theory that strain localisation may explain not only IFF but also the nonlinear shear-dominated behaviour before it.

Following the investigation of IFF and fibre compression failure in Chapter 4 and 5.2, a more complete, full-scale validation of the model is presented in Chapter 7, including investigations into possible scaling and mesh-dependency issues, the determination of optimal material parameters for the studied IM7/8552 material, and more realistic representation of the specimen geometry and boundary conditions. However, at this stage, the preliminary results already show the ability of the proposed localisation plane theory to describe all of the complex observed behaviour, while giving a simple and elegant explanation that essentially reduces the problem to a case of 2D plasticity along a specific plane.

One issue that has not been addressed in this section due to lack of experimental data and lack of time to perform such tests, is the material behaviour under cyclic or reverse loading. Future experimental work in this area is recommended as it will help to reveal how much of the nonlinear response is due to plastic strains or damage and whether isotropic or kinematic hardening should be used. In addition, micromechanical modelling may also help to show if the macroscopic nonlinear behaviour can be associated with micro-scale effects such as matrix yielding or fibre-matrix interface damage.

Finally, taking into consideration the model's physical basis and experimental observations regarding localisation planes leading to fracture, the next step is to verify whether IFF can, in fact, be predicted as a direct result of this same strain localisation along the same localisation planes, which will be investigated in the following section.

Chapter 4

Inter-fibre fracture initiation

Inter-fibre fracture in UD CFRPs has been one of the most studied modes of failure in these materials and, since the WWFE and LaRC reports [62,63,104], Puck's localisation plane theory for the complex observed behaviour [12] has become widely accepted, with various authors providing validation through both experimental and micromechanical modelling campaigns [44,54,56,62,104]. However, as discussed in section 2.1.4, the effects of strain rate on IFF have not been studied in the same depth. Therefore, in the current section, the effects of strain rate on different strength properties that define IFF failure and the size and shape of the failure envelope will be investigated using quasi-static and dynamic off-axis tension and compression data from the literature as well as a new set of in-house tests. In addition, following from the work in the previous section, the possibility of deriving the IFF failure envelope from the same LP model proposed to describe the nonlinear shear response will be evaluated.

4.1. Introduction

Under transverse loading, the matrix properties dominate the overall strength of UD CFRPs. However, unlike the orthotropic stiffness properties or the longitudinal tensile strength, the strength under transverse loading, especially in compression, cannot simply be estimated by the rule of mixtures [38,39]. Due to the frictional behaviour of the fibres in compression and the nonlinear rate-dependent behaviour of the matrix, at the macroscopic scale IFF failure exhibits complex interactions that result in the observed rate- and pressure-dependent behaviour and complex failure envelope.

The localisation plane theory proposed by Puck [12] provides the best physical explanation for these observed effects by assuming macroscopic failure is the result of micro-scale matrix damage localising along certain planes transverse to the fibre direction, which is predicted using a Mohr-Coulomb pressure-dependent criterion. As discussed in the literature review in section 2.1.4, Puck's IFF theory has been extensively validated in many experimental studies, such as the first and second WWFE [63,102,103] and the LaRC reports [62,104] among others. In addition, more recently micromechanical modelling has been used to show micro-scale damage localisation in agreement with Puck's LP theory and predictions [54,56].

However, these studies have mostly focused on failure at quasi-static loading rates and the effects of strain rate have not been studied in as much detail. Wiegand in [19] proposed the use of a single strain rate scaling function to make all of the IFF strength properties rate-dependent in the same proportion but lacked biaxial high-rate data for more complete validation. Later, Koerber compared the in-plane biaxial loading failure envelope from quasi-static and high strain rate SHPB tests in the order of 300 s^{-1}, showing that Puck's criterion calibrated with dynamic data could be used to fit the high-rate experimental data [44]. However, Koerber did not test a proper rate-dependent implementation of the IFF criterion. Instead, different dynamic tests carried out at different strain rates ranging from around 100 s^{-1} to over 300 s^{-1} were all grouped together under a single 'dynamic' envelope, neglecting any potential rate-effects within that range. Therefore, a more in-depth investigation into rate effects in IFF and how properties evolve from the quasi-static values has been carried out using a collection of literature and in-house test data described below.

In spite of the issues above, Koerber's work provided an extensive set of experimental data for different combinations of in-plane biaxial loading for the IM7/8552 composite at different strain rates, which can be used in the present investigation. In addition, a series of similar quasi-static and dynamic tests were performed in-house on the same material in order to: (a) calibrate material properties for the models and criteria used throughout the current project, and (b) verify that the acquired material matches the properties of other IM7/8552 laminates used in the literature, since CFRPs can show significant variation depending on their manufacturing. In addition, the high-rate SHPB tests performed in-house were carried out at slightly higher strain rates than the literature data from Koerber [44], providing additional data for the calibration of rate-dependent IFF behaviour.

Finally, since the study of the nonlinear behaviour in section 3.2 showed that the same type of localisation plane theory for IFF can also be used to explain the nonlinear shear behaviour, the relation between the two has been investigated further to determine whether the prediction of IFF can be derived from the proposed LP plasticity model.

However, before any of this, the original Puck IFF theory is explained in more detail in the following section.

4.1.1. Puck's IFF criterion

The leading principle behind Puck's localisation plane theory for IFF in UD CFRPs is the same as was used in section 3.2 for the proposed LP plasticity model. However, Puck's original formulation is more complex, in order to account for some of the particularities observed in this mode of failure.

In the same way as was described in section 3.2, Puck's criterion is based on the Mohr-Coulomb theory and treats the material as transversely isotropic with failure assumed to occur on a critical plane transverse to the fibre direction. Again, the behaviour along the critical localisation plane is governed by the same normal, σ_n, and shear, τ_{n1} and τ_{nt}, tractions acting upon it. However, as opposed to the linear Drucker-Prager yield criterion used in section 3.2.3, Puck's IFF criterion originally employed a quadratic failure criterion with different behaviour defined depending on the sign of the normal component, σ_n.

Therefore, Puck's IFF criterion is evaluated much in the same way as the yield criterion for the proposed LP plasticity model. A numerical search for the critical fracture plane, θ_{fr}, is performed by rotating the stresses onto different potential fracture planes using the same rotation matrix in eqn. (3.14), $\hat{\boldsymbol{\sigma}}_\theta = \boldsymbol{R}_\sigma[\theta]\,\hat{\boldsymbol{\sigma}}$, and using the reduced stresses, $\tilde{\boldsymbol{\sigma}}$, to evaluate the failure condition, f_{IFF}, on each [127,128]. The parabolic formulation of Puck's IFF failure condition from [127,128] is shown below, while other minor variations of this formulation are available in [118,129,130].

$$f_{IFF} = \begin{cases} \sqrt{(1-p_t)^2\left(\dfrac{\sigma_n}{R_\perp^+}\right)^2 + \left(\dfrac{\tau_{n1}}{R_{\perp\parallel}}\right)^2 + \left(\dfrac{\tau_{nt}}{R_{\perp\perp}^A}\right)^2} + p_t\dfrac{\sigma_n}{R_\perp^+} \geq 1 & \text{for } \sigma_n \geq 0 \\ \sqrt{\left(p_c\dfrac{\sigma_n}{R_{\perp\psi}^A}\right)^2 + \left(\dfrac{\tau_{n1}}{R_{\perp\parallel}}\right)^2 + \left(\dfrac{\tau_{nt}}{R_{\perp\perp}^A}\right)^2} + p_c\dfrac{\sigma_n}{R_{\perp\psi}^A} \geq 1 & \text{for } \sigma_n < 0 \end{cases} \tag{4.1}$$

here p_t and p_c, are frictional parameters for normal tensile and compressive behaviour in σ_n, and $R_\perp^+$, $R_{\perp\psi}^A$, $R_{\perp\parallel}$ and $R_{\perp\perp}^A$ are strength parameters for transverse tension, transverse compression, in-plane and out-of-plane shear, respectively [131].

When compared to the yield criterion in eqn. (3.16), the original Puck formulation is significantly more complex, relying on two different functions to describe the envelope under normal tension or under normal compression and additional interaction terms between the normal and shear components. While this gives the criterion more versatility to match the experimental data, as shown in Figure 4.1, the number of material parameters can make its characterisation and the study of rate effects more challenging.

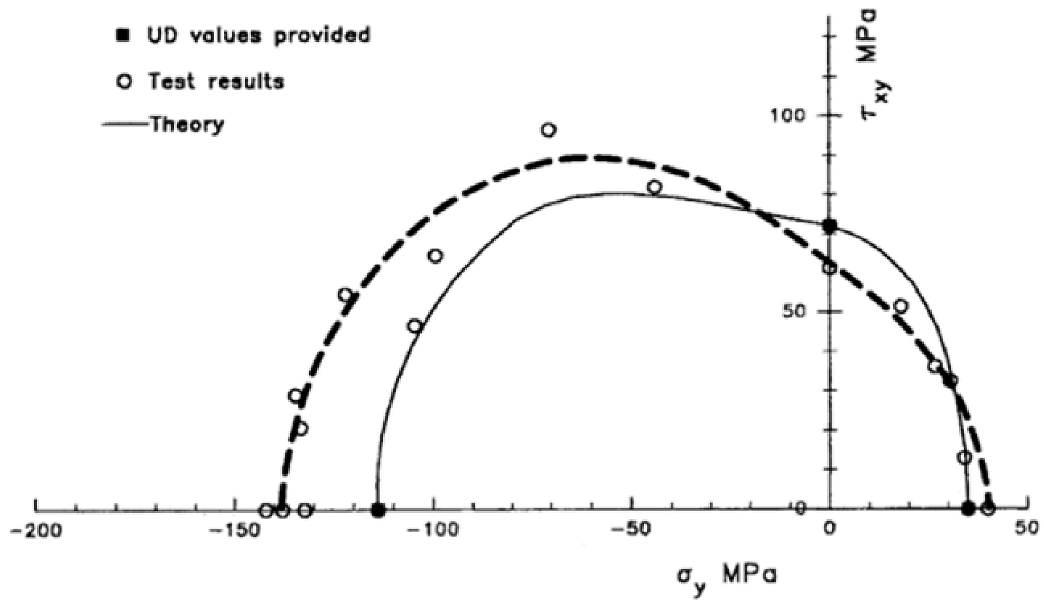

Figure 4.1. Puck’s IFF failure envelopes provided for the WWFE [63] calibrated with three test cases (solid) and with the complete experimental data set (dashed).

Calibration of these material parameters requires experimental measurements of the transverse tension and transverse compression strengths and either an in-plane shear test or other biaxial compression tests from which the shear strength can be extrapolated. In order to complete the model calibration, the remaining parameters can be obtained either by imposing that, in the transverse compression case, the failure condition is satisfied for at a specific fracture angle, usually around 50° to 60°, or by fitting the envelope to additional biaxial compression test data.

Since only three of the six properties required to define the failure envelope can be directly measured, the other three are based on a series of assumptions about how the material should behave. For example, in [44,104] the missing properties are determined by assuming that the relation between the frictional parameter and the shear strength should remain the same in the longitudinal and transverse directions. Different assumptions can result in slightly different properties and strain rate effects. However, since such assumptions cannot be easily tested, only the simplest of these will be explored at first. Its predictions, such as biaxial strengths, the shape of the failure envelope, or fracture plane orientations, will then be compared against quasi-static and dynamic data and only if they are not found satisfactory will other alternatives be considered.

Regarding the effects of strain rate, the most common assumption is that the strength parameters used in eqn. (4.1) remain proportional to each other, scaling at the same rate, while the fracture angle and frictional parameters remain constant. Effectively this means that the shape of the envelope does not change with strain rate, only its size, similar to the isotropic hardening behaviour in section 3.2.3. Wiegand and Koerber both used this approach in [19,49] but Wiegand lacked off-axis data for validation and Koerber, who did not have a fully rate-dependent model, used only a single ‘dynamic’ envelope to compare against all data from tests at significantly different rates. Alternatively, the work by Catalanotti in [132] and by Koerber in [44], where different frictional parameters were extracted for the quasi-static and dynamic envelopes, would appear to suggest a changing failure envelope under dynamic loading.

To address this issue, the current study will use the available experimental data for the IM7/8552 composite from [44] with new in-house test results presented in the following sections to evaluate how the rate-dependent IFF properties should be scaled.

4.2. In-plane off-axis loading tests

For the following analysis, a series of off-axis tension and compression tests were carried out on HexPly® UD IM7/8552 composite specimens at quasi-static and dynamic strain rates. The different combinations of transverse and in-plane shear loads were obtained by preparing specimens with different fibre orientations with respect to the loading direction, which were then tested to the point of failure at quasi-static rates using a screw-driven UTM and dynamic rates using SHPB and SHTB systems.

4.2.1. Specimen configuration

Two different specimen designs were used for the tension and compression tests, respectively. All specimens were obtained from a single 5 mm thick HexPly® IM7/8552 UD laminate comprised of 40 0.125 mm plies. Both tension and compression samples were machined to the specifications given in Figure 4.2 with a tolerance of ±0.05 mm using a water-cooled diamond disk saw far away from the borders of the laminate to avoid potential manufacturing defects near the edges.

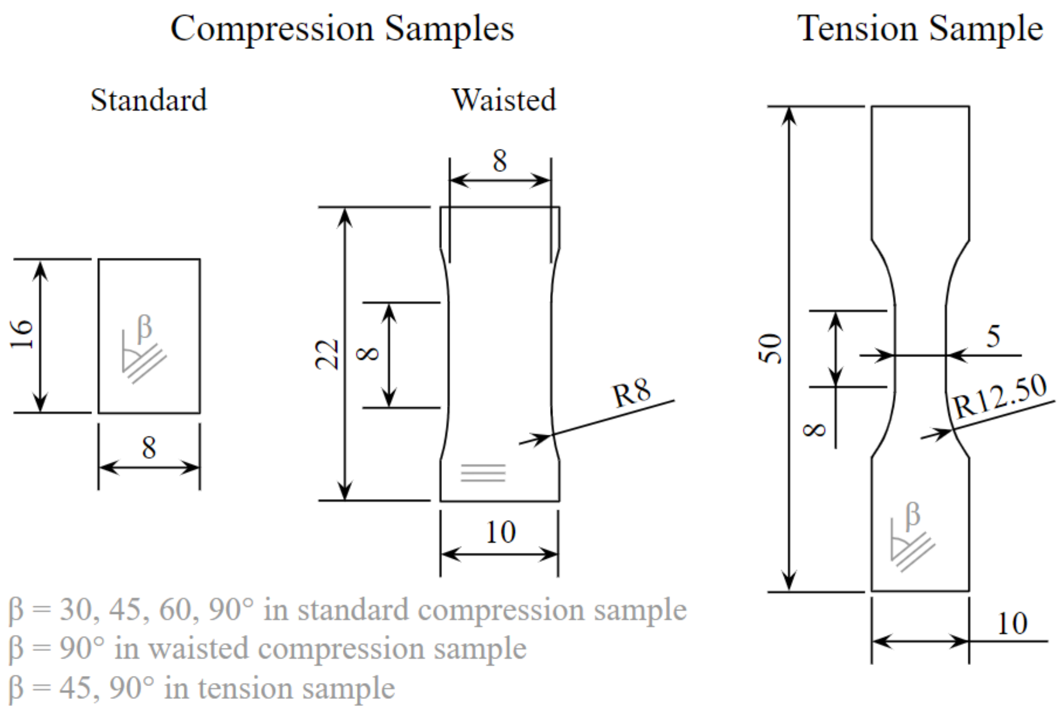

Figure 4.2. UD IM7/8552 composite samples used for quasi-static and dynamic biaxial loading tests.

The specimens for different off-axis tests were prepared by cutting the material at different orientations with respect to the fibre direction, as illustrated in Figure 4.2. For the biaxial compression tests, samples were prepared with 30°, 45°, 60° and 90° orientations, while the tension samples were prepared at 45 and 90°.

In addition, the dynamic tension specimens were bonded to M12 threaded steel end caps using a 3M DP490 adhesive in order to apply tensile loads through SHTB set-up.

Finally, a fine speckle pattern was applied to all specimens to allow for digital strain and strain field measurements using DIC.

4.2.2. Quasi-static experimental methodology

Both quasi-static tension and compression tests were conducted using a Zwick Roell 250 kN universal screw-driven testing machine under displacement control at a quasi-static loading rate of 0.01 mm/s. The compression specimens were placed directly between the two greased surfaces of the machine’s compression fixtures and the load was applied through positive displacement while, for the tension tests, the load was applied using tensile specimen grips and negative displacement control.

Throughout the duration of the tests, force-displacement data was extracted at a 400 kHz sampling rate from the test rig. In order to capture the deformation of the specimens throughout the tests with DIC, a digital camera was set to record one picture of approximately 9 x 16 mm at a 900 x 1600 px resolution every second. These images, together with the finely sprayed black and white speckle patterns on the surface of the specimens, allowed for the calculation of full field strain histories and virtual extensometer measurements to corroborate the displacements from the test rig. This was done by post-processing the images with the DIC analysis software GOM Aramis v6.1 [133] using a facet size 50 px and step size of 15 px, giving a spatial sensitivity of approximately 0.15 mm and strain resolution of 0.01%.

Finally, the extracted force and displacements were converted into stress and strain data using the initial specimen geometry measured before the test.

4.2.3. Dynamic experimental methodology

The dynamic tests, on the other hand, were performed using the SHTB and SHTB systems depicted in Figure 4.3. The basic test procedure for this high-rate test method, which consists in applying a high-strain-rate tensile or compressive pulse through the material from a high-speed projectile, is described below. However, a more detailed description of the configuration and characteristics of the Hopkinson bar system can be found in [30].

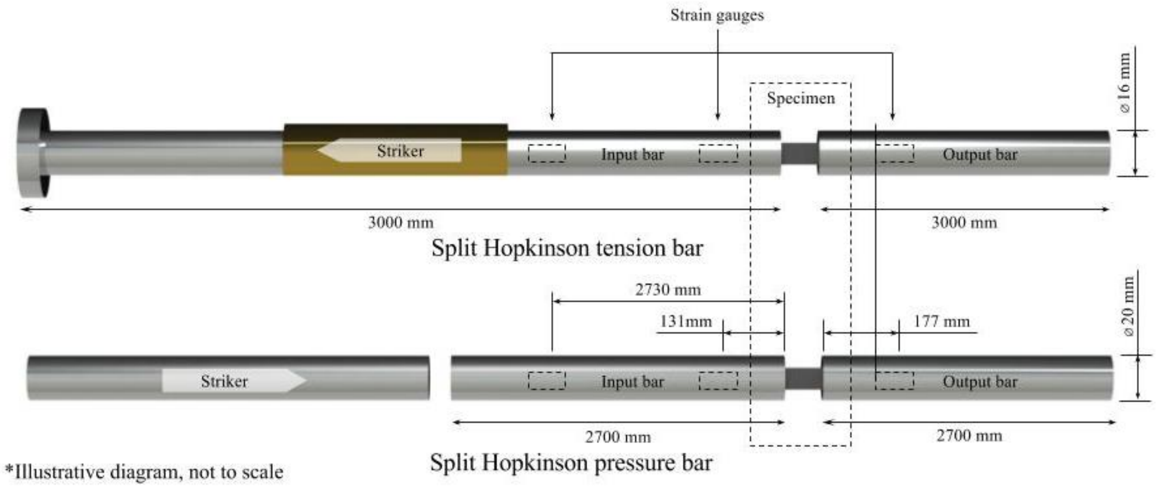

Figure 4.3. SHTB and SHPB set-ups used for the dynamic tension and compression tests.

The two SHTB and SHPB devices in this particular study are composed of the various titanium rods that make up the striker and input and output bars detailed in Figure 4.3. In both cases, the striker is fired from a compressed air chamber at the input bar, creating a tensile or a compressive pulse depending on the set-up. In the SHPB, the striker directly impacts the input bar along its axis in the direction of the specimen, sending a compressive wave towards it, while, in the SHTB, the striker travels in the opposite direction and connects with the protruding flange at the end of the input bar, creating a tensile wave. In both cases, different types of pulse shaper can be placed between the striker and input bar to produce a gentler rising wave.

The specimens are then placed between the input and output bars, with the SHPB specimens simply placed between the two flat surfaces and the SHTB specimens screwed into the M12 threaded holes in the bars. During the tests, strain gauges mounted along the bars in both set-ups, as shown in Figure 4.3, are used to measure the stress waves travelling into and out of the specimen, which allow for the forces at the input and output interfaces of the specimen to be computed using 1-dimensional (1D) wave propagation theory [134] and for the condition of dynamic equilibrium to be evaluated by comparing the two. Once dynamic equilibrium is established for each test, the axial strains and stresses can be computed using the specimen dimensions measured before the experiment.

For the specimen strains, more reliable measurements can usually be obtained using DIC, which can also be used to validate the 1D wave analysis results. However, only the 1D wave analysis can be used for the force measurements, $F_t[t]$, which are obtained from the transmitted strain histories, $\varepsilon_t[t]$, recorded from the full-bridge strain gauges mounted on the surface of the output bars, according to:

$$F_t[t] = A_b E_b \varepsilon_t[t] \tag{4.2}$$

where A_b and E_b are the cross-section area and the elastic modulus of the output bar respectively.

For this specific set of experiments, 0.5 mm thick cardboard disks were used to shape the incident pulses. At the same time, the tests were recorded using a Kirana high-speed camera by Specialised Imaging to obtain more reliable strain field data and validate the strain gauge measurements, verify that adequate testing conditions were met, and to observe the failure modes. The camera was connected to the oscilloscope to synchronise the images with the strain gauge data and the tests were recorded at 500.000 fps and a resolution of 924 x 768 pixels covering an area of approximately 25 x 20 mm. In addition, since a fine speckle pattern was applied to all specimens, the recorded footage allowed for strain-field and virtual extensometer data to be extracted using DIC with a facet size 15 px and a step size of 7 px to give a spatial sensitivity of approximately 0.2 mm and a strain resolution of around 0.01%.

With the above in place, for all specimens, the tests were fired at between 7 and 8 m/s, to produce strain rates of the order of 300 s^{-1}. The average strain rate measurements for each test type at the point of failure is given in Table 4.1, where the difference observed under different off-axis angles is due to the change in resultant axial stiffness of the specimens.

Table 4.1. Average measured experimental strain rate at yield for each set of off-axis compression tests and literature values from [44,50].

	Compression				Tension	
Off axis angle β	**90°**	**60°**	**45°**	**30°**	**45°**	**90°**
Strain rate [s^{-1}]	365	339	353	313	369	340
(Koerber [44,50])	(271)	(331)	(280)	(246)	(300)	(271)

Finally, the high-speed camera images taken during the failure process also allowed for rough measurements of the fracture plane orientation to be made using the open source image processing software, ImageJ [135], by tracing the observed fracture path on the specimen surface and rotating the measured angle onto the transverse plane in order to compare all measurements within the same frame of reference.

The results from these and the quasi-static tests are analysed and discussed in the following section.

4.2.4. Results and discussion

Overall, the obtained results were very similar to those produced by Koerber in [44], meaning that the material was of similar quality and that both sets of data can be combined with minimal negative consequences.

A few representative axial stress-strain curves for some of the off-axis compression tests are shown in Figure 4.4. Compared to the data from [44], the new quasi-static curves show very similar nonlinear behaviour with all tests failing around 250 MPa in the loading direction and each set of off-axis tests reaching similar strains to failure. For the high-rate tests, the general trend observed in [44] can also be seen in the new in-house results, with noticeable increases in stiffness and a reduction in ductility. However, with regard to Koerber's dynamic data, the in-house tests, which were carried out at slightly higher strain rates, also showed higher axial strengths, closer to 400 MPa.

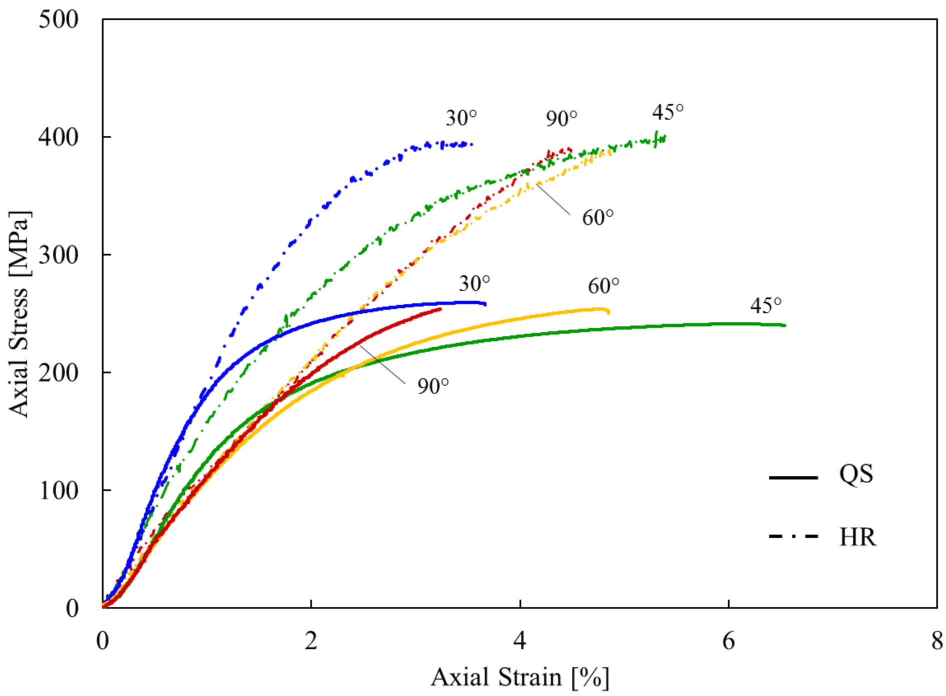

Figure 4.4. Representative axial stress-strain curves obtained from quasi-static and dynamic off-axis compression tests showing similar behaviour to that in [44].

For each of the tests, these measured axial strengths were rotated around the out-of-plane direction, 3, by the corresponding off-axis angle, β, onto the material coordinates $\{\sigma_{11}\ \sigma_{22}\ \tau_{12}\}$ in order to produce the failure envelope shown in Figure 4.5, with the quasi-static and dynamic test results from [44] added for comparison.

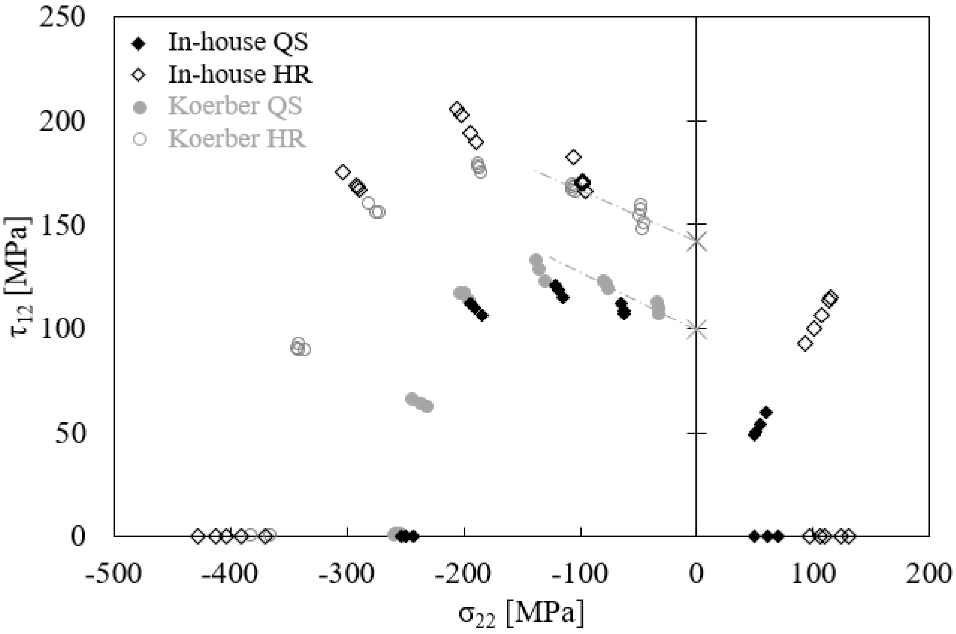

Figure 4.5. In-house quasi-static and dynamic failure data compared to the results obtained by Koerber in [44]. The in-plane shear strength in Koerber's results was extrapolated from the 15° and 30° tests.

In this format, the observations made from the stress-strain curves above can be seen more clearly, showing the good agreement between the quasi-static data from both sources and slightly higher strength measurements from the higher rate in-house tests. In addition, as suggested by Koerber's work in [44], the shape of the envelopes does appear to change slightly between quasi-static and dynamic tests.

4.3. Rate-dependent IFF criterion

Having collected the results above, it remains to be seen whether the apparent change in shape of the IFF failure envelope is simply an artefact of the variation in strain rates between tests or if it represents the actual material behaviour. This will also serve to determine a suitable approach for a rate-dependent IFF failure criterion to be implemented within the modelling framework presented in section 1.2.

Finally, the relation between the nonlinear shear and IFF will be examined by considering the possibility of building the failure criterion into the same LP plasticity model proposed in section 3.2.

Each of these aspects is investigated in the following sections using a preliminary implementation in MATLAB, before selecting a final IFF model to be used in the developed FE user material, which will be more thoroughly evaluated in Chapter 7.

4.3.1. Strain rate effects

To investigate this issue, the Puck IFF criterion from eqn. (4.1) was calibrated using the quasi-static data and the rate-scaling function in eqn. (4.3) below to predict the failure envelope at each of the average strain rates given in Table 4.1. The rate-dependency function was used to scale all strength properties equally using a single scaling factor, $K_f = 1 \cdot 10^{-3}$, calibrated from the transverse compression strength, which results in proportional scaling of the failure envelope with no change in shape.

$$r_f[\dot{\bar{\varepsilon}}] = 1 + \sqrt{K_f \dot{\bar{\varepsilon}}} \tag{4.3}$$

where $r_f[\dot{\bar{\varepsilon}}]$ is the scaling function for the IFF strength with the calibrated the rate-dependent parameter, K_f.

The comparison between these predictions and the collected experimental data is summarised in Figure 4.6 and Table 4.2, in most cases showing good agreement between the two. On average, the predicted strengths are within 2.6% of the experiments with the prediction of the 60° dynamic tests from Koerber showing the greatest discrepancy at

6.6%. Therefore, based on these results, there is not enough evidence to refute the assumption that IFF strength properties can be scaled proportionally with strain rate using a radical function of the type in eqn. (4.3) as was suggested in [19,49].

Table 4.2. Average exp strength and predicted strength using proportional strain rate scaling of Puck IFF criterion at the average measured strain rate for each set of tests.

	90° Strength [MPa]	**60° Strength [MPa]**	**45° Strength [MPa]**	**30° Strength [MPa]**
In-house exp	400 (365 s^{-1})	392 (339 s^{-1})	396 (353 s^{-1})	397 (313 s^{-1})
Predicted	388	392	375	389
Error (%)	3.0	0.1	5.5	2.2
Koerber [44]	371 (271 s^{-1})	365 (331 s^{-1})	354 (280 s^{-1})	370 (246 s^{-1})
Predicted	369	391	361	374
Error (%)	0.5	6.6	2.0	1.1

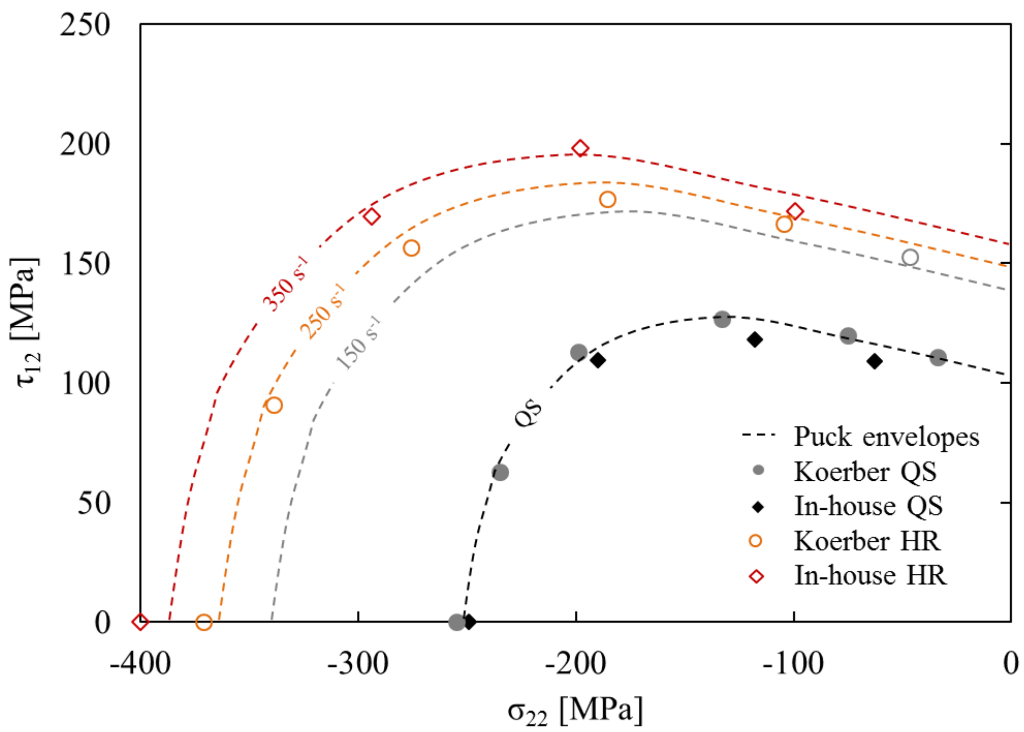

Figure 4.6. Comparison between predicted rate-dependent failure envelopes and off-axis compression data at different strain rates from [44] and in-house tests.

In addition, if the fracture angles shown in Figure 4.7 and Table 4.3 are considered, the proposed rate-dependent model gives significantly better predictions than the 'dynamic' fitted envelope in [44,132].

Table 4.3. Off-axis fracture plane orientations with respect to fibre direction from 90°, 60°, 45° and 30° experiments and simulations. Experimental fracture plane data is complimented with results from Koerber et al. [44] (in brackets).

		90°	**60°**	**45°**	**30°**
Exp. fracture angle	In-house	58.6	51.8	37.8	0
	Koerber [44]	(56.5)	(54.2)	(40.1)	(0)
Pred. fracture angle	Rate-dep.	55.5	50.8	41.8	0
	Rate-indep. (fit)	53	48	33.3	0

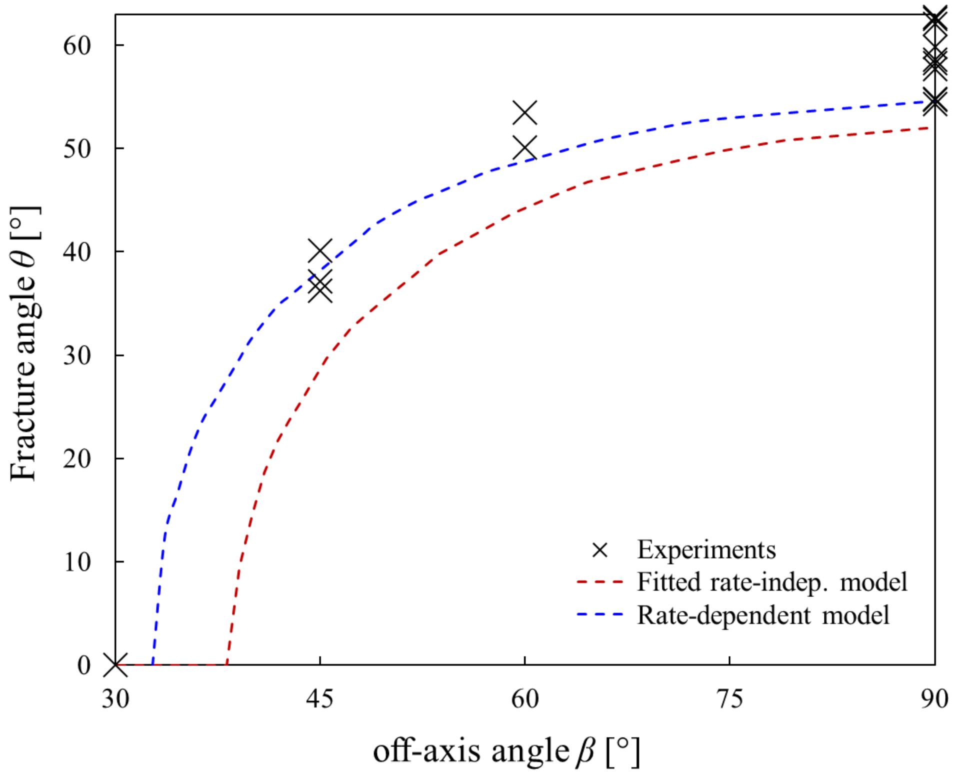

Figure 4.7. Comparison between measured dynamic fracture angles from in-house tests and [44] against predictions using the proposed rate-dependent model and a rate-independent model fitted with the dynamic data.

Based on these results, the proportional scaling method, which was suggested in [19,49] but had not yet been fully validated in a proper rate-dependent manner, can be said to produce good predictions of the IFF strength and fracture angle in different off-axis specimens and strain rates.

Since Puck's theory predicts IFF as a frictional shear-driven mode acting on the critical fracture plane, the use of a single rate-scaling factor can be justified by considering that the shear properties of the composite are all matrix-dominated, with any rate effects all deriving from the same rate-dependent properties of the matrix. Therefore, this approach assumes that the different strength parameters used in the IFF criterion all scale in the same proportion due to their relation to the properties of the matrix, while any rate effects on the frictional parameters are considered negligible in comparison.

In addition, in Chapter 3, the same kind of rate-scaling approach, with the same value of $K_y = 1 \cdot 10^{-3}$, was shown to successfully describe the matrix-dominated nonlinear behaviour, strengthening the argument for the use of a single rate-scaling parameter across all matrix-dominated strength properties.

4.3.2. Simplified LP-plasticity-based criterion

Finally, bearing in mind the many similarities observed between the nonlinear behaviour and IFF, the possibility of predicting IFF within the framework of the LP plasticity model proposed in section 3.2 has been investigated in order to further explore the relation between the two modes.

Since the proposed plasticity model is based on the same localisation plane theory as Puck's IFF criterion, the question that arises is whether the predicted yield planes and the effective stress employed in the yield criterion can be used to predict the ultimate strength as well as the nonlinear material response.

In order to test this hypothesis, an alternative IFF criterion is proposed by simply comparing the effective stress computed throughout the plasticity model to the rate-dependent in-plane shear strength instead of the yield stress:

$$f_{IFF} = \frac{\bar{\sigma}[\tilde{\boldsymbol{\sigma}}]}{S_{12} r_f[\dot{\bar{\varepsilon}}]} = \frac{\alpha\sigma_n + \sqrt{{\tau_{n1}}^2 + e{\tau_{nt}}^2}}{S_{12} r_f[\dot{\bar{\varepsilon}}]} \geq 1 \tag{4.4}$$

Where $\bar{\sigma}[\tilde{\boldsymbol{\sigma}}]$ is the effective stress defined in section 3.2 and S_{12} is the in-plane shear strength, corresponding to the parameter $R_{\perp\parallel}$ in Puck's criterion from eqn. (4.1).

Essentially, this equates to replacing the complex parabolic interaction between normal and shear tractions in Puck's failure criterion with a linear relation of the kind used in the proposed yield criterion. The failure envelope resulting from this approach is shown in Figure 4.8, using the same properties employed to calibrate the plasticity model in section 3.2.

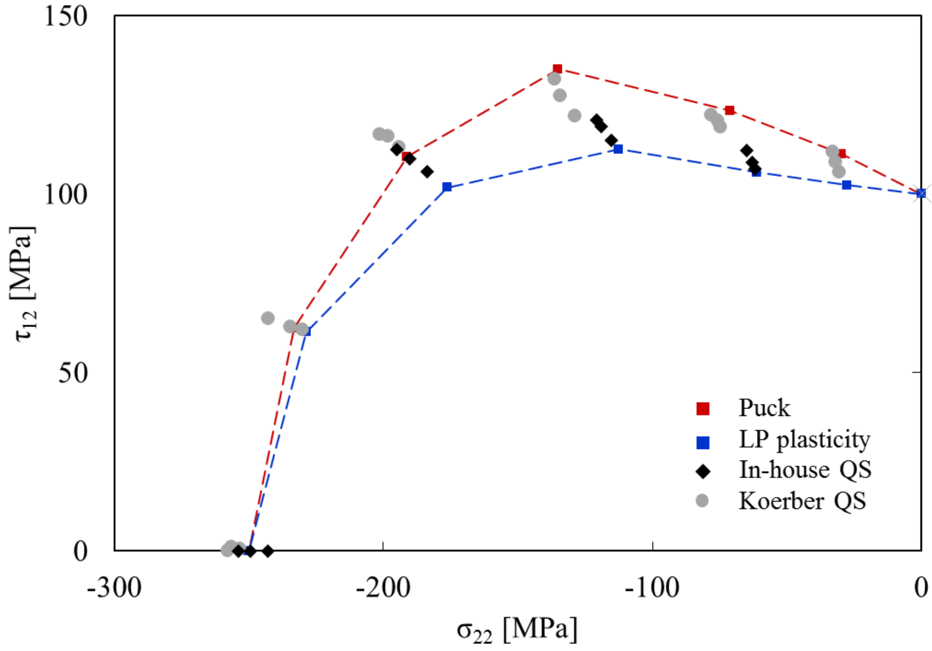

Figure 4.8. Failure envelope extrap from LP plasticity model vs indep calibrated og puck envelope

While the new envelope is clearly over-conservative compared to the traditional Puck criterion, it should be noted that the failure envelope is derived entirely from the nonlinear shear model and the single in-plane shear strength parameter. On the other hand, the Puck criterion relies on a number of additional strength and frictional parameters, which cannot be physically measured and in practice are often empirically calibrated to fit the expected results. With this in mind, the proposed criterion performs surprisingly well overall, which is another promising sign that the nonlinear shear behaviour in UD CFRPs may be based on the same or very similar mechanisms as IFF.

In terms of individual predictions, the results appear to be more conservative under significant biaxial loads, noticeable in the 30° to 60° tests, while the regions of in-plane shear and transverse compression show better agreement. This is because the initial slope of the yield envelope, defined in the LP model by the frictional parameter α, is less pronounced than that of the failure envelope. While using a higher value for the frictional parameter may produce a better prediction of the IFF envelope, it would likely come at the cost of the predicted yield envelope and nonlinear behaviour. It is possible that using a more complex formulation for the yield criterion, closer to Puck's, would give better predictions for both aspects of the matrix-dominated behaviour but it is also likely that the effects of pressure are in fact different at the point of failure than in the initial yielding behaviour. This may be due to a number of different factors. As observed in [51,52] large nonlinear shear strains can result in significant fibre rotation. In off-axis compression cases, this may cause a progressive increase in pressure from the moment the material begins to yield up to the point of failure and, as fibres rotate away from the loading direction, greater compression on the fracture planes may result in an increasing shear strength. Alternatively, it may be that other micro-scale mechanisms start to become active as the material becomes damaged, affecting the frictional behaviour and therefore the macro-scale pressure effects.

4.4. Conclusions

A series of in-plane biaxial loading tests have been performed at quasi-static and dynamic loading rates, using a Zwick UTM and SHB systems, in order to calibrate the material strength properties for the IM7/8552 composite of interest in the present study and to verify that literature data on this same material is representative.

Having validated that the quasi-static off-axis compression tests are in agreement with the results from Koerber's work in [44], the two sets of data can be used collectively to investigate the effects of strain rate on IFF failure.

The results of this study showed that the approach adopted in [19,49] of proportionally scaling the IFF strength properties using a radical rate-dependent function can account for the effects of strain rate on the ultimate strength and the fracture plane orientation with reasonable accuracy. Reported changes in shape of the failure envelope under dynamic loading in [44,132], are therefore most likely the effects of considering different tests at different rates within a single envelope.

Finally, following from the work in section 3.2, the possibility of using the proposed LP plasticity model to eventually predict the matrix-dominated failure under biaxial loading has been investigated.

Using the effective stress on the assumed yield planes together with the in-plane shear strength of the composite to predict IFF produced reasonable results, bearing in mind that they were entirely derived from the nonlinear shear model instead of calibrated IFF strength parameters. However, predictions for the IFF strength under significant combined shear and transverse compression were overly conservative, indicating some potential change in the effects of pressure between yielding and failure that were not accounted for.

While this will require further investigation, the obtained results are a promising sign that the physical mechanisms behind IFF and the nonlinear shear behaviour may be closely related.

Chapter 5

Fibre failure initiation

Thus far, the work in previous chapters has introduced the numerical framework for the developed FE material model in section 1.2. Within this framework the proposed model for the nonlinear constitutive behaviour has been developed in Chapter 3, including the baseline rate-dependent transversely isotropic elastic behaviour and the proposed rate-dependent localisation plane plasticity model. Then Chapter 4 introduced the matrix-dominated IFF failure criterion and investigated the effects of strain rate and its relation with the matrix-dominated nonlinear behaviour studied in Chapter 3.

Therefore, all that remains in order to complete the model is to describe the material response in fibre-dominated deformation modes. Since, other than minor effects of fibre rotation, the material response of UD CFRPs in the longitudinal direction has been shown to be linear elastic up to the point of failure, the constitutive response before failure can be described by the models presented in Chapter 3 and the work presented can focus only on the failure criteria for each of the two fibre failure modes.

For the sake of completeness, section 5.1 will briefly describe the approach implemented for the prediction of fibre tension failure, although no new developments have been made in this area. Section 5.2 will then present new experimental and numerical work done to study the more complex fibre kinking failure mode and its relation to the nonlinear shear behaviour, in particular, regarding strain rate effects and interactions between the two modes under multiaxial loading.

5.1. Fibre tension

As has been seen in the literature review, section 2.1.6, the behaviour of UD CFRPs in the longitudinal direction is mostly linear elastic both in tension and compression until the strength limit for each mode, where the material tends to fail in a sudden and catastrophic manner. In addition, the elastic properties in this direction are not affected by strain rate or temperature [6,42,43,88] and, while the fibre waviness present in most laminates can result in some degree of nonlinearity, this effect is almost negligible in terms of noticeable nonlinearity in the stress-strain curves [136–138]. However, the effect of this initial waviness does become more visible in the elastic modulus, which tends to be greater in tension than in compression [22,136–139]. For the IM7/8552 material studied in this project, Hexcel gives a modulus of 163 GPa in tension and 150 GPa in compression [6]. At the macro scale, this difference in the longitudinal modulus is usually ignored [19,49,50,112] but can also be accounted for by assigning the material different moduli for tensile or compressive strains, as shown below:

$$E_1 = \begin{cases} E_{1T} \text{ for } \varepsilon_{11} \geq 0 \\ E_{1C} \text{ for } \varepsilon_{11} < 0 \end{cases} \tag{5.1}$$

where E_{1T} and E_{1C} are the moduli in tension and compression, respectively, ε_{11} and is the strain in the fibre direction.

As for the point of failure itself, the longitudinal tensile strength of UD CFRPs can also be approximated by the rule of mixtures, although its stochastic nature often results in a slightly lower value in practice. Therefore, the common approach is to use a longitudinal strength value measured experimentally from the composite [18,19,49,50]. In addition, fibre tension failure in UD CFRPs has shown little to no interaction with other damage and failure modes, as reported in [62,63,104], and can therefore be predicted using a simple maximum stress criterion of the form:

$$f_{FT} = \frac{\sigma_{1T}}{X_T} \geq 1 \tag{5.2}$$

where σ_{1T} is the tensile stress in the longitudinal direction, meaning values of $\sigma_{11} > 0$, and X_T is the longitudinal tensile strength, which for IM7/8552 is given as 2724 MPa by Hexcel in [6].

No further numerical or experimental investigation has been carried out in this area, taking as valid the material properties supplied by the manufacturer and the previous research available in the literature, as greater importance was placed on the study of the material behaviour under longitudinal compression, presented in the following section.

5.2. Fibre kinking

Similar to what has been seen for fibre tension, under longitudinal compression, the material behaviour up to the point of failure can be described by a linear elastic response with a slightly lower elastic modulus than under tension due to fibre waviness present in the material.

However, longitudinal compression failure is a much more complex failure mode, in which the lower strength under compression due to fibre buckling appears to be driven by fibre rotation and the material nonlinear shear response. Thus, failure at the macroscopic scale is expected to show similar multiaxial, pressure, and strain rate effects as observed in the matrix-dominated modes. While fibre compression failure in general has been studied extensively over the years, some of these individual aspects have not received enough attention and will be investigated further in the following sections.

5.2.1. Introduction

Thanks to the great amount of that has been work done over the years to understand the micro-scale mechanisms involved, longitudinal compression failure, or fibre kinking, is widely recognised as a form of buckling instability in the fibres driven by the response of the supporting matrix. However, while the fundamental issues behind it seem to be well understood, there are still specific aspects of the micromechanics that remain to be explained. Leading fibre kinking theories, such as those by Budiansky and Fleck [23,95] and Pinho [18,140], can accurately predict failure under uniaxial compression given the initial misalignment or waviness of the fibres and the nonlinear shear response of the laminate. However, under multi-axial loading, different models start to give diverging predictions depending on how they address the evolution of fibre misalignment under transverse stresses [16]. In addition, even some of the aspects on which all models agree have yet to be fully verified experimentally, such as the effects of strain rate or temperature.

Matsuo and Kageyama [94] recently showed that the effects of temperature on the uniaxial compression strength of a thermoplastic CFRP composite were in good agreement with the predictions from Fleck’s fibre kinking theory, where the change in strength was directly related to the change in the nonlinear shear response of the laminate. However, due to the complexity of the experimental procedures, very little work has been done to characterise the longitudinal compression behaviour of FRPs under off-axis and dynamic loads, which is crucial for a more extensive validation of these fibre kinking models, especially for impact loading applications where the material is subjected to multi-axial stresses and high strain rates.

Without accurate and reliable experimental measurements of this kind, none of the fibre kinking theories can be properly evaluated under more complex loading scenarios. However, reliable testing of the critical load under longitudinal compression remains problematic, even for the uniaxial compression case. Because of the difference in strength between the fibre and transverse directions, if the tests are not designed and carried out correctly, matrix failure often occurs before fibre micro-buckling can occur [91,96]. Therefore, there are some serious experimental challenges that must be overcome before multiaxial loading and strain rate effects on fibre kinking failure can be adequately investigated.

To address these issues, first, a systematic experimental campaign was carried out to determine the most suitable test and specimen configurations for the measurement of longitudinal compression strength under quasi-static uniaxial loading, presented in section 5.2.2. Then, once optimal test and specimen configurations had been obtained in the first stage, a series of quasi-static and dynamic off-axis compression tests were performed in order to provide experimental data for a more in-depth study of the fibre kinking failure mechanisms, presented in sections 5.2.3 and 5.2.4.

Finally, in section 5.2.5, the resulting experimental data was used to investigate different fibre kinking theories under quasi-static and dynamic multi-axial loading and select a suitable failure criterion to be adopted within the rate-dependent modelling framework being developed throughout this project.

5.2.2. Test set-up and specimen design optimisation

As previously mentioned, one of the main challenges for the experimental study of fibre kinking is early matrix-dominated failure of the test specimen. Premature matrix splitting of this kind can be caused by the transverse stresses through the thickness of the laminate that arise due to the Poisson effect and stress concentrations at specimen boundaries. Commonly, the way to mitigate the effect of boundary conditions has been to add clamping fixtures that strengthen the matrix at the loading ends of the specimen and help to distribute the applied load by transmitting some of the compression through shear in the clamped interfaces [91,92]. However, this introduces the risk of new stress concentrations at the fixture boundaries and of over constraining the specimen, making the results highly sensitive to the test operator and set-up conditions, as reported in [91].

Another proposed solution has been the use of specimens with a waisted cross-section area that prevent fracture from occurring close to the specimen boundaries. However, the change in cross-section combined with the relatively low strength of the matrix can also cause critical stress concentrations, which may eventually lead to premature splitting.

In short, the determination of longitudinal compression strength properties using UD material can be quite problematic and the high sensitivity to boundary conditions should be a cause for concern whenever experiments of this kind are being considered. The large variation in reported compressive strength measurements for the UD IM7/8552 material in [91,96,141] are a good example of this.

In light of these issues, the extraction of longitudinal ply properties from multidirectional (MD) or cross-ply (CP) laminates, using classical lamination theory (CLT) has been suggested as a more viable alternative [91,142,143]. However, previous experimental studies have always shown significant differences between the strength measurements obtained from UD and MD laminates. For the IM7/8552 material, for example, Lee and Soutis [91] and Ploeckl et al. [96] reported strength measurements from quasi-isotropic (QI) specimens around 20% higher than the UD material. The use of CP laminates was also explored in the 1990s [142] and strengths higher than that of the plain UD material were again observed. In view of this previous work, it remains unclear whether the behaviour of MD laminate configurations under longitudinal compression can be representative of UD material and vice versa. However, if this can be established, the use of MD configurations, which have been shown to solve many of the issues that have plagued longitudinal compression in UD specimens, may alleviate the need for complex fixtures and specimen designs and, in turn, simplify the testing process and increase the level of confidence in the results.

5.2.2.1. Optimisation strategy

In order to verify whether multi-directional laminates could in-fact be used to determine the longitudinal strength properties of the UD material, two series of experiments were carried out, one on a set of different UD specimen designs and the other using CP specimens.

The aim for the first set of experiments was to get an accurate measure of the longitudinal compressive strength of the baseline UD material as well as to investigate different specimen designs and boundary conditions to determine whether any of these configurations could be suitable for the rest of the study.

Following that, two different cross-ply specimens were tested to compare against the previous UD results and determine whether the resulting strength measurements were representative and if this type of laminate was in fact better suited for longitudinal compression testing.

Specimen designs and test set-ups for each of these series of tests are described in following sections.

5.2.2.2. Specimen design

The specimens for all experiments were cut from two different IM7/8552 composite plates with different ply lay-ups, $[0°]_{26}$ UD and $[0°/90°]_{4S}$ CP. Both laminates were manufactured together in the same facility to ensure similar quality levels between the two, while noting that local fibre architecture will naturally differ slightly between UD and MD laminates. In addition, all specimens were carefully ground and polished to ensure their two loading faces were parallel with adequate surface quality to a tolerance of ±0.05 mm. This was done, in conjunction with the test set-up described in section 5.2.2.3, to minimise the possibility of bending in the specimens due to imperfections in the specimen, fixture or test procedure, which could otherwise affect the quality of the results [92].

The different UD specimen configurations tested, shown in Figure 5.1, were (a) a simple unclamped cuboidal (rectangular) specimen (UD Cub), (b) an unclamped waisted, or dog-bone, design (UD DBU), (c) a waisted dog-bone specimen with clamping fixtures (UD DBC), and (d) a clamped dog-bone specimen with adhesively bonded GFRP end tabs (UD tabbed DBC) to relax the constraint of the clamping fixtures on the UD material.

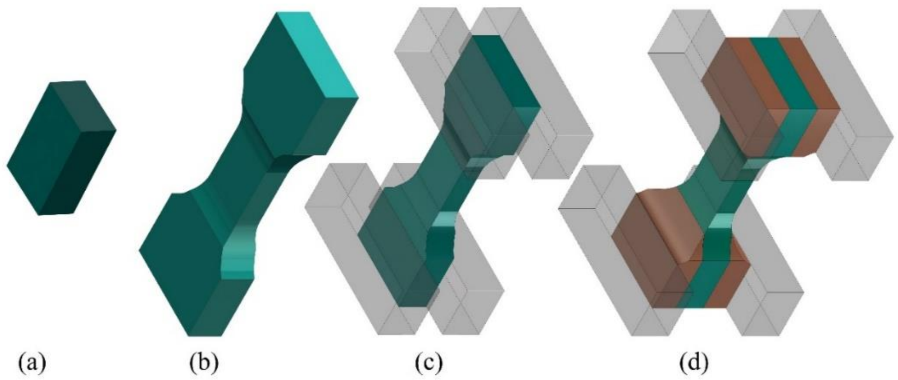

Figure 5.1. Unidirectional laminate specimen designs: (a) cuboid (UD Cub), (b) unclamped dog-bone (UD DBU), (c) clamped dog-bone (UD DBC), and (d) clamped dog-bone with GFRP end tabs (UD Tabbed DBC).

On the other hand, the tested CP specimen configurations, shown in Figure 5.2, were (a) an unclamped rectangular (CP Cub) similar to the UD Cub design, and (b) a clamped dog-bone specimen (CP DBC) similar to the UD DBC design.

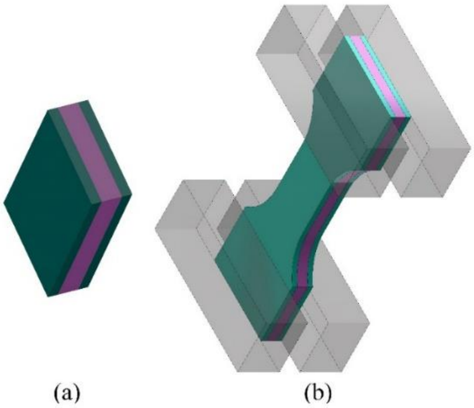

Figure 5.2. Cross-ply laminate specimen designs: (a) rectangular (CP Cub), (b) clamped dog-bone (CP DBC).

A gauge section of 5 x 5 mm^2 with a nominal thickness of 2 mm was kept constant throughout all specimen designs and, except for the use of clamping fixtures in some cases, the experimental methods used to test all of these UD and CP specimen designs, described in the following section, were the exact same for all tests.

5.2.2.3. Experimental set-up and data reduction

Similar to the quasi-static IFF tests in section 4.2, all the above experiments were conducted using a Zwick Roel 250 kN universal screw-driven testing machine under displacement control at a quasi-static loading rate of 0.01 mm/s. To ensure the alignment of the loading plates and avoid any eccentricity, the load was applied through two bearing balls and an aligning frame, Figure 5.3 (a), was installed. In addition, some cases required additional clamping fixtures, which are shown in more detail in Figure 5.3 (b).

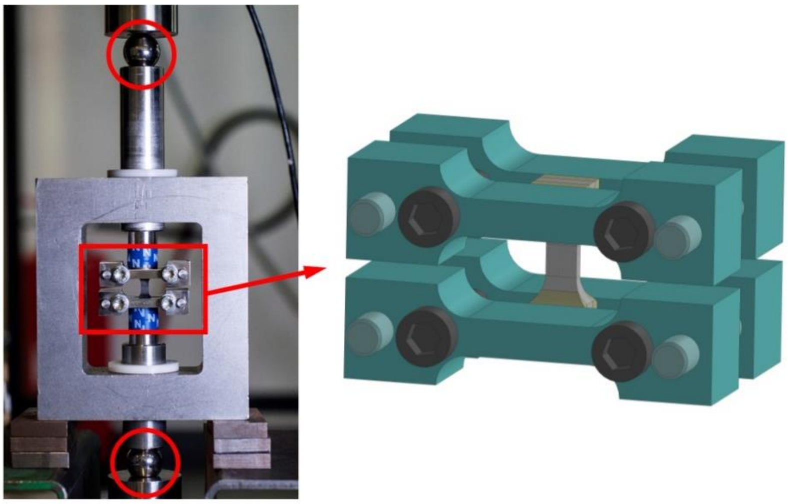

(a) Alignment fixture (b) Specimen clamping fixtures

Figure 5.3. Alignment and clamping fixtures used in fibre compression tests: (a) bearing balls (circled) and alignment frame set-up, which ensures a strictly axial load is applied to the specimens; (b) close-up view of the compact clamping fixtures is shown.

Throughout the duration of the tests, force-displacement data was extracted at a 400 kHz sampling rate from the test rig and a digital camera was set to record one picture of approximately 7 x 12 mm at a 512 x 760 px resolution every second. As in section 4.2.3, these images were used with the DIC analysis software GOM Aramis [133] to produce strain field and virtual extensometer measurements with a spatial sensitivity of approximately 0.2 mm and a strain resolution of around 0.01%. In addition, a number of tested samples were selected for closer post-failure analysis using optical microscopy (OM) and scanning electron microscopy (SEM).

Finally, in the case of CP specimens, as long as the tests met the conditions of small strains and linear behaviour, the longitudinal compression strength could be extracted from the axial stresses using the following CLT method [143].

First the $\boldsymbol{ABD}$ matrix, $\begin{Bmatrix} \boldsymbol{N} \\ \boldsymbol{M} \end{Bmatrix} = \begin{bmatrix} \boldsymbol{A} & \boldsymbol{B} \\ \boldsymbol{B} & \boldsymbol{D} \end{bmatrix} \begin{Bmatrix} \boldsymbol{\varepsilon}^0 \\ \boldsymbol{K} \end{Bmatrix}$, which relates the deformation of the laminate given by the in-plane strains $\boldsymbol{\varepsilon}^0 = \{\varepsilon_{11}^0\ \varepsilon_{22}^0\ \varepsilon_{12}^0\ \}^T$ and the laminate curvatures $\boldsymbol{K} =$

$\{\kappa_{11}\ \kappa_{22}\ \kappa_{12}\}^T$ to the resultant in-plane axial forces $\boldsymbol{N} = \{N_{11}\ N_{22}\ N_{12}\}^T$ and moments $\boldsymbol{M} = \{M_{11}\ M_{22}\ M_{12}\}^T$ per unit width is computed as:

$$A_{ij} = \sum_{k=1}^{n} \bar{Q}_{ij}^{k}(z_k - z_{k-1}) \tag{5.3}$$

$$B_{ij} = \frac{1}{2}\sum_{k=1}^{n} \bar{Q}_{ij}^{k}(z_k^2 - z_{k-1}^2) \tag{5.4}$$

$$D_{ij} = \frac{1}{3}\sum_{k=1}^{n} \bar{Q}_{ij}^{k}(z_k^3 - z_{k-1}^3) \tag{5.5}$$

where $\bar{Q}_{ij}$ is the reduced stiffness of each ply, z_k is the position of the ply from the midplane and n is the total plies in the laminate.

The compound ABD matrix is then inverted, which allows for the midplane strains, $\boldsymbol{\varepsilon}^0$, and curvatures, $\boldsymbol{K}$, to be determined for a given load using $\begin{Bmatrix} \boldsymbol{\varepsilon}^0 \\ \boldsymbol{K} \end{Bmatrix} = \begin{bmatrix} \boldsymbol{A} & \boldsymbol{B} \\ \boldsymbol{B} & \boldsymbol{D} \end{bmatrix}^{-1} \begin{Bmatrix} \boldsymbol{N} \\ \boldsymbol{M} \end{Bmatrix}$.

By applying the measured normal compressive load, $N_{11} < 0$, the midplane strains for each experiment can be obtained. The stress state of a longitudinal ply can then be determined with:

$$\boldsymbol{\sigma}_{long} = \bar{\mathbf{Q}}_{long}\boldsymbol{\varepsilon}^0 \tag{5.6}$$

By using this approach, the fibre compression strength of longitudinal plies in the CP specimens could be compared to the longitudinal compression strength measured directly in the UD specimens.

5.2.2.4. Results and discussion

Before such comparisons could be made, however, the validity of each individual set of test results was evaluated. For each of the two sets of experiments described in the previous section, stress-strain curves and specimen strengths were extracted and are discussed below. First, baseline strength measurements from the UD test results are reviewed and discussed and then the comparison of the CP results against the baseline UD measurements is shown, in order to establish the equivalence between the two.

Unidirectional specimens:

Four different types of UD specimens were tested to study the effects of the boundary conditions and obtain the most accurate strength measurement for this particular IM7/8552 material system and give reference strength values for the rest of the study. These results are summarised in Figure 5.4, Figure 5.5 and Table 5.1, which show the evolution of stress vs strain and a comparison of ultimate axial strengths between the different specimen designs, respectively. Since all specimens had the same stiffness, for the sake of clarity, only the rectangular and clamped dog-bone (DBC) specimens, which showed the minimum and maximum strength values, are shown in Figure 5.4.

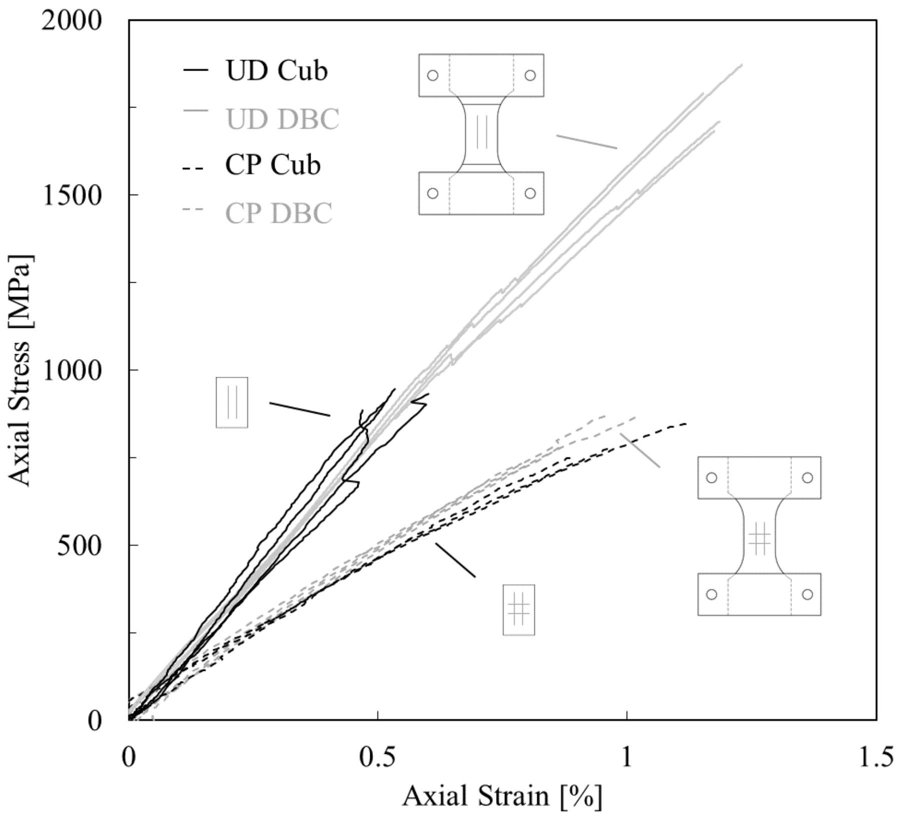

Figure 5.4. Comparison between UD (DBC, Cub) and CP specimens (DBC, Cub) axial stress-strain curves.

Table 5.1. Summary of UD (Cub, DBU, DBC and Tabbed DBC) and CP (Cub, DBC) fibre compression strength results. For the cross-play specimens the strength was extracted using CLT. The asterisk marks a specimen that failed prematurely due to stress concentrations at the boundary.

Axial Strength	**UD Cub [MPa]**	**UD DBU [MPa]**	**UD DBC [MPa]**	**UD Tabbed DBC [MPa]**	**CP Cub [MPa]**	**CP DBC [MPa]**
1	679	1499	1873	1773	1283*	1661
2	903	1340	1790	1506	1651	1423
3	945	1659	1710	1772	1558	1463
4	907		1683	1462	1710	1494
5				1381		
AVG	859	1499	1764	1579	1551	1510
STDV	121.2	159.5	85.6	182.6	189.2	104.6
CV (%)	14.1	10.6	4.9	11.6	12.8	6.9

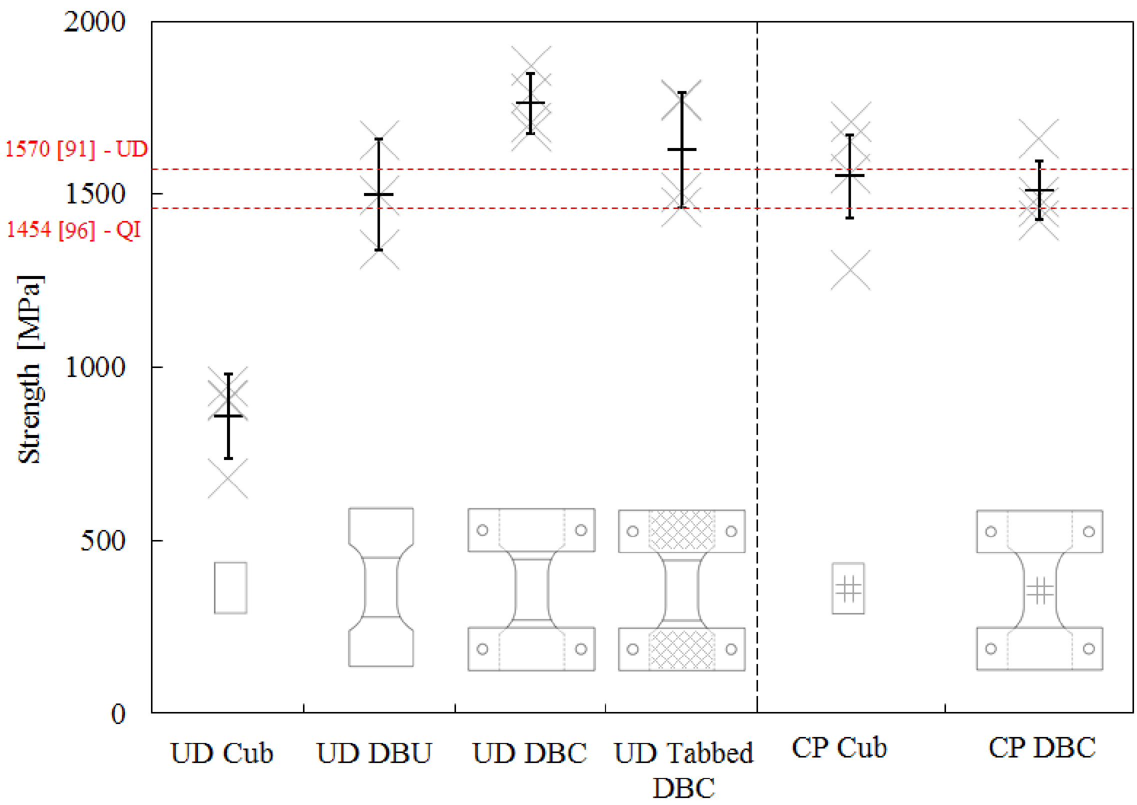

Figure 5.5. Axial strength comparison between the four tested UD and two CP specimen designs with literature data from IM7/8552 UD and QI specimens [91,96] added for reference. The cross-marks indicate the mean and standard deviation.

Next the strength data is analysed in more detail along with failure images obtained during the tests, Figure 5.6. Unfortunately, due to the shape of the fixtures, only the front surface was visible for all specimens, so there was no way of monitoring out-of-plane bending in the tests. This may have been the cause of the significant scatter observed for some of the specimens and should be monitored in future tests either by recording the side view of the specimen or by using back-to-back strain gauges, which was unfortunately not considered in the original experiment design.

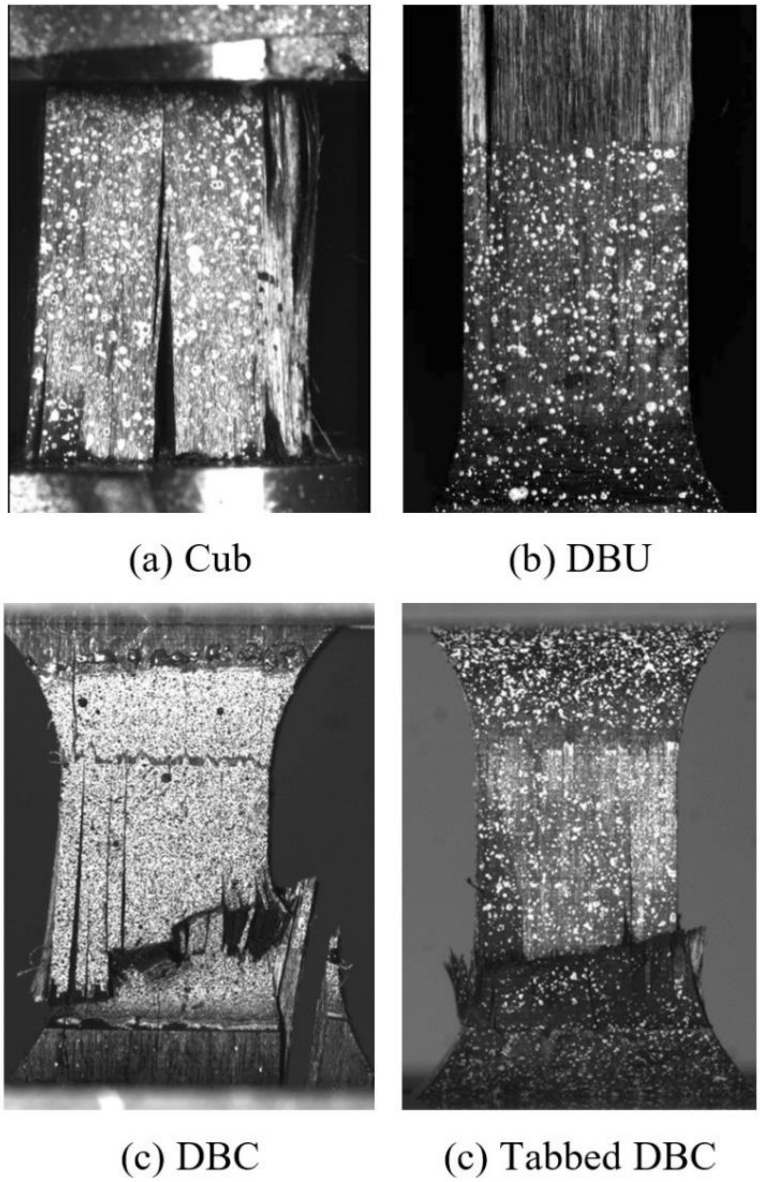

Figure 5.6. Failed UD specimens showing different observed failure modes: (a) Cub, (b) DBU, (c) DBC and (d) Tabbed DBC.

As expected, the unclamped rectangular samples failed far below the expected fibre kinking strength, which based on results from [91] should be around 1570 MPa, at around 858 MPa on average. The specimens failed catastrophically due to matrix splitting, which originated at the loading boundaries before fibre failure could occur, see Figure 5.6 (a). The unclamped dog-bone specimens (DBU), which were an attempt to mitigate the effect of stress concentrations at the loading edges, showed a considerable increase in strength, reaching 1499 MPa on average, but still ultimately failed due to matrix splitting, as can be seen in Figure 5.6 (b).

Therefore, it appeared to be necessary to resort to clamping fixtures, as used in [91,92,96], to strengthen the matrix in the transverse direction and apply combined loading compression (CLC) through combined end- and shear-loading at the clamps, as described in ASTM D6641/D6641M [92]. However, the cited studies both reported kinking failure originating at the fixtures, likely caused by stress concentrations from the abrupt change in boundary conditions. Therefore, the clamping fixtures were used in combination with dog-bone shaped specimens to reduce the effect of stress concentrations at the edges. Two different types of clamped specimen were tested: the simple dog-bone specimens (UD DBC), and the tabbed DBC specimens, which included an adhesively bonded layer of GFRP between the CFRP and the clamp surfaces.

Even in the DBC specimens, some matrix cracking, as observed in the DBU specimens, could not be completely prevented. However, in this case it only resulted in minor dips on the stress-strain curve, highlighted on the DBC curves in Figure 5.4, and did not significantly affect the stiffness, indicating that the load carrying ability was not affected. The DBC specimens continued to carry compressive loads far beyond this intermediate matrix splitting and eventually failed as desired in the form of kink bands within the gauge section, shown in Figure 5.6 (c), with an average strength of 1764 MPa.

On the other hand, the tabbed DBC specimen design was included to try and prevent the matrix splitting observed at the dog-bone radius in some of the DBC specimens. In addition, the direct application of compressive fixtures could over-constrain the material and affect the fibre kinking strength, dominated by localised matrix damage, which itself is strongly pressure-dependent [60,144,145]. Therefore, by relaxing the constraint on the UD material with the intermediate layer of GFRP between the fixtures, some insight could be gained into the effects of boundary conditions on this type of failure.

The tabbed DBC specimens failed at a much lower 1579 MPa on average but, interestingly, the results appeared to fall into two groups based on their failure stress and observed damage mode, although further testing would be required to verify this. One group of three specimens failed at around 1500 MPa, caused either by matrix splitting as in the unclamped specimens or by fibre kinking at the clamp the boundaries. The other two specimens failed at around 1700MPa, showing clear kink band formation within the gauge section and no noticeable matrix cracking, see Figure 5.6 (d), very similar to the previous DBC specimen results.

Based on these observations, it appears that two different failure or propagation modes may have been taking place. In Fleck's original fibre kinking theory [23], longitudinal compression failure is assumed to occur once fibre rotation due to the compressive stress becomes unstable, causing the fibres to buckle. However, Pinho [18,62] later added consideration for potential IFF failure before that point, which would weaken the matrix and could cause the fibres to buckle slightly earlier. It would appear from these results that, if the material is not sufficiently over-constrained, this initial matrix failure, as predicted by Pinho's model, may propagate as IFF in the fibre direction instead of forming the typically observed kink bands. In contrast, the additional lateral constraint and pressure effects from the fixtures in the UD DBC tests would have helped to prevent the propagation of this initial IFF damage, allowing eventual kink band propagation instead.

Therefore, the slightly lower strength at around 1500 MPa may be a more reasonable expectation of the longitudinal compression strength of the IM7/8552 composite than the 1764 MPa strength measured for the UD DBC specimens, which would appear to be artificially increased by over-constraining the material.

Cross-ply specimens:

In light of these issues with testing the thick UD specimens, a set of $[0°/90°]_{4S}$ cross-ply specimens was tested following suggestions in the literature that multi-directional laminates may be better suited for the determination of fibre kinking strength [91,96,143,146] as the transverse plies help to reinforce the longitudinal fibres, allowing them to reach their buckling strength without the need for additional external constraints.

For the cross-ply material, only two specimen designs were tested, an unclamped rectangular specimen (CP Cub) and a clamped dog-bone specimen (CP DBC), shown in Figure 5.2. The results are summarised in Table 5.1 and the axial stress-strain curves for both specimen types are shown in Figure 5.4. Since the stress-strain curves showed no noticeable nonlinearity and there were no signs of damage or fibre rotation in the specimens before fracture was observed, the use of linear CLT for the extraction of longitudinal ply properties [143] was considered valid and the ply strength data given in Table 5.1 and Figure 5.5 is used for the rest of the discussion below.

As expected, both geometries, CP Cub and CP DBC, presented similar axial stiffness and practically the same axial strength, with the Cub specimen showing slightly greater scatter. In addition, both specimens failed within the gauge section, Figure 5.7, from what appeared to be longitudinal compression failure in the central plies, which then propagated outwards. Unfortunately, because of this, no particularly useful failure images were captured on the outer layers during the test. However, section 5.2.3 includes more detailed microscopy images of different off-axis specimens showing typical failure propagation through longitudinal and transversal plies in CP specimens.

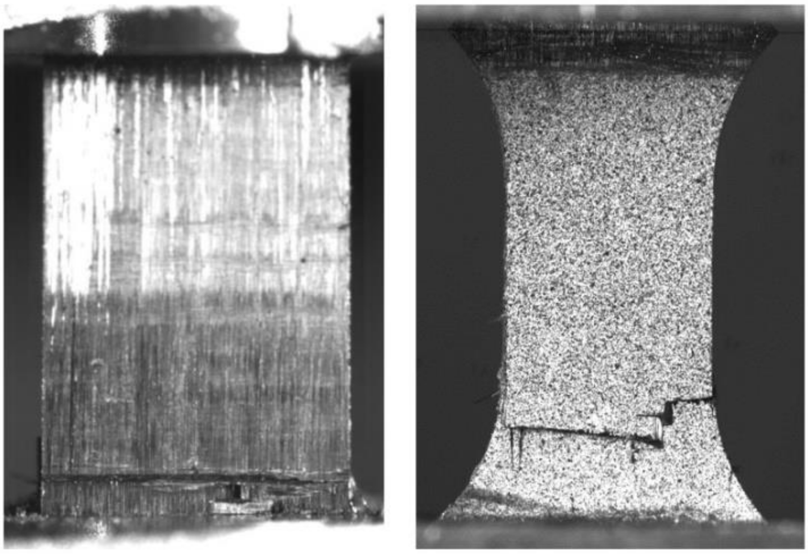

(a) Cub (b) DBC

Figure 5.7. Failed CP specimens showing failure on the outer plies after initiating and propagating outwards through the laminate. Left to right: (a) CP Cub and (b) CP DBC specimens.

At a first glance, these results show that the practical issues encountered in testing the UD material are in fact avoided when testing the CP laminates, as no complex specimen design or fixtures are required to produce the desired mode of failure. In addition, the clamping fixtures did not appear to affect the compressive strength, although they may have improved experimental scatter. However, significant experimental scatter is typically expected in this type of experiment due to the nature of fibre kinking failure, which is caused by local fibre misalignments, which can vary from one specimen to another. For reference, both the UD tests and the data from clamped QI specimens in [91,96] showed a similar variation in strength measurements.

However, when compared to the UD results, there are noticeable differences. Both CP specimens (CP Cub at 1551 MPa and CP DBC at 1510 MPa) failed at similar equivalent longitudinal ply strengths to the unclamped DBU and the subset of tabbed DBC specimens that failed due to matrix splitting. The UD specimens that reached fibre kinking strength, on the other hand, failed at around 1700 to 1800 MPa.

Previous studies on the same material showed longitudinal strength in QI laminates similar to that obtained here in the CP material, and UD strength 10-20% lower [91,96]. However, UD specimens in both were reported to fail at the clamp edges, indicating that they may have suffered from critical stress concentrations, causing local matrix damage and premature onset of fibre kinking failure.

As discussed in the previous section, for the UD material it can be assumed that the material properties and local fibre misalignment (typically up to 3° [147–149]) result in the onset of IFF damage at longitudinal compressive loads of around 1500 MPa and that the fibre micro-buckling strength of between 1700 and 1800 MPa is only reached with sufficient additional constraints on the longitudinal fibres to make up for the reduced matrix support.

Therefore, it would seem that the CP material tended to fail at the onset of IFF damage, similar to the unconstrained UD specimens, whereas the stronger constraints in the clamped UD specimens allowed for greater compressive loads and more stable kink band propagation to occur.

Taking the initial matrix failure instability as a valid strength measurement, which occurred for the UD specimens at around 1500 MPa, it would seem that CP or other multi-directional laminates can, in fact, be used to measure the longitudinal compression strength more reliably than UD material. In addition, if the objective is to characterise the behaviour of UD plies in a multidirectional laminate, taking into consideration possible size effects and differences in local fibre architecture such as those noted by Lee and Soutis [91], it can be argued that CP specimens will give a more representative measurement of the expected compressive strength, regardless of how the thick UD material behaves.

5.2.2.5. Conclusions

An experimental campaign has been carried out to investigate the optimal specimen design and test set-up for the determination of the longitudinal compression strength of UD CFRPs using two types of IM7/8552 specimens.

A first series of experiments was carried out on various UD specimen designs to obtain a reliable reference measure of the material's compressive strength, which highlighted the serious difficulty in reaching the desired fibre micro-buckling failure mode that has been reported in the literature.

First, it was found that waisted, or dog-bone, specimen designs were necessary to avoid stress concentrations at the edges causing premature failure regardless of the use of clamping fixtures. However, across the different waisted specimen designs, there appeared to be two different mechanisms dictating the compressive strength of the material depending on the boundary conditions of the experiment. For tests with more relaxed lateral constraints, including the completely unclamped specimens and the clamped specimens with GFRP end tabs between the clamping fixtures, the material tended to fail at around 1500 MPa due to matrix cracking and fibre kinking rarely occurred. On the other hand, the formation and propagation of stable kink bands was only consistently achieved when the specimens were over-constrained, with the clamping fixtures possibly helping to prevent immediate specimen collapse due to matrix failure and artificially allowing the load to reach up to 1700 to 1800 MPa. According to Pinho's fibre kinking criteria [18], longitudinal compression failure can be caused by reaching a point of unstable fibre rotation in the kink band and/or by matrix cracking in the vicinity of the misaligned fibres. After this point, based on the previous observations, propagation in the form visible kink bands rather than the matrix cracking along the fibre direction may require that the material be over-constrained, preventing the fibres from fraying. Therefore, the lower strength of around 1500 MPa may be a more reasonable expectation of the longitudinal compression strength of IM7/8552 than the higher limit reached in the over-constrained specimens, even if the first group did not develop clear kink bands.

In second place, two different CP specimen designs were tested to compare against the UD results: a rectangular unclamped specimen and a clamped dog-bone design. The two different specimens showed no significant differences between them, regardless of shape or the use of clamping fixtures, indicating reliable material and test design. Furthermore, the extracted longitudinal compression strength using CLT [143] coincided with the measured UD results at 1500 MPa.

Therefore, based on the previous discussion, it appears that CP specimens can in fact produce reliable results for the longitudinal compressive strength of the UD material. In addition, due to greater reliability and lower sensitivity to boundary conditions, it is strongly recommended that this type of material be used instead of UD laminates, especially if the goal is to characterise the behaviour of UD plies within multi-directional laminates.

Furthermore, thick UD material should be used with caution as the longitudinal compression strength can very easily be under or over estimated. Without the use of clamping fixtures, stress concentrations and edge effects can prematurely initiate matrix cracking and even fibre kinking, while the use of clamping fixtures can over-constrain the material and artificially increase the strength of the specimen in the same way that hydrostatic pressure delays the onset of IFF [58].

5.2.3. Quasi-static off-axis compression tests

Following the results of the previous study, where the cross-ply material was found suitable for longitudinal compression testing, a series of off-axis compression tests were carried out at quasi-static and dynamic loading rates using similar CP specimen designs.

To produce biaxial stress states in the material, the CP specimens were prepared at different off-axis angles with respect to the longitudinal orientation of the outer plies, similar to the approach used in section 4.2 to study IFF.

Starting with the quasi-static tests in the following sections and then the dynamic tests in section 5.2.4, the obtained results will finally be used in section 5.2.5 to study the effects of strain rate and off-axis loading on the longitudinal compression strength and evaluate some of the leading fibre kinking failure theories.

5.2.3.1. Specimen design and experimental set-up

Having established the validity of using CP specimens for the measurement of the UD longitudinal compression strength, a set of off-axis compression tests was carried out to determine range of validity in combined loading, which is critical for the evaluation of 3D failure kinking theories. A series of CP Cub samples cut at 0°, 3°, 6°, 10° and 15° with respect to surface fibre direction was tested in the same manner as the uniaxial compression test in section 5.2.2. Other than the material orientation, all specimens were prepared and tested in an identical manner to the uniaxial compression tests.

While the same type of test was attempted for UD DBC and CP DBC specimen designs, preliminary results showed several issues that made them unreliable. In both cases, the waisted design of the specimens, in combination with the slight misalignment of the fibres, resulted in a non-uniform strain distribution through the gauge section and stress concentrations at the change in section were greatly exaggerated in the off-axis specimens, Figure 5.8 (b). Because of this, any measure of the average stress state across the specimen cross-section would no longer be representative of the actual material conditions at failure. In addition, in the UD specimens, the same off-axis angles used in the CP specimens resulted in much greater shear stresses, producing significant fibre rotation and shifting the failure mode from fibre kinking to IFF.

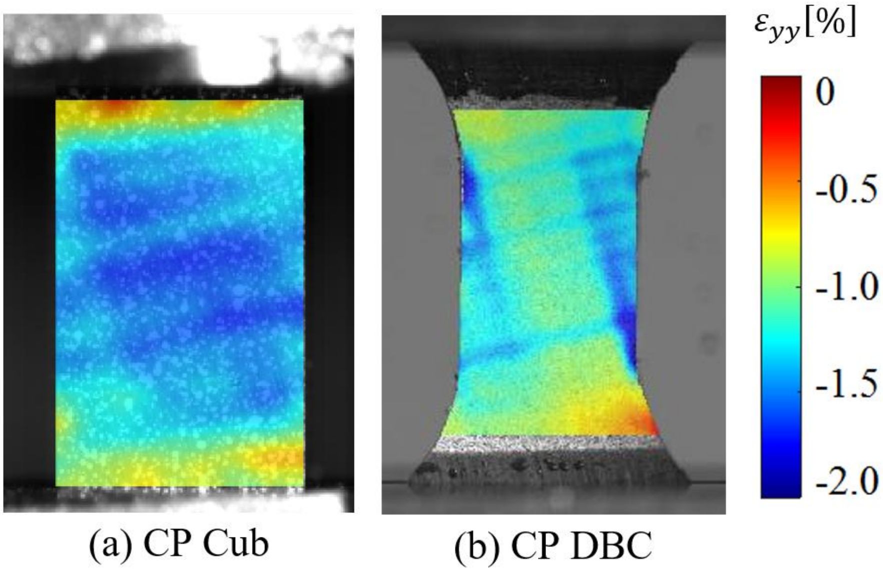

Figure 5.8. DIC longitudinal strain (ε_{yy}) overlay on two specimens showing non-uniform distribution in (a) a 15° off-axis CP Cub specimen compared to (b) a 15° DBC specimen.

In contrast, the rectangular CP specimens, Figure 5.8 (a), showed a much more uniform strain distribution throughout the gauge section, which allowed for average axial stresses to be used more reliably to extract individual ply stress states and ultimate strength measurements. Therefore, only the rectangular CP specimens were used in the present off-axis compression study and, in cases where the use of dog-bone specimens was necessary, such as the dynamic tests in section 5.2.4, the severity of the waist was reduced and greater off axis angles were avoided.

As in section 5.2.2, as long as the conditions were met, longitudinal ply strengths were extracted from the axial stress data for the off-axis CUB CP specimens using CLT. However, due to the different off-axis angles, these had to be rotated by the off-axis angle, β, to give the local stresses in the material coordinate system, $\{\sigma_{11}\ \sigma_{22}\ \tau_{12}\}^T$, as was done for the off-axis IFF tests in section 4.2.

Since the introduction of off-axis stresses was expected to cause some shear-dominated nonlinear behaviour, each set of results was analysed to determine the validity of the CLT method for the determination of UD compression strength.

For cases where the use of CLT could not strictly be considered valid due to excessive nonlinearity, approximate strength results were extracted by considering the additional fibre rotation due to shear, measured using DIC, in the CLT analysis and subsequent rotation. These last results, while less reliable, may still serve to give an idea of expected failure behaviour for the present study. However, for more accurate analysis, which will be done for the validation of the developed FE material model in Chapter 7, the axial data from these tests should be used instead.

5.2.3.2. Results and discussion

The results for each of these off-axis CP Cub specimens are summarized in Table 5.2, showing the axial strengths, and Figure 5.9, showing the axial stress-strain curves. A decrease in strength can be observed as the off-axis angle increases, with noticeable nonlinearity in the 10° and 15° specimens.

Table 5.2. Summary of off-axis (0°, 3°, 6°, 10° and 15°) CP Cub axial strength results.

Axial Strength	**CP Cub 0° [MPa]**	**CP Cub 3° [MPa]**	**CP Cub 6° [MPa]**	**CP Cub 10° [MPa]**	**CP Cub 15° [MPa]**
1	747	744	623	467	341
2	783	746	643	468	353
3	847	741	706	452	353
4			630	451	350
5				466	363
AVG	792	744	651	461	352
STDV	50.6	2.1	37.9	8.5	7.9
CV (%)	6.4	0.3	5.8	1.9	2.3

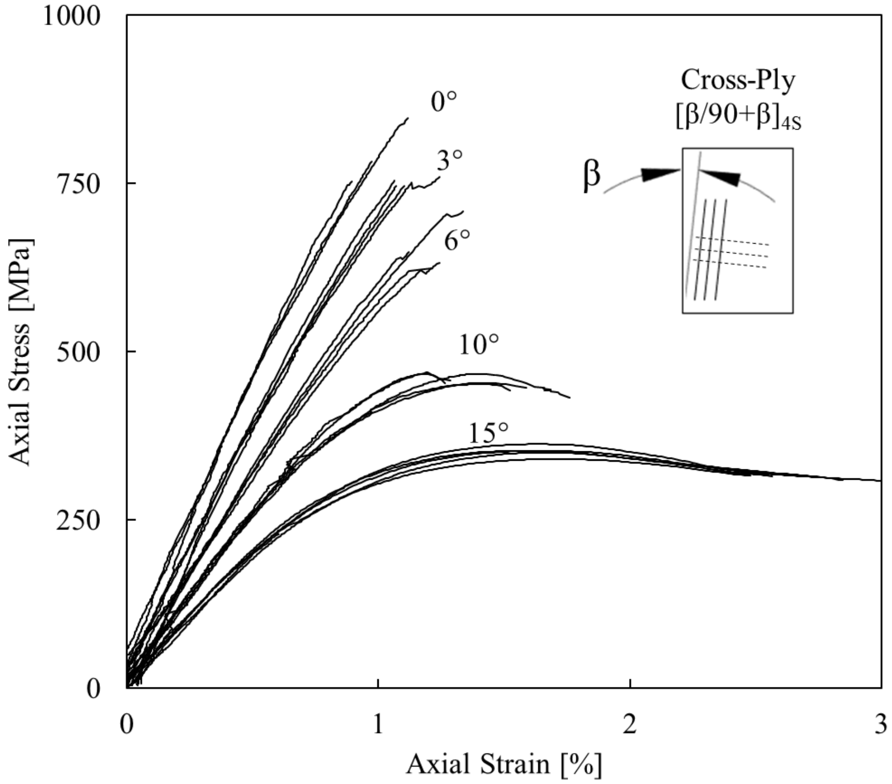

Figure 5.9. Comparison between the quasi-static axial stress-strain curves for the off-axis CP specimens with misalignment angles of 0°, 3°, 6°, 10° and 15° showing decreasing strength and noticeable nonlinearity after 6°.

As described in section 5.2.2, the longitudinal, σ_{11}, and shear, τ_{12}, stresses in material coordinates were extracted from each test using CLT and a stress rotation by the off-axis angle, β. These results are plotted in Figure 5.10 to show the shape of the failure envelope under combined longitudinal compression and shear. However, for the 10° and 15° tests, where the validity of the CLT method was questionable due to the significant nonlinear behaviour observed, only approximate data could be obtained by using the additional fibre rotation measured in each test.

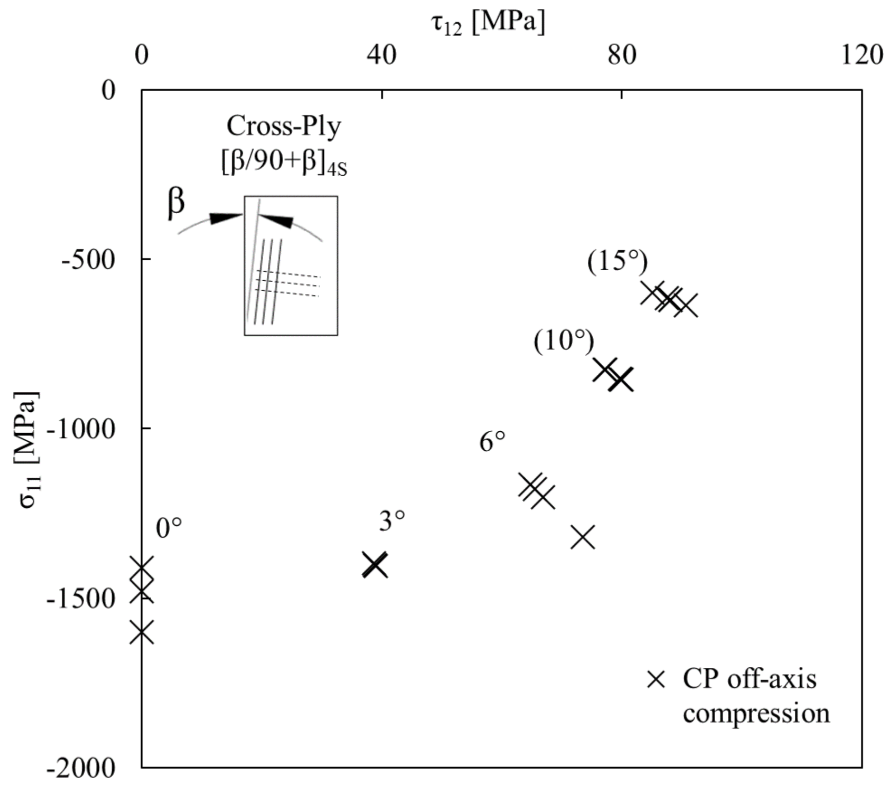

Figure 5.10. Longitudinal, σ_{11}, and shear, τ_{12} stress at failure for the variosu off-axis CP Cub specimens, extracted using CLT. Brackets around the 10° and 15° indicate approximate results due to fibre rotation and nonlinear shear behaviour.

The validity of the CLT method was investigated for all tests, not only the 10° and 15° tests, which showed clear nonlinear behaviour in the axial stress-strain curves. Up to 6°, however, there was no noticeable nonlinearity and no signs of damage or fibre rotation in the specimens before the point of failure. In addition, the shear stress-strain curve for IM7/8552 from [14,44] shows no significant nonlinearity below stresses of around 60 to

70 MPa and only the 10° and 15° tests were clearly above that limit, as can be seen in Figure 5.11. Therefore, the results extracted using linear CLT should be accurate for these 0° to 6° tests. For the 10° and 15° tests, the known nonlinear shear behaviour could be used to extract more accurate results using nonlinear CLT instead. However, this has not been pursued further at this stage.

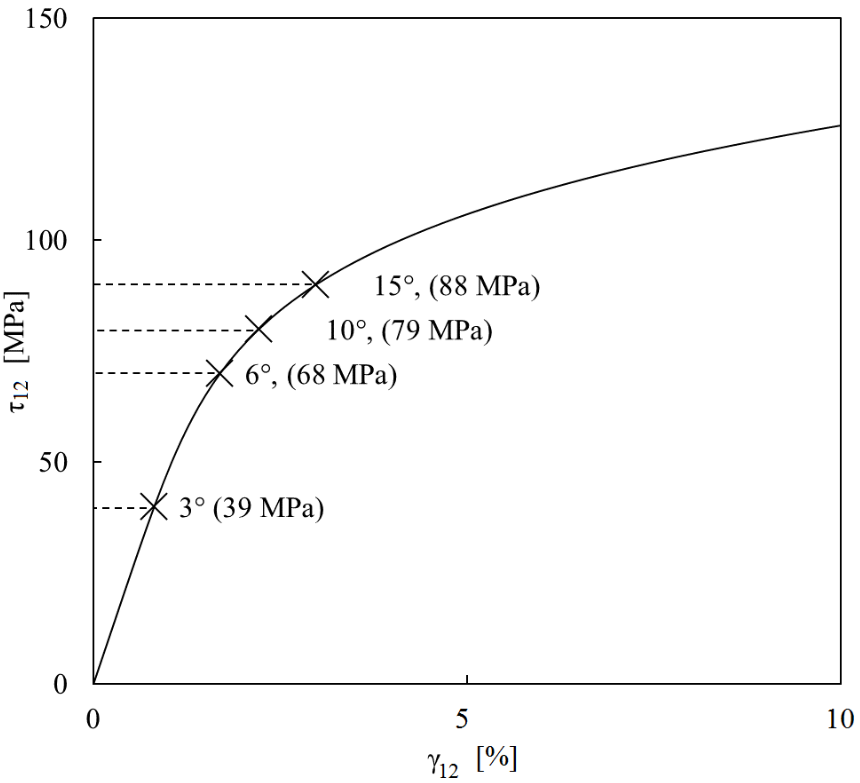

Figure 5.11. Average shear stresses from the 3 and 6° off-axis compression tests overlaid on the experimental shear stress–strain curve for IM7/8552 from [44].

Finally, post-mortem test and SEM images in Figure 5.12 were used to verify that the CP specimens did in fact fail due to fibre buckling. For the lower off-axis angles, from 0° to 6°, no clear kink bands were visible. However, SEM revealed groups of buckled fibres along the failure surfaces, which appeared to have failed in the out-of-plane direction following failure in the central plies. For the 10° and 15° specimens, clear kink bands were visible along the fibre direction of the transverse plies. Since failure was preceded by significant nonlinearity for these tests, shear localisation in the transverse plies may have promoted the propagation of fibre buckling along those planes.

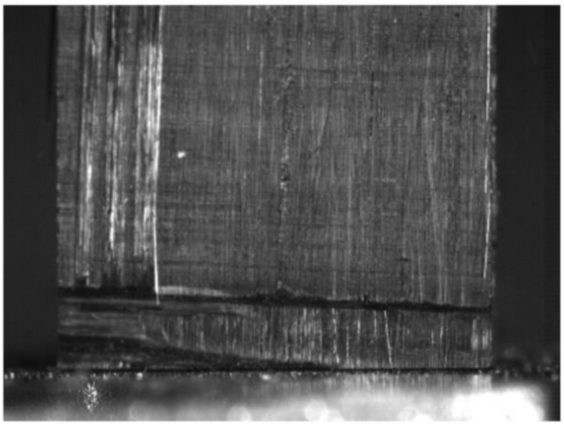

(a) 3° CP - failure surface

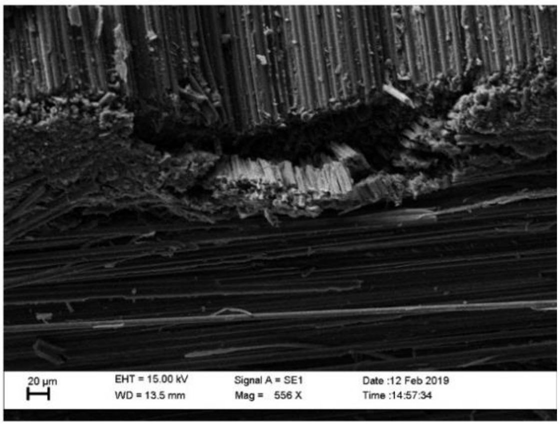

(b) 3° CP - through thickness SEM

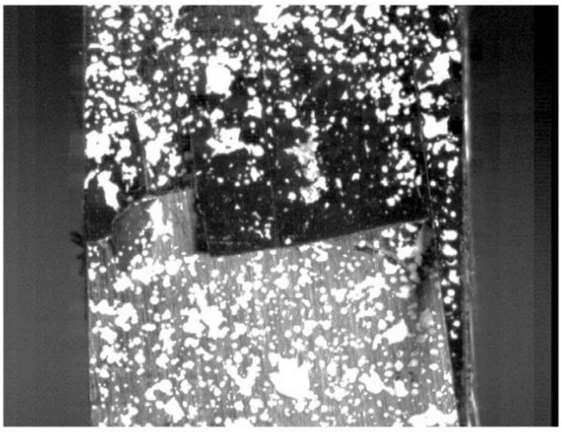

(c) 6° CP - failure surface

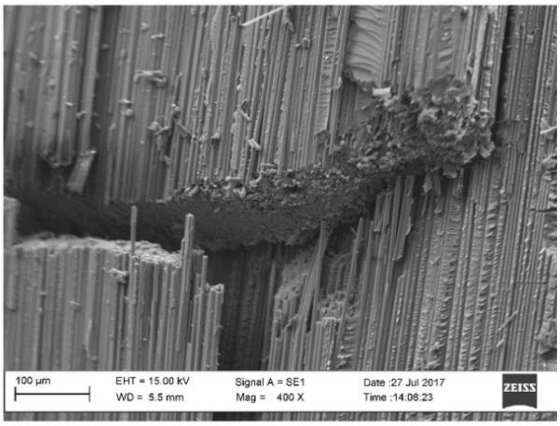

(d) 6° CP - through thickness SEM

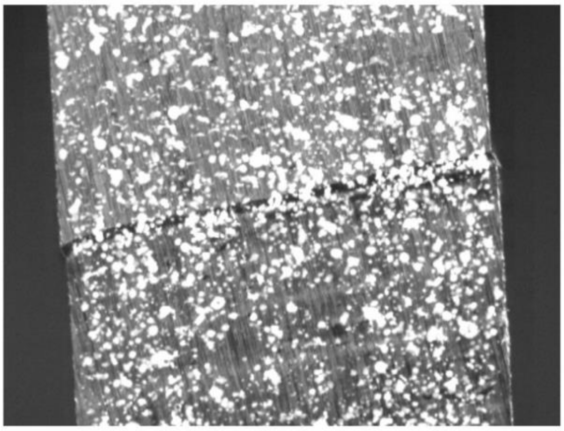

(e) 10° CP - failure surface

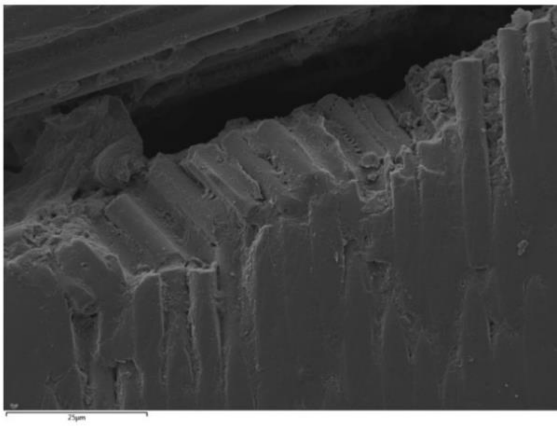

(f) 10° CP - through thickness SEM

Figure 5.12. Macroscopic (digital camera) and Scanning Electron Microscope (SEM) images of different failed 3°, 6° and 10° CP specimens showing signs of fibre kinking failure. The scale bars in the SEM images indicate 20 µm in (b), 100 µm in (d), and 25 µm in (f).

From the results and preliminary analysis above, it can be confirmed that the off-axis CP specimens did in fact fail due to the desired fibre failure mode and that the extracted strength data used in the failure envelope should be accurate for the 0° to 6° tests, while the 10° and 15° test data may be less reliable.

However, since many well-established fibre kinking theories predict much more severe effects of shear on the longitudinal compression strength, the results obtained above were compared against other experimental data from the literature to show that the observed behaviour is not an exception. Figure 5.13 shows normalised data from Shuart et al. [150], who used ±5° and ±10° angle-ply specimens; Soden et al. [61], who used CFRP tubes under torsion and compression; and the results from the present study, all following a similar trend, reinforcing the validity of the newly obtained results.

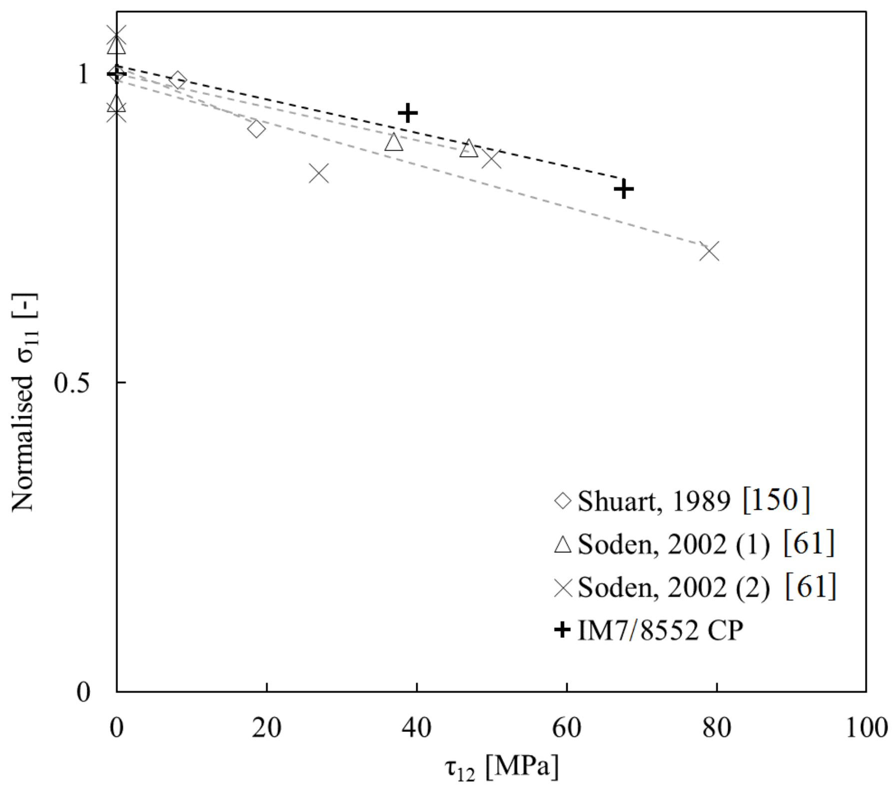

Figure 5.13. Comparison of biaxial loading envelopes for longitudinal compression failure between different materials and test methods, including data from [61,150], all normalised against the average uniaxial compression strength for each data set.

5.2.3.3. Conclusions

Having validated the use of the CP specimen design for the determination of longitudinal compression strength properties in section 5.2.2, a series of off-axis compression tests was carried out on 0°, 3°, 6°, 10°, and 15° specimens at quasi-static loading rates.

For the 0° to 6° tests, linear CLT was used to extract longitudinal ply stresses from the axial stress data, since the tests did not show noticeable nonlinear behaviour. However, for the 10° and 15° tests, due to significant nonlinearity, only approximate ply stress data could be extracted in this manner by correcting for the observed fibre rotation.

The results showed a gradual decrease in longitudinal compression strength as the off-axis angle and in-plane shear increased. However, even under large amounts of shear the strength was still greater than may be expected based on leading fibre kinking theories, such as [18,23].

In order to validate the observed behaviour, post-mortem SEM analysis was performed to verify that failure occurred due to fibre kinking of the longitudinal plies, and other data from the literature was compared, showing similar trends.

A more in-depth analysis will be performed in section 5.2.5 with these results and the dynamic off-axis compression data presented in the following section.

5.2.4. Dynamic off-axis compression tests

Following the quasi-static experiments in the previous section, a series of dynamic off-axis compression tests were performed using a similar cross-ply specimen configuration and data reduction methods to extract the longitudinal compression strength from the axial measurements. The specimens were tested at high strain rates using a Split-

Hopkinson Pressure Bar (SHPB) system, described in section 4.2.3, and longitudinal ply failure data was extracted from the axial specimen strengths using linear CLT, following the methodology described in section 5.2.2.3.

The obtained results are presented in section 5.2.4.2 and analysed in more detail in section 5.2.5 along with the quasi-static test data.

5.2.4.1. Specimen design and experimental set-up

First, some minor modifications to the quasi-static specimen design were necessary to make it suitable for dynamic loading, since the rectangular specimen design used in section 5.2.3 resulted in premature cracking and specimens rotating out of place during testing. Instead, a tabbed dog-bone design was used as shown in Figure 5.14.

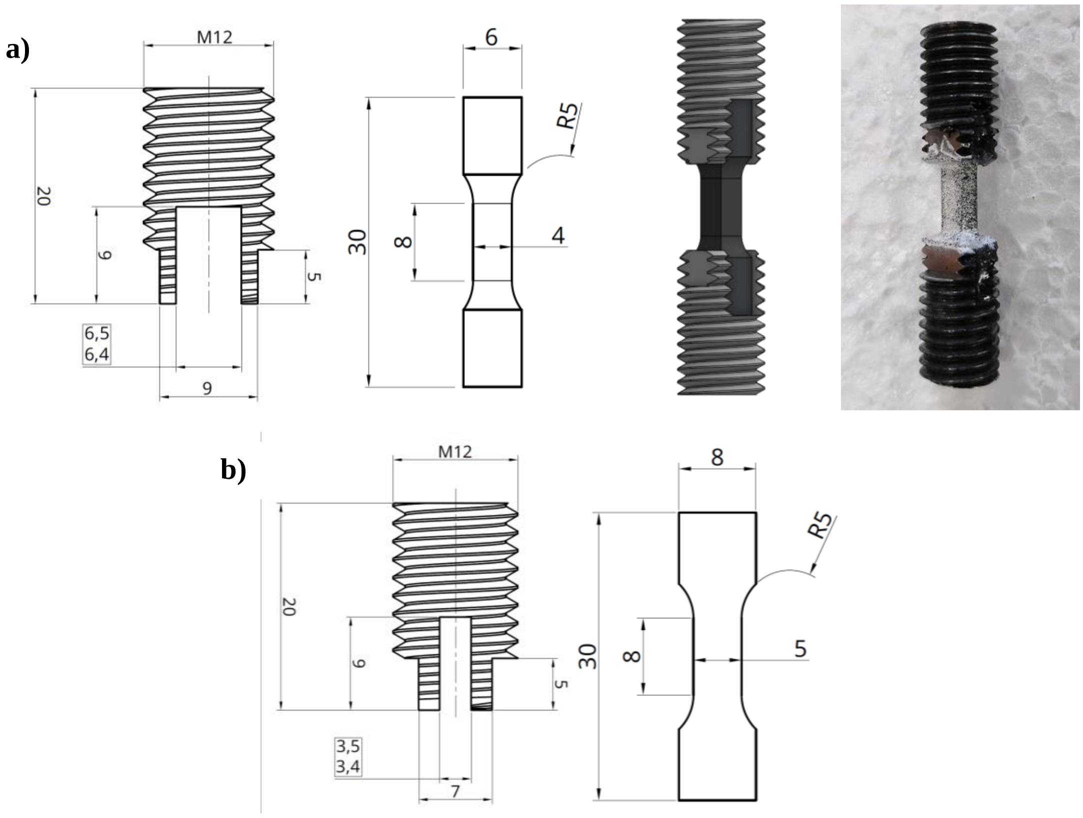

Figure 5.14. Cross-ply specimen and end cap design for dynamic loading: (a) IM7/8552 specimens from the 10 mm initial plate thickness used in this study; (b) simpler specimen successfully tested for a 3 mm plate with only in-plane dog-bone.

The screwed end caps allowed the specimen to be fitted into the SHPB input and output bars to ensure alignment throughout the test, while the dog-bone design mitigated the effects of noise and stress concentrations at the specimen-bar interfaces. In addition, the radius of the dog-bone was softened with respect to the CP dog-bone specimen design tested in section 5.2.2, which was not well suited for off-axis compression.

All specimens were cut from a 10 mm $[0/90]_{20S}$ IM7/8552 plate using a water jet cutter and were ground down to the final specifications, detailed in Figure 5.14. For the uniaxial compression tests, specimens were cut parallel to the fibre direction of the external plies and additional specimens were cut at 3°, 6°, and 10° to the surface fibre direction in order to produce different combinations of longitudinal compression and shear stresses.

Due to the excessive thickness of the 10 mm cross-ply laminate, a dog-bone shape was also ground in the out-of-plane direction, Figure 5.14 (a), to achieve the desired cross-section of 16 mm^2. It should be noted that a simpler dog-bone specimen design, Figure 5.14 (b), without the out-of-plane grinding, was also tested using a different material and produced equally reliable results. The more complex design used for the IM7/8552 composite was only necessary to reduce the thickness of the source material in order to facilitate the achievement of dynamic loading rates and material failure during SHPB experiments.

The SHPB set-up us shown in Figure 5.15. In order to ensure alignment throughout the test and avoid the introduction of spurious loading pulses, the input and output bars of the SHPB system were supported by low friction PTFE bushings at a pitch of 300 mm, Figure 5.15 (b), and the specimens were bonded to M12 threaded end caps using a 3M DP490 adhesive, allowing them to be fitted into the M12 threaded holes in the bars. The fixtures, end caps, and a mounted specimen are shown in more detail in Figure 5.15 (c).

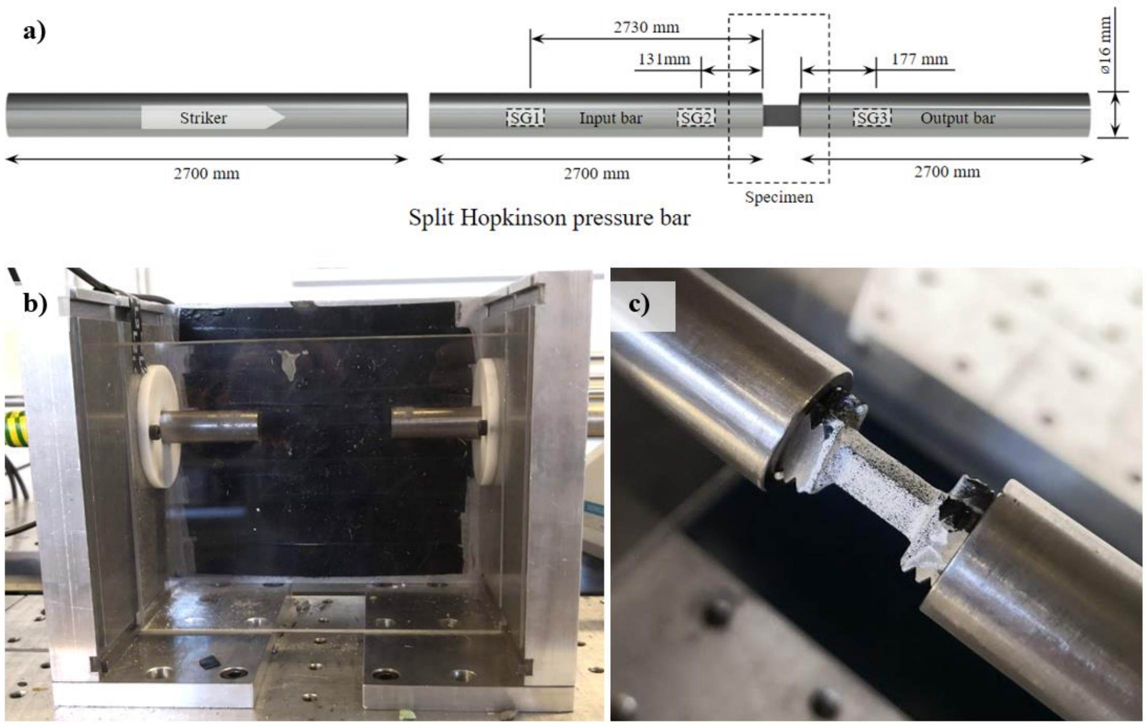

Figure 5.15. SHPB test set-up used for the dynamic compression tests. a) schematic of the SHPB system, b) alignment and containment fixtures, and c) inserted specimen with speckle pattern for DIC.

Finally, a fine speckle pattern was applied to all specimens, as shown in Figure 5.15 (c), and the specimens were fitted into the bars for testing. With the specimens fully prepared and mounted, the tests were carried out following the same methodology described in section 4.2.3 for the dynamic IFF tests and recorded using the same Kirana high-speed camera for the DIC, which was connected to the same oscilloscope used to record the signal from the strain gauges in order to synchronise the strain and force histories.

With the above in place, all tests were fired with a pressure of approximately 1 bar for a striker velocity of around 6 m/s to produce strain rates in the order of 100 s^{-1}.

5.2.4.2. Dynamic results and discussion

With the updated dynamic specimen design, the stress concentration and boundary effect issues observed in previous iterations were successfully avoided. The results, summarized in Figure 5.16 and Table 5.3 below, showed good repeatability, and the stiffnesses were in good agreement with the quasi-static results from section 5.2.3, giving confidence in the data acquisition and processing methods. Figure 5.16 shows the obtained axial stress-strain curves for each of the four specimen orientations compared to the quasi-static data and a summary of the strength data for all quasi-static and dynamic tests is given in Table 5.3. On average, a strain rate of 75 s^{-1} was achieved for the 0° uniaxial compression tests with this number increasing slightly in the off-axis tests as the axial stiffness decreased. The initial noise observed in some of the processed dynamic data has been omitted from the curves in Figure 5.16 as it was attributed to the error in the stress calculations before dynamic equilibrium was reached and therefore did not represent the material behaviour.

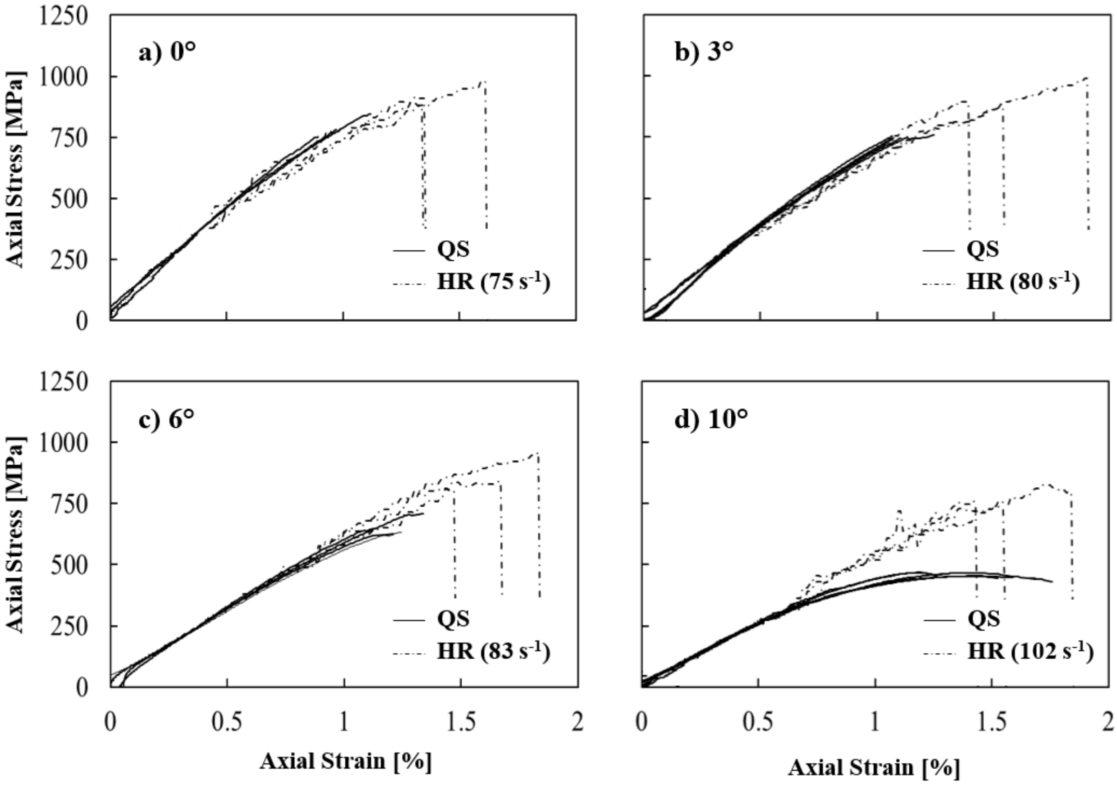

Figure 5.16. Axial stress-strain curves obtained for each of the CP specimen orientations at quasi-static (QS) and dynamic (HR) loading rates.

Table 5.3. Summary of dynamic off-axis (0°, 3°, 6°, and 10°) axial strength results. Average strain rates (SR) are given in the legend in s^{-1}.

Axial Strength	**0° [MPa]**	**3° [MPa]**	**6° [MPa]**	**10° [MPa]**
1	925	911	959	828
2	903	1001	814	823
3	986	900	873	798
AVG	938	937	882	816
STDV	43.1	55.3	73.4	15.9
CV (%)	4.6	5.9	8.3	1.9
SR [s^{-1}]	75	80	83	102

While these results will be analysed in more depth in the following sections, an increase in strength with regard to the quasi-static data was immediately visible across all specimens. In addition, the 10° tests noticeably lacked any significant nonlinear behaviour such as that observed in the quasi-static tests, Figure 5.16 (d). Both of these differences can be attributed to the viscous stiffening and hardening of the matrix at high strain rates.

Furthermore, as all tests showed linear stress-strain behaviour up to the point of failure, linear CLT could be used to extract longitudinal ply stresses from the axial data, following the procedure described in section 5.2.2.3.

This allowed for the longitudinal compression stress, σ_{11}, and in-plane shear stress, τ_{12}, in the longitudinal plies to be determined from the axial strength for each type of specimen, producing the failure envelopes shown in Figure 5.17. Because the quasi-static 10° tests showed significant nonlinear behaviour, the data obtained using linear CLT was less reliable and is shown in light grey in the plot.

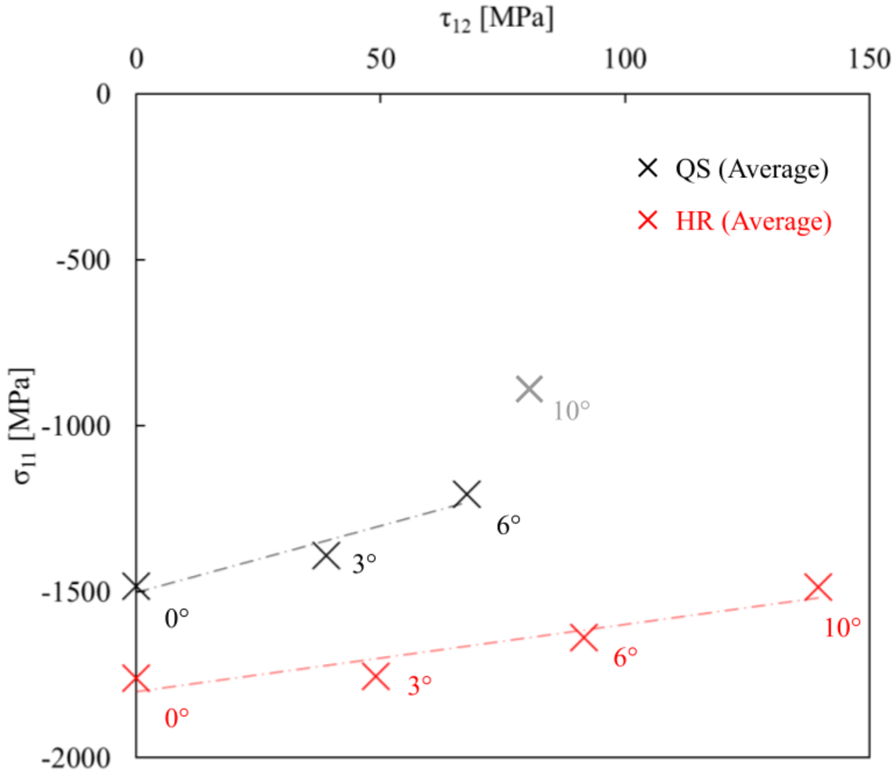

Figure 5.17. Quasi-static (QS) and dynamic (HR) failure envelopes extracted from axial strength data using linear CLT. X marks indicate the average strength for each specimen type and the dotted lines show the linear trend for each data set.

The new high strain rate results in Figure 5.17 followed a similar trend to the previous quasi-static data as well as some of the biaxial loading data found in the literature [61,150]. The longitudinal compression strength can be seen to decrease in an apparent linear trend as the shear stress increased but, as will be discussed in the following sections, the off-axis specimens still maintained significant strength in the 11 direction even at high amounts of shear, contradicting some of the leading fibre kinking theories. In addition, as mentioned above, a significant increase in strength with respect to the quasi-static data was observed across all specimen orientations. This increase was around 20-35% for strain rates of 75 to 85 s^{-1}, matching what was reported by Ploeckl et al. [96] for the uniaxial compression strength of a quasi-isotropic laminate.

Although, due to severe fragmentation, none of the specimens was suitable for post-mortem imaging to verify that the specimens did indeed fail due to fibre kinking of the longitudinal plies, the results from the quasi-static campaign and the repeatability of the new dynamic results gave enough confidence that the test results were valid. In addition, images from the high-speed camera, as shown for one of the tests in Figure 5.18, indicated that specimen failure was caused by the initial collapse of the external longitudinal plies, which are presumed to have buckled due to fibre kinking.

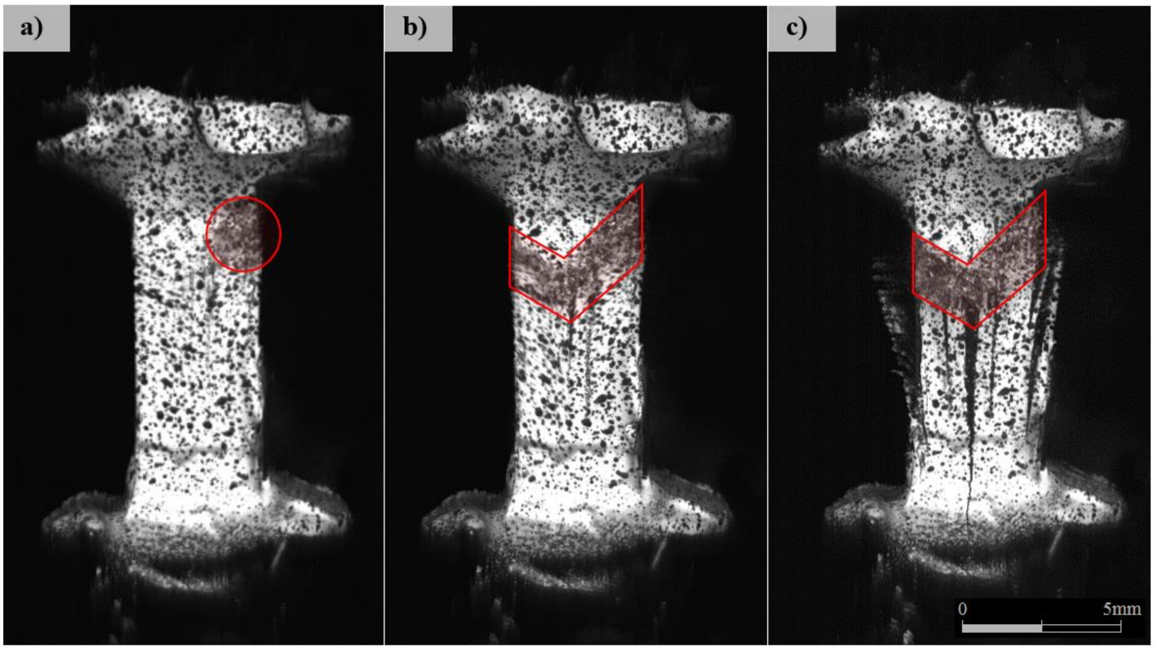

Figure 5.18. High-speed camera images of a 6° specimen at the point of failure. Failure can be seen to initiate in the highlighted outer longitudinal plies in a) and propagate through the rest of the specimen in b) and c).

5.2.4.3. Conclusions

Using a similar methodology to that used in section 5.2.3 above, a CP specimen design adapted for dynamic testing was successfully used to measure the off-axis longitudinal compression strength of an IM7/8552 composite laminate under high-rate loading.

The tests were carried out in a SHPB system at strain rates in the order of 75 to 100 s^{-1} and showed comparable stiffness to the previous quasi-static results. However, an increase in strength of 20-35% was measured with respect to the quasi-static data across all tests, in line with what was reported by Ploeckl in [96] for uniaxial compression of QI specimens.

Finally, linear CLT was used to extract the stress state of longitudinal plies at failure to produce dynamic failure envelope data which can be compared to the quasi-static envelope from section 5.2.3 and will be analysed in more detail in the following section.

5.2.5. Fibre kinking theory and failure criteria

With the experimental results obtained in the previous sections, a comprehensive set of fibre kinking failure data for a single material system at different loading rates and biaxial stress states has been obtained, which can be used to evaluate the leading failure theories and criteria.

As discussed in the literature review, longitudinal compression failure is widely accepted to follow the fibre kinking theory developed by Budiansky and Fleck [23,95], in which fibre rotation due to initial fibre misalignment and the nonlinear shear behaviour of the composite eventually becomes unstable, causing the fibres to buckle under the compressive load. In this section, the ability of Fleck's theory and the alternative implementation developed by Pinho [18,62,140] to describe the observed effects of off-axis and dynamic loading on the longitudinal compression strength will be investigated.

Each of these models is described in sections 5.2.5.2 and section 5.2.5.3, respectively, followed by a detailed analysis of their predictions for the quasi-static and dynamic off-axis compression cases.

In view of the limitations of these previous theories, an empirical modification to Fleck's fibre kinking criterion is proposed in section 5.2.5.4, which is able to predict more accurately the longitudinal compression strength of UD CFRPs under multiaxial loading.

5.2.5.1. Strain rate effects

While none of the investigated models was explicitly developed with rate-dependency in mind, they can all be adapted for dynamic loading relatively easily. They all have in common that they predict fibre kinking failure based the nonlinear shear stress-strain response of the composite. Therefore, by using rate-dependent nonlinear shear properties, the same models will be able to give predictions for different dynamic strain rates. Following the approach used in the rate-dependent nonlinear shear model, section 3.2, the in-plane shear properties of the composite were scaled by a function $r_y[\dot{\varepsilon}]$, given in eqn. (3.23), with the parameter K_y calibrated for the IM7/8552 data from [44] to obtain different dynamic values for each strain rate, $\dot{\varepsilon}$, as illustrated in Figure 5.19.

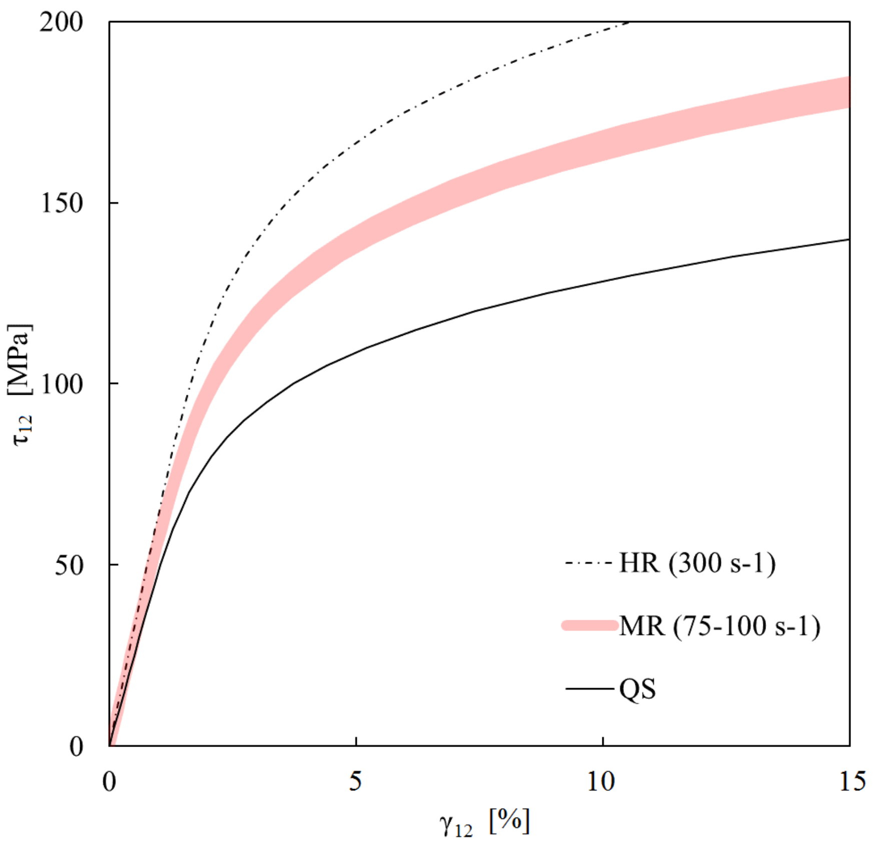

Figure 5.19. IM7/8552 shear stress-strain curves for different strain rates reproduced from [44]. The intermediate curves (MR) are extrapolated from the quasi-static and dynamic experimental data using eqn. (3.23).

5.2.5.2. Analytical fibre kinking theory

The advanced fibre kinking theory by Budiansky and Fleck [23,95] was based on the previous work by Rosen [107] and later Argon [108], who were the first to develop physical, micromechanics-based theories for the fibre kinking failure mechanism observed in UD CFRPs under longitudinal compression.

Rosen [107], originally predicted as an elastic micro-buckling problem using a beam buckling model for parallel, perfectly aligned columns in an elastic medium. This gave a compressive strength of the form:

$$\sigma_C = \frac{G_m}{\left(1 - V_f\right)} = G \tag{5.7}$$

where G_m is the shear modulus of the matrix and V_f the fibre volume fraction, resulting in a compressive strength equivalent to the shear modulus of the composite G, which severely over-predicted the strength of the material.

In 1972, Argon [108] argued that composites undergo plastic rather than elastic micro-buckling, with kinking occurring due to misaligned fibres, so that the compressive strength was obtained as a function of the yield stress in shear and the initial misalignment of the fibres.

This gave improved but not quite accurate predictions and paved the way for the work by Budiansky and Fleck [23,95], who built on these previous theories to include the effects of fibre rotation and nonlinear shear behaviour in the matrix by solving the equilibrium of the assumed kink-band geometry, shown in Figure 5.20, for different types of in-plane loading conditions.

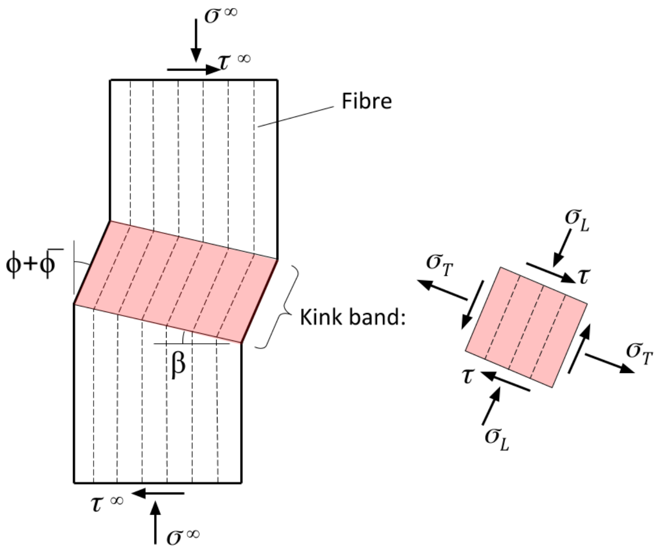

Figure 5.20. Typical kink band geometry and notation assumed by Budiansky and Fleck [23,95].

For the case of combined longitudinal compression, σ^∞, and in-plane shear, τ^∞, the following equilibrium relation can be obtained:

$$\sigma_C - 2\tau^\infty \tan\beta = \max\left(\frac{\tau - \tau^\infty + \sigma_T \tan\beta}{\phi + \bar{\phi}}\right) \tag{5.8}$$

Which, for the specific case of uniaxial loading ($\tau^\infty = 0$), results in a direct analytical expression for the critical compressive stress, σ_{C0}, at which the fibres will buckle:

$$\sigma_{C0} = \frac{G^*}{1 + nk^{1/n}\left(\frac{\bar{\phi}/\gamma_Y^*}{n-1}\right)^{(n-1)/n}} \tag{5.9}$$

With $G^* = \alpha^2 G$, $\gamma_Y^* = \gamma_y/\alpha$, and $\alpha = \sqrt{1 + \left(\frac{\sigma_{TY}}{\tau_Y}\right)^2 \tan^2\beta}$. Where G is the shear modulus of the composite, $\bar{\phi}$ is the initial fibre misalignment and β the kink band angle; σ_{TY} and τ_Y are yield stresses in transverse tension and shear; and n, k are Ramberg-Osgood [115] parameters for the nonlinear shear response of material, which is easily made rate-dependent by scaling the yield stress and shear modulus with eqn. (3.23):

$$\gamma = \frac{\tau}{G}\left[1 + k\left(\frac{\tau}{\tau_Y}\right)^{n-1}\right] \tag{5.10}$$

For off-axis compression, however, the solution becomes more complicated and an direct analytical solution cannot be obtained. Instead, an iterative approach, described in detail in [23], must be used.

The iterative solution for combined compression and shear was implemented in MATLAB with the rate-dependent Ramberg-Osgood equation for the nonlinear shear response as shown in Figure 5.19 to obtain the analytical failure envelope for quasi-static and dynamic loading at strain rates of 75 to 100 s^{-1}. The initial fibre misalignment was calibrated from the quasi-static uniaxial compression test and used to predict the off-axis quasi-static and all dynamic strengths. The predicted envelopes are plotted against the experimental results from the previous sections in Figure 5.21 below.

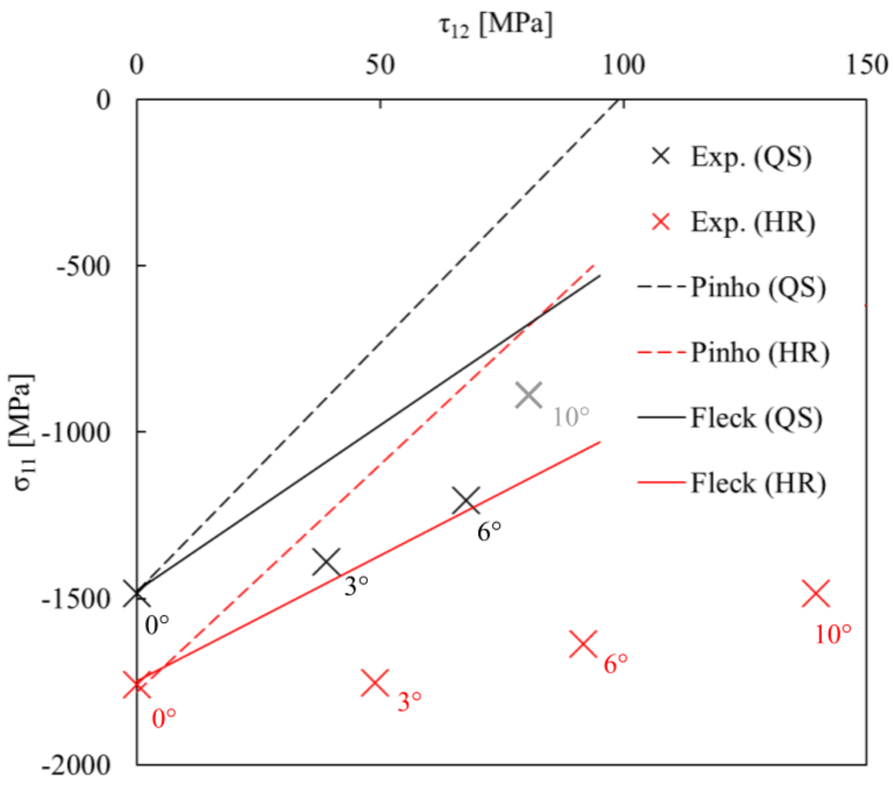

Figure 5.21. Experimental quasi-static (QS) and dynamic (HR) data compared against predictions from Pinho's LaRC criteria [18,62,140] and Budiansky and Fleck's analytical solution for longitudinal compression and shear [23,95].

As can be observed, the uniaxial compression prediction using Budiansky and Fleck's solution scales very well with the strain rate, similar to Matsuo and Kageyama's observations on its ability to predict the effects of temperature [94]. Interestingly, however, the effects of shear in the off-axis compression cases are over-predicted, excessively lowering the longitudinal strength, in both the quasi-static and dynamic envelopes. Even using the extended analytical solution from [23,151], which also accounts for the effects of transverse compression, σ_{22}, the off-axis predictions were not significantly improved.

5.2.5.3. LaRC failure criterion

Building on the above, Pinho [18,62,140] developed a numerical implementation of Fleck's kinking theory adapted for more general three-dimensional loading, whereas Fleck's solutions in [23,95] were only derived for in-plane loading conditions. In Pinho's LaRC model, a three-dimensional stress state is rotated onto the fibre misalignment frame, where matrix failure and fibre stability criteria are evaluated through iteration. Shear stresses in the rotated frame contribute to additional fibre rotation, which, in turn, may increase the shear stress in the misalignment frame. If a stable solution can be found, potential failure of the matrix is then evaluated using IFF criteria of the form:

$$f_{FK} = \begin{cases} \left(\dfrac{\sigma_n}{Y_T}\right)^2 + \left(\dfrac{\tau_T}{S_T}\right)^2 + \left(\dfrac{\tau_L}{S_L}\right)^2 \geq 1 & \text{for } \sigma_b \geq 0 \\ \left(\dfrac{\tau_T}{S_T - \mu_T \sigma_n}\right)^2 + \left(\dfrac{\tau_L}{S_L - \mu_L \sigma_n}\right)^2 \geq 1 & \text{for } \sigma_b < 0 \end{cases} \tag{5.11}$$

Where σ_b is the transverse stress on the misalignment frame; σ_n, τ_T and τ_L are normal and shear stresses on the IFF plane; and Y_T, S_T and S_L are the normal and shear strength properties of the composite, with frictional parameters μ_T and μ_L. An in-depth explanation of this implementation and the theory behind it is given in [18,62,140].

As with Fleck's analytical model in the previous section, an implementation of the LaRC model was used to obtain quasi-static and dynamic failure envelopes using the uniaxial compression case for calibration along with the rate-dependent nonlinear shear properties and, in this case, also the rate-dependent IFF strength parameters from [44]. The results are shown in Figure 5.21 next to the experimental data and Fleck's analytical predictions.

As expected, the LaRC predictions for the uniaxial compression case are almost identical to the analytical ones. However, the two envelopes begin to diverge with off-axis loading due, primarily, to: a) different assumptions regarding the kink band angle, β, between the two; and b) the fact that the LaRC model considers not only stability of the rotating fibres in the kink band but also potential IFF failure in the matrix if a stable rotation is achieved. However, while these differences cause a more pronounced drop in the σ_{11} strength under off-axis loading compared to Fleck's solution, they are arguably more physically sound, at least with regard to the treatment of potential matrix failure.

In any case, regardless of the minor differences between them, the shortcomings in both the previous models highlight the need for a better description of the fibre kinking failure mechanisms under off-axis compression loads. However, without a deeper look into the micromechanics of the problem, any potential changes to the underlying assumptions of the fibre kinking theory under off-axis loading would lack the strong physical basis of the original uniaxial compression theory. One way forward in this area, which should be considered in future work, may be micromechanical modelling of the kind done by Naya et al. in [139], as a similar study including off-axis loads could shed some light on the effects of shear on fibre rotation within the misalignment frame.

Keeping in mind the above concerns, a potential improvement to the fibre kinking model for off-axis compression cases is investigated in the following section.

5.2.5.4. Shear-damage model

Given that the 0º predictions in the previous sections were accurate and Budiansky and Fleck's fibre kinking theory [23,95] been extensively validated in the past for uniaxial compression cases, it seems that any inaccuracies in the off-axis predictions must come from the additional assumptions made for the effects of off-axis loads.

Under Budiansky and Fleck's assumed fibre kinking equilibrium and kinematics for the of off-axis loading case, any remote shear stress, τ^{∞}, would increase the waviness or additional rotation, ϕ, of the misaligned fibres. This additional rotation is one of the main reasons for the reduction in the strength under increasing shear stress and in [23,95] was accounted for in the form an additional shear knockdown factor that reduced the uniaxial compression strength from the analytical solution given in eqn. (5.9).

Therefore, the most likely cause for the under prediction of the off-axis compression strength in the previous sections is an over-estimation of the additional rotation, ϕ, in the misaligned fibres caused by the remote shear, τ^{∞}.

While further research would be necessary in order to confidently establish the micromechanics for the off-axis loading case, as an initial approximation and as a way to test the above hypothesis, it has been assumed instead that the effects of off-axis loads on the fibre waviness are negligible.

By neglecting this effect on the critical misalignment angle, the off-axis compression case can be treated in a simplified manner as the superposition of: (a) a uniaxial compressive load with no change to the fibre misalignment or the kinematics of the misaligned fibres, which is predicted by Fleck's uniaxial compression strength criterion, σ_{C0}, in eqn. (5.9);

and (b) an of off-axis load that may introduce matrix damage in the material, affecting the nonlinear shear behaviour in the kink band.

Therefore, under these assumptions, the off-axis compression case can be considered as a case of uniaxial compression where the shear properties of the material may be degraded by the off-axis loads. In this way, the off-axis compression strength can then be approximated by using eqn. (5.9) for the uniaxial compression strength and replacing damaged shear properties corresponding to the applied off-axis loads. By replacing the shear modulus, G, in eqn. (5.9) with the damaged modulus, G^D, the off-axis compression strength becomes:

$$\sigma_C[\tau, \dot{\gamma}] = \frac{G(1 - D_S[\tau, \dot{\gamma}])}{1 + n\, k^{1/n} \left(\frac{\bar{\phi} \,/\, \gamma_Y^*}{n-1}\right)^{(n-1)/n}} = \sigma_{C0}[\dot{\gamma}](1 - D_S[\tau, \dot{\gamma}]) \tag{5.12}$$

here $D_S[\tau, \dot{\gamma}]$ is introduced as a measure of the accumulated damage to the shear modulus from the off-axis loads. This allows the strength to be expressed in terms of the uniaxial compression strength, $\sigma_{C0}[\dot{\gamma}]$, and a shear damage term, $(1 - D_S[\tau, \dot{\gamma}])$, which is in agreement with the observations by Eyer et al. in [152] that the loss of longitudinal compression strength in CFRP tubes was directly proportionally to the loss of rigidity in the shear modulus.

While the above is admittedly a simplification of the true micromechanics of the problem, the aim here was to highlight the shortcomings in the current theory and investigate an alternative assumption for the material behaviour under off-axis compression until the micro-scale failure mechanisms are better understood.

In order to test this new assumption, the above criterion was implemented in MATLAB using the rate-dependent nonlinear shear properties obtained in section 5.2.5.1.

As an initial approximation, since no cyclic loading data was available to calibrate the progressive matrix damage in this material, the secant shear modulus was used as an estimate for the damaged shear modulus, so that:

$$G_D[\tau,\dot{\gamma}] = G_S[\tau,\dot{\gamma}] = G[\dot{\gamma}](1 - D_S[\tau,\dot{\gamma}]) \tag{5.13}$$

$$D_S[\tau,\dot{\gamma}] = 1 - \frac{G_S[\tau,\dot{\gamma}]}{G} \tag{5.14}$$

where $G_D[\tau,\dot{\gamma}]$ is the damaged shear modulus and $G_S[\tau,\dot{\gamma}]$ is the secant shear modulus for a given shear stress, τ, and strain rate, $\dot{\gamma}$, as illustrated in Figure 5.22 below.

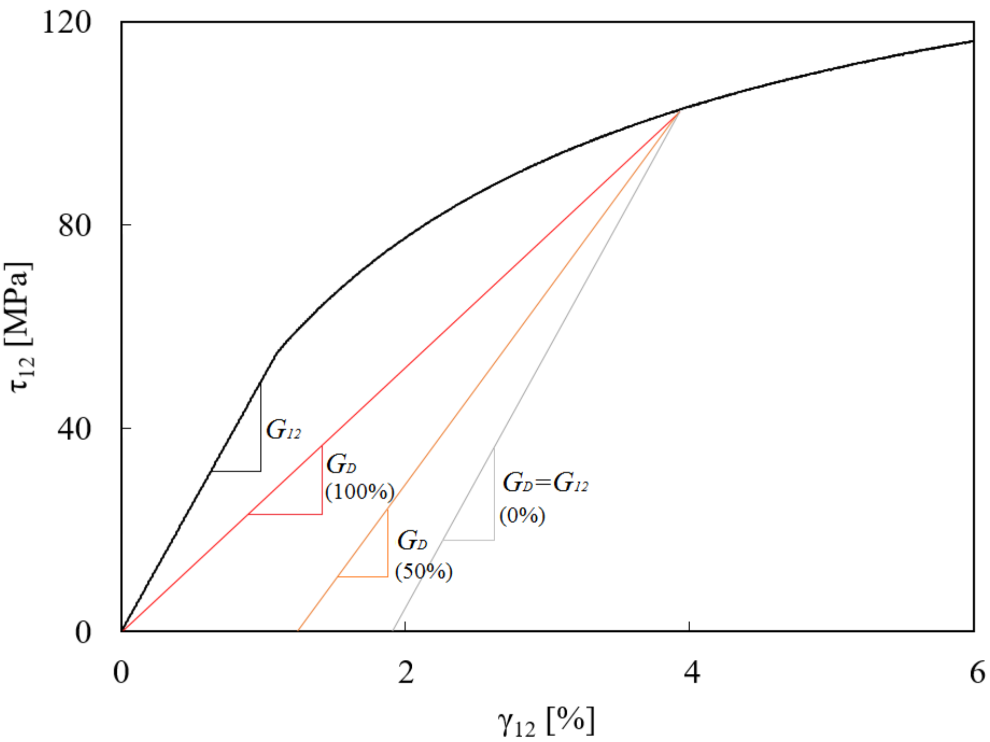

Figure 5.22. Different assumed proportions of shear damage, $G_D[\tau,\dot{\gamma}]$, illustrated for an arbitrary stress state under quasi-static loading conditions.

Therefore, for the MATLAB analysis, the initial misalignment, $\bar{\phi}$, was calibrated from the uniaxial quasi-static compression test, as was done in the previous sections, and the shear damage, $D_S[\tau,\dot{\gamma}]$, for each off-axis test case was approximated by the secant shear modulus from the Ramberg-Osgood nonlinear shear curves.

The resulting predictions, shown in Figure 5.23 below, agree remarkably well with the quasi-static experimental data for all off-axis test-cases but, based on the 10° dynamic test results, the dynamic predictions beyond 6° appear to be underestimated. However, this approach requires knowledge of progressive damage evolution and, based on the cyclic loading data from [48,57], the assumption that G_D equals to the secant modulus may result in overly conservative predictions. For illustrative purposes, the predicted envelopes assuming only 50% of damage to the shear modulus, indicated by the dotted lines in Figure 5.23, show how the predictions may change with different approximations of the shear damage.

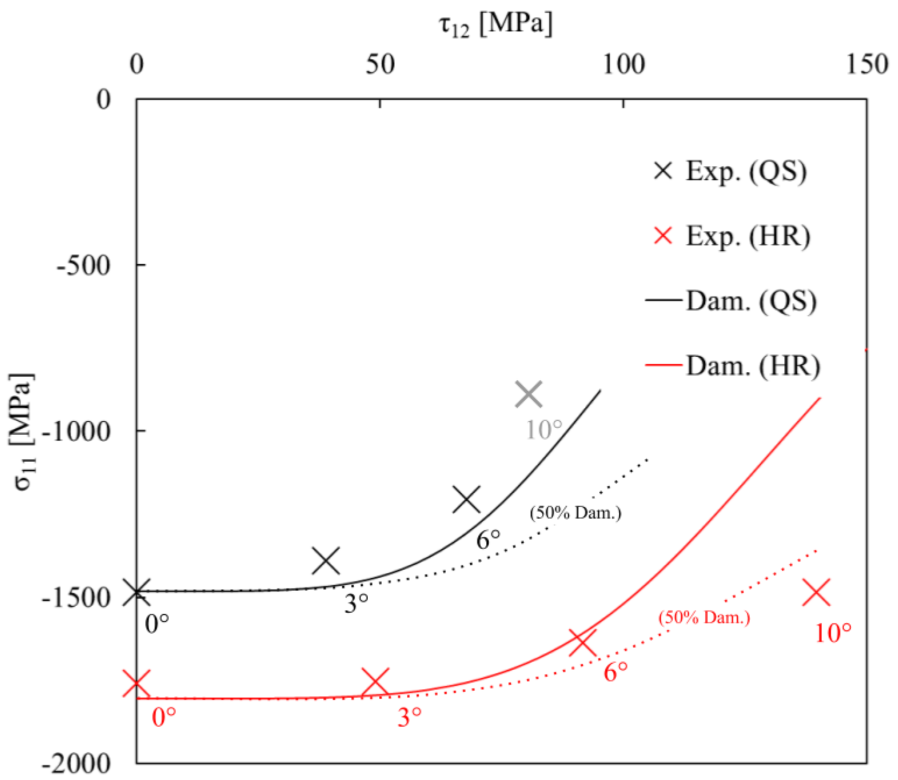

Figure 5.23. Predicted quasi-static and dynamic failure envelopes using proportional damaging of the shear modulus.

Following the positive initial results from the preliminary analysis above, the proposed criterion was implemented within the FE framework described in section 1.2 and coupled with the rate- and pressure-dependent constitutive model described in Chapter 3 for a more in-depth evaluation.

In this way, a more accurate representation of the stress states in the material could be obtained, as opposed to the analytical approximation obtained from the CLT, which only considered linear elastic behaviour. In addition, by using a multi-axial rate-dependent constitutive law for the nonlinear shear behaviour, both the uniaxial kinking strength, $\sigma_{C0}[\dot{\gamma}]$, and the off-axis damage, $D_S[\tau, \dot{\gamma}]$, in the proposed fibre kinking criterion automatically become pressure-dependent as well as rate-dependent.

The following section describes the implementation of the proposed criterion with the strength derived from the constitutive model in Chapter 3 instead of the Ramberg-Osgood relations used until this point.

5.2.5.5. Numerical implementation

In order to fully couple the proposed fibre kinking model with the developed LP plasticity model described in section 3.2, both the analytical solution for uniaxial compression strength, σ_{C0}, and the shear damage, D_S, under multi-axial loading need to be defined as a function of the constitutive nonlinear shear behaviour.

In Chapter 3, the material nonlinearity has been modelled as plastic deformation instead of damage due to lack of cyclic loading data for damage calibration. However, as previously mentioned, the literature suggests that at least part of the inelastic response is caused by damage to the shear modulus. This potential limitation was already identified in section 3.2.5 and should be addressed in the future, either through a cyclic or reverse loading experimental campaign or micromechanical modelling.

Lacking a direct measure for the damage, D_S, within the constitutive model, the expression shown below in eqn. (5.15), was found to approximate the secant modulus remarkably well as a function of the effective stress from the LP model in section 3.2, the yield stress, and the in-plane shear strength.

$$D_S[\tilde{\boldsymbol{\sigma}}, \bar{\varepsilon}_p, \dot{\bar{\varepsilon}}] = \frac{(\tau_Y[\bar{\varepsilon}_p] - A)\, r_y[\dot{\bar{\varepsilon}}]}{S_{12}\, r_y[\dot{\bar{\varepsilon}}] - \alpha\sigma_n} \tag{5.15}$$

where the numerator represents the amount of hardening from the initial yield strength, $A = \tau_{y0}$, from the LP plasticity model as defined in section 3.2, and the denominator is the rate-dependent shear strength from the IFF criterion in section 4.3 with the included effects of pressure on the fracture plane by $\alpha\sigma_n$.

Using this formulation, the rate- and pressure-dependent nonlinear shear stress-strain curves can be approximated by $\tau_{12} = G_{12}\left(1 - D_S[\tilde{\boldsymbol{\sigma}}, \bar{\varepsilon}_p, \dot{\bar{\varepsilon}}]\right)\gamma_{12}$, where G_{12} is the rate-dependent shear modulus from section 3.1.1. Figure 5.24 shows the approximate shear curves compared against the experimental and extrapolated data for the different strain rates used in the previous sections, where the quality of the damage approximation can be observed.

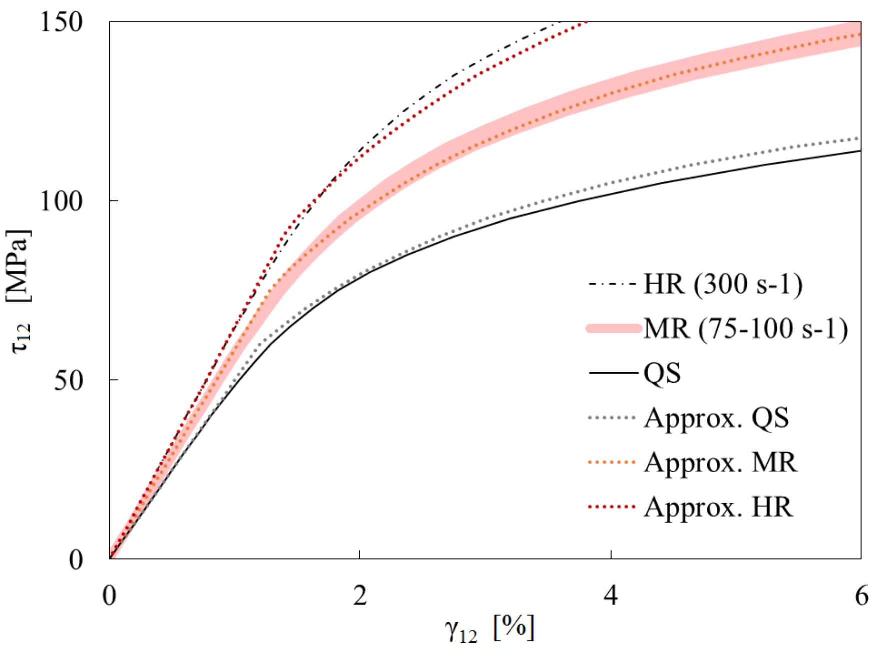

Figure 5.24. Rate-dependent nonlinear shear behaviour obtained using the damage approximation, eqn. (5.15), compared against the experimental and extrapolated data from Figure 5.19.

Finally, using this approximation, the uniaxial compression strength, σ_{C0}, was re-derived following the approach originally used by Fleck in [23,95]. However, by using a three-dimensional rate-dependent nonlinear shear model instead of the simple Ramberg-Osgood relation, the solution becomes pressure- and rate-dependent as well.

$$\sigma_{C0}[\tilde{\boldsymbol{\sigma}}, \dot{\varepsilon}] = \frac{G_{12}}{\dfrac{\tau_U^*}{\tau_U^* + \tau_y^* - \tau_C} + \dfrac{\bar{\phi}}{\gamma_y^*}\dfrac{\tau_y^*}{\tau_C}} \tag{5.16}$$

where τ_C is the critical shear stress for fibre kinking instability derived following the approach used in by Fleck in [23,95],

$$\tau_C[\tilde{\boldsymbol{\sigma}}, \dot{\varepsilon}] = \left(\tau_U^*[\tilde{\boldsymbol{\sigma}}, \dot{\varepsilon}] + \tau_y^*[\tilde{\boldsymbol{\sigma}}, \dot{\varepsilon}]\right) \frac{\sqrt{\tau_U^*[\tilde{\boldsymbol{\sigma}}, \dot{\varepsilon}]\; G_{12}\; \bar{\phi}} - G_{12}\; \bar{\phi}}{\tau_U^*[\tilde{\boldsymbol{\sigma}}, \dot{\varepsilon}] - G_{12}\; \bar{\phi}} \tag{5.17}$$

For clarity in the above equations, the rate- and pressure-dependent yield and ultimate shear strength properties are expressed as $\tau_y^*[\tilde{\boldsymbol{\sigma}}, \dot{\varepsilon}] = \mathrm{A}\, r_y[\dot{\varepsilon}] - \alpha\sigma_N$ and $\tau_U^*[\tilde{\boldsymbol{\sigma}}, \dot{\varepsilon}] = S_{12}\, r_y[\dot{\varepsilon}] - \alpha\sigma_n$, and $\gamma_y^* = \tau_y^*/G_{12}$ represents the strain at yield. As previously stated, here $A = \tau_{y0}$ is the initial quasi-static yield strength from the LP plasticity model as defined in section 3.2, and G_{12} is the rate-dependent shear modulus from section 3.1.1.

Having defined both terms as a function of the LP model from section 3.2, the longitudinal compression strength can be obtained by $\sigma_C = \sigma_{C0}(1 - D_S)$ and the failure condition for fibre kinking under multiaxial loading can therefore be written as:

$$f_{FK} = \frac{\sigma_{1c}}{\sigma_c\left[\tilde{\boldsymbol{\sigma}}, \bar{\varepsilon}_p, \dot{\varepsilon}\right]} = \frac{\sigma_{1c}}{\sigma_{co}[\tilde{\boldsymbol{\sigma}}, \dot{\varepsilon}]\left(1 - D_S\left[\tilde{\boldsymbol{\sigma}}, \bar{\varepsilon}_p, \dot{\varepsilon}\right]\right)} \geq 1 \tag{5.18}$$

where, σ_{1C} is the compression stress in the longitudinal direction, meaning values of $\sigma_{11} < 0$, and σ_{C0} and D_S are defined by eqn. (5.16) and (5.15), respectively.

5.2.6. Conclusions

In order to investigate the longitudinal compression failure mode, more reliable strength data, in particular for dynamic and off-axis loading conditions, was required. Following an initial test and specimen design optimisation campaign using IM7/8552 laminates, the use of cross-ply specimens was found to produce more reliable strength measurements than the traditionally used thick UD specimens.

Using cross-ply IM7/8552 specimens of this kind, a series of quasi-static and dynamic off-axis longitudinal compression tests were carried out to obtain experimental data on the effects of strain rate and off-axis loads on the fibre kinking strength. To do so, specimens were prepared at 0°, 3°, 6°, 10° and 15° with respect to the orientation of the external plies and tested in compression using a Zwick UTM at quasi-static loading rates and a SHPB at rates between 75 and 100 s^{-1}.

The results showed a significant increase in strength under dynamic loading, which decreased gradually as the off-axis angle and, therefore, the in-plane shear increased.

This data was then used to evaluate some of the leading failure criteria [18,23,62,95,140], showing that, when coupled with rate-dependent nonlinear in-plane shear properties, they were able to accurately predict the effects of strain rate on the longitudinal compression strength. However, the physically-based kinking theory was unable to capture the effects of shear, indicating a need for better understanding of the micromechanics of kink band formation under multiaxial loads.

Therefore, until better knowledge of the micromechanics of kink band formation is obtained and the physically-based theories can be updated, a simpler more phenomenological approach is recommended for better predictions of the compression strength of FRP laminates under multiaxial loads.

The proposed approach is derived from an alternative assumption regarding the kinematics of the fibre waviness under off axis loads, where the effect of remote shear loads on the critical misalignment angle is considered negligible. As a result of this assumption, a simplified failure criterion has been proposed that consists in using a measure of the shear damage to degrade the uniaxial compression strength as a way to account for the effect of off-axis stresses on the nonlinear shear properties of the kink band.

Finally, the proposed criterion was coupled with the rate- and pressure-dependent constitutive model from Chapter 3 and implemented within the material model developed throughout this work. To do so, both the shear damage and the uniaxial compression strength were derived from the physically-based LP model developed in section 3.2, so that all resulting multi-axial and rate effects on the kinking strength are directly related to the matrix-dominated nonlinear shear behaviour of the composite.

Next, having investigated the underlying constitutive behaviour in Chapter 3 and each of the failure criteria for the major failure modes in Chapter 4 and Chapter 5, a series of damage evolution laws were necessary in order to complete the material model. The implemented smeared damage formulation is described in following chapter.

Chapter 6

Damage evolution

While the focus of the present work was on the constitutive modelling and failure criteria, damage modelling is crucial in applications where it is important to predict not only whether any part of a component will fail but also how such potential failure might evolve and affect the rest of the structure. To meet jet engine certification standards, for example, it is necessary to ensure that, in the case of bird strike, failure be contained within the engine and that it result in a permissible amount of power loss [153,154].

Therefore, within the modelling framework described in section 1.2, every time step, the possibility of failure initiation must be checked within the material subroutine for each of the possible failure modes and, if the conditions for any of them are met, a stress degradation law must be defined to dictate the evolution of damage until complete failure.

As reviewed in section 2.2, various damage modelling solutions have been used to successfully describe failure propagation in UD CFRPs [18,109–111,155–158]. Out of these, the smeared formulation proposed by Pinho in [18] was recently used by Hoffmann to study the effects of strain rate of the fracture energy and damage evolution [72]. Therefore, a similar approach has been adopted here.

This type of formulation has been described extensively in [18,62,72] and no major new developments have been made in the present work but, for the sake of completeness, a brief summary of the implemented damage evolution laws is given below.

6.1. Smeared damage formulation

Essentially, in this formulation, damage is defined in such a way as to produce a linear stress degradation from the onset of failure to the point of complete failure, as shown in Figure 6.1. The degradation path is calculated in terms of an effective traction and an effective displacement acting on the fracture plane, with the rate of degradation defined by the fracture area and the fracture toughness, G_C, associated with the relevant failure mode.

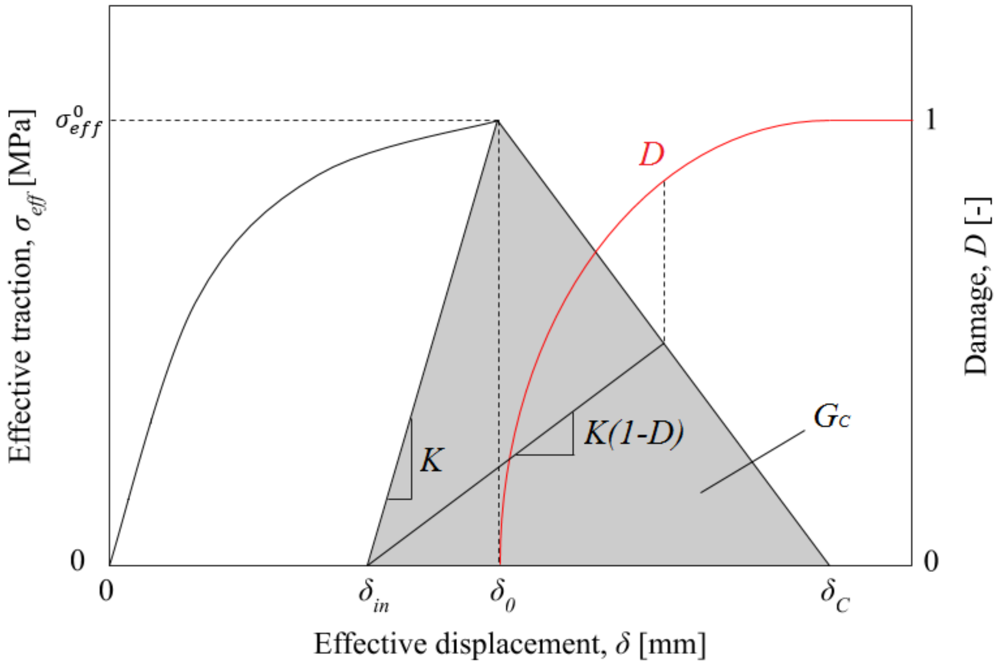

Figure 6.1. Illustration of the smeared damage formulation proposed for UD CFRPs by Pinho in [18].

The damage variable, D, that defines this path for each of the failure modes is given by:

$$D = \frac{\delta_C\,(\delta^* - \delta_0)}{\delta^*(\delta_C - \delta_0)} \quad \text{with} \quad \delta^* = \begin{cases} \delta^* = \delta & \text{for } \delta_{in} = 0 \\ \delta^* = \delta - \delta_{in} & \text{for } \delta_{in} > 0 \end{cases} \tag{6.1}$$

where δ^* are the effective displacements, determined from the effective driving strain, ε_{eff}, and the characteristic element length, l_C, as $\delta^* = l_C \varepsilon_{eff}$. Here l_C is introduced as a measure of the fracture area in the element along the predicted fracture plane to alleviate mesh dependency issues [62,159].

$$A_C = \frac{V}{l_C} \tag{6.2}$$

where A_C is the fracture area and V is the element volume.

This damage variable, D, can then be used to degrade the strength and stiffness of the material by multiplying the undamaged stress components relevant to each failure mode investigated as:

$$\widehat{\boldsymbol{\sigma}}^D = \widehat{\boldsymbol{\sigma}}\,(1 - \boldsymbol{D}) \tag{6.3}$$

where $\boldsymbol{D}$ contains the damage variables developed by each one of the failure modes: fibre tension D_{FT}, fibre kinking D_{FK} and inter fibre failure D_{IFF}.

For all damage modes, to determine the damage, D, from eqn. (6.1), the initial effective displacement δ_0 and stress σ_{eff}^0 are recorded at the onset of failure and δ_{in} is computed with σ_{eff}^0/K. The ultimate effective displacement at complete failure, δ_C, is then calculated as:

$$\delta_C = \frac{2G_c}{\sigma_{eff}^0} \tag{6.4}$$

where σ_{eff}^0 is the effective traction at the onset of failure and G_C is the relevant fracture toughness for each failure mode.

Once the effective displacement reaches δ_C, all of the fracture energy is considered to have been released. Therefore, the element can be considered fully damaged and is removed from the computation to avoid numerical instabilities.

However, this smeared damage approach does have an important limitation in that the fracture energy across the total fracture area within an element, $G_c A_C$, must be greater than the elastic strain energy at the onset of damage, $\frac{1}{2}V\sigma\varepsilon$, to prevent unphysical dissipation. Therefore, in practical terms there is a limit on the element dimensions in order to ensure that for each failure mode, M, there is a large enough fracture area:

$$l_C = \frac{V}{A_C} < \frac{2G_{c,M}E_M}{(\sigma^0_{eff,M})^2} \tag{6.5}$$

where $2G_{c,M}$, E_M, and $\sigma^0_{eff,M}$ are the fracture toughness, Young's modulus, and strength properties relevant to each failure mode, and the relation between the characteristic length, l_C, and the element dimensions depends on fibre direction and the orientation of the fracture plane, since these will dictate the relative fracture area.

For reference, using typical quasi-static IM7/8552 material properties and a mesh aligned with the material coordinate system, the fibre failure properties determine the maximum element length in the fibre direction, of approximately 3 mm, while the IFF properties determine the maximum width in the transverse direction, of almost 0.5 mm. Above these dimensions the model may become unstable or result in excessive dissipation.

Finally, having outlined the general formulation above, all that remains in order to complete the damage model is to detail some of the particularities for each of the main failure modes, such as the definitions of σ_{eff}, ε_{eff}, and G_C, for each case, which are described in the following sections.

6.2. IFF damage evolution

Within the generic smeared formulation from the previous section, a number of particularities for the specific case of IFF damage are given below.

First of all, in this case, the effective tractions and strains that drive the failure process are defined as a function of the stress and strain components on the fracture plane by:

$$\sigma_{eff} = \sqrt{\sigma_n^2 + \tau_{n1}^2 + \tau_{nt}^2} = \sqrt{\sigma_n^2 + \tau_{eff}^2} \quad (6.6)$$

$$\varepsilon_{eff} = \sqrt{\varepsilon_n^2 + \gamma_{n1}^2 + \gamma_{nt}^2} = \sqrt{\varepsilon_n^2 + \gamma_{eff}^2} \quad (6.7)$$

where σ_n and ε_n are the components normal to the fracture plane, and τ_{eff} and γ_{eff} are the effective shear components. Here the driving strains must include only the elastic portion of the strain so as to accurately represent the elastic energy released during crack propagation, illustrated by the highlighted area in Figure 6.1.

Next, since the fracture plane for this mode is given by the angle, theta, around the fibre direction, the characteristic element length, l_C, is calculated to reflect the finite element's dimension orthogonal to the fracture plane [19].

$$l_C = \max(|p_{17}|, |p_{28}|, |p_{35}|, |p_{46}|) \quad (6.8)$$

where $\boldsymbol{p}_{ij}$ are the projections of the element diagonals onto the vector normal to the fracture plane, obtained by:

$$\boldsymbol{p}_{ij} = \boldsymbol{n'}_i - \boldsymbol{n'}_j \quad (6.9)$$

$$\boldsymbol{n'}_i = \text{proj}_{\boldsymbol{s}}\boldsymbol{n}_i = \frac{\boldsymbol{n}_i \cdot \boldsymbol{s}}{|\boldsymbol{s}|^2} \quad (6.10)$$

Here the vectors $\boldsymbol{n'}_i$ are defined as the projections the node positions in global coordinates, $N_i[x\ y\ z]$, onto the vector $\boldsymbol{s}$ that defines the normal to the fracture plane, with $\boldsymbol{n}_i = \overrightarrow{ON_i}$ where O is the origin of the global reference frame.

In addition, since failure can occur by opening, shearing, or a combination of the two, a measure of the mixed mode fracture toughness is used to determine the ultimate displacement. This is computed from the mode I, or opening, and mode II, or shear, energies depending on the direction of the tractions acting on the fracture plane:

$$G_{C,IFF} = \begin{cases} \dfrac{G_{IC}G_{IIC}(1+\eta^2\lambda)}{G_{IIC}+G_{IC}\eta^2\lambda} & \text{for } \gamma_{eff} \neq 0 \\ G_{IIC} & \text{for } \gamma_{eff} = 0 \end{cases} \tag{6.11}$$

where G_{IC} and G_{IIC} are the mode I and mode II fracture toughness, respectively, γ_{eff} is the effective shear strain on the fracture plane, η is the mixed mode ratio, and $\lambda = E_2/G_{12}$ is the stiffness ratio between opening, transverse, and shear moduli.

Finally, with the previous definitions, the damage variable for IFF, D_{IFF}, can be obtained following eqn. (6.1). This is then applied to the localisation plane tractions in the following manner so that the stiffness in compression normal to the fracture plane is not affected:

$$\sigma_n^D = \sigma_n \left(1 - D_{FT}\frac{\langle\sigma_n\rangle}{\sigma_n}\right) \tag{6.12}$$

$$\tau_{n1}^D = \tau_{n1}\,(1 - D_{IFF}) \tag{6.13}$$

$$\tau_{nt}^D = \tau_{nt}\,(1 - D_{IFF}) \tag{6.14}$$

which are then rotated by $\hat{\boldsymbol{\sigma}}^D = \boldsymbol{R}_\sigma\left[-\theta_y\right]\hat{\boldsymbol{\sigma}}_\theta^D$ to obtain the damaged stress components in material coordinates.

6.3. Fibre damage evolution

In the case of fibre failure, whether by tension or compression, the procedure is greatly simplified. First of all, in both cases, the driving effective tractions and strains are simply given by the respective longitudinal components:

$$\sigma_{eff} = |\hat{\sigma}_{11}| \tag{6.15}$$

$$\varepsilon_{eff} = |\hat{\varepsilon}_{11}| \tag{6.16}$$

The characteristic length is again obtained by projecting the element diagonals onto the fracture plane normal, however in this case the vector is known to be the longitudinal, 1, direction. In the case of fibre kinking failure, the fracture plane could be defined instead by the kink band angle, beta, typically assumed to be around 30°.

Next, since the fracture toughness for fibre failure is orders of magnitude greater than the values for matrix shearing or opening, mixed mode effects can be ignored:

$$G_{C,FF} = \begin{cases} G_{FT} & \text{for} \quad \hat{\varepsilon}_{11} > 0 \\ G_{FT} & \text{for} \quad \hat{\varepsilon}_{11} < 0 \end{cases} \tag{6.17}$$

Finally, the obtained damage variables, D_{FT} for fibre tension and D_{FK} for compression, are used to degrade the stress components in material coordinates. In both cases, fibre damage is assumed to affect the transverse and shear components. However, for fibre tension failure, the stiffness in the longitudinal direction is preserved under compression while, for fibre kinking failure it is degraded along with the other components.

For fibre tension damage this can be written as:

$$\hat{\sigma}_{ii}^{D} = \hat{\sigma}_{ii}\left(1 - D_{FT}\frac{\langle\hat{\sigma}_{ii}\rangle}{\hat{\sigma}_{ii}}\right) \text{ for } i = 1,2,3 \tag{6.18}$$

to indicate that the normal components are not damaged under compression, and

$$\begin{Bmatrix} \hat{\tau}_{12}^{D} \\ \hat{\tau}_{23}^{D} \\ \hat{\tau}_{13}^{D} \end{Bmatrix} = (1 - D_{FT})\begin{Bmatrix} \hat{\tau}_{12} \\ \hat{\tau}_{23} \\ \hat{\tau}_{13} \end{Bmatrix} \tag{6.19}$$

to indicate the damage to the shear components.

Whereas, for fibre kinking damage this can be written as:

$$\begin{gathered} \hat{\sigma}_{11}^{D} = \hat{\sigma}_{11}(1 - D_{FK}) \\ \hat{\sigma}_{ii}^{D} = \hat{\sigma}_{ii}\left(1 - D_{FK}\frac{\langle\hat{\sigma}_{ii}\rangle}{\hat{\sigma}_{ii}}\right) \text{ for } i = 2,3 \end{gathered} \tag{6.20}$$

to indicate that only the longitudinal component, $\hat{\sigma}_{11}$, is damaged under compression, and

$$\begin{Bmatrix} \hat{\tau}_{12}^{D} \\ \hat{\tau}_{23}^{D} \\ \hat{\tau}_{13}^{D} \end{Bmatrix} = (1 - D_{FK}) \begin{Bmatrix} \hat{\tau}_{12} \\ \hat{\tau}_{23} \\ \hat{\tau}_{13} \end{Bmatrix} \tag{6.21}$$

to indicate the damage to the shear components.

With this, the implemented damage is fully defined for each for the three failure modes and the complete material model can be more thoroughly evaluated.

Chapter 7

Model validation and benchmarks

Having investigated each of the aspects of the material behaviour as set out in the initial objectives, the developed LP plasticity model from section 3.2 the rate-dependent IFF criterion from section 4.3, the fibre tension failure criterion in section 5.1 and the fibre kinking failure model from section 5.2 have been implemented as a user-defined material model for UD CFRPs in LS-DYNA, following the numerical modelling framework described in section 1.2, and coupled with a smeared damage formulation described in the previous chapter.

Each of the developed models and criteria is physically based, as the use of purely empirical methods has been avoided whenever possible. In addition, the IFF and fibre kinking models, as well as all the effects of pressure, multi-axial loading, and strain rate across all failure and deformation modes were derived from the matrix-dominated nonlinear shear model, limiting the number of independent assumptions and material parameters.

Therefore, the complete user material, summarized in Table 7.1 and 7.2, only requires calibration of the nonlinear shear properties, a single in-plane shear strength for the IFF criterion, and a single uniaxial compression strength from which initial fibre misalignment angle is obtained for the FK model. The original Puck IFF criterion was also implemented and calibrated in parallel, as the analysis in section 4.3 showed that the predictions derived from the LP plasticity model may be over conservative.

Table 7.1. Model summary table with the main constitutive equations and criteria.

Constitutive equations	**Eqn. #**
Localisation plane plasticity	
$f_y[\tilde{\boldsymbol{\sigma}}, \bar{\varepsilon}_p, \dot{\bar{\varepsilon}}] = \bar{\sigma}[\tilde{\boldsymbol{\sigma}}] - \tau_y[\bar{\varepsilon}_p] \cdot r_y[\dot{\bar{\varepsilon}}] = 0$	(3.16)
$\bar{\sigma}[\tilde{\boldsymbol{\sigma}}] = \alpha\sigma_n + \sqrt{{\tau_{n1}}^2 + e{\tau_{nt}}^2} = \alpha\sigma_n + \tau_{eff}$	(3.17)
$g[\tilde{\boldsymbol{\sigma}}] = \alpha_g\sigma_n + \sqrt{{\tau_{n1}}^2 + e_g{\tau_{nt}}^2}$	(3.19)
$\tau_y[\bar{\varepsilon}_p] = A + B_1(1 - e^{-C_1\bar{\varepsilon}_p}) + B_2(1 - e^{-C_2\bar{\varepsilon}_p})$	(3.22)
$r_y[\dot{\bar{\varepsilon}}] = 1 + \sqrt{K_y\dot{\bar{\varepsilon}}}$	(3.23)
IFF criterion (Puck)	
$f_{IFF} = \begin{cases} \sqrt{(1-p_t)^2\left(\frac{\sigma_n}{R_\perp^+}\right)^2 + \left(\frac{\tau_{n1}}{R_{\perp\parallel}}\right)^2 + \left(\frac{\tau_{nt}}{R_{\perp\perp}^A}\right)^2} + p_t\frac{\sigma_n}{R_\perp^+} \geq 1 & \text{for } \sigma_n \geq 0 \\ \sqrt{\left(p_c\frac{\sigma_n}{R_{\perp\psi}^A}\right)^2 + \left(\frac{\tau_{n1}}{R_{\perp\parallel}}\right)^2 + \left(\frac{\tau_{nt}}{R_{\perp\perp}^A}\right)^2} + p_c\frac{\sigma_n}{R_{\perp\psi}^A} \geq 1 & \text{for } \sigma_n < 0 \end{cases}$	(4.1)
IFF criterion (simplified)	
$f_{IFF} = \frac{\bar{\sigma}[\tilde{\boldsymbol{\sigma}}]}{S_{12}r_f[\dot{\bar{\varepsilon}}]} = \frac{\alpha\sigma_n + \sqrt{{\tau_{n1}}^2 + e{\tau_{nt}}^2}}{S_{12}r_f[\dot{\bar{\varepsilon}}]} \geq 1$	(4.4)
Fibre tension failure criterion	
$f_{FT} = \frac{\sigma_{1T}}{X_T} \geq 1$	(5.2)
Fibre kinking failure criterion	
$f_{FK} = \frac{\sigma_{1c}}{\sigma_c[\tilde{\boldsymbol{\sigma}}, \bar{\varepsilon}_p, \dot{\bar{\varepsilon}}]} = \frac{\sigma_{1c}}{\sigma_{co}[\tilde{\boldsymbol{\sigma}}, \dot{\bar{\varepsilon}}](1 - D_S[\tilde{\boldsymbol{\sigma}}, \bar{\varepsilon}_p, \dot{\bar{\varepsilon}}])} \geq 1$	(5.18)
Damage evolution	
$D = \frac{\delta_C\,(\delta^* - \delta_0)}{\delta^*(\delta_C - \delta_0)} \quad \text{with} \quad \delta^* = \begin{cases} \delta^* = \delta & \text{for } \delta_{in} = 0 \\ \delta^* = \delta - \delta_{in} & \text{for } \delta_{in} > 0 \end{cases}$	(6.1)
$\hat{\boldsymbol{\sigma}}^D = \hat{\boldsymbol{\sigma}}\,(1 - \boldsymbol{D})$	(6.3)
$\delta_C = \frac{2G_c}{\sigma_{eff}^0}$	(6.4)
$G_{C,IFF} = \begin{cases} \frac{G_{IC}G_{IIC}(1+\eta^2\lambda)}{G_{IIC} + G_{IC}\eta^2\lambda} & \text{for } \gamma_{eff} \neq 0 \\ G_{IIC} & \text{for } \gamma_{eff} = 0 \end{cases}$	(6.11)
$G_{C,FF} = \begin{cases} G_{FT} & \text{for} \quad \hat{\varepsilon}_{11} > 0 \\ G_{FT} & \text{for} \quad \hat{\varepsilon}_{11} < 0 \end{cases}$	(6.17)

Table 7.2. IM7/8552 model calibration data. Elastic and plastic properties obtained through numerical optimisation using single element models, and strength and damage properties from in-house tests and literature data.

Property / Parameter			**Value**	**Source**
Elastic properties	Stiffness	E_{11T}	160 GPa	Calibrated from [44]
		E_{11C}	140 GPa	“
		$E_{22} = E_{33}$	8000 MPa	“
		$G_{12} = G_{13}$	4000 MPa	“
		G_{23}	2150 MPa	“
	Rate	K_C	1.5E-4	“
Plastic properties	Yield	τ_y	60 MPa	Calibrated from [44]
		α	0.1	“
		α_g	0.23	“
		e	0.9	“
		e_g	1	“
	Hardening	B_1	33	“
		C_1	130	“
		B_2	25	“
		C_2	10	“
	Rate	K_y	1E-3	“
Failure	IFF	S_{12}	95 MPa	Section 4.2, [44]
		Y_T	70 MPa	Section 4.2, [50]
	(Puck)	Y_C	250 MPa	Section 4.2, [44]
		θ_0	52°	Assumed, [44]
	FT	X_T	2724 MPa	[6]
	FK	X_C	1500 MPa	Section 5.2, [91,96]
		φ_0	1.5°	Calibrated from X_C
Damage	IFF	G_{IC_M}	0.2 N/mm	[65]
		G_{IIC_M}	0.66 N/mm	[160]
	FT	G_{C_FT}	82 N/mm	[75]
	FK	G_{C_FK}	100 N/mm	[79]

The model was calibrated for the UD IM7/8552 material used throughout this study with a combination of data from the literature and new test data presented in the previous chapters. The quasi-static and dynamic off-axis compression tests on UD IM7/8552 specimens in [44] were used to calibrate the nonlinear shear properties and the rate-dependent factor using the parameter optimisation software LS-OPT [161] with a series of single-element FE test cases. The baseline in-plane shear strength for IM7/8552 was extrapolated from the quasi-static off-axis compression tests in [44] and, finally, the quasi-static uniaxial compression strength from the tests in section 5.2 for the same IM7/8552 material was used to calibrate the fibre kinking model. In the case of the original Puck IFF criterion that was evaluated in parallel to the nonlinear shear derived criterion, the parameters were calibrated independently to fit the quasi-static envelope from [44], and throughout the model, a single rate-dependent factor, calibrated for the nonlinear shear model, was used for all rate-dependent behaviour and failure criteria.

For damage modelling, however, which has not been investigated in this project, fracture toughness and rate-dependency properties for each failure mode were taken directly from the literature.

With the above fully developed and calibrated material model for IM7/8552, a number of validation and benchmark tests are presented in the following sections.

Section 7.1 contains a more thorough validation of the overall FE implementation and each of the developed criteria is presented using the UD in-plane biaxial loading results from [44,50] and the CP off-axis longitudinal compression data obtained in section 5.2. These validation tests consist of a first set of FE models at different levels of mesh refinement to verify the mesh-independence of the solution and, second, a series of full-scale FE models of the specimen and test conditions to compare against the experimental stress-strain curves.

Following the validation, section 7.2 contains a series of more extreme test cases carried out in order to benchmark the model’s performance for potential large-scale industrial applications where it may be pushed to or beyond its limits. This includes the extrapolation of material properties to strain rates above what the model was developed and calibrated for and other concessions such as the omission of interface elements for delamination or the use of element sizes beyond the recommended limit given in Chapter 6. For this purpose, a series of ballistic impact tests were performed on IM7/8552 laminate plates at velocities between around 50 to 100 m/s and compared against these simplified FE simulations using the material model developed throughout this work.

7.1. Model validation: off-axis loading tests

Before evaluating the model’s performance against the experimental data, however, a series of off-axis compression tests was modelled using different levels of mesh refinement to verify the convergence and mesh independence of the implemented nonlinear shear model in particular.

First, a 0.25 mm cubic block of material was meshed with a single element, 4x4x8 elements, and 4 x 4 x 16 elements to test different element sizes and aspect ratios. Nodal constraints and prescribed displacements were applied in order to define the test conditions and the material coordinate system was defined at different off-axis angles for different test cases.

In addition, a 20 x 10 x 4 mm^3 compression specimen like the one used in [44], was modelled with two different levels of mesh refinement, one using 0.2 mm cubic elements and another using 0.5 mm cubic elements. For more realistic boundary conditions, the relative displacement was applied through two rigid walls with a 0.2 friction coefficient, one fixed at one end of the specimen and the other with a prescribed displacement in compression. The meshes used in each of these cases are shown in Figure 7.1.

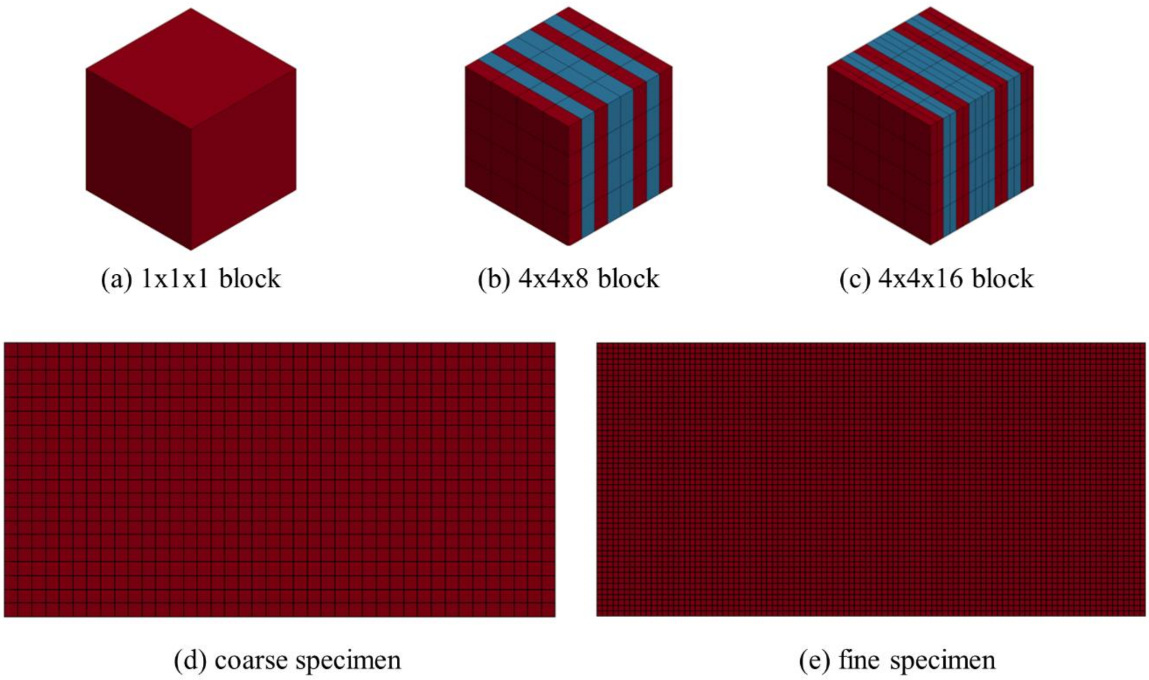

Figure 7.1. Different mesh refinements used for the convergence and mesh independence study.

Some difference was to be expected between the block and specimen simulations due to the different geometry and boundary conditions. However, the results were still remarkably close across all tests regardless of model geometry and mesh refinement, as can be seen in Figure 7.2 for the 45° and 60° tests.

The small discrepancy observed at greater strains was found to be due to the differences in geometry and boundary conditions, which resulted in different amounts of rotation between the full specimen and the block model, affecting the axial stiffness.

Therefore, these results can be used to establish the convergence and mesh independence of the implementation. In addition, since element size and aspect ratio have been shown to have minimal impact on the results, simplified models of the specimen geometry and boundary conditions can be used in the following sections.

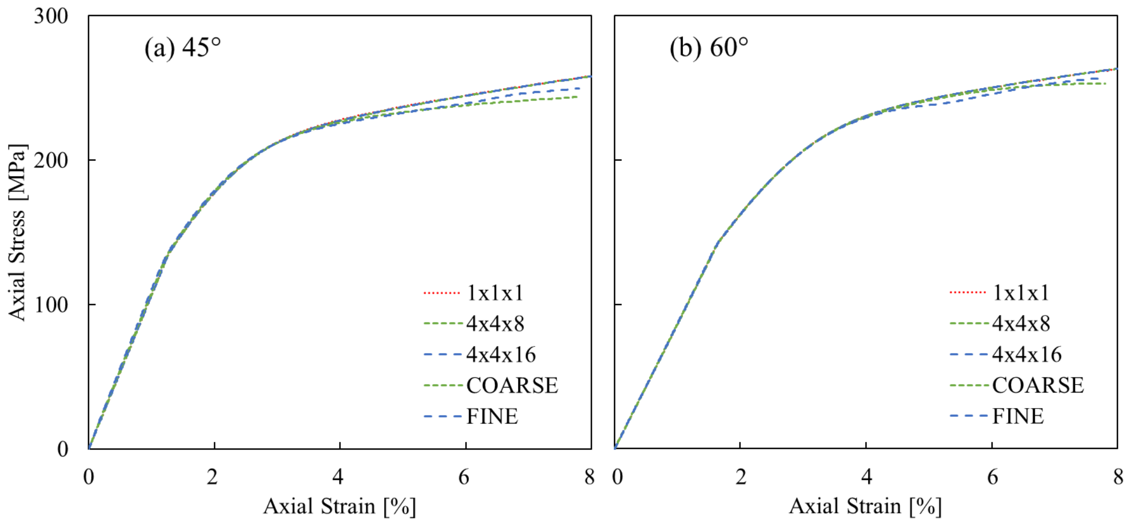

Figure 7.2. Comparison between stress-strain results for different UD off-axis compression test cases across different mesh refinements.

In addition, a closer look at the results from the fine mesh full specimen simulations in Figure 7.3 shows strain localisation starting before IFF failure. These predictions are in good agreement with observations by Koerber in [44], both in terms of the existence of such localisation behaviour before fracture and in their orientations, showing the model's ability to capture the deformation mechanisms at a small scale as well as the macro-scale stress-strain response.

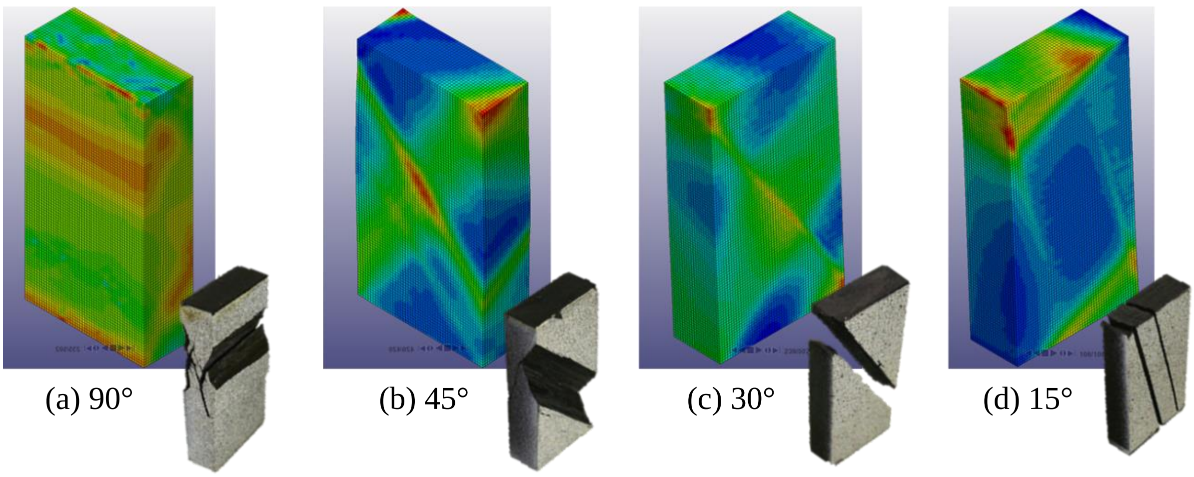

Figure 7.3. Strain localisation predicted in different off-axis compression simulatinons compared against the fracture planes observed in failed specimen images extracted from [44].

Finally, with confidence in the numerical implementation, a more exhaustive validation of the complete model was carried out, presented in the following sections, starting with the IFF tests from Koerber [44,50] and then the fibre kinking tests from section 5.2.

7.1.1. Nonlinear behaviour and IFF strength

For the validation of the developed LP plasticity model and IFF criteria, the full set of in-plane biaxial load tests from [44,50] was used instead of the in-house data obtained in section 5.2, since these sources provided additional off-axis test cases. The work by Koerber et al. in [44] gives axial stress-strain curves for quasi-static and dynamic off-axis compression tests on 20 x 10 x 4 mm^3 UD IM7/8552 specimens with off-axis angles of 15°, 30°, 45°, 60°, 75° and 90°. To complement this, Koerber et al. [50] carried out a series of quasi-static and dynamic off-axis tension tests on 62 x 8 x 1.5 mm^3 UD specimens with a free length of 20 mm at off-axis angles of 15°, 30°, 45° and 90°.

Having shown that mesh size and aspect ratio did not significantly affect the results, the specimen geometry for each test was modelled using large 1 x 1 x 0.125 mm^3 elements, with the 0.125 mm thickness corresponding to the nominal ply thickness, as shown in Figure 7.4. One reason for this was to validate the model under the type of conditions in which it will be used for larger scale simulations, where coarse elements with a poor aspect ratio like these are often necessary for the sake of computational cost.

For both tension and compression tests, the loading conditions were applied by fixing nodal displacements in the axial direction at one end of the specimen and applying prescribed displacements with a velocity and direction corresponding to each test at the other end. To represent the different specimen orientations, different material coordinate systems were defined, corresponding to each of the tested off-axis angles.

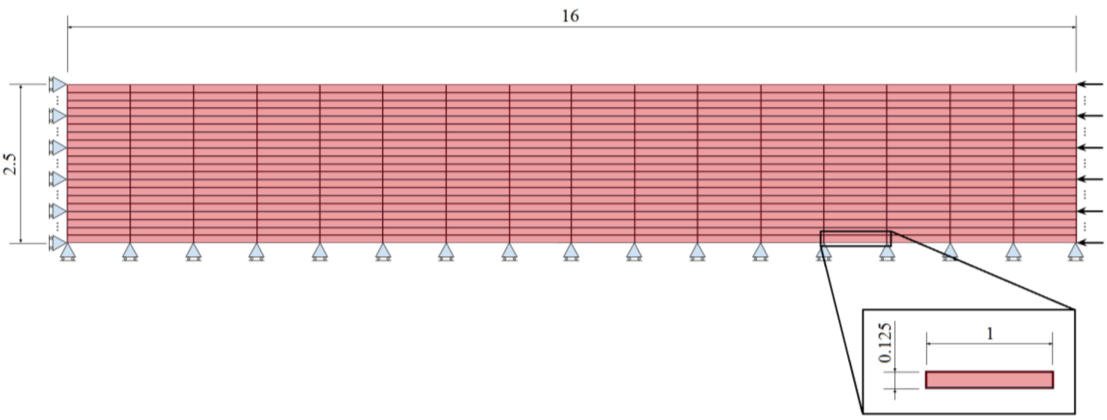

Figure 7.4. Side view of the simplified 16 x 8 x 2.5 mm^3 FE mesh used to model the UD IM7/8552 specimens for the off-axis transverse compression tests.

The results of the off-axis compression simulations are shown in Figure 7.5 below, showing that, overall, the nonlinear behaviour is captured extremely well across all tests. The only exception is the dynamic 15° test. However, for the 15° tests, Koerber noted in [44] that stick-slip behaviour was observed due to excessive friction, which would explain the noise in the test results and the higher than expected stiffness.

While the performance of the LP plasticity model could be expected having seen the previous tests before this point, the IFF criteria have not yet been thoroughly validated against the raw axial stress-strain data.

The curves shown in Figure 7.5, were obtained using the original Puck IFF criterion, as it tended to give higher strength predictions, so that the drop-off at failure indicates the original Puck IFF strength whereas circle marks indicate the strength predictions derived from the LP plasticity model.

As expected from the work in section 3.2, the LP-based IFF predictions slightly underestimate the strength in the 30° and 45° test cases compared to original Puck criterion. However, in these higher fidelity models, the results are not as far apart as they appeared from the initial comparison of the failure envelopes, indicating that this approach could well be used without as big an impact on the resulting predictions.

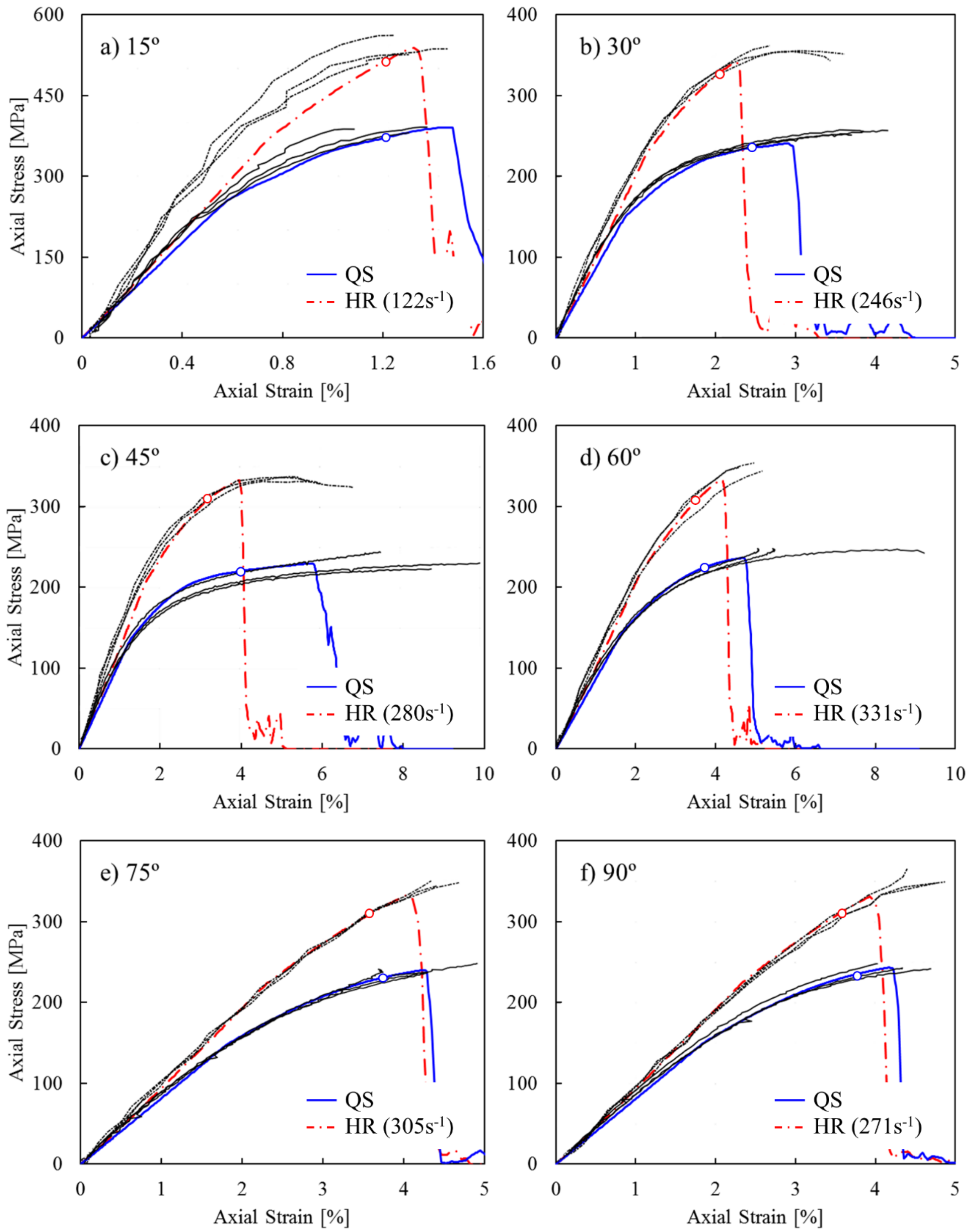

Figure 7.5. Predicted axial stress-strain curves for each of the off-axis transverse compression specimens at quasi-static and dynamic loading rates compared against experimental data from [44]. Circle marks indicate the strength predictions derived from the LP plasticity model in section 3.2.

However, as some of the tests showed significant nonlinear behaviour and plateauing stresses, with the use of stress-based criteria, small variations in strength properties resulted in large variations in strain to failure. Therefore, while both criteria were able to predict the ultimate axial stresses within a small margin of error, they failed to capture the ultimate strains with as much accuracy, indicating that strain-based instead of stress-based criteria may be more suitable for this material.

For the off-axis tension tests, the results of the simulations are shown in Figure 7.6 below against the axial stress-strain data from [50]. In tension, the predicted strengths using the original Puck IFF and the LP derived IFF criteria were practically identical, so only one set of results is shown.

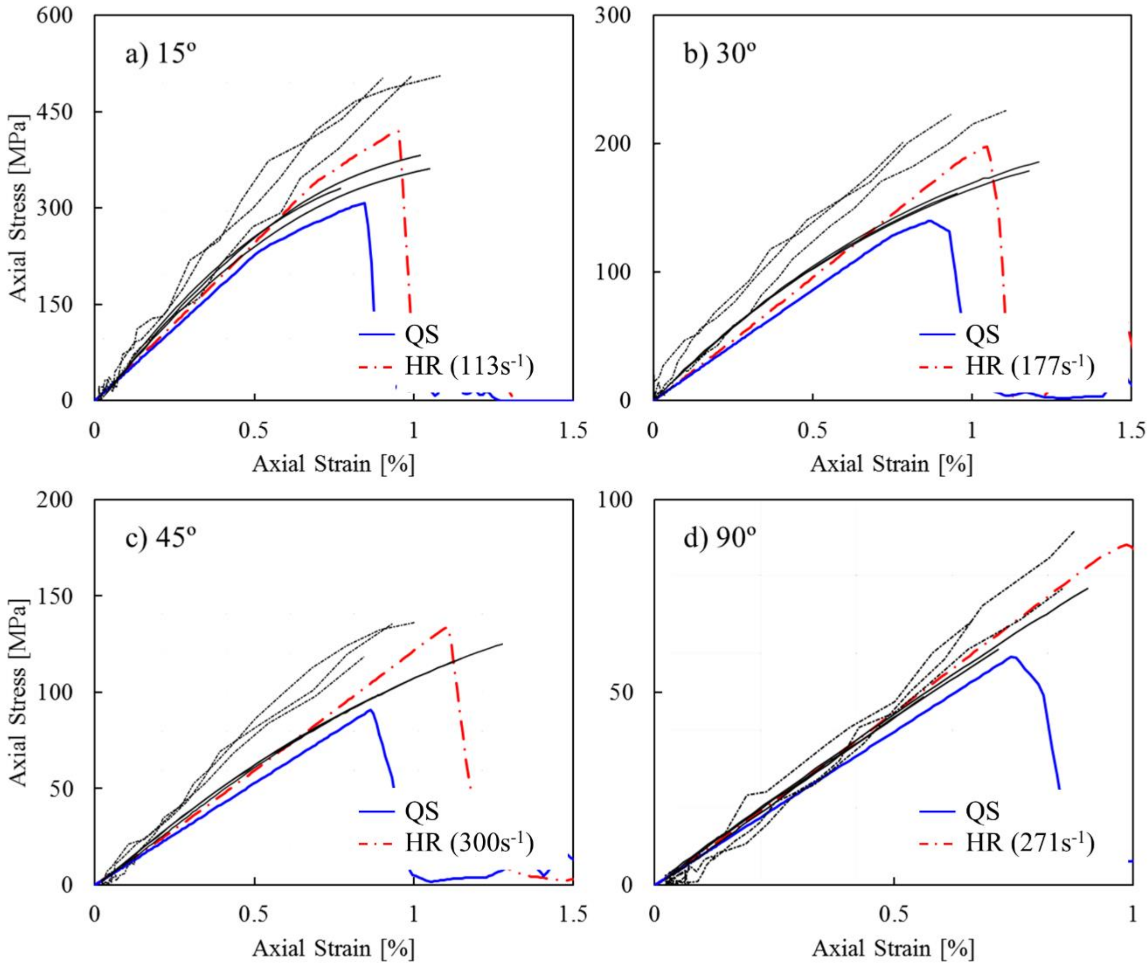

Figure 7.6. Predicted axial stress-strain curves for each of the off-axis transverse tension tests compared against quasi-static and dynamic data from [50].

Overall, the degree of nonlinearity across the different tests is fairly well captured. However, as the material properties were calibrated from the off-axis compression tests, the transverse stiffness modulus appears to have been underestimated, which should be easily correctible with a more extensive calibration campaign.

As for the axial strength predictions, quasi-static IFF failure in tension appears to be slightly under-predicted for both criteria. While the predictions match average measured strength for the 90° case, the transverse tension strength may have been underestimated due to the large experimental scatter in the results.

Overall, in spite of some minor calibration issues, the developed model has been shown to produce very good predictions for the nonlinear shear behaviour and IFF across a number of different off-axis test cases, even when using a coarse mesh with poor aspect ratios and simplified boundary conditions, as shown in Figure 7.5 and Figure 7.6.

7.1.2. Fibre kinking strength

Having validated the developed model for the prediction of the nonlinear behaviour and IFF, the off-axis longitudinal compression tests from section 5.2 were simulated to evaluate the model's ability to predict fibre kinking failure.

While the initial development of the fibre kinking criterion in section 5.2 was done using an implementation in MATLAB with data obtained from linear CLT, the following FE analysis should provide more accurate stress states for the material in the longitudinal and transverse plies and, therefore, a more accurate evaluation of the proposed model.

As in the previous section, a simplified specimen geometry and boundary conditions were used to represent the off-axis cross-ply specimens. These were meshed using the same large 1 x 1 x 0.125 mm^3 elements, but, due to the coarse mesh size, only the central gauge section was modelled, as shown in Figure 7.7. Again, in the same way as for the previous section, the nodes at one end of the specimen were fixed in the axial direction while at the opposite end prescribed displacements at the average relative velocity between input and output bars were applied for each of the test cases.

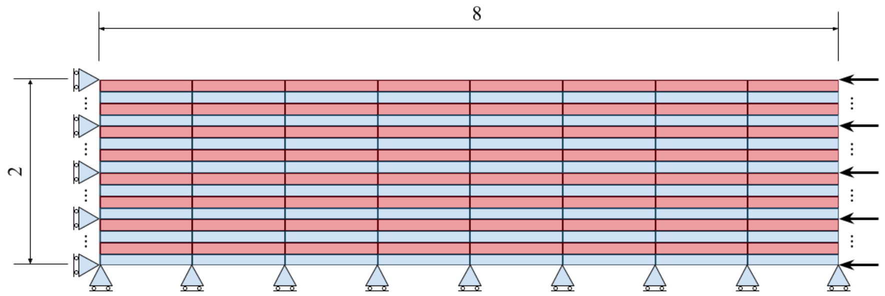

Figure 7.7. Side view of the simplified 8 x 4 x 2 mm^3 FE mesh used to model the CP IM7/8552 specimens for the off-axis compression tests.

Only half of the specimen was modelled, taking advantage of the laminate symmetry, and the different material orientations for the longitudinal and transverse plies in each test case were applied using different sets of coordinate systems.

A comparison between the stress-strain curves from the simulations and from the quasi-static and dynamic experiments is shown in Figure 7.8.

As in the preliminary analysis in section 5.2, the new FEA predictions were, again, in very good agreement with the experimental data in the 0° to 6° test cases, before any significant nonlinearity was observed, falling within the experimental scatter in all cases.

For the 10° case, the predicted envelope in section 5.2 slightly overestimated the quasi-static strength while severely underestimating the dynamic strength. In these results, the quasi-static strength is again slightly overestimated, but the dynamic strength is much closer to the experimental curves, possibly due to the more accurate representation of the stress state in the material and the fully rate-dependent implementation.

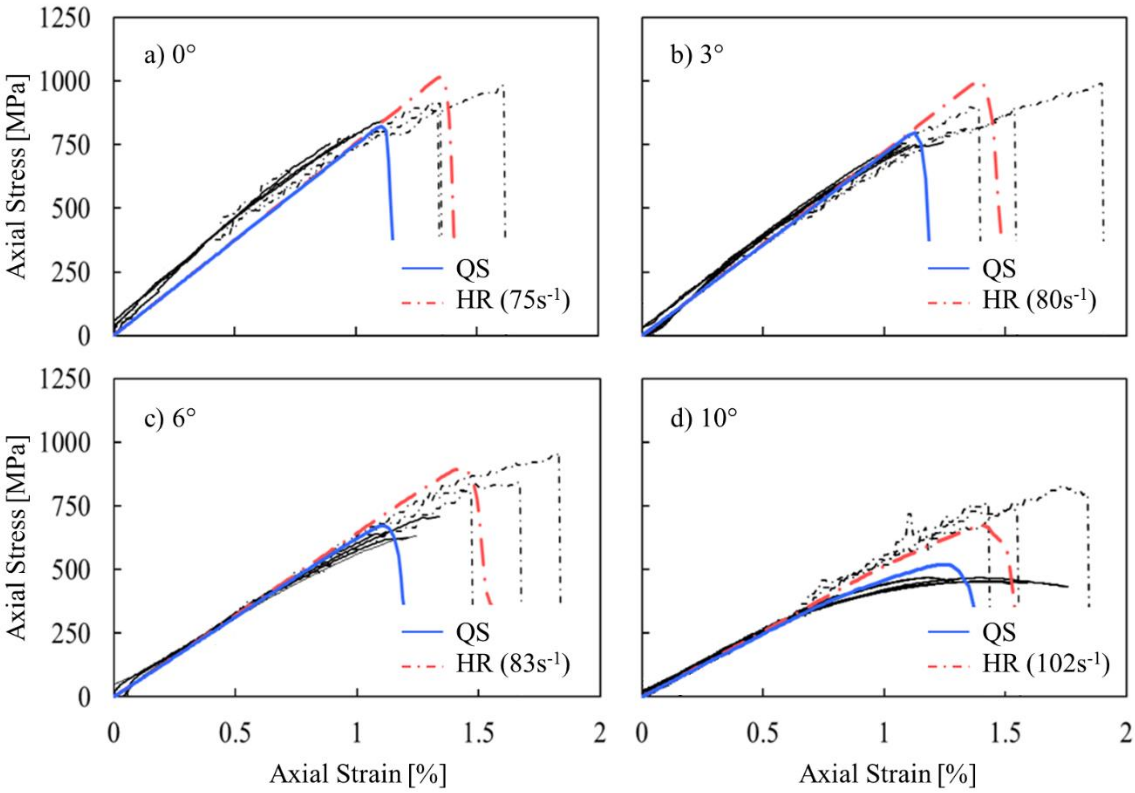

Figure 7.8. Predicted axial stress-strain curves for each of the off-axis specimens at quasi-static (blue, solid) and dynamic (red, dotted) loading rates plotted over the experimental data from section 5.2 (black).

More importantly, the quasi-static 10° simulation did not accurately represent the nonlinear shear behaviour observed in the experiments. Since the nonlinear behaviour was well captured in all the UD simulations, based on these results and the work in [51,157], it may be necessary to include fibre rotation effects when modelling multi-directional laminates with coarse meshes like the one used here, which may otherwise restrict shear deformation between opposing plies.

However, overall the model gives good predictions for the longitudinal compression strength in most cases and, even in those tests where the results were less accurate, the FE implementation still performed better than expected based on the initial analysis in section 5.2.

Therefore, until the micromechanics of fibre kinking under multi-axial loads are better understood and a more accurate physically-based model can be developed, the proposed shear damage criterion can provide better predictions of the compressive strength under combined loading and different strain rates, while still being based entirely on the same principles that dictate the uniaxial compression strength and the nonlinear shear behaviour.

7.2. Benchmarks: Ballistic impact tests

With the full-fledged validation tests in the previous sections, the implemented FE material model has been shown to describe all of the major deformation and failure modes in UD IM7/8552 at quasi-static and dynamic loading rates in the order of 100 to 300 s^{-1} with good accuracy overall, even using a coarse mesh with poor aspect ratios.

The following set of benchmark tests was designed to test the limits of the developed model and explore its performance in larger scale industrial applications, where a number of compromises are often necessary due to the size of the simulations or the more extreme loading conditions.

For this purpose, a series of normal and oblique ballistic impact experiments was carried out on 200 x 200 mm^2 laminate plates at different velocities and compared against FE simulations of the same test cases. The specimen and test set-up for the different tests are described in section 7.2.1, and the characteristics of the numerical simulations are described in section 7.2.2.

By evaluating the developed model under these more extreme conditions, with strain rates far beyond the limits of the calibration data and widespread inter- and intra-laminar damage, this final study may give some insight into the model's ability to extrapolate rate-dependent behaviour and may point towards some of its current limitations and areas for future work.

In addition, for the sake of computational cost, the element size was pushed beyond the recommended limit for the damage model given in Chapter 6 and the laminates were modelled without interface elements for delamination, both compromises which are sometimes necessary in large scale simulations.

In order to avoid numerical instabilities in the damage model, where necessary, the fracture toughness properties were scaled up within the subroutine depending on the failure mode, fracture plane orientation, element geometry, and strain-rate effects. However, the effect of this this might not be as critical as it may seem, since the element dimensions were always within the acceptable limits for both of the fibre failure modes and for the 90º IFF mode corresponding to delamination failure.

7.2.1. Experimental set-up and data reduction

The test samples were prepared from a UD IM7/8552 quasi-isotropic laminate with a $[0/45/90/-45]_{5S}$ stacking lay-up and a nominal thickness of 5mm. CT scans of all panels were performed before testing to ensure that there were no defects introduced from the manufacturing process and the 200 x 200 mm^2 plates were machined using a water-cooled diamond disk saw.

The plates were supported by a specially designed fixture, consisting of four ball bearings 20 mm in diameter spaced 100 mm apart, and were held in place using rubber bands, as shown in Figure 7.9. The fixture was designed to allow different plate orientations with respect to the projectile and to produce easily reproduceable boundary conditions for the FE analysis. The rubber bands were only used to hold the plates in place during testing and their effect on the boundary conditions throughout the impact can be safely ignored due to their low moduli and strength with respect to all other elements in the system.

The plates were mounted on the fixture at 90° normal and 45° oblique angles and impacted with a 20 mm, 32.7 g steel ball embedded in a foam sabot and fired out of a 70 mm gas gun at different velocities.

Ten plates were tested at each orientation, with impact velocities ranging from 21 m/s up to 157 m/s, to produce different combinations of damage and failure modes.

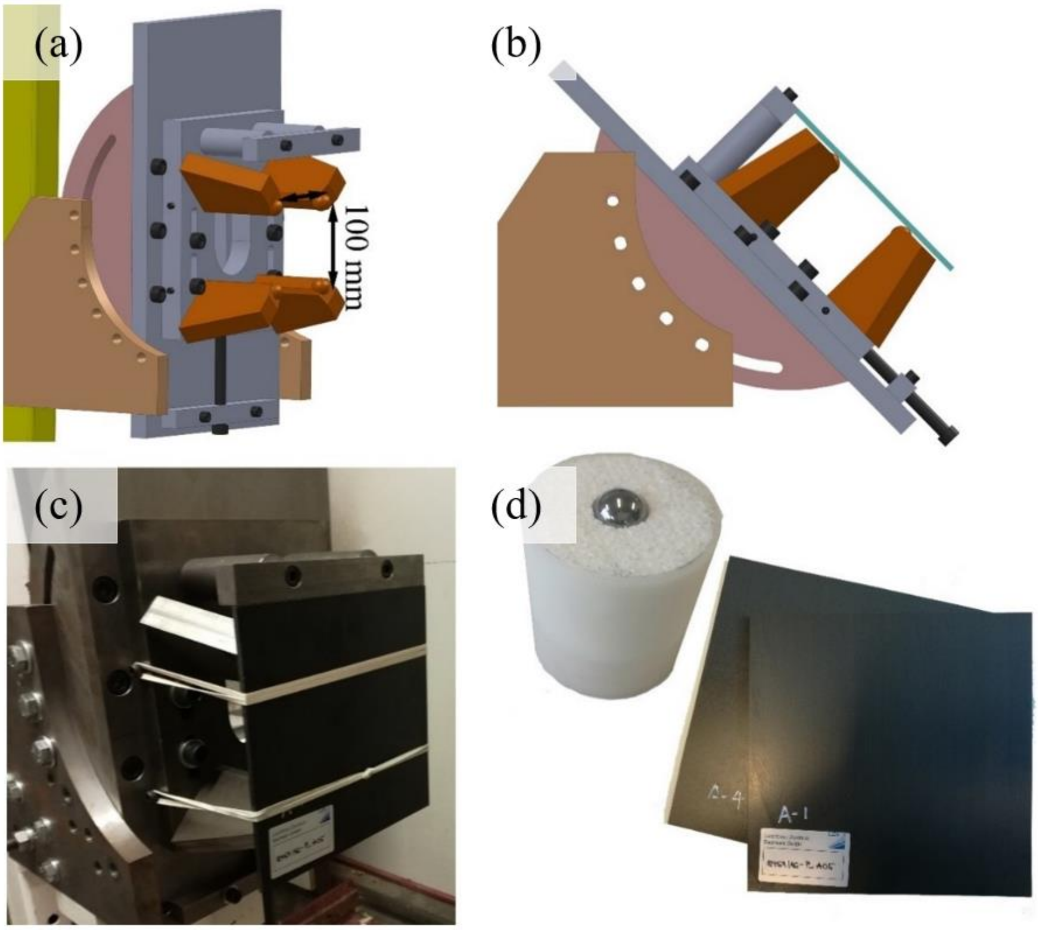

Figure 7.9. Plate impact fixture for (a) the 90° impact, and (b) the 45° impact. The tested IM7/8552 plate is shown in (c) mounted on the fixture and in (d) next to the projectile and foam sabot.

For all tests, a Photron high-speed camera was employed to capture the impact event and DIC was used to track the displacement and velocity of the projectiles, which were painted white with black dots for this purpose. In addition, a light curtain at the end of the gas gun measured the initial velocity of the projectile, which was used to validate the DIC measurements as both were within a 5% error margin of each other.

Since the impact force could not be measured experimentally and no CT scan results were available at the time, only the DIC projectile velocity and visual inspection of the plates after impact were used for comparison against the simulation results.

In addition, due to the computational cost of simulations at this scale, only four tests were selected for the modelling benchmarks, covering the two extremes for each plate orientation: both a full rebound with barely visible impact damage (BVID) test case, and complete perforation case for both the normal and the oblique laminate orientations.

7.2.2. Model set-up

For the benchmark simulations, the test conditions and specimen geometry were modelled in LS-DYNA with the user-defined material subroutine developed and calibrated throughout this work, as shown in Figure 7.10. Since the focus of the present work has been on the intralaminar behaviour within the UD ply material, no ply interface damage modelling methods, such as cohesive elements, were used to explicitly model delamination damage between plies. Instead, the ability of the implemented damage model, Chapter 6, to capture delamination effects in certain scenarios, as suggested by Pinho in [18] and Wiegand in [19], was explored.

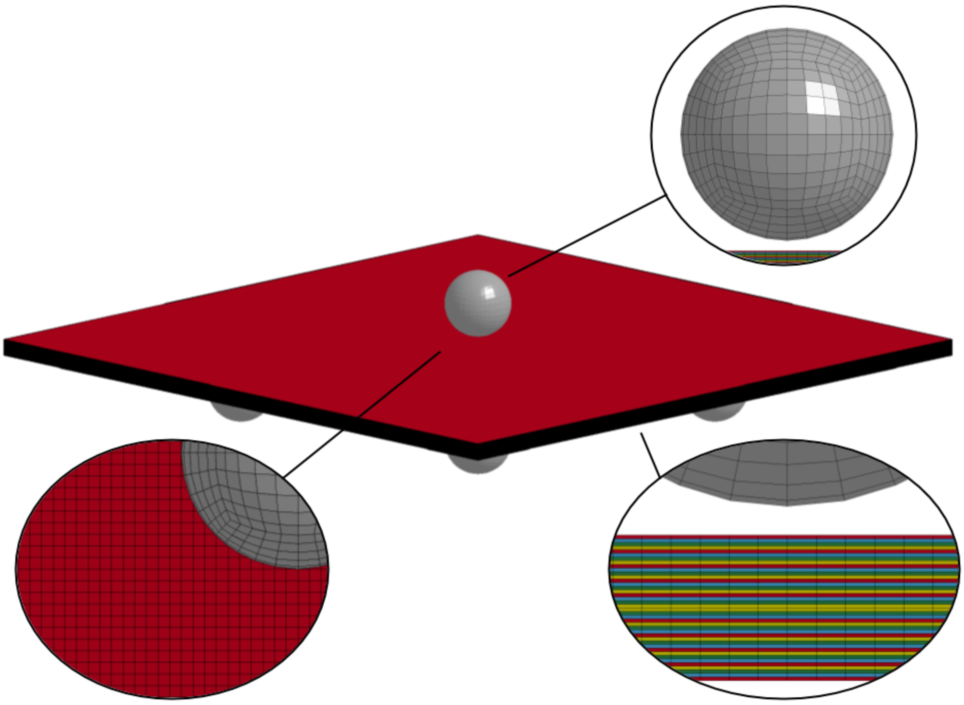

Figure 7.10. Ballistic impact FE model showing the suports, projectile and laminate meshes. Each colour in the laminate represents a different ply orientation, in order to match the [0/45/90/-45]$_{5S}$ quasi-isotropic lay-up.

Therefore, the plates were modelled using 1x1x0.125 mm^3 solid elements, the same as used in section 7.1, with one element per ply through the thickness of the laminate. Each ply was assigned a different coordinate system according to the stacking lay-up and all elements were fully attached, with no interface elements or cohesive contact definitions.

The supports and projectile were modelled as rigid bodies using 3D solid elements of approximately 2 mm in length, with the supports completely fixed and the projectile given an initial velocity corresponding to each test case, defined either in the normal or oblique direction.

7.2.3. Results

The four selected test cases were: a 59 m/s normal impact, a 55 m/s oblique impact, both showing BVID, and two 106 m/s normal and oblique impacts with complete perforation.

For each of these test cases, the simulation results were compared against the projectile velocity histories extracted from the test footage and visual inspection of the damage.

7.2.3.1. 59 m/s normal impact

For the 59 m/s 90° impact, the projectile rebounded completely, recovering to a velocity of over 20 m/s, and showed barely any damage, although some small permanent deformation was visible on the surface at the point of impact.

In this case, the model was able to predict the rebound of the projectile but showed excessive damage at the location of impact, Figure 7.11. Under closer inspection, it appears that the model showed excessive initial rigidity and, while some delamination damage was predicted through the thickness of the laminate, it did not propagate, resulting in a great initial impact force which may have caused some of the excessive damage.

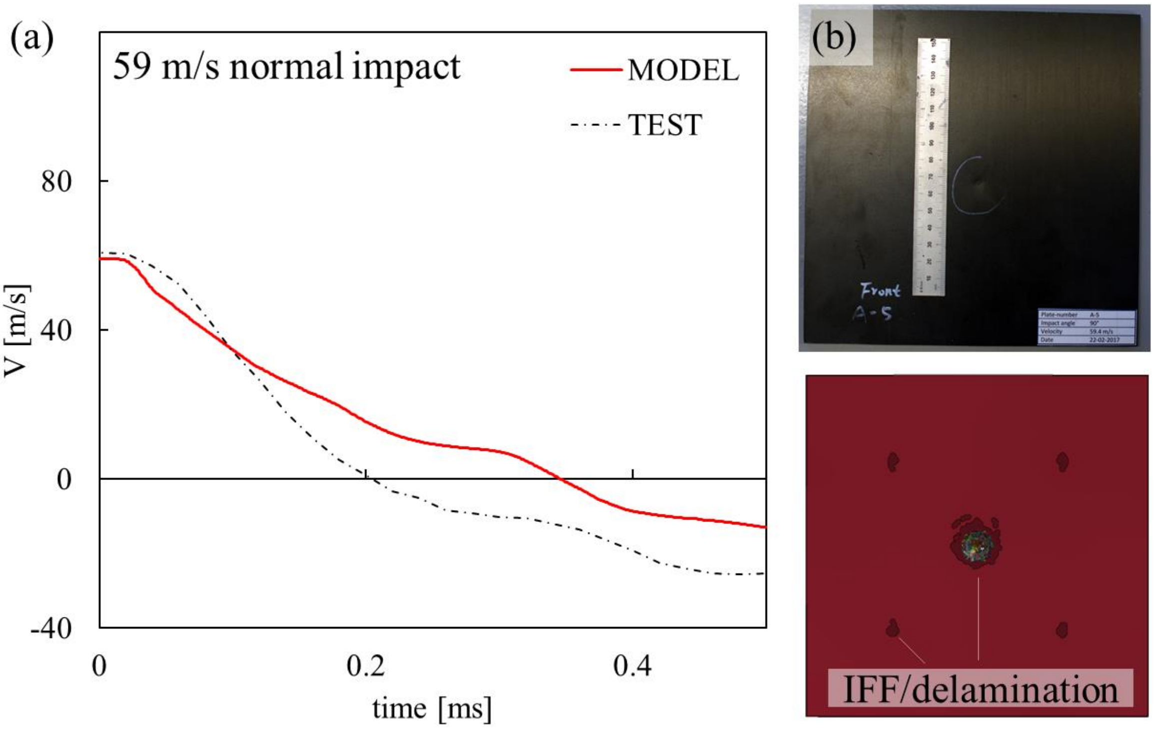

Figure 7.11. (a) Projectile velocity history from the test and simulation for the 59 m/s normal impact, and (b) extent of damage observed in the test and in the model.

7.2.3.2. 55 m/s oblique impact

For the 55 m/s 45° impact, the projectile also rebounded completely with barely any damage, recovering to around 40 m/s after impact. In this case, the normal impact velocity was only around 39 m/s, compared to the 59 m/s test in the previous section, and showed almost no signs of damage, as can be seen in Figure 7.12.

In addition, the model produced a much closer match with the experiment than in the previous case, which was expected because of the lower impact velocity. However, as with the previous case, the model showed excessive rigidity compared to the experiment. Once again, this may have been due to delamination damage below the surface, although no CT scan data was available for verification.

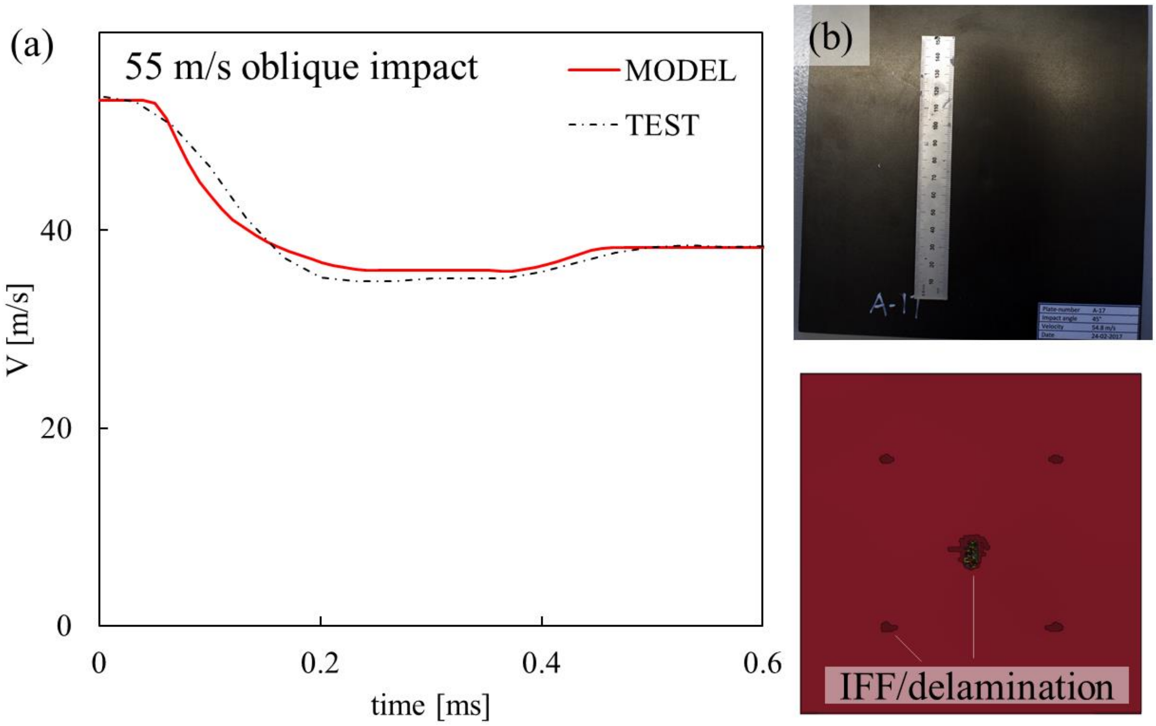

Figure 7.12. (a) Projectile velocity history from the test and simulation for the 55 m/s oblique impact, and (b) extent of damage observed in the test and in the model.

7.2.3.3. 106 m/s normal impact

For the 106 m/s 90° impact, the projectile easily perforated the laminate with a residual velocity of over 60 m/s, causing large amounts of delamination, matrix splitting, and fibre failure, visible throughout and after the test, as can be seen in Figure 7.13.

For this test, the model was able to very accurately reproduce the experimental behaviour with a very close match in the rigidity, residual velocity, and observed failure modes, except for delamination. While the energy dissipation was well predicted, in the simulation this occurred by fully damaging and deleting elements in the projectile's path whereas, in the experiment, matrix splitting and delamination allowed the projectile to pass through rather than punch a large hole in the plate.

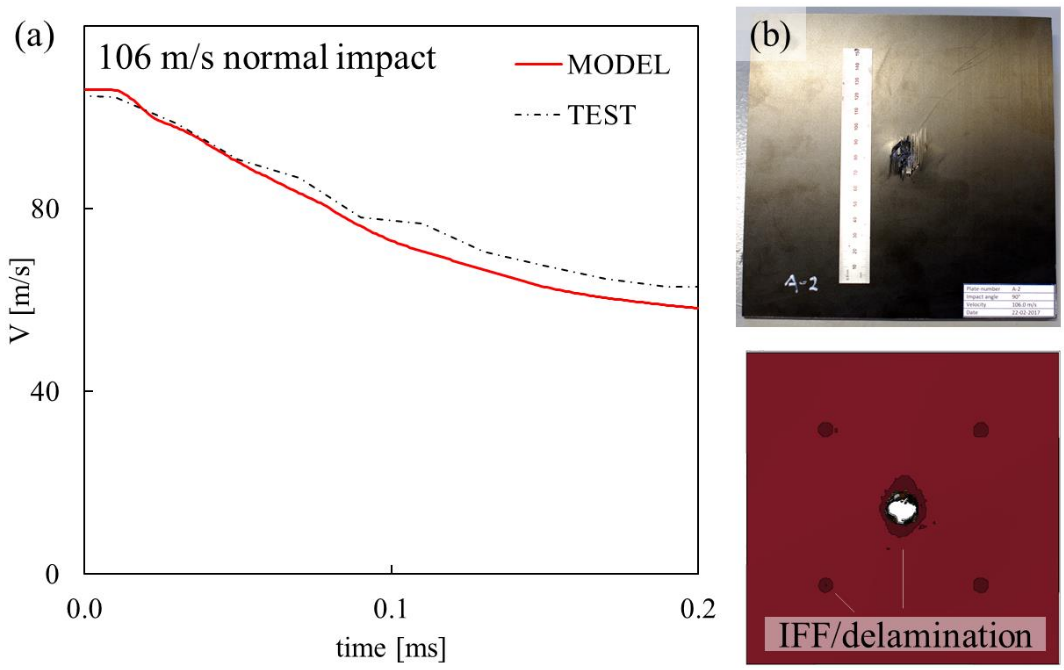

Figure 7.13. (a) Projectile velocity history from the test and simulation for the 106 m/s normal impact, and (b) extent of damage observed in the test and in the model.

7.2.3.4. 106 m/s oblique impact

Finally, for the 106 m/s 45° impact, the projectile once again easily perforated the plate, exiting with a residual velocity of almost 70 m/s and producing similar amounts of delamination, matrix splitting, and fibre failure, as can be seen in Figure 7.14.

This was arguably the most difficult test case to capture, as the normal impact velocity of 75 m/s was closer to the ballistic limit. In addition, without allowing explicit delamination in the model, the projectile was forced to damage a much larger amount of material, whereas in the experiment, delamination and matrix splitting allowed individual plies to bend away after the initial damage, allowing the projectile to pass through more easily. Because of this, the model failed to fully capture the observed behaviour, with the projectile struggling to perforate the plate and losing a much greater amount of energy in the process.

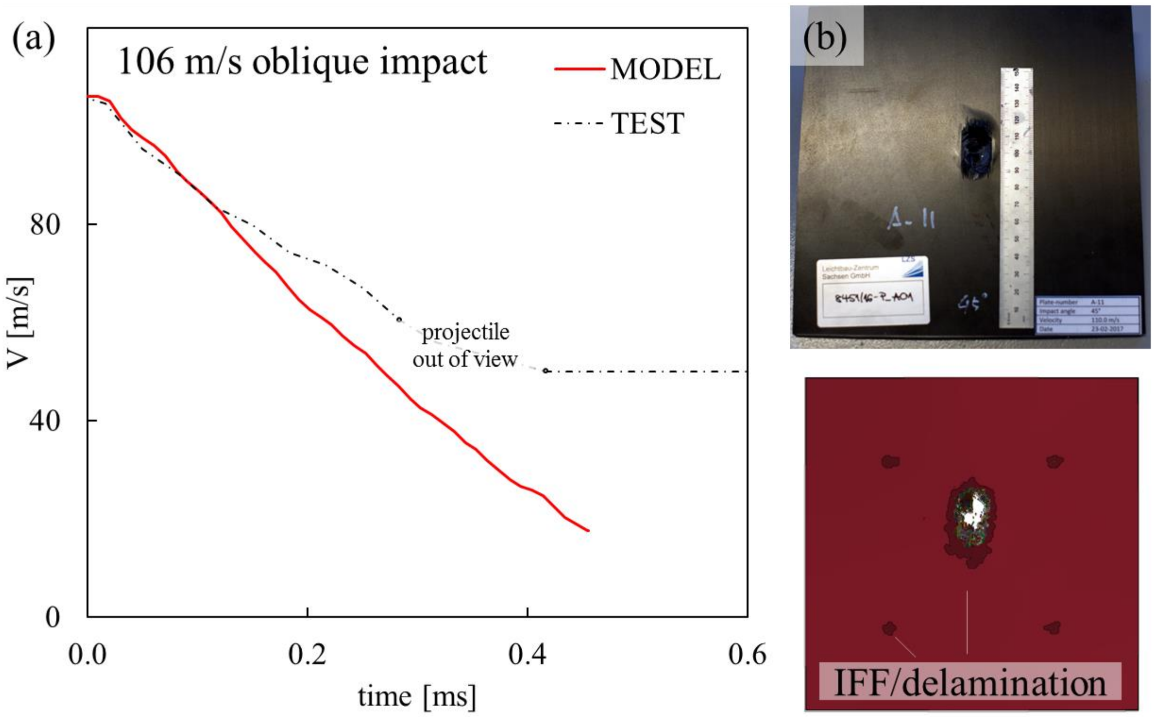

Figure 7.14. (a) Projectile velocity history from the test and simulation for the 106 m/s oblique impact, and (b) extent of damage observed in the test and in the model.

7.2.4. Discussion

Overall, this series of tests was designed to push the developed model to its limits and identify areas for future work following the successful validation of the coupon-scale behaviour in section 7.1. A few aspects made these test cases particularly challenging:

First, the model was developed and calibrated using a bottom-up approach, based entirely on physical criteria and material properties to describe the material behaviour in small test specimens, with only two different tests used to calibrate the rate-dependency. By simulating experiments like these at a much larger scale and strain rates far above the calibrated values, the model's ability to scale up in both size and strain rate were tested, relying completely on extrapolated properties for the failure predictions. In contrast, a common approach for impact simulations uses rate-independent models calibrated to match the same test results.

In addition, the impact loading cases produced predominantly out-of-plane stresses and widespread delamination damage, whereas no out-of-plane test data was used to develop or calibrate the failure models and delamination was never explicitly considered, either in the constitutive model development or in the FE simulation set-up. For delamination, the model instead relied on the IFF criterion and damage formulation to predict damage parallel to the ply surfaces.

However, in spite of these challenges, the model performed surprisingly well in most cases, showing good agreement between the experiments and simulations in the measured projectile velocities and energy dissipation, shown in Figure 7.15, in spite of using element dimensions above the recommended limit. From this, it appears that the failure criteria and material properties were able to scale well with strain rate and capture the effects of out-of-plane and 3D stress states beyond what was tested during development and calibration.

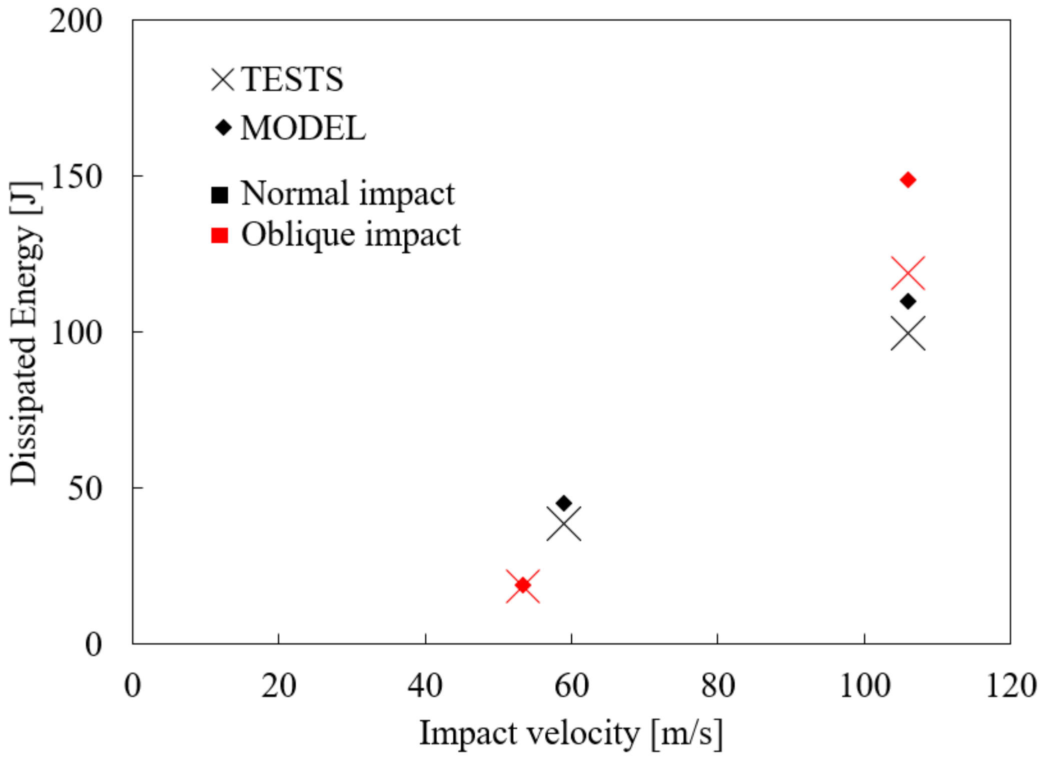

Figure 7.15. Comparison between energy dissipation in the experiments and simulations across the four different test cases.

It was the lack of explicit interface modelling for delamination damage, in particular, that posed the biggest challenge. In the low velocity impact cases, this resulted in excessive surface damage, as the lack of delamination resulted in an overly rigid response and caused damage to concentrate in the impact location, while in the high velocity impacts, it required the projectile to damage much larger volumes of material rather than splitting and pushing through it as happened in the tests. The high-velocity 45° test, especially, provides a very useful large-scale validation case, as it relies on a complex combination of failure and damage interactions for an accurate prediction.

In conclusion, the UD CFRP material model developed and calibrated from small specimen tests was able to capture some of the key aspects of the large-scale ballistic impact experiments, such as the dissipated energy after impact, even after the significant simplifications and concessions discussed in the previous sections. However, its greatest shortcoming proved to be the model's inability to accurately capture the propagation of delamination damage. This was critical for some of the test cases, in particular the oblique impacts, and would require the use of interface elements and may even call for the development of an additional rate-dependent interface model and further research into strain rate and pressure effects on this failure mode.

Chapter 8

Conclusions and future work

Throughout the work presented in the previous chapters, each of the major deformation and failure modes observed in UD CFRPs has been investigated with the aim of improving the understanding of, and predictive capabilities for this type of material under dynamic or impact loading conditions.

One of the main focus points throughout this work was on the effects of strain rate and pressure, or multi-axial loading, on each of these modes, since such loading conditions tend to result from impact loading and are known to affect the behaviour of the matrix in CFRPs.

In addition, since not only the above effects but also many of the complex stress interactions in some of the main failure modes appear to derive from the matrix properties as well, the various models and criteria developed throughout the project have been derived from the matrix-dominated shear response, where possible. In this way, a simple, intuitive, and more unified constitutive model was obtained, in which all of the complex behaviour across different modes was related, reducing the number of individual assumptions and material parameters.

The modelling work in this thesis builds on previous work by Puck [12], who first developed the localisation plane theory for IFF failure; Pinho [18], who used Puck's and other physically based criteria to develop more complete 3D models for FEA; and finally

Wiegand [19] and Koerber [49], who began to expand the previous models into dynamic loading.

8.1. Conclusions

The numerical framework for user-defined material modelling FEA using LS-DYNA was introduced in section 1.2, in which all of the developed models and criteria in the following chapters were implemented.

8.1.1. Matrix-dominated nonlinear behaviour

Chapter 3 focused on the underlying constitutive behaviour, starting with viscoelastic behaviour in section 3.1 and then the nonlinear behaviour in 3.2.

One of the main new developments in the present work was the proposal of a physically-based localisation plane plasticity model, which uses some of the same concepts behind Puck's localisation plane theory for IFF [12] to describe the complex yielding and nonlinear deformation observed in UD CFRPs under transverse loads. The proposed model was able to capture the complex effects of multi-axial loading, pressure, and strain rate as the result of shear-dominated frictional yielding behaviour by using a linear Drucker-Prager type yield function on the critical localisation plane. The additional complexity in this approach comes from the need to determine the critical localisation plane for a given state of stress, which is found as the plane that maximises the yield function and is what gives the model its complex anisotropic or multi-axial response.

However, as will be discussed in the future work section, further research is still needed to establish the physical meaning behind some of the model parameters and their relation to the constituent properties, especially with regard to the effects of strain rate, for which the model currently relies on a phenomenological rate-scaling function fitted to the experimental data.

8.1.2. Inter-fibre fracture initiation

With the nonlinear shear model in place, Chapter 4 investigated the IFF failure mode that dictates the material strength under these same transverse loads.

First a series of off-axis tension and compression tests was carried out at quasi-static and dynamic rates to complement the data available in the literature and validate the suggestions by Wiegand [19] and Koerber [49] that IFF strength properties and therefore the failure envelope could be scaled proportionally with the strain rate following a radical scaling function.

This was shown to produce accurate predictions for both the new tests and literature data, and previously reported changes in shape of the envelope under dynamic loading were shown to be most likely caused by combining dynamic data at different strain rates.

Finally, since the nonlinear shear model in 3.2 was based on the same localisation plane theory used to predict IFF, the relation between these two modes was investigated, showing that the effective stress and critical localisation planes used in the plasticity model could be used to predict eventual IFF failure as well.

8.1.3. Fibre failure initiation

Following the transverse damage and failure modes in the previous chapters, Chapter 5 focused on longitudinal failure. From the literature review, fibre tension failure was shown not to exhibit any significant strain rate effects or stress interactions, and a simple maximum stress criterion was therefore used in 5.1.

Section 5.2 studied the failure of UD CFRPs under longitudinal compression, possibly the most complex failure mode for this type of material. A review of the literature on this topic revealed a lack of reliable experimental data, so a series of experimental campaigns were carried out to study this failure mode.

First, a series of quasi-static uniaxial compression tests was performed on different UD and cross-ply specimen designs to establish the optimal set-up for the determination of the longitudinal compression strength. The cross-ply specimens were found to produce accurate repeatable results, from which the longitudinal ply strength could be extracted using CLT, whereas the UD specimens were highly susceptible to premature failure and easily influenced by the boundary conditions.

Therefore, cross-ply specimens were used for the two following experimental studies, where off-axis compression tests were carried out at quasi-static and dynamic loading rates to investigate the effects of shear and strain rate on fibre kinking failure.

From these results it was shown that the widely accepted fibre kinking theory by Fleck [23], which was also used in the LaRC models [62,104], was unable to adequately explain the effects of off-axis loading on the longitudinal compression strength. Instead, until further insight into the micromechanics of the problem can be gained, an alternative approach has been proposed based on experimental observations, where, under off-axis loads, the physically based solution for the uniaxial compression strength from Fleck is degraded proportionally to the in-plane shear damage, obtained from the localisation plane plasticity model. In this way, Fleck's physical model for the uniaxial compression case is preserved, while the effects of strain rate, pressure, or multi-axial loading are directly derived from the nonlinear shear model in 3.2.

8.1.4. Validation and benchmarks

Finally, the complete constitutive model was benchmarked and validated in a series of FEA tests in Chapter 7.

First, in 7.1 the model was used to simulate a series of biaxial loading specimens at different loading rates from the in-house and literature tests in sections 4.2 and 5.2, showing its ability to accurately describe the nonlinear behaviour and failure across different deformation and failure modes and strain rates.

Next in 7.2, having fully validated the model in the range of biaxial test specimens and rates used throughout the previous sections, a series of ballistic impact tests was performed to benchmark its performance under more complex loading conditions. These tests were designed to push the model to its limits, as the consisted of predominantly out-of-plane loading, strain rates far above what was available for the model's calibration, and large amounts of delamination damage.

Keeping in mind that the constitutive model was developed and calibrated using small in-plane specimens with only two different strain rates for calibration of the rate-dependency, and that delamination was not explicitly modelled in the simulations, the results were very promising. In most test cases, the model was able to give good predictions of the projectile velocity throughout the test as well as the dissipated energy during impact, after rebounding or perforating the plate. However, without the use of cohesive elements or similar for delamination modelling, cases where delamination played an important role in damage evolution were not so successfully predicted, such as the high velocity oblique impact.

8.2. Future work

Overall, throughout the project, a series of physically-based rate-dependent models and failure criteria for UD CFRPs has been developed where all rate-, pressure-, and complex multi-axial stress interaction effects are derived from the matrix-dominated nonlinear shear behaviour, which itself has been shown to follow the type of localisation plane behaviour observed during IFF. The models have been shown to accurately describe the nonlinear behaviour and material strength of UD CFRPs under various biaxial loading conditions at both quasi-static and dynamic loading rates and even showed good ability to extrapolate the material behaviour up to ballistic impact velocities and multi-directional laminates. However, the ability of the IFF criterion in combination with a smeared damage formulation to capture effects of delamination, as suggested by Pinho in [18] and Wiegand in [19], appeared to be limited to certain simple loading conditions and may not be suitable for more complex impact scenarios, especially for oblique impact cases with expected perforation.

For more realistic modelling of high-velocity impact cases with significant delamination damage or perforation, explicit delamination modelling techniques such as cohesive elements or contacts, should be used, although for meaningful physically-based predictions, the constitutive laws and material parameters, including potential rate dependencies, would need to be investigated further, similarly to what has been done throughout this study for the UD material in the plies.

While this inability to accurately describe the effects of delamination within the continuum was perhaps the most clearly identified limitation of the developed model, this is a well-known issue with many possible solutions beyond those mentioned above.

However, throughout this work a number of other, perhaps less obvious, areas for future work have also been identified.

In section 3.2, focused on the nonlinear shear behaviour, the rate-scaling approach, while validated in this and many previous works, is still empirically based. For a more physically-based model, the question of whether the relation between elastic properties and strain rate can be derived from the viscoelastic properties of the matrix should be investigated. Similarly, the nonlinear shear behaviour is currently calibrated from the macroscopic in-plane shear curve, but if this can be associated with micro-scale matrix and fibre-matrix interface damage it may allow for more reliable modelling, including whether nonlinearity should be modelled as the effect of damage or inelastic strains and whether isotropic or kinematic hardening should be used. This would help define the material behaviour under cyclic or reverse loading, which has not been investigated in the current study. In addition, some of the results in the model validation tests in 7.1 showed that it may be important to include fibre rotation effects when modelling multi-directional laminates, which should be investigated further in future work.

In Chapter 4, on IFF failure, it was found that the yield criterion used to describe the nonlinear shear behaviour could be used to predict IFF with relatively good accuracy. However, IFF failure showed greater pressure-dependency and required a greater frictional parameter for best results. If IFF is in fact a direct consequence of strain localisation along the planes defined by the nonlinear shear behaviour, the reason for this difference in pressure-dependency would have to be explained. Furthermore, the model validation tests in 7.1, showed that stress-based criteria struggled to predict the ultimate strain in cases with large nonlinear deformation and strain or energy based criteria may be better suited to this task. Finally, from the results in 7.2, the smeared damage formulation showed very limited ability to capture large delamination effects and other, more suitable, yet still physically-based approaches should be investigated.

In section 5.2, on longitudinal compression failure, a lack of knowledge on the micromechanics of fibre kinking under multi-axial loading was exposed. For more physically-based predictions, the effects of external shear and transverse loads on the micro-scale fibre rotation within the misalignment frame, or kink band, should be investigated, something that may only be possible through micromechanical modelling.

Finally, overall, the developed models and criteria have relied, in most cases, on in-plane testing, with little or no triaxial or out-of-plane test results available to inform the model development, calibration, or validation. Instead, the material behaviour under such loading conditions is simply inferred from the off-axis loading data. Validation of the developed models under such loading conditions is crucial for impact loading, in particular. If possible, triaxial and out-of-plane testing should be performed to evaluate the current damage and failure theories more extensively.

Of the many areas for future work identified above, several seem to revolve around the micro-scale behaviour of the matrix and fibre-matrix interface. In the future, multi-scale modelling may be the key to more reliable, physically-based, predictions of complex large-scale impact events, at least in the sense of using micro-scale modelling to inform the development and calibration of meso- or macro-scale models like the ones developed in the present work.

As a final illustrative test case, going back to the introduction and the initial motivations for the present work, a simplified fan blade impact test, shown in Figure 8.1 below, has been simulated using the developed models for UD CFRPs to illustrate the importance of some of the work done throughout this project in more practical industrial applications.

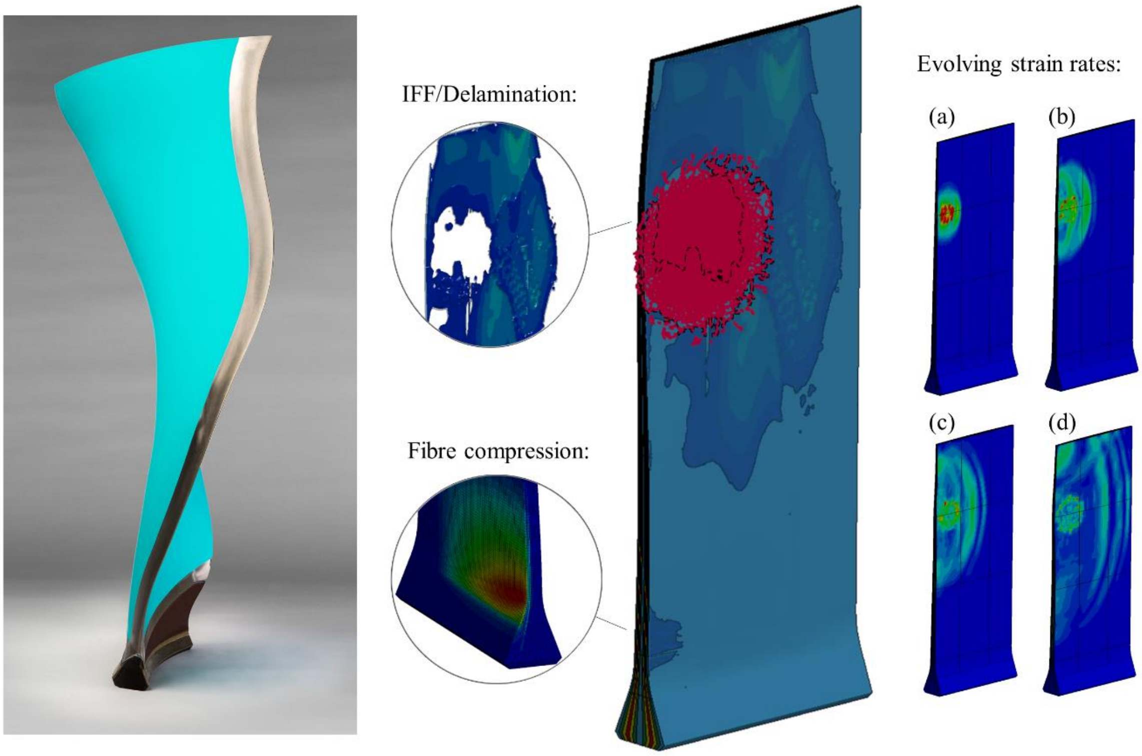

Figure 8.1. Simplified blade impact model based on the NASA report in [162] used to illustrate the key benefits of the developed models in applications such as the pictured Rolls Royce CTi fan blade [4].

The simplified blade model was replicated from the NASA report in [162], using the same [0/+22/0/-22] ply lay-up and approximate blade geometry, and the gelatine projectile was modelled using smoothed particle hydrodynamics (SPH) elements with a third degree polynomial equation of state (EOS) calibrated with the parameters given in [163].

This test case is particularly interesting because there are two key areas where failure may occur, the impact location and the blade root. The results of this simulation show how the strain rate evolves from the point of impact to the blade root due to dissipation from damage and changes in geometry, which reinforces the need for truly rate-dependent models instead of rate-independent models calibrated with dynamic data. In addition, while damage at the impact location is limited to IFF, delamination, and fibre tension, as observed in the ballistic impact tests in 7.2, at the blade root, the oscillations caused by the impact and the different ply orientations result in significant longitudinal compression and multi-axial stress states. Consequently, in such cases, accurately accounting for the effects of off-axis loading and strain rate on the fibre kinking strength, as was investigated in section 5.2, may also have a big impact on the reliability of the numerical predictions.

Therefore, while more work remains to be done on the modelling of CFRPs under dynamic loading, the models and criteria developed throughout this project may already allow for significant improvements in certain industrial applications where impact is a critical design scenario, as illustrated by the blade impact test above.

Bibliography

[1] European Comission. Reducing emissions from aviation | Climate Action. https://ec.europa.eu/clima/policies/transport/aviation_en

[2] European Comission. Reducing CO2 emissions from passenger cars | Climate Action. https://ec.europa.eu/clima/policies/transport/vehicles/cars_en

[3] Rolls Royce plc. Future products. https://www.rolls-royce.com/products-and-services/civil-aerospace/future-products.aspx#section-overview

[4] Rolls Royce plc. Advance and UltraFan engine designs. https://live.staticflickr.com/5152/14337390264_b90c4803b6_k.jpg

[5] Rolls Royce plc. Advance and UltraFan engine designs. https://live.staticflickr.com/2922/14151460559_ef7ce6f791_b.jpg

[6] Hexcel. (2016). HexPly 8552 Data Sheet.

[7] Hexcel. (2018). HexTow IM7 Carbon Fiber Data Sheet.

[8] LSTC Inc. Time integration — Welcome to the LS-DYNA support site. https://www.dynasupport.com/tutorial/ls-dyna-users-guide/time-integration

[9] LSTC Inc. (2019). LS-DYNA Theory Manual.

[10] LSTC Inc. LS-DYNA | Livermore Software Technology Corp. https://www.lstc.com/products/ls-dyna

[11] LSTC. (2016). LS-DYNA R9.0 Manual Volume I Keyword.

[12] Puck A, Schurmann H. (1998). “Failure analysis of FRP laminates by means of physically based phenomenological models,” *Composites Science and Technology,* 58:1045–67.

[13] Thomson D M, Erice B, Cui H, Hoffmann J, Wiegand J, Petrinic N. (2018). “A Puck-based localisation plane theory for rate- and pressure-dependent constitutive modelling of unidirectional fibre-reinforced polymers,” *Composite Structures*, 184:299–305.

[14] Erice B, Thomson D M, Ponnusami S A, Pathan M V, Petrinic N. (2018). “On the Rate-dependent Plasticity Modelling of Unidirectional Fibre-reinforced Polymeric Matrix Composites,” *EPJ Web of Conferences*, 183:01055.

[15] Thomson D M, Cui H, Erice B, Hoffmann J, Wiegand J, Petrinic N. (2017). “Experimental and numerical study of strain-rate effects on the IFF fracture angle using a new efficient implementation of Puck’s criterion,” *Composite Structures*, 181:325–35.

[16] Thomson D, Cui H, Erice B, Petrinic N. (2019). “A study on the longitudinal compression strength of fibre reinforced composites under uniaxial and off-axis loads using cross-ply laminate specimens,” *Composites Part A: Applied Science and Manufacturing*, 121:213–22.

[17] Thomson D, Quino G, Pellegrino A, Cui H, Erice B, Petrinic N. (2019). “Strain-rate and off-axis loading effects on the fibre compression strength of CFRP laminates: experiments and constitutive modelling,” *Composites Science and Technology,* (under review).

[18] Pinho S T. (2005). *Modelling failure of laminated composites using physically-based failure models*. PhD thesis, Imperial College London, Department of Aeronautics.

[19] Wiegand J. (2009). *Constitutive modelling of composite materials under impact loading*. PhD thesis, University of Oxford, Department of Engineering Science.

[20] Cui H, Thomson D, Eskandari S, Petrinic N. (2019). “A critical study on impact damage simulation of IM7/8552 composite laminate plate,” *International Journal of Impact Engineering*, 127:100–109.

[21] Irving E, Soutis C. (2014). *Polymer composites in the aerospace industry*, No. 50. Elsevier.

[22] Hsiao H M, Daniel I M. (1996). “Effect of fiber waviness on stiffness and strength reduction of unidirectional composites under compressive loading,” *Composites science and technology,* 56(5): 581–593.

[23] Budiansky B, Fleck N A. (1993). “Compressive failure of fibre composites,” *Journal of the Mechanics and Physics of Solids, 41*(1):183–211.

[24] Othman R, Guégan P, Challita G, Pasco F, LeBreton D. (2009). “A modified servo-hydraulic machine for testing at intermediate strain rates,” *International Journal of Impact Engineering*, 36:460–467.

[25] Gilat A, Seidt J D, Matrka T A, Gardner K A. (2019). “A New Device for Tensile and Compressive Testing at Intermediate Strain Rates,” *Experimental Mechanics*, 59:725–731.

[26] Hsiao H M, Daniel I M. (1998). “Strain rate behavior of composite materials,” *Composites Part B: Engineering*, *29*(5):521–533.

[27] Hopkinson B. (1914). “A Method of Measuring the Pressure Produced in the Detonation of High Explosives or by the Impact of Bullets,” *Philosophical Transactions of the Royal Society of London. Series A, Containing Papers of a Mathematical or Physical Character,* 213(497-508):437–456.

[28] Kolsky H. (1949). “An Investigation of the Mechanical Properties of Materials at very High Rates of Loading,” *Proceedings of the physical society. Section B*, 62(11):676.

[29] Gama B A, Lopatnikov S L, Gillespie J W. (2004). "Hopkinson bar experimental technique: A critical review," *Applied mechanics reviews,* 57(4):223–250.

[30] Gerlach R, Kettenbeil C, Petrinic N. (2012). "A new split Hopkinson tensile bar design," *International Journal of Impact Engineering*, 50:63–67.

[31] Staab G H, Gilat A. (1991). "A direct-tension split Hopkinson bar for high strain-rate testing," *Experimental Mechanics*, 31:232–235.

[32] Jenkins G M, Jenkins A, Kawamura K. (1976). *Polymeric carbons: Carbon Fibre, Glass and Char*. Cambridge University Press.

[33] Wang Y, Zhou Y, Xia Y, Jeelani S. (2007). "Statistical analysis on high strain rate tensile strength of T700 carbon fiber," In *ASME 2007 International Mechanical Engineering Congress and Exposition* (pp. 557–560). American Society of Mechanical Engineers.

[34] Quino G, Pellegrino A, Tagarielli V L, Petrinic N. (2018). "Measurements of the effects of pure and salt water absorption on the rate-dependent response of an epoxy matrix," *Composites Part B: Engineering*, 146:213–21.

[35] Gerlach R, Siviour C R, Petrinic N, Wiegand J. (2008). "Experimental characterisation and constitutive modelling of RTM-6 resin under impact loading," *Polymer*, 49(11), 2728–2737.

[36] Zhou J, Lucas J P. (1999). "Hygrothermal effects of epoxy resin. Part I: the nature of water in epoxy," *Polymer*, 40:5505–5512.

[37] Zhou J, Lucas J P. (1999). "Hygrothermal effects of epoxy resin. Part II: variations of glass transition temperature," *Polymer*, 40:5513–5522.

[38] Voigt W. (1889). "Ueber die Beziehung zwischen den beiden Elasticitätsconstanten isotroper Körper," *Annalen der physik*, *274*(12):573–587.

[39] Reuss A. "Berechnung der Fließgrenze von Mischkristallen auf Grund der Plastizitätsbedingung für Einkristalle," *ZAMM-Journal of Applied Mathematics and Mechanics/Zeitschrift für Angewandte Mathematik und Mechanik*, *9*(1):49–58.

[40] Daniel I M, Ishai O. (1994). *Engineering mechanics of composite materials* (Vol. 3, pp. 256–256). New York: Oxford University Press.

[41] Zhang X, Shi Y, Li Z-X. (2019). "Experimental study on the tensile behavior of unidirectional and plain weave CFRP laminates under different strain rates," *Composites Part B: Engineering*, 164:524–36.

[42] Taniguchi N, Nishiwaki T, Kawada H. (2007). "Tensile strength of unidirectional CFRP laminate under high strain rate," *Advanced Composite Materials*, 16:167–80.

[43] Gilat A, Goldberg R K, Roberts G D. (2002). "Experimental study of strain-rate-dependent behavior of carbon/epoxy composite," *Composites Science and Technology*, 62:1469–1476.

[44] Koerber H, Xavier J, Camanho P P. (2010). "High strain rate characterisation of unidirectional carbon-epoxy IM7-8552 in transverse compression and in-plane shear using digital image correlation," *Mechanics of Materials*, 42:1004–1019.

[45] Tanner R. (2000). *Engineering rheology*. Oxford: Oxford University Press.

[46] Vasiukov D, Panier S, Hachemi A. (2015). "Non-linear material modeling of fiber-reinforced polymers based on coupled viscoelasticity–viscoplasticity with anisotropic continuous damage mechanics," *Composite Structures, 132*:527–535.

[47] Papanicolaou G C, Zaoutsos S P. (2019). "Viscoelastic constitutive modeling of creep and stress relaxation in polymers and polymer matrix composites," In *Creep and fatigue in polymer matrix composites* (pp. 3–59). Woodhead Publishing.

[48] Treutenaere S. (2016). *Modelling of the fabric reinforced polymers behaviour with delamination prediction for impact-type loading*. PhD thesis, Université de Valenciennes et du Hainaut-Cambresis.

[49] Körber H. (2010. *Mechanical response of advanced composites under high strain rates*. PhD thesis, University of Porto.

[50] Koerber H, Kuhn P, Ploeckl M, Otero F, Gerbaud P-W, Rolfes R, Camanho P P. "Experimental characterization and constitutive modeling of the non-linear stress–strain behavior of unidirectional carbon–epoxy under high strain rate loading," *Advanced Modeling and Simulation in Engineering Sciences*, 5(1):17.

[51] Cui H, Thomson D, Pellegrino A, Wiegand J, Petrinic N. (2016). "Effect of strain rate and fibre rotation on the in-plane shear response of ±45° laminates in tension and compression tests," *Composites Science and Technology*, 135:106–115.

[52] Sket F, Enfedaque A, Alton C, González C, Molina-Aldareguia J M, Llorca J. (2014). "Automatic quantification of matrix cracking and fiber rotation by X-ray computed tomography in shear-deformed carbon fiber-reinforced laminates," *Composites Science and Technology*, 90:129–138.

[53] Schultz J, Lavielle L, Martin C. (1987). "The Role of the Interface in Carbon Fibre-Epoxy Composites," *The Journal of Adhesion*, 23:45–60.

[54] Naya F, González C, Lopes CS, Van der Veen S, Pons F. (2017). "Computational micromechanics of the transverse and shear behavior of unidirectional fiber reinforced polymers including environmental effects," *Composites Part A: Applied Science and Manufacturing*, 92:146–157.

[55] Herráez M, Mora D, Naya F, Lopes CS, González C, LLorca J. (2015). "Transverse cracking of cross-ply laminates: A computational micromechanics perspective," *Composites Science and Technology*, 110:196–204.

[56] González C, Llorca J. (2007). "Mechanical behavior of unidirectional fiber-reinforced polymers under transverse compression: Microscopic mechanisms and modeling," *Composites Science and Technology*, 67:2795–2806.

[57] Lafarie-Frenot MC, Touchard F. (1994). "Comparative in-plane shear behaviour of long-carbon-fibre composites with thermoset or thermoplastic matrix," *Composites Science and Technology*, 52:417–425.

[58] Pae K D, Rhee K Y. (1995). "Effects of hydrostatic pressure on the compressive behavior of thick laminated 45° and 90° unidirectional graphite-fiber/epoxy-matrix composites," *Composites Science and Technology*, 53:281–287.

[59] Shin E S, Pae K D. (1992). "Effects of Hydrostatic Pressure on the Torsional Shear Behavior of Graphite/Epoxy Composites," *Journal of composite materials, 26*(4), 462–485.

[60] Shin E S, Pae K D. (1992). "Effects of Hydrostatic Pressure on In-Plane Shear Properties of Graphite/Epoxy Composites," *Journal of composite materials*, *26*(6), 828–868.

[61] Soden P D, Hinton M J, Kaddour A S. (2002). "Biaxial test results for strength and deformation of a range of E-glass and carbon fibre reinforced composite laminates: failure exercise benchmark data," *Composites Science and Technology*, 62:1489–1514.

[62] Pinho S T, Dávila C G, Camanho P P, Iannucci L, Robinson P. (2005). "Failure Models and Criteria for FRP Under In-Plane or Three-Dimensional Stress States Including Shear Non-linearity."

[63] Hinton M J, Kaddour A S, Soden P D. (2004). *Failure criteria in fibre reinforced polymer composites: the world-wide failure exercise*. Elsevier.

[64] Iwamoto M, Ni Q-Q, Fujiwara T, Kurashiki K. (1999). "Intralaminar fracture mechanism in unidirectional CFRP composites: Part I: Intralaminar toughness and AE characteristics," *Engineering Fracture Mechanics*, 64:721–745.

[65] Czabaj M W, Ratcliffe J G. (2013). "Comparison of intralaminar and interlaminar mode I fracture toughnesses of a unidirectional IM7/8552 carbon/epoxy composite," *Composites Science and Technology*, 89:15–23.

[66] Blackman B R K, Dear J P, Kinloch A J, Macgillivray H, Wang Y, Williams J G, Yayla P. (1995). "The failure of fibre composites and adhesively bonded fibre composites under high rates of test," *Journal of Materials Science*, 30:5885–5900.

[67] Blackman B R K, Kinloch A J, Wang Y, Williams J G. (1996). "The failure of fibre composites and adhesively bonded fibre composites under high rates of test," *Journal of Materials Science*, 31:4451–66.

[68] Kuhn P, Catalanotti G, Xavier J, Camanho P P, Koerber H. (2017). "Fracture toughness and crack resistance curves for fiber compressive failure mode in polymer composites under high rate loading," *Composite Structures, 182*:164–175.

[69] Kuhn P, Catalanotti G, Xavier J, Ploeckl M, Koerber H. (2018). "Determination of the crack resistance curve for intralaminar fiber tensile failure mode in polymer composites under high rate loading," *Composite Structures*, *204*:276–287.

[70] Catalanotti G, Xavier J, Camanho P P. (2014). “Measurement of the compressive crack resistance curve of composites using the size effect law,” *Composites Part A: Applied Science and Manufacturing*, *56*:300–307.

[71] Catalanotti G, Arteiro A, Hayati M, Camanho P P. (2014). “Determination of the mode I crack resistance curve of polymer composites using the size-effect law,” *Engineering Fracture Mechanics*, *118*:49–65.

[72] Hoffmann J. (2018). *An investigation into the characterisation and modelling of the impact response of CFRP*. PhD Thesis, University of Oxford, Department of Engineering Science.

[73] Hansen U, Gillespie J W. (1998). “Dependence of intralaminar fracture toughness on direction of crack propagation in unidirectional composites,” *Journal of Composites, Technology and Research*, *20*(2):89–99.

[74] May M, Lässig T R, Hiermaier S J. (2016). “An Investigation on the Influence of Loading Rate on the Fracture Toughness of UHMW-PE Composites,” In *Proceedings of the 17th European Conference on Composite Materials*.

[75] Hoffmann J, Cui H, Petrinic N. (2018). “Determination of the strain-energy release rate of a composite laminate under high-rate tensile deformation in fibre direction,” *Composites Science and Technology*, 164:110–119.

[76] Jacob G C, Starbuck J M, Fellers J F, Simunovic S, Boeman R G. (2005). “The effect of loading rate on the fracture toughness of fiber reinforced polymer composites,” *Journal of applied polymer science*, *96*(3):899–904.

[77] Varandas LF, Arteiro A, Bessa MA, Melro AR, Catalanotti G. (2017). "The effect of through-thickness compressive stress on mode II interlaminar crack propagation: A computational micromechanics approach." *Composite Structures*, 182:326-334.

[78] Cui W, Wisnom M R, Jones M L. (1994). "Effect of through thickness tensile and compressive stresses on delamination propagation fracture energy." *Journal of Composites, Technology and Research*, 16(4):329–335.

[79] Kuhn P, Catalanotti G, Xavier J, Camanho P P, Koerber H. (2017). “Fracture toughness and crack resistance curves for fiber compressive failure mode in polymer composites under high rate loading,” *Composite Structures*, 182:164–175.

[80] Tsai J L, Guo C, Sun C T. (2001). “Dynamic delamination fracture toughness in unidirectional polymeric composites,” *Composites Science and Technology*, 61:87–94.

[81] May M. (2016). “Measuring the rate-dependent mode I fracture toughness of composites - A review,” *Composites Part A: Applied Science and Manufacturing*, 81:1–12.

[82] Lu X, Ridha M, Chen B Y, Tan V B C, Tay T E. (2019). "On cohesive element parameters and delamination modelling," *Engineering Fracture Mechanics*, 206:278–96.

[83] Li X, Hallett S R, Wisnom M R. (2008). "Predicting the effect of through-thickness compressive stress on delamination using interface elements," *Composites Part A: Applied Science and Manufacturing*, 39:218–30.

[84] Fenske M T, Vizzini A J. (2001). "The inclusion of in-plane stresses in delamination criteria," *Journal of Composite Materials*, *35*(15):1325–1342.

[85] Hou J, Petrinic N, Ruiz C. (2001). "A delamination criterion for laminated composites under low-velocity impact," *Composites Science and Technology*, 61:2069–74.

[86] Smiley A J, Pipes R B. (1987). "Rate effects on mode I interlaminar fracture toughness in composite materials," *Journal of composite materials*, 21(7):670-687.

[87] Smiley A J, Pipes R B. (1987). "Rate Sensitivity of Mode II Interlaminar Fracture Toughness in Graphite/Epoxy and Graphite/PEEK Composite Materials," *Composites Science and Technology*, 29(1):1–15.

[88] Parry T V, Wronski A S. (1982). "Kinking and compressive failure in uniaxially aligned carbon fibre composite tested under superposed hydrostatic pressure," *Journal of Materials Science*, 17:893–900.

[89] Opelt C V, Cândido G M, Rezende M C. (2018). "Compressive failure of fiber reinforced polymer composites – A fractographic study of the compression failure modes," *Materials Today Communications*, 15:218–227.

[90] Herráez M, Bergan AC, González C, Lopes C S. (2018). "Modeling Fiber Kinking at the Microscale and Mesoscale."

[91] Lee J, Soutis C. (2007). "A study on the compressive strength of thick carbon fibre–epoxy laminates," *Composites Science and Technology*, 67:2015–26.

[92] Standard, ASTM. (2009). "D6641/D6641M-09." *Standard Test Method for Compressive Properties of Polymer Matrix Composite Materials Using a Combined Loading Compression (CLC) Test Fixture*. W Conshohocken: ASTM International.

[93] Wang Y, Burnett T L, Chai Y, Soutis C, Hogg P J, Withers P J. (2017). "X-ray computed tomography study of kink bands in unidirectional composites," *Composite Structures*, 160:917–24.

[94] Matsuo T, Kageyama K. (20187). "Compressive failure mechanism and strength of unidirectional thermoplastic composites based on modified kink band model," *Composites Part A: Applied Science and Manufacturing*, 93:117–25.

[95] Fleck N A. (1997). "Compresssive failure of fiber composites," *Advances in applied mechanics*, *33*(6):7.

[96] Ploeckl M, Kuhn P, Grosser J, Wolfahrt M, Koerber H. (2017). “A dynamic test methodology for analyzing the strain-rate effect on the longitudinal compressive behavior of fiber-reinforced composites,” *Composite Structures*, 180:429–438.

[97] Martinez G M, Piggott M R, Bainbridge D M R, Harris B. (1981). “The compression strength of composites with kinked, misaligned and poorly adhering fibres,” *Journal of Materials Science*, 16:2831–2836.

[98] Piggott M R, Harris B. (1981). “Compression strength of hybrid fibre-reinforced plastics,” *Journal of Materials Science*, 16:687–693.

[99] Liu K-S, Tsai S W. (1998). “A progressive quadratic failure criterion for a laminate,” *Composites Science and Technology*, 58:1023–32.

[100] Soden P D, Kaddour A S, Hinton M J. (2004). “Recommendations for designers and researchers resulting from the world-wide failure exercise,” *Composites Science and Technology*, 64:589–604.

[101] Hinton M, Kaddour A. (2012). “The background to the Second World-Wide Failure Exercise,” *Journal of Composite Materials*, 46:2283–2294.

[102] Kaddour A, Hinton M, Smith P, Li S. (2013). “A comparison between the predictive capability of matrix cracking, damage and failure criteria for fibre reinforced composite laminates: Part A of the third world-wide failure exercise,” *Journal of Composite Materials*, 47:2749–79.

[103] Kaddour A S, Hinton M J. (2012). “Benchmarking of triaxial failure criteria for composite laminates: comparison between models of ‘Part (A)’of ‘WWFE-II,’” *Journal of Composite Materials*, *46*(19-20), 2595-2634.

[104] Davila C, Jaunky N, Goswami S. (2003). “Failure criteria for FRP laminates in plane stress,” In *44th AIAA/ASME/ASCE/AHS/ASC Structures, Structural Dynamics, and Materials Conference* (p. 1991).

[105] Hashin Z. (1980). “Failure Criteria for Unidirectional Fiber Composites,” *Journal of Applied Mechanics*, 47:329–34.

[106] Sun C, Tao J. (1998). “Prediction of failure envelopes and stress/strain behaviour of composite laminates,” *Composites Science and Technology*, 58:1125–36.

[107] Rosen B W. (1965). “Mechanics of composite strengthening,” *Fiber Composite Materials*, Ohio: American Society for Metals, pp. 37–75.

[108] Argon A S. (1972). “Fracture of composites,” *Treatise on materials science and technology*, 1:79-114.

[109] Chaboche J L. (1984). “Anisotropic creep damage in the framework of continuum damage mechanics,” *Nuclear engineering and design*, 79(3), 309-319.

[110] Lemaitre J, Chaboche J L. (1990). “Elements Of The Physical Mechanisms Of Deformation And Fracture,” *Mechanics of solid materials*, Cambridge university press.

[111] Ladeveze P, Le Dantec E. (1992). “Damage modelling of the elementary ply for laminated composites,” *Composites Science and Technology,* 43:257–67.

[112] Hartmann S. (2013). “Neue Materialmodelle für Composites in LS-DYNA.”

[113] Vyas G M, Pinho S T, Robinson P. (2011). “Constitutive modelling of fibre-reinforced composites with unidirectional plies using a plasticity-based approach,” *Composites Science and Technology,* 71:1068–1074.

[114] Sun C T, Chen J L. Sun, (1989). “A simple flow rule for characterizing nonlinear behavior of fiber composites,” *Journal of Composite Materials, 23*(10):1009–1020.

[115] Ramberg W, Osgood W R. (1943). “Description of stress-strain curves by three parameters.”

[116] Drucker D C, Prager W. (1952). “Soil mechanics and plastic analysis or limit design,” *Quarterly of applied mathematics, 10*(2), 157-165.

[117] Swanson S R, Messick M J, Tian Z. (1987). “Failure of Carbon/Epoxy Lamina Under Combined Stress,” *Journal of Composite Materials,* 21:619–30.

[118] Kaddour A, Hinton M. (2013). “Maturity of 3D failure criteria for fibre-reinforced composites: Comparison between theories and experiments: Part B of WWFE-II,” *Journal of Composite Materials,* 47:925–66.

[119] Kaddour A, Hinton M. (2012). “Input data for test cases used in benchmarking triaxial failure theories of composites,” *Journal of Composite Materials, 46*(19-20), 2295-2312.

[120] Sket F, Enfedaque A, Díaz López C, González C, Molina-Aldareguía J, LLorca J. (2016). “X-ray computed tomography analysis of damage evolution in open hole carbon fiber-reinforced laminates subjected to in-plane shear,” *Composites Science and Technology*, 133:40–50.

[121] Pan B, Qian K, Xie H, Asundi A. (2009). “Two-dimensional digital image correlation for in-plane displacement and strain measurement: a review,” *Measurement Science and Technology,* 20:062001.

[122] Vogler M, Rolfes R, Camanho P P. (2013). “Modeling the inelastic deformation and fracture of polymer composites – Part I: Plasticity model,” *Mechanics of Materials*, 59:50–64.

[123] Puck A, Mannigel M. (2007). “Physically based non-linear stress–strain relations for the inter-fibre fracture analysis of FRP laminates,” *Composites Science and Technology,* 67:1955–1964.

[124] Voce E. (1948). “The relationship between stress and strain for homogeneous deformations,” *Journal of the Institute of Metals, 74*:537-562.

[125] Gerlach R, Siviour C R, Wiegand J, Petrinic N. (2013). “The Strain Rate Dependent Material Behavior of S-GFRP Extracted from GLARE,” *Mechanics of advanced materials and structures, 20*(7), 505-514.

[126] Simo J C, Hughes T J R. (2004). *Computational Inelasticity* (Vol. 7). Springer Science & Business Media.

[127] Puck A. (1996). *Festigkeitsanalyse von Faser-Matrix-Laminaten Modelle für die Praxis*. Munich: Hanser Verlag.

[128] Cuntze R G, Deska R, Szelinski B, JeltschFricker R, Meckbach S, Huybrechts D, et al. (1997). *Neue Bruchkriterien und Festigkeitsnachweise fuer unidirektionalen Faserkunststorverbund unter mehrachsiger Beanspruchung -Modellbildung und Experimente*. Duesseldorf: VDI Verlag.

[129] Deuschle H M, Kroplin B H. (2012). "Finite element implementation of Puck's failure theory for fibre-reinforced composites under three-dimensional stress," *Journal of Composite Materials*, 46:2485–2513.

[130] Deuschle H M, Puck A. (2013). "Application of the Puck failure theory for fibre-reinforced composites under three-dimensional stress: Comparison with experimental results," *Journal of Composite Materials,* 47:827–46.

[131] Puck A, Kopp J, Knops M. (2002). "Guidelines for the determination of the parameters in Puck's action plane strength criterion," *Composites Science and Technology*, 62:371–378.

[132] Catalanotti G. (2010). *Multi-material joints for high-speed train structures*. PhD Thesis, Universidade do Porto.

[133] GOM. (2009). *ARAMIS User Manual* v6.1.

[134] Nemat-Nasser S, Isaacs J B, Starrett J E. (1991). "Hopkinson Techniques for Dynamic Recovery Experiments," *Proceedings of the Royal Society A: Mathematical Physical and Engineering Sciences*, 435:371–91.

[135] Schneider C A, Rasband W S, Eliceiri KW. (2012). *NIH Image to ImageJ: 25 years of image analysis*. Nature Methods 9:671–675.

[136] Tarnopol'skii Y M, Portnov G G, Zhigun I G. (1971). "Effect of fiber curvature on the modulus of elasticity for unidirectional glass-reinforced plastics in tension," *Polymer Mechanics*, 3:161–166.

[137] Hsiao H M, Daniel I M. (1996). "Elastic properties of composites with fiber waviness," *Composites Part A: Applied Science and Manufacturing*, 27:931–41.

[138] Karami G, Garnich M. (2005). "Effective moduli and failure considerations for composites with periodic fiber waviness," *Composite Structures*, 67:461–475.

[139] Naya F, Herráez M, Lopes C S, González C, Van der Veen S, Pons F. (2017). "Computational micromechanics of fiber kinking in unidirectional FRP under different environmental conditions," *Composites Science and Technology,* 144:26–35.

[140] Pinho S T, Iannucci L, Robinson P. (2006). "Physically-based failure models and criteria for laminated fibre-reinforced composites . Part I: Development," *Composites Part A: Applied Science and Manufacturing*, 37:63–73.

[141] Kaddour A, Hinton M, Smith P, Li S. (2013). "Mechanical properties and details of composite laminates for the test cases used in the third world-wide failure exercise," *Journal of Composite Materials*, 47:2427–2442.

[142] Johnson W, Masters J, Wilson D, Welsh J, Adams D. (1996). "Unidirectional Composite Compression Strengths Obtained by Testing Cross-Ply Laminates," *Journal of Composites Technology & Research*, 18:241–248.

[143] Welsh J S, Adams D F. (1997). "Testing of angle-ply laminates to obtain unidirectional composite compression strengths," *Composites Part A: Applied Science and Manufacturing*, 28:387–96.

[144] Hine P J, Duckett R A, Kaddour A S, Hinton M J, Wells G M. (2005). "The effect of hydrostatic pressure on the mechanical properties of glass fibre/epoxy unidirectional composites," *Composites Part A: Applied Science and Manufacturing*, 36:279–289.

[145] Hoppel C P R, Bogetti T A, Gillespie J W. (1995). "Literature Review-Effects of Hydrostatic Pressure on the Mechanical Behavior of Composite Materials," *Journal of Thermoplastic Composite Materials*, *8*(4), 375–409.

[146] Welsh J S, Adams D F. (1997). "An Experimental Investigation of the Mini-Sandwich Laminate as Used to Obtain Unidirectional Composite Compression Strengths," *Journal of Composite Materials*, 31:293–314.

[147] Czabaj M W, Riccio M L, Whitacre W W. (2014). "Numerical reconstruction of graphite/epoxy composite microstructure based on sub-micron resolution X-ray computed tomography," *Composites Science and Technology*, 105:174–182.

[148] Yurgartis S W. (1987). "Measurement of small angle fiber misalignments in continuous fiber composites," *Composites Science and Technology*, 30:279–293.

[149] Sutcliffe M P F, Lemanski S L, Scott A E. (2012). "Measurement of fibre waviness in industrial composite components," *Composites Science and Technology*, 72:2016–2023.

[150] Shuart M J. (1989). "Failure of compression-loaded multidirectional composite laminates," *AIAA Journal*, 27:1274.

[151] Slaughter W S, Fleck N A, Budiansky B. (1993). "Compressive Failure of Fiber Composites: The Roles of Multiaxial Loading and Creep," *Journal of Engineering Materials and Technology*, 115(3):308–313.

[152] Eyer G, Montagnier O, Hochard C, Charles J P. (2017). "Effect of matrix damage on compressive strength in the fiber direction for laminated composites," *Composites Part A: Applied Science and Manufacturing*, 94:86–92.

[153] FAA. (2009). "AC 33.76-1A - Bird Ingestion Certification Standards."

[154] EASA. (2009). "Bird strike damage & windshield bird strike final report."

[155] Maimí P, Camanho P P, Mayugo J A, Dávila C G. (2007). "A continuum damage model for composite laminates: Part I – Constitutive model," *Mechanics of Materials,* 39:897–908.

[156] Maimí P, Camanho P P, Mayugo J A, Dávila C G. (2007). "A continuum damage model for composite laminates: Part II – Computational implementation and validation," *Mechanics of Materials,* 39:909–19.

[157] Eskandari S, Andrade Pires F M, Camanho P P. (2016). "Intralaminar damage in polymer composites in the presence of finite fiber rotation: Part I – Constitutive model," *Composite Structures,* 151:114–26.

[158] Eskandari S, Andrade Pires F M, Camanho P P. (2016). "Intralaminar damage in polymer composites in the presence of finite fiber rotation: Part II – Numerical analysis and validation," *Composite Structures,* 151:127–41.

[159] Camanho P P, Dávila C G, Pinho S T, Iannucci L, Robinson P. (2006). "Prediction of in situ strengths and matrix cracking in composites under transverse tension and in-plane shear," *Composites Part A: Applied Science and Manufaturing, 37*(2), 165-176.

[160] Yasaee M, Mohamed G, Pellegrino A, Petrinic N, Hallett S R. (2017). "Strain rate dependence of mode II delamination resistance in through thickness reinforced laminated composites," *International Journal of Impact Engineering,* 107:1–11.

[161] LSTC. (2019). LS-OPT | Livermore Software Technology Corp. https://www.lstc.com/products/ls-opt

[162] General Electric Co. (1974). "Aircraft Engine Group. Impact resistance of composite fan blades."

[163] Selezneva M, Stone P, Moffat T, Behdinan K, Poon C. (2010). "Modeling Bird Impact on a Rotating Fan: The Influence of Bird Parameters," In *11th International LS-DYNA Users Conference*.

[164] May M, Nossek M, Petrinic N, Hiermaier S, Thoma K. (2013). "Adaptive multi-scale modeling of high velocity impact on composite panels," *Composites Part A: Applied Science and Manufacturing,* 58:56–64.

Appendix A

Localisation plane angle search

Many of the models presented throughout the previous work are based on Puck's localisation plane theory [12], which relies on the determination of a critical localisation plane for the evaluation of the yield and IFF criteria and for the calculation of fracture area in the damage evolution model. For in-plane stress states, the work in [18] showed that it can be enough to evaluate handful of potential localisation angles: $\theta = 0°$, $\theta = 45°$, $\theta = 30°$, and $\theta = \theta_0$ which is typically assumed to be 52°. However, for 3D stress states, a more thorough search is recommended.

Traditionally, this has been done by evaluating all potential localisation planes between $\theta = -90°$ and $\theta = 90°$ to a resolution of 1°, which can incur a significant computational cost in large FE simulations. Therefore, the work presented in the following sections aims to improve the efficiency of the localisation plane angle search while maintaining the benefits of a high-accuracy solution.

This has been achieved thanks to developments in two main areas. On one hand, the cost of evaluation has been reduced by improving the efficiency of the fracture angle search and, on the other, two upper bound limit functions have been proposed to narrow down the range of stress states where the yield or failure criteria must be evaluated.

A.1. Semi-analytical approximation

By using a direct semi-analytical solution to the yield or failure condition as an initial approximation, the exact solution can then be quickly obtained through a numerical iteration and the cost of the search is greatly reduced. This section describes the calculation of the semi-analytical approximation.

In localisation plane-based criteria, the stress exposure is obtained as a function of the three tractions, σ_n, τ_{n1} and τ_{nt}, acting on the potential fracture plane. Each of these tractions is obtained from the rotation of the three-dimensional Cauchy stress tensor in material coordinates, $\hat{\boldsymbol{\sigma}}$, by the rotation matrix $\boldsymbol{R}_\sigma[\theta]$ from eqn. (3.14). Therefore, the three fracture plane tractions, can be given as a function of the stresses in the material coordinates and the angle, θ:

$$\begin{cases} \sigma_n = \hat{\sigma}_{22}\cos^2\theta + \hat{\sigma}_{33}\sin^2\theta + \hat{\tau}_{23} 2\sin\theta\cos\theta \\ \tau_{n1} = \hat{\tau}_{12}\cos\theta + \hat{\tau}_{13}\sin\theta \\ \tau_{nt} = -\hat{\sigma}_{22}\sin\theta\cos\theta + \hat{\sigma}_{33}\sin\theta\cos\theta + \hat{\tau}_{23}(\cos^2\theta - \sin^2\theta) \end{cases} \tag{A.1}$$

By simplifying each of these expressions into single sinusoidal functions of θ, the role of the fracture angle in the yield or failure criteria can be studied more clearly.

This was achieved using basic trigonometric relations and the superposition of sinusoidal waves of the same frequency, whereby two sinusoidal waves of amplitude A and B and offset by phases α and β can be combined into a single cosine by:

$$\begin{gathered} A\cos(\theta+\alpha) + B\cos(\theta+\beta) = \\ \sqrt{[A\cos(\alpha) + B\cos(\beta)] + [A\sin(\alpha) + B\sin(\beta)]} \\ \cdot \cos\left\{\theta + \tan^{-1}\left[\frac{A\sin(\alpha) + B\sin(\beta)}{A\cos(\alpha) + B\cos(\beta)}\right]\right\} \end{gathered} \tag{A.2}$$

The resulting expressions, given below, separate the effect of the stresses from the effect of the rotation angle to a certain extent, allowing for a clearer interpretation of the three fracture plane tractions that define the likelihood of yielding or matrix failure:

$$\begin{cases} \sigma_n = \left(\frac{\hat{\sigma}_{22} + \hat{\sigma}_{33}}{2}\right) + \sqrt{\left(\frac{\hat{\sigma}_{22}}{2} - \frac{\hat{\sigma}_{33}}{2}\right)^2 + \hat{\tau}_{23}{}^2} \cos\left(2\theta + tan^{-1}\left[\frac{-2\hat{\tau}_{23}}{\hat{\sigma}_{22} - \hat{\sigma}_{33}}\right]\right) \\ \tau_{n1} = \sqrt{\hat{\tau}_{12}{}^2 + \hat{\tau}_{13}{}^2} \cdot \cos\left(\theta + \tan^{-1}\left[\frac{\hat{\tau}_{13}}{\hat{\tau}_{12}}\right]\right) \\ \tau_{nt} = \sqrt{\left(\frac{\hat{\sigma}_{22}}{2} - \frac{\hat{\sigma}_{33}}{2}\right)^2 + \hat{\tau}_{23}{}^2} \cos\left(2\theta + \tan^{-1}\left[\frac{|\hat{\sigma}_{22} - \hat{\sigma}_{33}|}{2\hat{\tau}_{23}}\right]\right) \end{cases} \tag{A.3}$$

From these expressions, σ_n and τ_{nt} are sinusoidal waves of the same amplitude and frequency with a phase offset of 45º, where both the amplitude and offset are defined by $\hat{\tau}_{23}$ and the absolute difference between $\hat{\sigma}_{22}$ and $\hat{\sigma}_{33}$. On the other hand, τ_{n1} has a frequency half of that of σ_n or τ_{nt} and its offset is defined only by $\hat{\tau}_{12}$ and $\hat{\tau}_{13}$.

Independently, the maxima location for each of the three tractions is trivial. For a sinusoidal wave of the type $A\cos(n \cdot \theta + \alpha) + C$, the location of its maximum is defined by its phase shift, $-\alpha/n$, and its value at this point is the sum of the amplitude and vertical shift, $A + C$. These values are given below for the three waves described by the fracture plane tractions in eqn. (A.3).

Maxima Location	Value	
$\boldsymbol{\sigma_n}$: $\theta_1 = \frac{1}{2} tan^{-1}\left[\frac{2\hat{\tau}_{23}}{\hat{\sigma}_{22} - \hat{\sigma}_{33}}\right]$	$\sigma_n^{MAX} = \left(\frac{\hat{\sigma}_{22}+\hat{\sigma}_{33}}{2}\right) + \sqrt{\left(\frac{\hat{\sigma}_{22}}{2} - \frac{\hat{\sigma}_{33}}{2}\right)^2 + \hat{\tau}_{23}{}^2}$	(A.4)
$\boldsymbol{\tau_{nt}}$: $\theta_{2,3} = \theta_1 \pm \frac{\pi}{4}$	$\tau_{nt}^{MAX} = \sqrt{\left(\frac{\hat{\sigma}_{22}}{2} - \frac{\hat{\sigma}_{33}}{2}\right)^2 + \hat{\tau}_{23}{}^2}$	(A.5)
$\boldsymbol{\tau_{n1}}$: $\theta_4 = -tan^{-1}\left[\frac{\hat{\tau}_{13}}{\hat{\tau}_{12}}\right]$	$\tau_{n1}^{MAX} = \sqrt{\hat{\tau}_{12}{}^2 + \hat{\tau}_{13}{}^2}$	(A.6)

However, both the yield and failure criteria, eqn. (3.16) and (4.1), are obtained as a combination of all three tractions and, while their individual maxima are easily determined, the combined solution is not so simple.

Nevertheless, the individual maxima given above may still provide a reasonable initial approximation for the solution of the more complex criteria. More specifically, each of the tractions, σ_n, τ_{n1} and τ_{nt}, can be seen as promoting their preferred localisation planes, θ_1 to θ_4, towards which they will attract the resulting global localisation plane. Therefore, when one of σ_n^{MAX}, τ_{nt}^{MAX}, or τ_{n1}^{MAX} is dominant with respect to the others, the resulting fracture plane will tend to the respective value of θ_1 to θ_4, associated with that traction.

However, in a more general case, while each traction promotes failure along its preferred fracture planes, the final outcome is decided by the interaction between these tractions and the resulting potential fracture plane will lie in between these values.

Therefore, in practice, the simplest approach is to consider these four angles, θ_1 to θ_4, as initial candidates for the resulting global maximum and take the plane with the highest exposure as the starting point for a numerical search of the kind described in [19]. In this way the cost of the search is greatly reduced by simplifying the search for a global maximum to that of a local one.

An illustrative example for an arbitrary stress state $(\hat{\sigma}_{22} = \hat{\sigma}_{33} = -10\ \mathrm{MPa}, \hat{\tau}_{12} = 5\ \mathrm{MPa}, \hat{\tau}_{23} = -15\ \mathrm{MPa}, \text{and}\ \hat{\tau}_{13} = 0\ \mathrm{MPa})$ is shown in Figure A.1. On the left the sinusoidal waves described by each of the three fracture plane tractions, σ_n, τ_{n1} and τ_{nt}, across the potential localisation planes, θ, are shown with their individual maxima, and on the right the shape of the resulting stress exposure function, eqn. (4.1), is represented. The red vertical lines in both figures indicate the preferred fracture planes for each traction, which, as can be seen, closely approximate the local maxima of the overall exposure function.

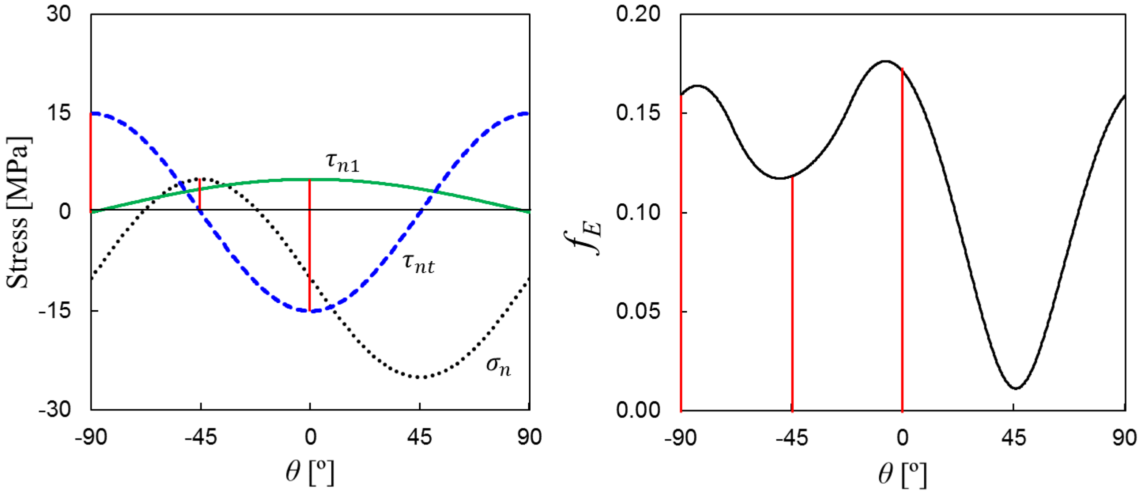

Figure A.1. Localisation plane candidates taken from the maxima of the three traction plane stresses (left) copmared to the Puck IFF exposure (right) for an arbitrary stress state given in material coordinates ($\hat{\sigma}_{22} = \hat{\sigma}_{33} = -10$ MPa, $\hat{\tau}_{12} = 5$ MPa, $\hat{\tau}_{23} = -15$ MPa, and $\hat{\tau}_{13} = 0$ MPa).

A.2. Upper bound limit

Even with the improvements from the previous section, the fact remains that, in a numerical FE simulation, the evaluation of the yield and failure criteria is repeated at every time step and integration point, resulting in a significant addition to the overall computational cost.

Taking inspiration from the idea of a discretisation refinement criterion in [164], the following upper limits to the yield and failure conditions have been defined to determine if the current stress state is close enough to yielding or matrix failure to warrant the full evaluation of the criteria:

$$f_{y+Lim} = \frac{\alpha\sigma_n^{MAX} + \sqrt{{\tau_{n1}^{MAX}}^2 + e{\tau_{nt}^{MAX}}^2}}{\tau_y[\bar{\varepsilon}_p]\, r_y[\dot{\bar{\varepsilon}}]} \geq 1 \qquad \text{(A.7)}$$

$$f_{IFF+Lim} = \sqrt{(1-p_t)^2 \left(\frac{\sigma_n^{MAX}}{R_\perp^+}\right)^2 + \left(\frac{\tau_{n1}^{MAX}}{R_{\perp\parallel}}\right)^2 + \left(\frac{\tau_{nt}^{MAX}}{R_{\perp\perp}^A}\right)^2} + p_t \frac{|\sigma_n^{MAX}|}{R_\perp^+} \geq 1 \qquad \text{(A.8)}$$

Therefore, before these upper bound limits are met, the full yield and failure criteria do not need to be evaluated, reducing the number of times the angle search is performed.